*Measurement artefacts, ion mobility and other observations in environmental mass spectrometry analyses*

HART, Jeremy R.

## A Sheffield Hallam University thesis

# Measurement Artefacts, Ion Mobility and Other Observations in Environmental Mass Spectrometry Analyses

**Jeremy R. Hart**
Biomolecular Sciences Research Centre
Sheffield Hallam University

Supervisors
Professor Malcolm Clench (Director of Studies),
Professor Simona Francese and Dr Vikki Carolan

A thesis submitted in partial fulfilment of the requirements of
Sheffield Hallam University for the degree of
Doctor of Philosophy

May 2020

Sheffield Hallam University | Biomolecular Sciences Research Centre

# Abstract

Many laboratories are engaged in the measurement of persistent organic pollutants, particularly polychlorinated dibenzo-*p*-dioxins (PCDDs), polychlorinated dibenzo-furans (PCDFs) and polychlorinated biphenyls (PCBs), to satisfy various investigative needs and compliance requirements worldwide. However, from a mass spectrometry perspective, the current mandated methods have changed little since their origins in the 1980s and 1990s and fail to address certain issues that can lead to the erroneous rejection or filtering of data, and conversely, to the acceptance of data that may be considered questionable.

Notwithstanding any legislative requirements, since the goal of these analyses is ultimately related to human or animal health, producing accurate and reliable data is of the utmost importance. This research highlights various areas of concern and aims to improve upon the current peak identification and measurement practices that can lead to such false negatives, false positives and other errors. A key contribution made by this thesis concerns the role of ion statistics in peak area measurement and its subsequent effect on isotope ratio determination – a primary parameter (together with chromatographic retention time) for compound identification in both high-resolution mass spectrometry (HRMS) and tandem mass spectrometry (MS/MS) methods.

In an allied area of research, a comprehensive study of all mono- to deca-chlorinated biphenyls using atmospheric pressure chemical ionisation, both for fragmentation analysis and in conjunction with ion mobility spectrometry (IMS), was undertaken. An additional original contribution described in this thesis shows that, in addition to certain structural information – especially in relation to the degree of chlorine ortho substitution – there are some unusual shifts in the measured IMS arrival time distributions of certain PCB isotopologues and isotopomers suggesting the occurrence of isomerisation in the gas phase. Other patterns emerging from these data are indicative of the toxicity of certain PCBs, both correlating with known toxic congeners and others that are currently classified as non-toxic.

# Candidate's Declaration

I hereby declare that:

1. I have not been enrolled for another award of the University, or other academic or professional organisation, whilst undertaking my research degree.
2. None of the material contained in the thesis has been used in any other submission for an academic award.
3. I am aware of and understand the University's policy on plagiarism and certify that this thesis is my own work. The use of all published or other sources of material consulted have been properly and fully acknowledged.
4. The work undertaken towards the thesis has been conducted in accordance with the SHU Principles of Integrity in Research and the SHU Research Ethics Policy.
5. The word count of the thesis is 39,989.

| | |
|---|---|
| Name | Jeremy Rupert Hart |
| Date | May 2020 |
| Award | PhD |
| Faculty | Health and Wellbeing |
| Director of Studies | Professor Malcolm Clench |

# Acknowledgements

I would particularly like to thank my Director of Studies, Prof Malcolm Clench, who, with my other supervisors from the Biomolecular Sciences Research Centre (BMRC) at Sheffield Hallam University, Prof Simona Francese and Dr Vikki Carolan, provided such invaluable help and guidance throughout this study. I would also like to thank the following from the BMRC: Prof Nicola Woodroofe, who, together with Prof Clench, had sufficient faith in my original project ideas to accept me onto the PhD programme. Dr David Smith for the discussions on ion mobility, Dr Alex Hamilton for his introduction to molecular modelling, and Prof Christine Le Maitre and Prof Tom Smith for their continuing support. Finally, my fellow students and the many other academic, technical and admin staff with whom I have been involved and who have made such a difference to this experience.

My work with mass spectrometry started at VG/Micromass/Waters (Manchester, UK) in the 1980s and there are a number of former colleagues who mentored me during my career development – too many for me to name them all, but a few, some sadly no longer with us, cannot go unacknowledged: Bob Moffatt, Alf Monks, Brian Green, Bob Bateman, John Race, John Bill, Dr Keith Hall, Dr Bob Bordoli and Dr Norman Lynaugh amongst many others. I would also like to express my thanks to the many scientists and technicians I came to know over the years, either directly through my work with the MS instrument companies or the various ASMS, BMSS, Dioxin and other conferences.

In 2000, my mass spec career took to me to the USA, an opportunity that arose from my association with another long-time friend and colleague, Dr Yves Tondeur. I would particularly like to thank him for the many interesting and challenging discussions, and expanding my knowledge of environmental mass spectrometry beyond the confines of an instrument manufacturer and into the much broader realm of a commercial laboratory – it was a remarkable time at Analytical Perspectives (later SGS) and which cemented some of the questions that I sought to answer with this research. I would also like to thank Yves and Dr Phillip Hanna for being my local supervisors during the early days of my PhD while still in North Carolina. I would like to thank Dr Bryan Vining and the team in Wilmington as well as my former US and European SGS colleagues for their

support. This is also an opportunity to remember another friend and colleague, the late Bill Luksemburg. Bill and I had worked together on many occasions since the early 1990s, initially through my role in the UK, and later through the association between our lab in NC and his in California.

Over the last few years, I have also become increasingly involved with the EU Reference Laboratories for the testing of PCDD/Fs and PCBs in food and feed. This introduced me to certain regulatory aspects of the EU testing methods, their approach to measurement uncertainty and the idea of developing the congener profiling software. I would like to thank all those with whom I have been involved, but especially to those at the Freiburg lab, formerly led by Dr Rainer Malisch (ret'd), now by Dr Alexander Schächtele.

For the recent APCI-based PCB fragmentation and ion mobility analyses, I had the opportunity to work again with some of my former colleagues, now at the Waters R&D centre in Wilmslow, UK. This has proved to be pivotal to some of the work shown in this thesis and I would therefore like to express my sincere thanks to Brian Smith and Dr Mike Morris for facilitating this, and particularly to Rhys Jones for his invaluable help with the Synapt instrument and for the many discussions along the way.

I would also like to thank my friends and family for their support, and also mention my father, who had instilled, in the (much) younger me, the wonder of all things scientific and technical… even though he never lived to see the career that I ended up pursuing, let alone a PhD, I know he would have loved it!

Finally, I would especially like to thank my wife, Bernadette, for her incredible love and encouragement throughout this whole process – I couldn't have asked for anything more and I dedicate this to her.

> "No problem is insoluble in all conceivable circumstances."
>
> Isaac Asimov, from "The Last Question", 1956

# Table of Contents

# List of Figures

# List of Tables

# List of Terms

*Isomer* – one of a set of compounds with the same chemical formula that differ (for the compounds studied in this thesis) only in the substitution pattern of the halogen atom(s) on the benzene/phenyl rings, e.g. 2,3,7,8-TCDF and 1,2,3,4-TCDF are both isomers of tetrachlorodibenzofuran where the numbers indicate the respective positions of the chlorine atoms.

*Congener* – one of a related set of compounds that share the same base structure, e.g. there are 209 polychlorinated biphenyl (PCB) congeners where one or more chlorine atoms may be substituted in place of any of the 10 hydrogens of the biphenyl molecule. (Note that "poly" in this context includes "mono", i.e. monochlorobiphenyl, of which there are 3 possible isomers.)

*Homologue (group)* – in the context of the published methods for the analysis of the halogenated compounds discussed in this thesis, refers to a subset of congeners with the same chemical formula, e.g. there are 46 possible pentachlorobiphenyls (that are all isomers).

*Isotopologue* – one of a set of compounds with the same chemical formula and structure but with a different isotopic composition of one or more atoms, e.g. $^{12}C_{12}H_4OCl_4$-2,3,7,8-TCDF and $^{12}C_{11}{}^{13}CH_4OCl_4$-2,3,7,8-TCDF are both isotopologues of 2,3,7,8-TCDF. (These molecules therefore have different atomic masses and relative intensities of their isotopes in the molecular ion cluster.)

*Isotopomer* – one of a set of isotopologues that differ in the position of one or more isotopes, e.g. $C_{12}H_4O^{35}Cl_3$-2,[3-$^{37}$Cl],7,8-TCDF and $C_{12}H_4O^{35}Cl_3$-2,3,[7-$^{37}$Cl],8-TCDF are isotopomers that differ in the position of the $^{37}$Cl. (These molecules therefore have identical atomic masses and relative intensities of their isotopes in the molecular ion cluster.)

# List of Abbreviations

| | |
|---|---|
| ADC | analogue-to-digital converter |
| AhR | aryl hydrocarbon receptor |
| AP | atmospheric pressure [ionisation] |
| APCI | atmospheric pressure chemical ionisation |
| ASMS | American Society for Mass Spectrometry |
| ATD | arrival time distribution |
| BEQ | bioanalytical equivalent [concentration] |
| BMSS | British Mass Spectrometry Society |
| CALUX | chemical activated luciferase gene expression |
| CCS | collisional cross section |
| CE | collision energy |
| CID | collision induced dissociation |
| CoM | centre(s)-of-mass |
| CSV | comma separated values |
| DAC | digital-to-analogue convertor |
| DBE | double bond equivalent |
| DeCB | decachlorobiphenyl |
| DFT | density functional theory |
| DiCB | dichlorobiphenyl |
| DL-PCB | dioxin-like polychlorinated biphenyl |
| DSA | DriftScope Analyser |
| DT | drift time |
| DTIMS | drift tube ion mobility spectrometry |
| EDL | estimated detection limit |
| EFSA | European Food Safety Authority |
| EI | electron ionisation |
| EPA | Environmental Protection Agency |
| EU | European Union |
| FAIMS | field asymmetric ion mobility spectroscopy |
| FTICR | Fourier-transform ion cyclotron resonance |
| FWHM | full-width at half-maximum |
| GABA | *gamma*-aminobutyric acid |
| GC | gas chromatograph(y) |
| HpCB | heptachlorobiphenyl |
| HpCDD | heptachlorodibenzo-*p*-dioxin |
| HpCDF | heptachlorodibenzofuran |
| HRMS | high-resolution mass spectrometry |

| | |
|---|---|
| HxCB | hexachlorobiphenyl |
| HxCDD | hexachlorodibenzo-*p*-dioxin |
| HxCDF | hexachlorodibenzofuran |
| IARC | International Agency for Research on Cancer |
| IM(S) | ion mobility (separation) |
| IMS-MS | ion mobility separation – mass spectrometry |
| IR | infrared |
| IRMS | isotope-ratio mass spectrometry |
| IUPAC | International Union of Pure and Applied Chemistry |
| λ (lambda) | the Poisson rate parameter |
| LC | liquid chromatograph(y) |
| LOD | limit of detection |
| LOQ | limit of quantification/quantitation |
| LRMS | low-resolution mass spectrometry |
| $m/z$ | mass-to-charge [ratio] |
| MoCB | monochlorobiphenyl |
| MRM | multiple reaction monitoring |
| MS | mass spectrometry |
| MS/MS | tandem mass spectrometry |
| NATO | North Atlantic Treaty Organization |
| ND | non-detect(ed) |
| NDL-PCB | non-dioxin-like polychlorinated biphenyl |
| NMR | nuclear magnetic resonance |
| NoCB | nonachlorobiphenyl |
| OcCB | octachlorobiphenyl |
| OCDD | octachlorodibenzo-*p*-dioxin |
| OCDF | octachlorodibenzofuran |
| PA | projection approximation [method] |
| p/p | peak-to-peak |
| PBDE | polybrominated diphenyl ether |
| PCA | principal component analysis |
| PCB | polychlorinated biphenyl |
| PCDD | polychlorinated dibenzo-*p*-dioxin |
| PCDD/F | combined PCDD and PCDF |
| PCDF | polychlorinated dibenzofuran |
| PCT | polychlorinated terphenyl |
| PDB | protein database |
| PeCB | pentachlorobiphenyl |
| PeCDD | pentachlorodibenzo-*p*-dioxin |
| PeCDF | pentachlorodibenzofuran |
| PFK | perfluorokerosene |

|  |  |
|---|---|
| POP | persistent organic pollutant |
| ppm | parts per million |
| ppq | parts per quadrillion |
| ppt | parts per trillion |
| Q-TOF | quadrupole – time-of-flight [mass spectrometer] |
| RF | radio-frequency |
| RMS | root mean square |
| RPD | relative percent difference |
| RRT | relative retention time |
| RSD | relative standard deviation |
| RHF | restricted Hartree-Fock |
| RT | retention time |
| σ (sigma) | standard deviation |
| s/n | signal-to-noise [ratio] |
| SIM | selected ion monitoring |
| SRM | selected reaction monitoring |
| TCDD | tetrachlorodibenzo-*p*-dioxin |
| TCDF | tetrachlorodibenzofuran |
| TeCB | tetrachlorobiphenyl |
| TEF | toxic equivalency factor |
| TEQ | toxic equivalent [concentration] |
| TJ | trajectory [method] |
| TOF | time-of-flight [mass spectrometer] |
| TrCB | trichlorobiphenyl |
| TWIMS | travelling wave ion mobility spectrometry |
| UNEP | United Nations Environment Programme |
| USEPA | United States Environmental Protection Agency |
| VB | Visual Basic |
| VBA | Visual Basic for Applications |
| WHO | World Health Organization |

# Chapter 1

# Thesis Overview, Aims and Objectives

## 1.1 Introduction

Concern surrounding the adverse health effects associated with exposure to persistent organic pollutants (POPs) now spans many decades of growing scientific knowledge together with several landmark incidents that have also highlighted the problems in the eyes of the public.

The term "POPs" is used to include several organic chemical classes that:

- Are persistent, i.e. stable in the environment over many years – and also therefore able to be transported both locally and over long distances, principally by water (often bound to sediments) and atmospheric mechanisms
- Are toxic to both humans and animals
- Are bioaccumulative (lipophilic)

The POPs focussed upon in this thesis are those of greatest concern to health due to their high toxicity, e.g. through their binding ability to the cellular aryl hydrocarbon receptor (AhR) (Safe *et al.*, 1985; Sorg, 2014) and their known carcinogenicity (IARC, 2012): specifically certain polychlorinated dibenzo-*p*-dioxins (PCDDs) and polychlorinated dibenzofurans (PCDFs) – often termed simply (if not entirely accurately) as "dioxins" and "furans" by many working in this field[*] – and certain polychlorinated biphenyls (PCBs). The principles discussed can however be directly applied to many other POPs such as polybrominated diphenyl ethers (PBDEs), polybrominated biphenyls (PBBs) and organochlorine pesticides (OCPs).

It was concern on the observed adverse effects of exposure to OCPs, together with other pesticides and herbicides, that perhaps first caught mainstream attention following the publication of Rachel Carson's seminal book, "*Silent Spring*" (Carson, 1962). This has often been credited as signalling the beginnings of wider environmental awareness and

---

[*] Furthermore, the term "dioxins" is often used to reference both PCDDs and PCDFs – as is the case with the European Food Safety Authority (EFSA).

ultimately to the foundation of the United States Environmental Protection Agency in 1970.

PCDDs, PCDFs and PCBs were also amongst the 12 initial POPs[*] listed in the Stockholm Convention (UNEP, 2001). They comprise aldrin[A], chlordane[A], DDT[B], dieldrin[A], endrin[A], heptachlor[A], hexachlorobenzene[A,C], mirex[A], toxaphene[A], PCBs[A,C], PCDDs[C] and PCDFs[C], where the superscript(s) indicate the Convention's annex(es) to which the compounds belong.

The international convention requires its signatories[†] to agree to:

- Eliminate the production and use of chemicals listed under Annex A
- Restrict the production and use of those chemicals listed under Annex B[‡]
- Take measures to reduce the unintentional release of chemicals listed under Annex C

It is important to note that PCBs are included in both A and C annexes since, in addition to their historical manufacture for industrial purposes, they can also be formed as an inadvertent by-product of combustion and other processes.

In 2017, a further 16 POPs were added to the list including: pesticides, such as lindane and endosulfan; fire retardants, such as hexabromocyclododecane, and tetra- and penta-bromodiphenyl ethers; industrial chemicals such as pentachlorobenzene, polychlorinated naphthalenes, perfluorooctane sulfonic acid and short-chain chlorinated paraffins (UNEP, 2017).

Other chemicals currently under review for inclusion are dicofol [1,1-bis(4-chlorophenyl)-2,2,2-trichloroethanol], perfluorooctanoic acid and perfluorohexane sulfonic acid and their related compounds (UNEP, 2018).

---

[*] Also informally known as "the dirty dozen".

[†] As of November 2019, there are 152 signatory countries; notable exceptions are the USA, Italy, Israel and Malaysia (UNEP, 2019).

[‡] Certain restricted uses are permitted, e.g. the use of DDT in the control of malaria where there is no viable alternative.

## 1.2 The chemical structures of PCDDs, PCDFs and PCBs

The following figures show the generic structures for PCBs (Figure 1.1), PCDDs (Figure 1.2) and PCDFs (Figure 1.3) with the chlorine substitution numbering used throughout this thesis, and specific structures of the most toxic compound in each class: 3,3’,4,4’,5-pentachlorobiphenyl (PeCB) (Figure 1.4) – more commonly known by its BZ number (Ballschmiter and Zell, 1980) as PCB-126; 2,3,7,8-tetrachlorodibenzo-*p*-dioxin (TCDD) (Figure 1.5) and 2,3,4,7,8-pentachlorodibenzofuran (PeCDF) (Figure 1.6).

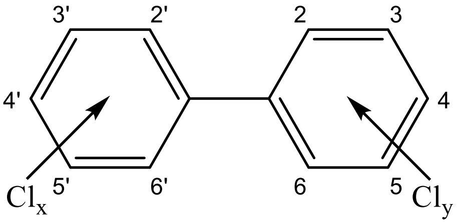

$C_{12}H_{(10-x-y)}Cl_{(x+y)}$

where x + y = 1 to 10

Figure 1.1 Generic polychlorinated biphenyl (PCB) structure

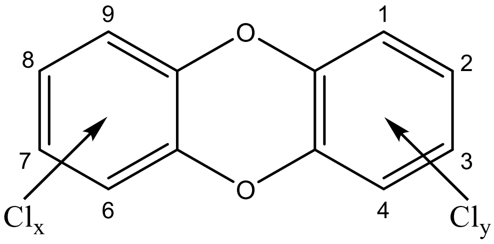

$C_{12}H_{(8-x-y)}Cl_{(x+y)}O_2$

where x + y = 1 to 8

Figure 1.2 Generic polychlorinated dibenzo-*p*-dioxin (PCDD) structure

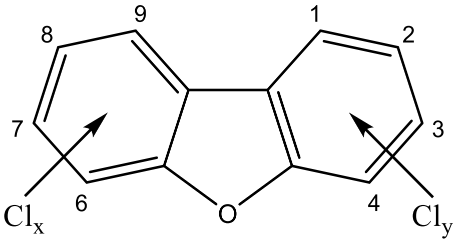

$C_{12}H_{(8-x-y)}Cl_{(x+y)}O$

where x + y = 1 to 8

Figure 1.3 Generic polychlorinated dibenzofuran (PCDF) structure

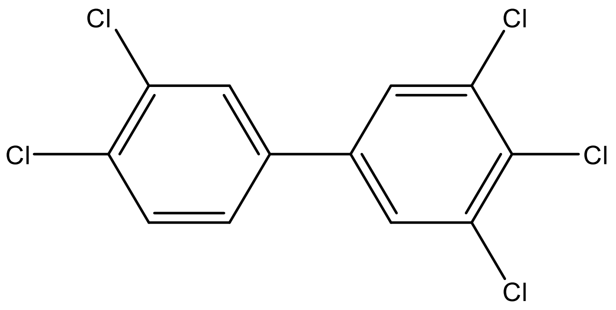

$C_{12}H_5Cl_5$

Figure 1.4 Structure of 3,3’,4,4’,5-pentachlorobiphenyl (PCB-126)

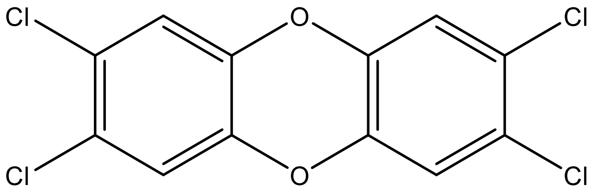

$C_{12}H_4Cl_4O_2$

Figure 1.5 Structure of 2,3,7,8-tetrachlorodibenzo-*p*-dioxin (2,3,7,8-TCDD)

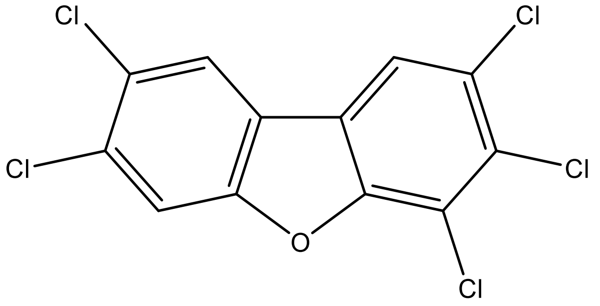

$C_{12}H_3Cl_5O$

Figure 1.6 Structure of 2,3,4,7,8-pentachlorodibenzofuran (2,3,4,7,8-PeCDF)

It is important to note that not all PCDDs, PCDFs or PCBs are currently considered as toxic compounds, as defined by the World Health Organization (WHO) (Van den Berg *et al.*, 2006); of the 210 possible PCDD and PCDF congeners, there are 17 currently classified as being toxic: 7 PCDDs and 10 PCDFs. These are all tetra- to octa-chlorinated with chlorine substitutions in the 2, 3, 7 and 8 positions, and in up to 4 other positions.

Of the 209 PCB congeners, 12 are currently considered as toxic: these are all tetra to hepta-chlorinated with chlorine substitutions in both para (4, 4’) positions, two or more meta (3, 3’, 5, 5’) positions and either zero or one ortho (2) position (i.e. non-ortho or mono-ortho).

Complete lists of the toxic (WHO) PCDD/Fs and PCBs can be found in Table 1.4 (p. 27) and Table 1.5 (p. 27) respectively.

## 1.3 Sources of PCBs, PCDDs and PCDFs

PCBs were manufactured from the 1930s to the late 1970s with an estimated global yield of more than 1 million tons, with more than half having been produced in the U.S. (Erickson, 1997). Commercial PCB production was usually as mixtures of PCB congeners such as the Aroclor™ series manufactured by Monsanto[*]. These were referenced by a 4-digit number, e.g. Aroclor 1254, where the last 2-digits represented the approximate percentage of chlorine by weight[†].

Their excellent electrical insulation, heat transfer, chemical stability and low flammability made them ideal for use within power transformers (Takasuga *et al.*, 2006) and capacitors [‡] (Erickson, 1997). These components, mostly used in electrical distribution systems at power stations, sub-stations and large buildings, accounted for approximately 75% of PCB usage with the remainder being in certain building materials such as sealants and caulks (Klosterhaus *et al.*, 2014), in adhesives, paints and printing inks, and as lubricants and hydraulic fluids (Erickson and Kaley, 2011).

Due to the adverse health effects attributed to PCB exposure (as will be discussed in section 1.4), they were ultimately banned (or phasing-out procedures begun) from manufacture in the USA by the USEPA[§] in 1979 (USEPA, 1979), in Europe[**] in 1985 (European Council, 1985) and in other countries in accordance with the Stockholm Convention of 2001 that came into force in 2004 (UNEP, 2001).

In contrast, although PCDDs and PCDFs were never intentionally produced, they have been, and continue to be, formed as by-products from various industrial activities and

---

[*] Monsanto were the primary (>90% by volume) manufacturer of PCBs in the U.S. (and hence globally) with their Aroclor product range. More than 20 other brands existed, including Clophen (Germany), Kanechlor (Japan) and Sovol (the former USSR), and although these names do appear in the literature, the Aroclor name continues to predominate and is still used in a regulatory context within several American States.

[†] With the exception of Aroclor 1016 as it was already established in the marketplace before the introduction of this naming convention.

[‡] Previously known as “condensers”. Although this is an obsolete term in electronics (and has been so since ca. the 1960s) its use has continued in much PCB related literature.

[§] United States Environmental Protection Agency – henceforth referred to as EPA. [Although many countries have their own EPA (or equivalent body), for the purposes of this thesis, EPA will refer to the US Agency.]

[**] The European regulation also extends to polychlorinated terphenyls (PCTs).

accidental causes. Although no longer manufactured, PCBs can also be formed by many of these same processes. Some of the principal sources are: combustion, such as in (hazardous) waste incineration (Rivera-Austrui *et al.*, 2011), metal smelting or reprocessing (Colombo *et al.*, 2011) and some natural processes such as forest fires (Salamanca, Chandía and Hernández, 2016).

Domestic waste burning (often called "barrel burning" in the US) is also a significant contributor – due to the uncontrolled conditions (relatively low temperatures and incomplete combustion) – where levels can exceed those of municipal waste incineration (Lemieux *et al.*, 2000). Although such burning is less common in many European countries, there can be unusual instances: in the UK, every 5th of November, "Bonfire Night", sees PCDD/F emissions that, over the few days around that event, are of the same order (30 g vs. 38 g) as those produced annually from iron ore sintering used in UK iron and steel manufacturing (Anderson and Fisher, 2002).

Product contamination due to poor manufacturing processes, negligence or accident has also resulted in elevated levels of exposure to these chemicals. Poisoning due to contaminated cooking (rice) oils occurred in the Yusho (Japan, 1968) and the almost identical Yucheng (Taiwan, 1979) incidents. In the Yusho case, a leaking pipe in a heating system used to process the oil led to a commercial PCB mix (Kanechlor 400) with ~48% chlorine content being introduced into the final product at concentrations up to 3,000 ppm (Kuratsune *et al.*, 1972).

PCB contamination also continues to be found in certain pigments used in dyes and paints, e.g. PCB-11 (3,3'-DiCB[*]) in the diarylide "Pigment Yellow 14" ($C_{34}H_{30}Cl_2N_6O_4$) due to synthesis with 3,3'-dichlorobenzidine, PCB-52 (2,2',5,5'-TeCB[†]) in "Pigment Red 9" ($C_{24}H_{17}Cl_2N_3O_3$) due to 2,5-dichloroaniline, and PCB-56 (2,3,3',4'-TeCB) in "Dioxazine Violet" ($C_{34}H_{22}Cl_2N_4O_2$) due to 2,2',5,5'-tetrachlorobenzidine (Anezaki and Nakano, 2014; Anezaki, Kannan and Nakano, 2015). PCB-11 is an additional concern due to its ready volatilisation from paint surfaces leading to its presence in ambient air, particularly in urban environments (Hu, Martinez and Hornbuckle, 2008).

---

[*] Dichlorobiphenyl ($C_{12}H_8Cl_2$)

[†] Tetrachlorobiphenyl ($C_{12}H_6Cl_4$)

Perhaps the most notorious case of contamination was that of "Agent Orange". This refers to the spraying of herbicides (used as defoliants) over large areas of South Vietnam (as it was then known) during the Vietnam War. Several different herbicides were used – known as the "Rainbow Herbicides" due to the various colour stripes marked as identification on their storage drums. Agent Orange, a mix of 2,4-dichloro- and 2,4,5-trichloro-phenoxyacetic acid, was the most predominant of these with ~40 million litres used between 1962 and 1971; it was however contaminated with ~3 ppm of 2,3,7,8-TCDD (Schecter *et al.*, 1995).

Several industrial accidents have also led to the toxic releases of POPs, as exemplified by that in Seveso, Italy in July 1976. During the manufacturing of 2,4,5-trichlorophenol at the ICMESA chemical company, an explosion caused the release of ~30 kg of PCDDs into the surrounding (~18 km$^2$) environment (Mocarelli *et al.*, 1986).

Building fires and disasters are also an on-going source of these compounds – though understandably, any environmental impact is often overshadowed by the loss-of-life and injury. The first (known, documented) case was in 1981 when an electrical panel failure and the subsequent overheating of a transformer in the basement of an 18-storey building in Binghamton (NY, USA) led to the leakage of ~700 litres of transformer fluid. This consisted of a mix of PCBs[*] (Aroclor 1254) and tri- and tetra-chlorobenzenes, and the subsequent fire led to the formation of other PCBs and PCDD/Fs at concentrations in the parts-per-thousand range in the soot (Schecter and Tiernan, 1985).

In 2001, the collapse of the twin towers in the 9/11 World Trade Center disaster resulted in the release of a dust cloud laden with PCDD/Fs created from the towers' building materials and contents, and the ensuing fires (Rayne *et al.*, 2005). More than a decade later, elevated (> 7x) serum levels of PCDD/Fs in adolescents living or attending school in the affected area were observed (Kahn *et al.*, 2018).

In 2017, a major fire – the deadliest in a UK residential environment since World War II – at the Grenfell Tower in London led to a ~50-fold increase in the soil concentration of

---

[*] Although this event postdates the ban on PCBs, there was no legislative requirement to replace existing equipment.

PCDD/Fs in the immediate vicinity of the building relative to urban background measurements (Stec *et al.*, 2019).

Non-anthropogenic sources of PCDD/Fs also exist, e.g. as shown by certain clays. Ball clay (principally kaolinite) and bleaching clay (e.g. bentonite), can be a concern as they have multiple uses as fillers and anti-caking materials in animal feed products, and as filtration materials in the processing of edible oils and nutritional supplements (Ferrario, Byrne and Cleverly, 2000; Tondeur *et al.*, 2012).

Although, as in the above examples, there can be specific occupational and other incidents resulting in exposure to these chemicals, the primary pathway affecting the general public is through food – accounting for more than 90% of an adult's daily intake (Weber *et al.*, 2018). In addition to the chlorinated compounds that are the primary focus of this study, mixed poly-brominated/chlorinated biphenyls have been found to be widespread contaminants in food (Falandysz, Rose and Fernandes, 2012). Serious food related product contamination incidents are fortunately rare; however, they do continue to occur – as shown by the following examples – and stress the importance of continual monitoring of food and animal feed supplies.

Belgium, 1999: a mix of PCBs was accidentally added to recycled fat used in the production of animal feed supplied to over 2,500 farms. The resultant feedstock was found to contain PCBs that were primarily due to a mix of Aroclor 1260 and 1254, and was also contaminated with PCDD/Fs (Bernard and Fierens, 2002). Ultimately, ~7 million chickens and ~60,000 pigs were culled and the damage to the Belgian economy was estimated to be in excess of €1.5 billion (Covaci *et al.*, 2007).

Ireland, 2008: elevated PCB levels were found in a random sampling of animal kidney fat samples by the Irish National Residues Monitoring Programme. Following analysis of the feed material, the source was traced to dried breadcrumbs (from recycled waste dough and bread). A direct drying process had been used with heating fuel found to be contaminated with PCBs, primarily Aroclor 1260 – presumed to be from illegal dumping. In total, over 5,000 cattle and 170,000 pigs were destroyed – the latter being ~10% of the entire pig population (Tlustos *et al.*, 2012).

## 1.4 Health effects from exposure to PCBs, PCDDs and PCDFs

Concern over the health effects of these compounds is not new: an early report associating the skin condition chloracne with industrial exposure to chlorine-based chemicals dates to the beginning of the 20th century, however the cause was then attributed to chlorine gas rather than to any specific compound (Bettmann, 1901). In 1937, a paper reported on the incidence of liver disease in workers in the electrical industry where chlorinated naphthalenes and chlorinated diphenyls (as PCBs were originally known) were used in the manufacture of wire and cable insulation materials (Drinker, Warren and Bennett, 1937).

Although no human deaths are known to have been directly related to these compounds, there have been multiple poisoning and contaminations incidents (Weber, Tysklind and Gaus, 2008). One of the most unusual cases of dioxin poisonings is the (allegedly) intentional one of Viktor Yushchenko in 2004. During his candidacy for Ukrainian presidency, Yushchenko suffered acute pancreatitis, and later exhibited facial jaundice and severe chloracne – well-known symptoms of high-level dioxin exposure. His blood serum levels of 2,3,7,8-TCDD were determined to be some 50,000-fold greater than that of the general population (Sorg *et al.*, 2009).

For many years, cancer has been considered as the primary endpoint for dioxin exposure, and this has been exemplified by the studies examining the effects on the health of Vietnam Veterans due to Agent Orange (Frumkin, 2003). In a more contemporary study, increased rates of certain cancers affecting those involved in rescue and recovery operations following the World Trade Center 9/11 disaster have also been reported (Solan *et al.*, 2013).

PCDD/Fs are currently classified as known human carcinogens by the International Agency for Research on Cancer (IARC) (IARC, 2012) and in 2013 this classification was extended to include the dioxin-like PCBs (DL-PCBs) (Lauby-Secretan *et al.*, 2013). It is interesting to note the authors' comment:

> *"It is important to note that the evaluation of dioxin-like PCBs as carcinogenic to humans (group 1) does not preclude a carcinogenic activity of the other PCB congeners."*

Certain non-dioxin-like PCBs (NDL-PCBs) have demonstrated *in vitro* toxicity through non-AhR mechanisms such as transthyretin binding (Hamers *et al.*, 2011). A 2015 congener-specific meta-analysis study showed that 3 NDL-PCBs (PCB-99, 183 and 187) were linked to an increased risk of breast cancer, and which did not correlate with exposure to DL-PCBs (Leng *et al.*, 2016).

The long-term effect of dioxin exposure on the immune system was identified in a follow-up study on the Seveso incident where plasma immunoglobulin IgG levels, taken 20-years after the event from subjects in the highly exposed group, were found to be inversely correlated to 2,3,7,8-TCDD blood concentration (Baccarelli *et al.*, 2002). It has been reported that paternal dioxin exposure, also following the Seveso incident, has led to a reduced sex-ratio (male-to-female) of their children with rates of less than 0.4 for those with the highest 2,3,7,8-TCDD serum levels (Mocarelli *et al.*, 2000).

The role of dioxin as an endocrine disruptor is evident in multiple adverse reproductive health effects including endometriosis, a severe condition affecting the lining of the womb and/or uterus in women of reproductive age (Birnbaum and Cummings, 2002).

Other mechanisms including the ryanodine receptor (Pessah, Cherednichenko and Lein, 2010; Wayman *et al.*, 2012) and the $GABA_A$ receptor (Antunes Fernandes *et al.*, 2010) have also been shown to be responsive to NDL-PCBs, particularly in relation to neurodevelopmental disorders.

Neurotoxic disorders and damage to the central nervous system were also identified in those – particularly women – affected by the Yucheng poisoning (Lin *et al.*, 2008). The Yucheng cohort also showed links with diabetes and, as with the above neurotoxicity study, women were significantly more affected (Wang *et al.*, 2008).

## 1.5 Ultratrace Analysis Methods for Persistent Organic Pollutants

Knowledge of the levels of POPs in environmental sources, in food – the primary route of exposure to humans – and in targets such as serum and tissue, is key to understanding the mechanisms involved in formation, transport and effects of these compounds. To fill this gap in knowledge, various methods have been developed for ultratrace analysis, i.e. at parts-per-trillion (ppt) and parts-per-quadrillion (ppq) concentrations, and quantification of POPs using gas chromatography[*] coupled to high-resolution mass spectrometry (GC-HRMS). The focus here is on the mass spectrometry elements of PCDD/Fs and PCB analysis, however certain aspects of sample preparation that directly relate to the measurement process are also discussed, e.g. the addition of various isotopically labelled standards in the sampling, extraction, clean-up and pre-injection stages.

There are multiple methods and variants in use worldwide for GC-HRMS analyses of POPs, but they all derive from the prototypical EPA Method 8290, *"Polychlorinated Dibenzodioxins (PCDDs) and Polychlorinated Dibenzofurans (PCDFs) by High Resolution Gas Chromatography/High Resolution Mass Spectrometry (HRGC/HRMS)"* (Tondeur *et al.*, 1989), and its successor, EPA Method 1613, *"Tetra- through Octa-chlorinated Dioxins and Furans by Isotope Dilution HRGC/HRMS"* – first published in 1990, now "1613B" (USEPA, 1994).

Examples of other current methods are:

- EPA Method 1668C: Chlorinated Biphenyl Congeners in Water, Soil, Sediment, Biosolids and Tissue by HRGC/HRMS (USEPA, 2010)
- EPA Method 1614: Brominated Diphenyl Ethers in Water Soil, Sediment and Tissue by HRGC/HRMS (USEPA, 2007a)
- EPA Method 1699: Pesticides in Water, Soil, Sediment, Biosolids and Tissue by HRGC/HRMS (USEPA, 2007b)

---

[*] Several methods continue to refer to this as high-resolution gas chromatography (HRGC) which originally signified the use of capillary, rather than (their predecessor) packed, columns. Since all current GC practice in this field uses capillary columns (and has done so for more than 30 years) this use of "HR" is effectively redundant.

- BS EN 16215:2012: Animal feeding stuffs. Determination of dioxins and dioxin-like PCBs by GC/HRMS and of indicator PCBs by GC/HRMS (CEN, 2012)

To meet these methods' requirements in terms of mass resolution, sensitivity and dynamic range, the analyses are still predominately performed on traditional magnetic sector GC-HRMS instruments, although, as discussed in section 1.13, recent instrument developments now allow for the use of tandem mass spectrometry (GC-MS/MS) for certain analyses.

The principal concepts for discussion are:

- The need for high-resolution to achieve adequate mass separation between the target compounds and other isobaric interferences.
- Data acquisition using the selected ion monitoring (SIM) mode to achieve the required sensitivity with the monitoring of 2 ions for each homologue[*] group of compounds. (An additional ion pair is also used for the $^{13}$C-labelled standards associated with each homologue group.)
- Compound identification and confirmation based on GC retention time and isotopic abundance.
- The role of "isotope dilution", i.e. using fully-labelled[†] $^{13}$C standards for calibration and subsequent sample quantification purposes, and determination of congeners' recoveries.

---

[*] A homologue group represents all isomers at a particular chlorination level, e.g. the <u>tetra</u>chlorodibenzo-*p*-dioxin (TCDD) group comprises 22 isomers: 1,2,3,4-TCDD, 1,2,3,6-TCDD, 2,3,7,8-TCDD, etc.

[†] Where all $^{12}$C atoms in the target compound are substituted by the stable $^{13}$C isotope, thus forming a standard that accurately mimics the chemical behaviour of the native analyte but with each of its isotope peaks displaced to a higher mass according to the number of carbon atoms present in the molecule, e.g. 12 Da in the case of dioxins or PCBs, thus allowing separate measurement by the mass spectrometer.

## 1.6 The need for high resolution

The extraction, fractionation and clean-up processes, defined within the above EPA and related methods, are designed to concentrate the target compounds and remove, or at least minimise, certain interferences. Such residual interferences may give rise to isobaric peaks (i.e. with ions formed at the same nominal mass as those of interest), and in some cases, these peaks' intensities can be several orders of magnitude greater than those of interest. This is often a significant problem with environmental samples due to the presence of other chlorinated compounds that would largely prevent any meaningful measurements using low-resolution mass spectrometry (LRMS) at the ultratrace levels sought for the target compounds. For this reason, high-resolution, i.e. ≥ 10,000 ($m/\Delta m$, 10% valley definition[*]), is specified by these methods for its ability to discriminate between the mass of the target compounds' ions and those due to the most common interferences.

High-resolution is also required to isolate ions from isotopically labelled standards (spiked into the samples for quantification purposes), from perfluorokerosene[†] (PFK), a reference compound that is continuously admitted into the ion source for lock-mass purposes (i.e. to correct for any mass drift) and to indicate instrument stability, and from background ions from GC column bleed or other extraneous sources.

Figure 1.7 illustrates six potential isobaric interfering peaks from polychlorinated compounds in the region of TCDD's molecular ion base peak at *m/z* 321.8937; these are each annotated with their *m/z*, mass difference relative to the TCDD peak (in ppm) and the resolution required for separation.

It is important to note that chemical interferences can still be of concern, even at a mass resolution that is nominally sufficient for their separation from the target analytes' ions,

---

[*] Magnetic sector HRMS has traditionally used the 10% valley definition for mass resolution – defined as $m/\Delta m$ – and this will be assumed throughout this thesis unless otherwise specified. An alternative measure, Full-Width Half-Maximum (FWHM), equivalent to a 50% valley definition, is commonly used when expressing resolution for other instruments such as those based on Time-Of-Flight (TOF).

[†] Other reference compounds such as heptacosafluorotributylamine (commonly "heptacosa" or "FC43") are sometimes used in this application, but PFK remains the most prevalent due to its well-spaced peaks and mass range that extends to ca. *m/z* 1,000 making it also suitable for the analysis of polybrominated compounds.

due to peak “tails” that can arise from poor abundance sensitivity (Murray *et al.*, 2013). Such tails – resulting from instrument tuning artefacts, focussing aberrations or ion scattering due to inadequate analyser vacuum – can extend to several peak widths and lead to “break-through” interference peaks, particularly from high-level contaminants.

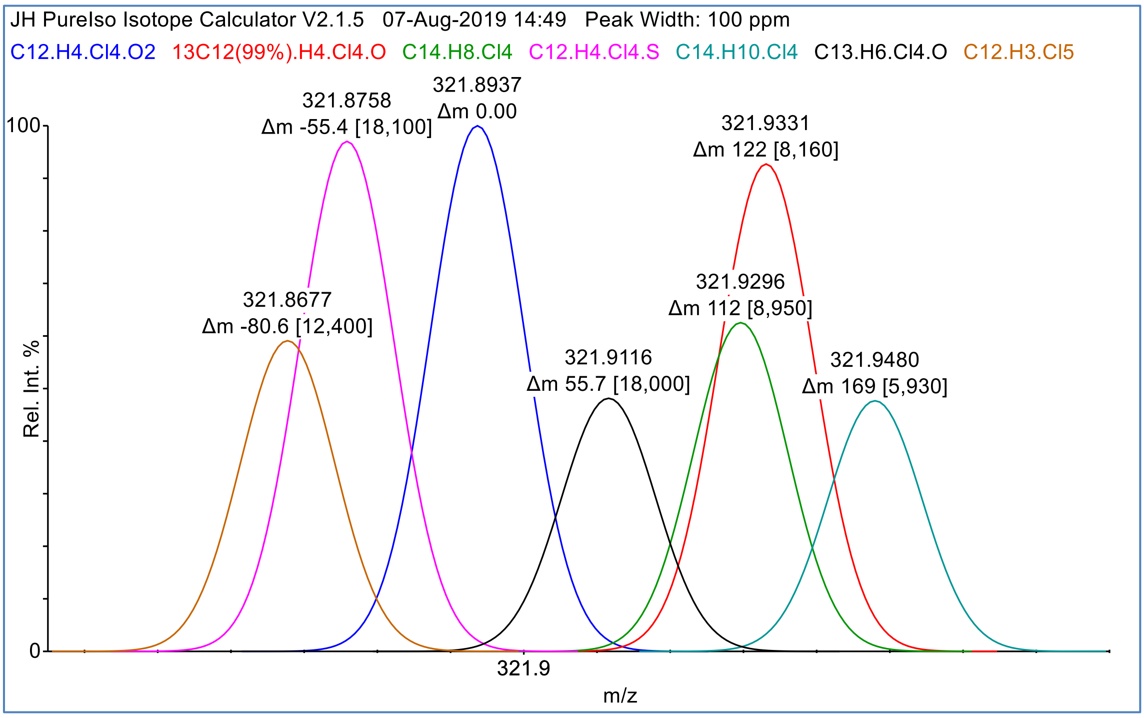

Figure 1.7 Illustration showing potential interferences in the region of the *m/z* 321.8937 peak of TCDD.

The peaks are each annotated with their exact *m/z*, mass difference relative to TCDD (Δm, ppm) and the corresponding mass resolution (to 3 significant figures) required for separation. The peaks shown (from left) are:

$C_{12}H_3{}^{35}Cl_5$ (321.8677) – product ion due to the loss of $Cl_2$ from heptachlorobiphenyl (HpCB)

$C_{12}H_4{}^{35}Cl_3{}^{37}ClS$ (321.8758) – tetrachlorodibenzothiophene

$C_{12}H_4{}^{35}Cl_3{}^{37}ClO_2$ (321.8937) – tetrachlorodibenzo-*p*-dioxin (TCDD)

$C_{13}H_6{}^{35}Cl_2{}^{37}Cl_2O$ (321.9116) – tetrachloroxanthene

$C_{14}H_8{}^{35}Cl^{37}Cl_3$ (321.9296) – dichlorodiphenyldichloroethylene (DDE)

${}^{13}C_{12}H_4{}^{35}Cl^{37}Cl_3O$ (321.9331) – ${}^{13}C$-labelled tetrachlorodibenzofuran (TCDF)

$C_{14}H_{10}{}^{35}Cl_2{}^{37}Cl_2$ (321.9480) – dichlorodiphenyldichloroethane (DDD)

(Peak intensities are arbitrarily scaled for clarity.)

The underlying reasons for the original (EPA-8290) method's mass resolution specification of 10,000[*] are undocumented, but the value would appear to be a reasonable compromise given the performance of contemporary[†] magnetic sector instruments and the 1 ppt detection limit requirement for TCDD and TCDF from a 10 g soil/sediment sample. This corresponds with the ability to detect a low-point, 1 pg/µL, calibration standard at a signal-to-noise ratio ≥ 10 whilst simultaneously providing sufficient mass separation for routine analyses. This mass resolution is also well-suited to the precision governed by the use of an 18-bit digital-to-analogue converter (DAC) for the primary mass selecting electronics, i.e. the electrostatic analyser and accelerating voltage references, of ~4 ppm (i.e. from $1 / 2^{18}$).

## 1.7 The need for high sensitivity

To achieve the required sensitivity, and the associated limits of detection and quantification, the MS data are acquired using the SIM mode[‡] rather than conventional full-scan analysis. Although the latter would, in principle, better characterise the data by allowing the use of spectral library searching and/or accurate mass measurements to confirm compound identification, its much lower sensitivity (for any one mass) – typically 2 to 3 orders of magnitude – precludes its use for these ultratrace analyses.

This difference in sensitivity is directly related to the number of ions detected for any particular *m/z* which in turn is proportional to the amount of time spent at that *m/z*. This is equally true for any type of scanning instrument[§], i.e. one where only a single

---

[*] Nevertheless, 10,000 remains the specified resolution in current versions of these methods.

[†] The original development of this method having been done on a VG ZAB-3F (VG Analytical, Manchester, UK) HRMS from the early 1980s at the EPA (Las Vegas, NV, USA) laboratories.

[‡] Specifically, voltage-SIM (rather than magnet-SIM) to provide the required mass specificity and speed of switching between masses.

[§] This is not the case for time-of-flight (TOF) instruments since all ions from any one extraction pulse ("push") reach the detector. There are nevertheless losses due to duty-cycle limitations in TOF analyses since a proportion of ions are effectively lost between pushes since, to avoid overlap, it is necessary for all high *m/z* ions to reach the detector before any low *m/z* ions from the subsequent push arrive. (This can be ameliorated in certain hybrid Q-TOF instruments where the use of a travelling-wave tube can optimise the grouping of ions according to their *m/z* prior to TOF analysis.)

mass or mass loss transition can reach the detector at any one time, e.g. magnetic sector or quadrupole (in either MS or MS/MS operation).

The time-per-peak ($T_p$, seconds) in a magnet scan experiment on a sector HRMS instrument at a given mass resolution ($Res$, m/Δm), scan rate ($R_{scan}$, seconds/decade) and rate constant[*] ($k_{rate}$) of 2.3 is approximately:

$$T_p \approx R_{scan} / (k_{rate} \times Res) \qquad (1.1)$$

For example, given that the methods of interest specify a nominal mass resolution of 10,000, from the above equation (1.1), the $T_p$ at a 1 second/decade (magnet) scan rate is: 1 / (2.3 × 10,000) ≈ 43 µs.

Compared to the SIM experiment, where only a limited number (typically 10 to 20) of characteristic *m/z* for the target compounds and their standards are monitored at any one time, with a typical cycle[†] time of 1 second, 20 *m/z* channels would result in an average channel time of 50 ms and therefore a dwell[‡] time of 40–45 ms per channel – or about 1,000x greater than that obtained in full-scan mode. It is important to note that, although mass resolution is a key parameter in the calculation of $T_p$ in the full-scan acquisition mode, it plays no role in SIM.

In full-scan acquisition, $T_p$ could be increased by reducing the scan rate, but that would have to be done in conjunction with reducing the mass range such that the overall cycle time was effectively the same in order to provide sufficient[§] data points across each GC peak. For example, a PCB experiment comprising all masses from monochlorobiphenyl

---

[*] The rate constant (*k*) of 2.3 (or more exactly 2.3026) derives from the exponential magnet scan law. This is described in more detail in Appendix C.1.

[†] The cycle time is the total time spent recording data for each *m/z* (dwell time) and the switching time between consecutive *m/z* in any one function. This is also sometimes used in a full-scan experiment to indicate the sum of the scan time and any inter-scan delay.

[‡] The dwell time is the actual time spent recording the ion intensity data at each *m/z* of interest; it is less than the channel time due to the time required to switch between *m/z* – typically, 5-10 ms on a HRMS and < 5 ms on a quadrupole instrument.

[§] At least 7 data points are required to adequately define a peak for integration purposes with 10 or more preferred. Given the typical GC peak width in these experiments of approximately 10 seconds (at the peak's baseline), the required overall scan or cycle time should therefore be no more than 1 second.

(MoCB, $C_{12}H_9Cl$) to decachlorobiphenyl (DeCB, $C_{12}Cl_{10}$) would require a low mass of ~180 Da and a high mass of ~510 Da (this mass range would also be sufficient to include suitable calibration masses); this represents approximately half a decade of mass [i.e. $\log_{10}$ (510 / 180)]. Such a change would therefore allow the scan rate to be changed to 2 seconds/decade and still achieve the same number of data points across a GC peak, however, $T_p$ has only increased by a factor of 2, which is negligible compared to the gains from using SIM acquisition.

Further improvements could be made by splitting the acquisition into several functions – as is usually done in SIM experiments – such that a limited mass range, covering just the masses of interest that elute over a pre-determined retention time window, is analysed. This could give a further 5-fold improvement in some instances but would still fall far short of the comparable SIM signal. Using discrete acquisition functions with smaller mass ranges would also permit the use of voltage scanning but this would offer no advantage in terms of sensitivity as the *average* $T_p$ in this mode would be approximately equal to that in magnet scanning given the same cycle time. It is important to note that, unlike in magnet scanning where $T_p$ is constant across the mass range, $T_p$ varies throughout a voltage scan such that it is proportionately greater at the low mass relative to the high mass by a factor of high mass / low mass.

Another factor affecting instrument sensitivity is the ion source's electron energy: as with the rationale behind the choice of mass resolution in EPA-8290, a requirement for this to be between 28 and 40 eV to optimise performance appeared in the 1600-series methods without any references or explanation even though this was notably different to the 70 eV traditionally used for EI analyses.

The underpinnings of this low eV range for EI can be traced back to a 1986 ASMS poster presentation (Green *et al.*, 1986) showing that the use of lower electron energies gave an overall improvement in sensitivity by decreasing the level of helium[*] ionisation, that in turn results in less suppression of analyte ions exiting the source due to reduced space-charge effects. Therefore, although it would have been reasonable to include this as a recommendation – or indeed as a historic observation – it seems inappropriate to

---

[*] Helium being the preferred choice of GC carrier gas for this application.

have it as a mandatory requirement as different source designs and/or configurations of the ion extraction optics may result in other optimal values.

## 1.8 The need for high dynamic range

The current version of the PCB method, EPA-1668C (USEPA, 2010), specifies a calibration range from 0.2 to 2000 pg/µL for each compound thus defining a $10^4$:1 linear, dynamic range requirement. However, this only states the case for PCBs at single chlorination level.

Figure 1.8 shows the modelled molecular ion cluster for monochlorobiphenyl (MoCB) with most of the charge distributed over just 4 ions (> 1%) and with ~67% present in the base peak; this compares to 12 ions (> 1%) for decachlorobiphenyl (DeCB), with ~25% in the base peak as shown in Figure 1.9.

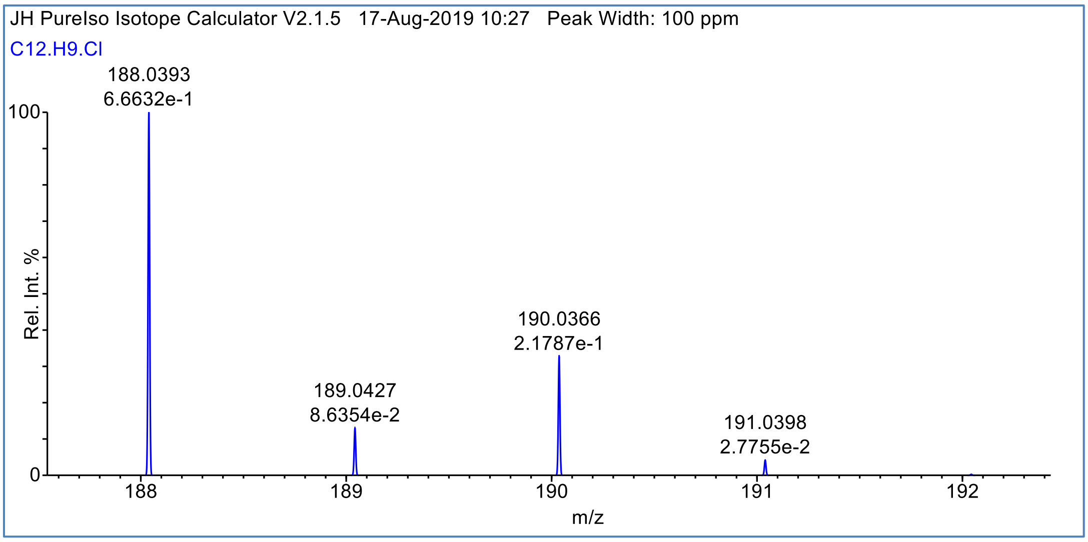

Figure 1.8 Modelled molecular ion distribution for monochlorobiphenyl (MoCB, $C_{12}H_9Cl$) showing exact *m/z* and abundances.

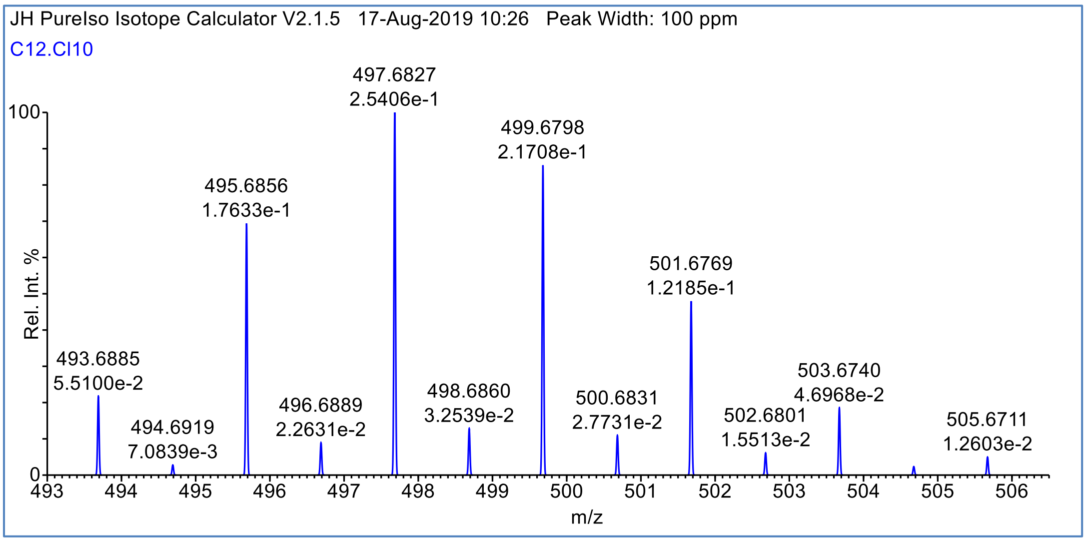

Figure 1.9 Modelled molecular ion distribution for decachlorobiphenyl (DeCB, $C_{12}Cl_{10}$) showing exact *m/z* and abundances.

Given the additional factor of the GC peak width of DeCB being ~11 secs, compared to ~7 secs for MoCB, it would be expected that the MoCB base peak would be ~4.2x more intense than that for DeCB (for the same amount). Experimental data shows this to be ~6.4x – the difference being likely due to greater fragmentation of DeCB – and therefore the required instrument dynamic range should, in practice, be at least ~$10^5$:1 to allow for this and any other variations in instrument performance. This is within the performance specification of both HRMS (in SIM mode) and quadrupole-based MS/MS [in multiple reaction monitoring[*] (MRM) mode] instruments where up to $10^6$ dynamic range is available, but is at, or greater than, the range currently achievable with ion trap or time-of-flight (TOF) based instruments[†].

---

[*] MRM (also known as selected reaction monitoring or SRM) follows the same principles as SIM in terms of sensitivity vs. scanning acquisition; the key difference being that the data acquired are due to product ions from selected precursor ions.

[†] Manufacturers' specifications (as of Sep. 2019): Waters AutoSpec-Ultima (HRMS) – $10^6$:1, Agilent 6495 (triple-quadrupole MS) – $10^6$:1, Thermo Scientific Orbitrap – $10^5$:1, Waters Synapt Q-TOF > $10^4$:1.

## 1.9 SIM experiment overview

As referenced in section 1.7, SIM experiments can be optimised by splitting the masses to be acquired over several functions (groups) such that a minimum number are acquired at any one time, and in the case of magnetic sector HRMS instruments, to limit the high *m/z* to low *m/z* ratio within any one function to 2:1[*]. In PCB analysis, this is further constrained by the overlapping GC retention time windows, as shown in Table 1.1.

| **Function** | **PCB's acquired** | ***m/z* range** | **Magnet *m/z* [1]** | **Voltage ratio[2]** |
|---|---|---|---|---|
| 1 | Mono, Di | 188–236 | 178 | 1.33 |
| 2 | Di, Tri, Tetra | 222–304 | 216 | 1.41 |
| 3 | Tri, Tetra, Penta | 254–340 | 240 | 1.42 |
| 4 | Tetra, Penta, Hexa, Hepta | 290–408 | 278 | 1.47 |
| 5 | Penta, Hexa, Hepta, Octa | 324–442 | 314 | 1.41 |
| 6 | Hepta, Octa, Nona | 394–476 | 390 | 1.22 |
| 7 | Deca | 498–512 | 490 | 1.04 |

Table 1.1 Acquisition function setup for the HRMS SIM analysis of PCBs.
For each function, the chlorination levels (Mono–Deca) acquired are shown with their required *m/z* range. [1]For each function, the magnet is set ~3 *m/z* units lower than the PFK reference *m/z* immediately below the lowest acquired *m/z*. [2]The resulting voltage ratio is then determined from the acquisition high mass relative to the magnet mass.

During the acquisition of any one function, the *m/z* channels are cycled through in sequence and, as with all magnetic sector HRMS instruments operating in the voltage-SIM mode, these are selected by proportional changes to the voltages supplied to the ion source, electrostatic analysers and other focussing lenses. Each *m/z* change requires a certain inter-channel delay, typically 5–10 ms – principally limited by the switching speed of the ion source's high-voltage (nominally 8 kV for the AutoSpec-Ultima) power supplies – for the instrument to reach and stabilise on each successive *m/z* peak prior to recording its intensity for a specified dwell time.

The dwell time for each *m/z* can be the average value determined from the cycle time (as discussed in section 1.7), or optimised according to the sensitivity requirement of a

---

[*] Although not a hard limit, the 2:1 ratio limit arises from the adverse effects of dropping the accelerating voltage (and other focussing elements' supplies) by that proportion; these include loss of resolution and sensitivity.

specific *m/z*, i.e. increasing the dwell times for target analytes' *m/z* that require greater sensitivity/signal-to-noise, relative to that needed for the $^{13}$C-labelled standards that are present at (nominally) constant, relatively high, concentrations. (The underlying theory behind this is discussed in depth in Chapter 2.)

In addition to the analytes' and standards' *m/z*, an additional reference (PFK) *m/z* channel is used for lock-mass purposes. This is a single-point determination intended to compensate for any drift in the magnet's transmitted *m/z* (primarily due to drift in its control electronics), and it is assumed that the same correction can be applied equally to all channels. Its operation consists of a narrow-range voltage scan, usually 2 peak-widths (i.e. 200 ppm at a mass resolution of 10,000), over the reference *m/z*, such that its peak centroid, and thus any departure from the centre of the *m/z* window, can be measured and an appropriate correction applied. A further channel, often at the same *m/z* as the lock-mass channel, is used as a quality-control (QC) check to indicate correct lock-mass operation and to signal any variations in the ion source's response. Table 1.2 shows an example of the *m/z* descriptors used for function 4 of the PCB experiment.

| ***m/z*** | **Delay (ms)** | **Dwell (ms)** | **Description** | **Formula** |
|---|---|---|---|---|
| 289.9224 | 20 | 60 | Tetra-CB M+0 | $C_{12}H_6{}^{35}Cl_4$ |
| 291.9194 | 6 | 60 | Tetra-CB M+2 | $C_{12}H_6{}^{35}Cl_3{}^{37}Cl$ |
| 301.9626 | 10 | 10 | $^{13}$C-labelled Tetra-CB M+0 | $^{13}C_{12}H_6{}^{35}Cl_4$ |
| 303.9597 | 6 | 10 | $^{13}$C-labelled Tetra-CB M+2 | $^{13}C_{12}H_6{}^{35}Cl_3{}^{37}Cl$ |
| 323.8834 | 6 | 60 | Penta-CB M+0 | $C_{12}H_5{}^{35}Cl_5$ |
| 325.8804 | 6 | 60 | Penta-CB M+2 | $C_{12}H_5{}^{35}Cl_4{}^{37}Cl$ |
| 327.8775 | 6 | 40 | Penta-CB M+4 | $C_{12}H_5{}^{35}Cl_3{}^{37}Cl_2$ |
| 330.9792 | 6 | 20 | PFK lock-mass QC check | $C_7F_{13}$ |
| 330.9792 | 5 | 50 | PFK lock-mass | $C_7F_{13}$ |
| 337.9207 | 10 | 10 | $^{13}$C-labelled Penta-CB M+2 | $^{13}C_{12}H_5{}^{35}Cl_4{}^{37}Cl$ |
| 339.9177 | 6 | 10 | $^{13}$C-labelled Penta-CB M+4 | $^{13}C_{12}H_5{}^{35}Cl_3{}^{37}Cl_2$ |
| 359.8415 | 6 | 50 | Hexa-CB M+2 | $C_{12}H_4{}^{35}Cl_5{}^{37}Cl$ |
| 361.8385 | 6 | 50 | Hexa-CB M+4 | $C_{12}H_4{}^{35}Cl_4{}^{37}Cl_2$ |
| 371.8817 | 10 | 10 | $^{13}$C-labelled Hexa-CB M+2 | $^{13}C_{12}H_4{}^{35}Cl_5{}^{37}Cl$ |
| 373.8788 | 6 | 10 | $^{13}$C-labelled Hexa-CB M+4 | $^{13}C_{12}H_4{}^{35}Cl_4{}^{37}Cl_2$ |
| 393.8025 | 10 | 50 | Hepta-CB M+2 | $C_{12}H_3{}^{35}Cl_6{}^{37}Cl$ |
| 395.7995 | 6 | 50 | Hepta-CB M+4 | $C_{12}H_3{}^{35}Cl_5{}^{37}Cl_2$ |
| 405.8428 | 10 | 10 | $^{13}$C-labelled Hepta-CB M+2 | $^{13}C_{12}H_3{}^{35}Cl_6{}^{37}Cl$ |
| 407.8398 | 6 | 10 | $^{13}$C-labelled Hepta-CB M+4 | $^{13}C_{12}H_3{}^{35}Cl_5{}^{37}Cl_2$ |

Table 1.2 Example of the SIM *m/z* descriptors used for the Tetra to Hepta-CB function of a HRMS PCB experiment.

## 1.10 Compound identification: retention time and isotope ratio

Since the methods examined in this thesis are focussed on chlorinated compounds (although the ideas discussed would apply to many other analytical situations, and particularly to those used for other, singly or mixed, halogenated compounds) two[*] ions are monitored for each compound, or group of isomers, of interest. The ions chosen are usually[†] the two most intense found in the molecular ion cluster and which are principally formed due to the varying contributions of the two naturally occurring chlorine isotopes[‡], $^{35}Cl$ and $^{37}Cl$. An example of the calculated molecular ion cluster of octachlorobiphenyl (OcCB) is shown in Figure 1.10 with the two major ions at *m/z* 427.76 and 429.76.

During GC-HRMS or GC-MS/MS analysis, the elution of a compound of interest will produce chromatographic peaks at a known retention time in each ion trace being monitored. The two peaks must coelute within 1 second to be considered valid and their peak areas calculated, and summed, for quantification purposes. In addition, the isotope ratios of these compounds – directly calculated from the ratio of the two peak areas – can then be compared with their corresponding theoretical values.

---

[*] With one exception: during PCDD/F analysis, a $^{37}Cl_4$-2,3,7,8-TCDD labelled standard is used to monitor sample clean-up efficiency (in addition to the usual $^{13}C_{12}$-labelled standards used for extraction/recovery purposes), since this only contains $^{37}Cl$ isotopes, just one ion is recorded.

[†] In certain cases, interferences from reference compounds or other background sources such as “bleed” from the GC column or injector septum, necessitate other choices.

[‡] Isobaric contributions due to the naturally occurring isotopes of C, H (and O for dioxins and furans) are also present and not separated even at high (≥ 10,000) mass resolution, however their intensities are sufficiently lower (< 1%) than the major isotope peaks and therefore do not need to be included in the general discussion. As an example, the most intense peak of the OcCB molecular ion cluster discussed in this section is *m/z* 429.7606 ($C_{12}H_2{}^{35}Cl_6{}^{37}Cl_2$) at 100%; the next 2 most intense peaks are *m/z* 429.7702 ($^{12}C_{10}{}^{13}C_2H_2{}^{35}Cl_7{}^{37}Cl$) and *m/z* 429.7732 ($^{12}C_{11}{}^{13}CHD^{35}Cl_7{}^{37}Cl$) with contributions of 0.68% and 0.0027% respectively.

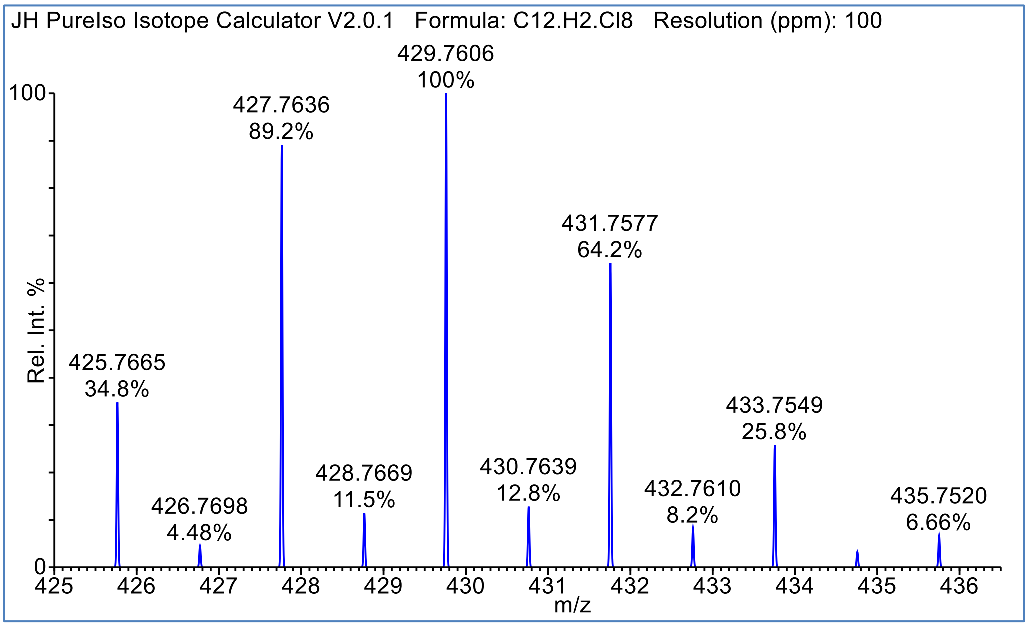

Figure 1.10 Modelled molecular ion distribution for octachlorobiphenyl (OcCB, $C_{12}H_2Cl_8$) showing exact *m/z* and relative abundances.

In the OcCB example above, this is 89% from the abundances of *m/z* 427.76 and 429.76. The agreement of these values (subject to the method's ±15% tolerance), typically together with the method's RT criterion (e.g. -1 s to +3 s for a toxic PCB relative to its labelled standard) determines whether the compound is considered as being positively identified. It should be stressed that for an ultratrace SIM experiment, the *only* criteria available for positive compound identification are the ion abundance ratio and the retention time (or relative retention time).

To illustrate this, Figure 1.11 shows the mass chromatograms for several OcCB congeners: the traces show data for the M+2 ($C_{12}H_2{}^{35}Cl_7{}^{37}Cl$) and M+4 ($C_{12}H_2{}^{35}Cl_6{}^{37}Cl_2$) ions from the molecular ion cluster of the naturally occurring (native) species, and the corresponding M+2 ($^{13}C_{12}H_2{}^{35}Cl_7{}^{37}Cl$) and M+4 ($^{13}C_{12}H_2{}^{35}Cl_6{}^{37}Cl_2$) chromatograms for the fully $^{13}$C-labelled OcCB standard used for quantification purposes. The lower trace, *m/z* 366.9792 ($C_{10}F_{13}$), is due to the perfluorokerosene (PFK) reference compound that is continuously admitted into the ion source for lock-mass purposes (i.e. to correct for any instrument mass drift) and to indicate instrument stability.

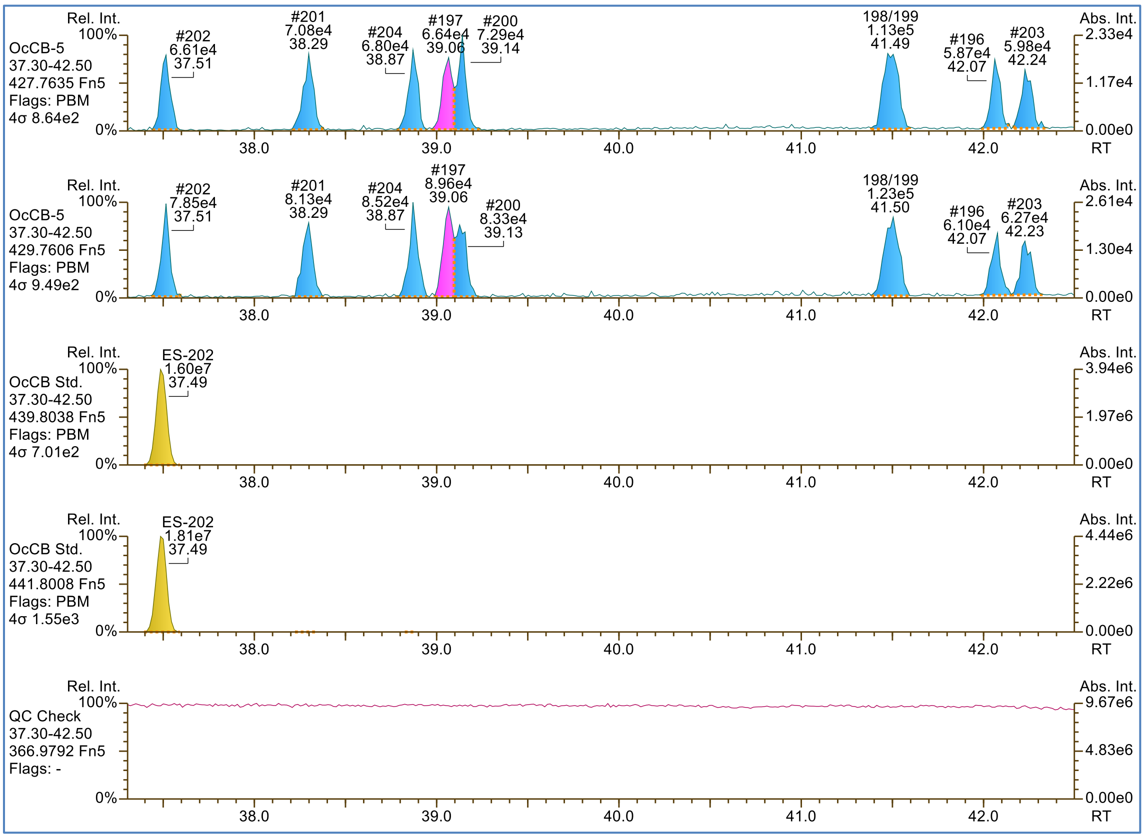

Figure 1.11 Chromatograms for the native OcCB M+2 (*m/z* 427.7635) and M+4 (*m/z* 429.7606) ions, $^{13}$C-labelled OcCB M+2 (*m/z* 439.8038) and M+4 (*m/z* 441.8008) ions, and the QC check ion (PFK, *m/z* 366.9792).
Data acquired using an AutoSpec-Ultima GC-HRMS instrument (Waters, Wilmslow, UK) using the experimental conditions described in section 2.3.
Peak colour code: blue – native PCB (in-ratio), magenta – native PCB (out-of-ratio), yellow – $^{13}C_{12}$-labelled PCB standard.

Of the 9 native isomers present – including the peak doublet at RT 41.49 formed from the coelution of PCB-198 and PCB-199 – all are within the accepted ion abundance ratio with the exception of PCB-197, as indicated by the purple shading. These data are summarised in Table 1.3. For each peak, the actual ($Ra_{Act}$) and theoretical isotope ratio ($Ra_{Theo}$) are shown together with the ratio error ($Err_{Ra}$), simply calculated as shown in equation (1.2).

$$Err_{Ra} = \frac{Ra_{Act}}{Ra_{Theo}} - 1 \tag{1.2}$$

The “Ratio OK” flag is set according to the current EPA-1668C method’s ±15% tolerance. The errors show a typically random spread centred close to zero (-2.3%) and with no evidence of any significant systematic bias.

| Congener | GC Retention Time | Measured Isotope Ratio | Theoretical Isotope Ratio | Measured Isotope Ratio Error | Error within ± 15% |
|---|---|---|---|---|---|
| PCB-202 | 37.51 | 0.84 | 0.89 | -5.4% | Yes |
| PCB-201 | 38.29 | 0.87 | 0.89 | -2.2% | Yes |
| PCB-204 | 38.87 | 0.80 | 0.89 | -10.3% | Yes |
| PCB-197 | 39.06 | 0.74 | 0.89 | -16.7% | No |
| PCB-200 | 39.14 | 0.88 | 0.89 | -1.7% | Yes |
| PCB-198/199 | 41.49 | 0.92 | 0.89 | 2.9% | Yes |
| PCB-196 | 42.07 | 0.96 | 0.89 | 8.0% | Yes |
| PCB-203 | 42.24 | 0.95 | 0.89 | 7.0% | Yes |
|  |  |  | **Mean** | **-2.3%** |  |

Table 1.3 Measured vs. theoretical isotope ratios and errors for a set of OcCB congeners from the data shown in Figure 1.11.

The above data therefore identify one of the key questions of this thesis: why, given that the sample analysed here is a mix of known PCB standards, were not all peaks positively identified? Although, in this case, just a single peak fell outside the (usual) 15% tolerance criterion, as discussed in Chapter 2, this is an arbitrary value. A key proposal outlined is that errors introduced into the measurement system due to ion statistics give rise to sufficient random variability in the peak areas and are the most predominant cause of peaks failing the isotope ratio test.

The isotope ratio check was originally established to confirm the presence of those compounds targeted by the method and reject those from interfering peaks from giving rise to false positives, and it might seem that the significance of weak peaks being rejected is minor, i.e. that they represent low concentrations; this may be true, but low recoveries and other sensitivity considerations can result in peaks that are weaker, and hence noisier, than expected given their actual concentration. In addition, toxicity calculations – as discussed in the following section – can lead to further distortion of the data.

## 1.11 Toxic equivalency factors and toxic equivalent concentrations

Regulations concerning PCDD/Fs and PCBs, such as those governing their acceptable levels in food products within the European Union (EU) (European Commission, 2006), are based on a sample's overall toxicity. However, since these compounds have varying degrees of toxicity, their concentrations cannot be simply added; instead for each compound, its concentration is multiplied by its corresponding toxic equivalency factor (TEF) prior to summation into a toxic equivalent concentration (TEQ).

For n compounds:

$$TEQ = \sum_{i=1}^{n} Conc_i \times TEF_i \tag{1.3}$$

Several different sets of TEF values have existed since their origins in the 1980s, from the US, Canada, the Scandinavian countries, Germany, and from the North Atlantic Treaty Organization[*] (NATO) and the World Health Organization (WHO) (Bhavsar *et al.*, 2008). Certain US States have also developed their own TEFs that were applicable to air emission regulations, e.g. Massachusetts, that, unusually, included factors for mono, di and tri-chlorinated, and other non-2,3,7,8 substituted dioxins and furans (Massachusetts Department of Environmental Protection, 1991).

The original version of the WHO TEFs, in "*Toxic equivalency factors (TEFs) for PCBs, PCDDs, PCDFs for humans and wildlife*" (Van den Berg *et al.*, 1998), also considered different taxa with separate mammalian, avian and aquatic TEF values. As a result of various revisions and harmonisation of the above schemas, two sets of TEFs remain in current, widespread use for both toxicity studies and regulatory work: the International-TEFs (I-TEFs) (Kutz *et al.*, 1990) and the WHO TEFs[†] (Van den Berg *et al.*, 2006).

---

[*] Specifically, its Committee on the Challenges of Modern Society (1988).

[†] Also commonly referred to (including within this thesis) as the WHO-2005 TEFs to differentiate them from the previous 1998 TEFs.

In all cases, the factors are based on the AhR binding activity relative to 2,3,7,8-TCDD – as (currently) the most toxic PCDD/F or PCB with its value of 1 – and encompass over four orders of magnitude. Any other PCDD/F or PCB congener not listed is deemed non-toxic with a TEF of zero. Table 1.4 lists the I-TEFs and WHO-2005 TEFs for PCDD/F and Table 1.5 lists the WHO-2005 TEFs for PCBs.

| PCDD/F | I-TEFs | WHO 2005 TEF |
|---|---|---|
| 2,3,7,8-TCDD | 1 | 1 |
| 1,2,3,7,8-PeCDD | 0.5 | 1 |
| 1,2,3,4,7,8-HxCDD | 0.1 | 0.1 |
| 1,2,3,6,7,8-HxCDD | 0.1 | 0.1 |
| 1,2,3,7,8,9-HxCDD | 0.1 | 0.1 |
| 1,2,3,4,6,7,8-HpCDD | 0.01 | 0.01 |
| OCDD | 0.001 | 0.0003 |
| 2,3,7,8-TCDF | 0.1 | 0.1 |
| 1,2,3,7,8-PeCDF | 0.05 | 0.03 |
| 2,3,4,7,8-PeCDF | 0.5 | 0.3 |
| 1,2,3,4,7,8-HxCDF | 0.1 | 0.1 |
| 1,2,3,6,7,8-HxCDF | 0.1 | 0.1 |
| 1,2,3,7,8,9-HxCDF | 0.1 | 0.1 |
| 2,3,4,6,7,8-HxCDF | 0.1 | 0.1 |
| 1,2,3,4,6,7,8-HpCDF | 0.01 | 0.01 |
| 1,2,3,4,7,8,9-HpCDF | 0.01 | 0.01 |
| OCDF | 0.001 | 0.0003 |

Table 1.4 I-TEFs and WHO-2005 TEFs for PCDDs and PCDFs.

| BZ # | PCB | Type | WHO 2005 TEF |
|---|---|---|---|
| PCB-77 | 3,3’,4,4’-TetraCB | Non-ortho | 0.0001 |
| PCB-81 | 3,4,4’,5-TetraCB | " | 0.0003 |
| PCB-126 | 3,3’,4,4’,5-PentaCB | " | 0.1 |
| PCB-169 | 3,3’,4,4’,5,5’-HexaCB | " | 0.03 |
| PCB-105 | 2,3,3’,4,4’-PentaCB | Mono-ortho | 0.00003 |
| PCB-114 | 2,3,4,4’,5-PentaCB | " | 0.00003 |
| PCB-118 | 2,3’,4,4’,5-PentaCB | " | 0.00003 |
| PCB-123 | 2,3’,4,4’,5’-PentaCB | " | 0.00003 |
| PCB-156 | 2,3,3’,4,4’,5-HexaCB | " | 0.00003 |
| PCB-157 | 2,3,3’,4,4’,5’-HexaCB | " | 0.00003 |
| PCB-167 | 2,3’,4,4’,5,5’-HexaCB | " | 0.00003 |
| PCB-189 | 2,3,3’,4,4’,5,5’-HeptaCB | " | 0.00003 |

Table 1.5 WHO-2005 TEFs for PCBs.
(I-TEF values have not been established for PCBs.)

Notwithstanding the necessity of the TEF/TEQ methodology in determining a sample's toxicity, it is important to recognise that the effect of any errors in peak measurement and/or identification due to weak ion statistics (discussed in Chapter 2) or fragmentation effects (discussed in Chapter 4) can be magnified using these factors. If a peak is erroneously included or disregarded, this may be considered of little relevance if it is of very low or zero toxicity, but for a highly toxic congener, with its associated high TEF, the 'gearing' effect on the reported data can be significant. This not only distorts the results for the sample in question – with possible serious compliance implications – but can also lead to misleading comparisons with other samples, e.g. using pattern matching or other database assessments.

The TEF/TEQ model's importance is further established in risk assessment studies. The European Food Safety Authority (EFSA) Panel on Contaminants in the Food Chain, in "*Risk for animal and human health related to the presence of dioxins and dioxin-like PCBs in feed and food*" (Knutsen *et al.*, 2018), has established a new* tolerable weekly intake (TWI) level of 2 pg $TEQ_{WHO\text{-}2005}$/kg (body weight).

The development of tables for neurotoxic equivalence is also being undertaken where, in a complementary approach to the AhR activity used for the above TEQ tables, the PCB potencies in respect of (e.g.) ryanodine receptor activity and inhibition of dopamine uptake are established; however this work is not considered sufficiently robust at this time (Simon, Britt and James, 2007; Pradeep *et al.*, 2019).

---

* The previous EFSA TWI (2001) was 14 pg $TEQ_{WHO\text{-}1998}$/kg (body weight).

## 1.12 Isotope dilution: the use of stable isotopically labelled standards

This concept of "isotope dilution", in the context of these methods, means that a compound's concentration is primarily[*] quantified using the ratio of its response (the sum of its peak areas) to that of an isotopically labelled standard. For example, 2,3,7,8-TCDD would have its concentration determined by reference to the labelled, $^{13}C_{12}$-2,3,7,8-TCDD, standard.

A key benefit of isotope dilution is that variations in the analytes' recoveries during the sample extraction and/or clean-up processes (which may be unavoidable with certain sample matrices) do not lead to incorrect concentration determinations. Since the target analytes and their labelled standards only differ in whether their molecules are formed of $^{12}C$ or $^{13}C$ atoms, their chemistries are nominally identical and are thus equally affected throughout the processing stages.

It is important to note that this form of *true* isotope dilution only applies to those compounds that have a labelled standard with an identical isomer configuration (i.e. isotopologues), however, since the availability of $^{13}C$-labelled standards is limited[†] to the toxic compounds and a subset of the remainder (e.g. the first and last eluters at each level of chlorination), compromises are invariable needed, e.g. 1,4,6,9-TCDD, in the absence of its $^{13}C$ counterpart, would also be quantified against $^{13}C_{12}$-2,3,7,8-TCDD. Such approximations are considered acceptable within the methods given the (arguably) lesser importance of these compounds.

These labelled standards are added (spiked) to the sample prior to any extraction or other processing – in essence, this spiking event defines "the sample" from the laboratory's perspective, since it is at this point that the relationships between the native target compounds and their corresponding standards are first established (Tondeur and Hart, 2009). This distinction can be critical if a sample is split into multiple

---

[*] Other factors include the (mean) relative response factor obtained during calibration, spiking amounts and sample weight or volume. However, solvent dilutions are not factored into these concentration calculations since, as with analyte recovery calculations, the native and standard responses would be equally affected.

[†] Even if/as additional $^{13}C$-labelled standards become available, it should be noted that they add significant cost to the analysis. E.g. > US$ 5,000 (Aug. 2019) for a set of EPA-1613 PCDD/F standards [containing 500 ng per component (i.e. sufficient for ~250 samples)].

aliquots prior to spiking – if these are not homogenous then the subsequent analysis of another aliquot could yield significantly different results. Sediment samples are a case in point, where large variations in particle size and other aspects of the material are not uncommon. This can be problematical enough at the typical 10 g sample size, but the effect can be further amplified when dealing with heavily contaminated samples and the consequent need to work with smaller sample sizes such as 1 g to keep within the calibration range of the instrument[*].

Although the most immediate benefits of isotope dilution relate to concentration precision and accuracy, e.g. as demonstrated by interlaboratory studies (Eppe *et al.*, 2008), the use of these labelled standards also allows the (extraction) recoveries of the target compounds to be calculated. For this purpose, the standards' responses are measured relative to an additional labelled standard added at the final stage of sample preparation immediately prior to GC-MS analysis, e.g. $^{13}C_{12}$-1,2,3,4-TCDD would be used to determine the recovery of $^{13}C_{12}$-2,3,7,8-TCDD.

Such recovery information can also help address the issue when there is no (expected) response for a certain compound and the question is raised as to whether it is truly absent from the sample (or at least below the analytical limit of detection), or, could the compound possibly have been present in the original sample, but subsequently lost from the sample extract during its processing? Similarly, other labelled standards can be added at intermediate sample preparation stages such that any recovery related problems can be isolated to a particular stage of the process, e.g. extraction, aliquot splitting, clean-up or concentration.

The isotope dilution approach also inherently corrects for the effect of certain other analytical artefacts: in-source fragmentation at different electron energies within electron ionisation (EI) sources or protonated ion formation in atmospheric pressure (AP) ion sources; variation in collision cell conditions and subsequent fragmentation in MS/MS. Isotope dilution is therefore at the heart of expanding these existing methods beyond their original (EI based) GC-HRMS based scope.

---

[*] Sample dilution can be used to reduce peak responses, for example, to bring them into the instrument's operational or linear range, but this does not alter their relationship to the calibration curve – although it is often incorrectly assumed to do so in order to bring compounds' responses within the calibration range.

Other benefits associated with isotope dilution are that variations in the instrument's detector gain, actual sample injection volume, solvent dilution and certain other parameters that would also equally affect both the target compound and its standard, can therefore be (correctly) ignored in any concentration calculation. However, although a particular compound's calculated concentration may be invariant with recovery and certain other conditions (since its relative response is unchanged), its detection limit, measurement uncertainty, and hence analytical fitness-for-purpose can be affected (since its absolute response has changed).

## 1.13 Alternative technologies: MS/MS

GC-MS/MS is an alternative to GC-HRMS for the analysis of POPs as it can effectively filter isobaric interferences (such as those discussed in section 1.6) which, due to their different structures, would not produce the same fragment ions and hence not be detected. E.g. for TCDD analysis, transitions corresponding to the loss of COCl (63 Da) would be monitored, e.g. *m/z* 319.9 > 256.9 and *m/z* 321.9 > 258.9.

MS/MS has been previously shown to be a useful alternative to HRMS for the analysis of POPs and, in cases where mass resolutions of > 10,000 are required, may be the preferred choice (Charles and Tondeur, 1990). However, this work, based on hybrid magnetic sector / quadrupole instrumentation, had been mostly confined to areas of fundamental research rather than routine analyses. More recently, improvements in triple-quadrupole instrument stability and sensitivity, including the use of atmospheric pressure chemical ionisation (APCI), have shown that this technique is now viable for routine analysis of PCDD/Fs (van Bavel *et al.*, 2015; Organtini *et al.*, 2015) and other POPs such as halogenated flame retardants (Megson *et al.*, 2016).

At the time of writing, it remains the case that only magnetic sector HRMS instruments operating in the SIM mode can meet the requirement specifications for *all* ultratrace methods (PCDD/F, PCB, PBDE and organochlorine pesticides) for *all* matrices. However since 2017, considering the above advances and comparative studies with EI/HRMS data (ten Dam *et al.*, 2016), GC-MS/MS, using triple-quadrupole mass spectrometry, has been approved for use within the EU for confirmatory[*] analyses of food and animal feed products but this is only for measurement of the subset of 17 PCDD/Fs and 12 PCBs for which WHO TEFs have been defined, and is not applicable to other sample matrices (European Commission, 2017).

The EU also permits the use of GC-LRMS (e.g. single-quadrupole instruments) for analysis of the 6 Indicator PCBs, namely PCB-28, 52, 101, 138, 153 and 180. This small subset of the 209 PCB congeners have been deemed to be representative of a sample's toxicity but are typically present in food/feed products at much higher concentrations than the actual (WHO) toxic PCBs, thus enabling their analysis using LRMS. This therefore allows a lower-cost option that can be used for batch screening purposes, however any samples exceeding the statutory levels set for those compounds require confirmatory analyses using GC-HRMS or GC-MS/MS (European Commission, 2017).

Other mass spectrometry techniques – e.g. Q-TOF (hybrid quadrupole time-of-flight) based MS/MS, high-resolution TOF and high-resolution ion trap MS – will undoubtedly enter this analytical sphere as their performance continues to improve, but have yet to be shown as viable replacements for GC-HRMS on which the methods, and regulations, are currently based. The latter point on regulations may also hinder the adoption of new methodologies for work involving litigation since clients may continue to express a preference for, or demand the use of, conventional methods to avoid any uncertainty in data presented for scrutiny[†].

---

[*] Confirmatory analyses are required to determine whether a product exceeds its legal limits for any particular matrix. Such testing often follows lower cost screening analyses used to tentatively identify problematic samples.

[†] Based on the author's personal discussions with clients of large-scale (> $1M) projects.

## 1.14 Alternative technologies: bioanalytical analysis

In an area related to TEQ determination, it should be mentioned that immunoassay based analyses such as chemical-activated luciferase gene expression (CALUX) (Murk *et al.*, 1996) are a commonly used alternative to mass spectrometry based methods for the assessment of PCDD/Fs and PCBs in terms of a sample's bioanalytical equivalent concentration (BEQ) (Baston and Denison, 2011). Such analyses are based on certain cell lines having a measurable response to AhR activity – widely thought to be the main mechanism of dioxin toxicity, and specifically carcinogenicity, though this remains contentious (Sorg, 2014).

This technique is now accepted as a screening tool within the EU for the analysis of PCDD/Fs and PCBs in food and feed (European Commission, 2017), subject to a sufficient number of samples being confirmed by GC-MS. In principle, the BEQs should match the TEQs derived from GC-HRMS or GC-MS/MS data (i.e. with the appropriate TEFs applied), however many data show variances of up to 3x (both lower and higher) for certain matrices. For the higher BEQ results this is perhaps indicative of the presence of other compounds, such as polybrominated biphenyls or polychlorinated naphthalenes that were not analysed in the GC-MS data, and for the lower BEQ results, in there being inconsistencies between the CALUX data and the WHO TEF model (Croes *et al.*, 2013).

It is important to note that an important limitation of these bioassay methods is that the practice of isotope dilution is implicitly not possible. This is because any isotopically labelled standards would create responses indistinguishable from those of the target compounds, therefore any sample extraction or clean-up problems leading to low recoveries – and the ensuing measurement errors – would not be apparent.

Another potential weakness is that current regulations are based on TEQ limits, and these could be revised if toxicity via other receptor mechanisms becomes sufficiently well understood – and ultimately regulated: e.g. several PCBs have been suggested as being neurotoxic, but their mechanisms of action are via the ryanodine receptor (Pessah *et al.*, 2010; Wayman *et al.*, 2012) and the $GABA_A$ receptor (Antunes Fernandes *et al.*, 2010), rather than via the AhR, and would therefore not be measured using these existing techniques.

## 1.15 Thesis outline, aims and objectives

Many laboratories are engaged in the measurement of PCDD/Fs and PCBs in food, animal feed, environmental (e.g. air, water, soil), industrial and other samples to fulfil the needs of various regulatory standards worldwide. In addition to such compliance work, numerous studies are being continually performed to determine the effects and fate of these compounds in epidemiological studies and in cases of historical and/or ongoing contamination incidents.

Such programmes can vary considerably in their scope: from small scale projects consisting of a few samples, to multi-year investigations involving thousands of samples from a wide geographical spread or from epidemiological studies. For example, projects relating to the modelling, and subsequent remediation, of contaminated waterways require complementary studies to characterise multiple locations with the analysis of the various POPs from multiple matrices: e.g. water, sediments (surface, core), fish, benthic, etc. Such projects inevitably require multiple instruments and personnel, and with the work often split across multiple laboratories. Furthermore, sampling and analysis can occur in multiple episodes with wide-ranging timescales from a few days or weeks to open-ended projects spanning years. Even if a project's initial design specifies sampling over a certain period, this can be subject to change due to adverse weather, personnel, sampling or laboratory equipment problems, etc. It is therefore critical to have consistent sampling, analytical and reporting criteria for the resultant data to be meaningful and comparable.

The established GC-HRMS methods, for the measurement and quantification of PCDD/Fs and PCBs in real-world samples at ultratrace levels (introduced in section 1.5), contain the detailed procedures required to fully complete a sample's analysis – from initial preparation (extraction, clean-up, concentration, etc.) through to HRMS analysis and data processing with all associated calibration and quality-control. However, these methods, as typified by EPA-1613 (USEPA, 1994) and its derivatives, have changed little in principle since their origins in the 1980s and 1990s and fail to address several important issues; in certain cases, their prescriptive approach can lead to the erroneous rejection or filtering of data, and conversely, to the acceptance of data that may be considered dubious.

A key example is where the data from a presumptive compound fails the isotope ratio test, which, together with GC retention time is just one of 2 criteria required for positive identification using the current methods. Although intended as a means of rejecting chemical interferences – since it was assumed that, with HRMS data, any interfering compounds would not share the same isotope ratio – false negative results can arise from otherwise valid peaks due to the statistical nature of the data giving rise to out-of-ratio peaks, particularly with low-level[*] signals. Similarly, false positives can occur from interference peaks – that would otherwise not pass the ratio criterion – but could do so if certain measurement errors result in an in-ratio peak assessment.

Chapter 2 discusses the mass spectrometer's peak detection process and the ion statistics associated with the peak intensity and subsequent area measurements used to determine the isotope ratio and other results. Although this, as mentioned above, is a key peak identification parameter, the underlying mechanisms have been completely overlooked in the current methods with fixed ratio tolerances being used without any supporting rationale.

An important aspect of this thesis is therefore to explain these processes as such errors are direct artefacts related to the number of ions recorded at the instrument's detector, and from which there is a calculable probability as to whether the ratio test will pass or fail. This information could be used to enhance the methods' identification criteria and hence lead to improved data quality.

As part of the study concerning isotope ratios in Chapter 2, it was necessary to obtain published ratios for comparison purposes – this highlighted several inconsistencies between values published in the various methods and computed values made using the instrument's software. As no references were available as to the sources of the masses and abundances used, or to the software's calculation methods, an *ab initio* program was created to allow for known parameters and processes to be used throughout.

Chapter 3 examines the development of this program and compares its calculated masses and abundances with those promulgated in the published methods and those

---

[*] Though not necessarily at a low concentration since a low-level signal could also be, for example, due to low recovery of the target compound, suppression in the ion source or the immediate ion extraction area due to space charge effects from excessive levels of coeluting interferences, or from other instrument performance or setup deficiencies.

generated using other sources. An additional benefit from this software development is that it allows for isotopically labelled standards of varying purities to be modelled – in contrast to the instrument's and other software that incorrectly assume 100% purity. The software also permits the calculation of abundances using modelled Gaussian peaks to consider the contribution from the minor isotopologues at specific masses over mass windows according to the instrument's resolution.

In a related area, errors in the measured isotope abundances and *m/z* due to mixed charge-exchange and protonation during atmospheric pressure ionisation are also discussed.

Another potential source of data errors is due to that of ion fragmentation during PCB analysis: as discussed in Chapter 4, because several homologue groups have overlapping chromatographic retention time windows, product ions, due to the loss of 1 or 2 chlorine atoms or of HCl from higher-chlorinated species, can interfere with various target compounds leading to potential false positives, false negatives or incorrect concentration determinations. Although the current version of the PCB method, EPA-1668C, cautions as to the possibility of interfering fragment ions being generated, it provides no indication as to the scale of any such errors, or of the markedly different effects on the target compounds according to the fragment loss involved, e.g. -Cl, -2Cl.

A further aim of this thesis is therefore to characterise these fragmentation effects with focus on the WHO toxic PCB congeners where even small errors can lead to significant differences in a sample's reported overall toxicity. The references to fragmentation in the current method (and its predecessors) were based on the use of GC-HRMS with EI – being the only viable technique at the time of the method's writing. Given the increasing use of APCI and GC-MS/MS, PCB fragmentation with this form of ionisation and at various collision energies is also examined in Chapter 4. An unexpected observation made during this work suggested that Cl/H exchange or $H_2$ adduct formation was also occurring concurrently with the loss of Cl for certain PCBs.

A new research area for the analysis of PCBs, ion-mobility separation combined with mass spectrometry (IMS-MS), is described in Chapter 5. This technique provides structural information, in terms of an ion's rotationally averaged collisional cross-section (CCS) area, to be determined from its ion-mobility arrival time distribution (ATD) data and related parameters. Given that a given PCB's toxicity is related to its ability to bind to various cell receptors – itself a function of the compound's structure – this work examines the correlation between the ATDs of the 209 PCBs, their resultant CCS values, structures and known toxicities. Comparisons are also made between the experimental and published data, and that derived from molecular modelling.

An examination of the IMS-MS data of fragment ions also supported the anomalies reported in the previous chapter concerning Cl/H exchange or $H_2$ adduct formation. An unusual discovery from this work is that certain PCBs – predominantly those with the ortho positions occupied by Cl atoms – exhibit a bi-modal ATD profile for some, but not all, isotopologue ions with the data suggesting that partial isomerisation is occurring.

---

Notwithstanding any legislative requirements, since the goal of many of these analyses is ultimately related to human or animal health, producing accurate and reliable data is of the utmost importance. The overall aim of this research is to bring a greater understanding of the underlying science of mass spectrometry to the world of environmental analysis to improve data quality: this entails making the methods truly "performance-based" with dynamic rather than fixed criteria for peak identification, and that not only allows the appropriate use of newer and alternative technologies but also encourages it.

# Chapter 2

# Ion Statistics in Ultratrace Environmental Mass Spectrometry

## 2.1 Introduction

The central elements for compound identification and quantification in the ultratrace analyses of PCDD/F and PCB data acquired in the SIM mode were introduced in section 1.10. This chapter examines the role of ion statistics in those peak intensity measurements and the, often unobserved, errors that can ensue.

For any compound, its peak areas are determined from the chromatographic traces of two characteristic *m/z* in the molecular ion cluster* at a predetermined retention time (RT). As with all MS measurements, these peak areas are subject to a certain statistical variance as the production of ions in the instrument's source can be described by the Poisson process (2.1). This follows since the formation of an ion is a discrete event, its average rate – for a constant flux of material within the source – is constant and its occurrence is independent of the formation of any previous ions.

$$P(k) = \frac{\lambda^k e^{-k}}{k!} \quad , k = 0, 1, 2 \ldots \qquad (2.1)$$

Where P(k) is the Poisson probability of observing k events in each interval and λ (lambda) is the rate parameter, i.e. the average number of events per interval.

A fundamental property of a Poisson distribution is that its variance is equal to the mean (Rice, 2007); given that the mean is directly proportional to the number of ions in any given (chromatographic) peak – which can be derived from the peak's area measurement – its variance can therefore be calculated, and hence its standard deviation (σ) and relative standard deviation (RSD).

---

* This is the case for all PCDD/Fs and PCBs, but for certain compounds, e.g. methoxychlor, where significant fragmentation (in EI) of the molecular ion makes this impractical, suitable fragment ions are used instead.

Although any errors in the peaks' responses would proportionately affect subsequent concentration calculations, a far more significant impact can result from the measured isotope ratio and its deviation from the theoretical value[*]: if this exceeds a specified tolerance, such as the 15% value used in current PCDD/F and PCB GC-HRMS methods, then whether the compound's concentration is reported at its calculated value or is treated as a non-detect (ND) depends either on the method in use or on the client's requested reporting parameters.

For example, in EPA-8290 (USEPA, 1998), the concentration would be reported but with a qualifying flag indicating that it is a *possible* candidate due to the ratio error. However, in other commonly used environmental methods, such as those from the EPA-1600 series[†], e.g. EPA-1613 for PCDD/Fs (USEPA, 1994) or EPA-1668C for PCBs (USEPA, 2010), an out-of-ratio based value would simply be reported as a ND.

Clearly that application of a simple tolerance and its binary pass/fail logic can have significant impact on the data in cases where affected peaks are of particular significance – whether due to their high toxicity, their importance as a key parameter within an epidemiological or other study, or their influence on any congener profiling (pattern-matching) program.

The problem is not limited to low-level signals: more intense peaks, where random variations should be negligible, can have ratio errors that are within, but close to the limit and these should be considered with additional scrutiny; in other words, the ratio tolerance applied to such peaks may be inappropriately high and therefore allow peaks to be considered valid that should possibly be rejected.

The aim of this chapter is to characterise and document the calculations underlying the relevant ion statistics and their effect on data quality, and to suggest refinements to the

---

[*] Some methods, e.g. EPA-1613, allow an alternative approach where the isotope ratio errors can be calculated from ratios obtained from a recently analysed reference standard (rather than comparison to theoretical values), but with a smaller, 10%, acceptance tolerance. Although this would provide some mitigation from any systematic biases in the ratio measurements it should be used with caution as such errors could be indicative of instrument setup issues or fault conditions that would not be addressed by this approach.

[†] Some laboratories will report the out-of-ratio concentration separately, even if ostensibly following a 1600-series method, thus leaving the decision as to whether it is used to the client.

current analytical methods to improve overall data quality, such as the use of dynamic, rather than static, isotope ratio tolerances.

## 2.2 Ion statistics and a Monte Carlo based simulation model

In many data sets, such as in the trivial example shown in Figure 1.11 (p. 24), peaks are observed that are known to be valid but yet fail the isotope ratio criterion. To investigate the theory that these random errors are due to ion statistics, a mathematical model was developed to estimate the isotope ratios, and hence the ratio errors, that would be likely to occur given peaks of various intensities and sampling (dwell) times.

A simulation program, "RaStats", based on Monte Carlo methods (Metropolis and Ulam, 1949) was developed *ab initio* to determine the probability of whether the tolerance criterion, e.g. the ±15% used in the methods under consideration, would be met based on the supplied RSD values of the two peaks being examined. For the simulations, the transforms shown below (Box and Muller, 1958) were used to create two random factors, $z_1$ and $z_2$, with normal (Gaussian) distributions:

$$z_1 = cos(2\pi \times r_1) \times \sqrt{-2.0 \times ln(r_2)} \tag{2.2}$$

$$z_2 = sin(2\pi \times r_1) \times \sqrt{-2.0 \times ln(r_2)} \tag{2.3}$$

Where $r_1$ and $r_2$ are uniformly distributed random numbers greater than 0 and less than or equal to 1.

For the Poisson distribution, the two factors ($z_1$, $z_2$) were created using iterative routines[*] based on Atkinson's multiplication and rejection methods (Atkinson, 1979). The distributions were tested for normality against the 68.3/95.5/97.7 rule with Anscombe's transformation (Anscombe, 1948) applied to the Poisson data prior to testing.

---

[*] See Appendix A.4.1 for details of the software procedures.

For larger values of λ, that are appropriate for the number of ions being considered, the Poisson distribution approximates to a normal distribution, e.g. with a 0.999 correlation coefficient at λ = 40, and therefore both models can be used for comparison purposes.

Using these factors, and given the theoretical areas and standard deviations of the two peaks, we can calculate the modelled areas for each peak:

$$area(model)_{peak1} = area(theo.)_{peak1} + SD_{peak1} \times z_1 \tag{2.4}$$

$$area(model)_{peak2} = area(theo.)_{peak2} + SD_{peak2} \times z_2 \tag{2.5}$$

And hence a sample's isotope ratio (Ra)* or relative abundance from these two peaks:

$$Ra_{sample} = \frac{area(model)_{peak1}}{area(model)_{peak2}} \tag{2.6}$$

This calculated ratio is then compared to the theoretical ratio to determine whether it lies within the acceptance tolerance:

$$Ra_{err}(\%) = 100\frac{Ra_{sample} - Ra_{theoretical}}{Ra_{theoretical}} \tag{2.7}$$

This process is then repeated over many trials (e.g. $10^6$) to ensure adequate convergence (< 0.1%) and the results summed to deduce the overall pass/fail rate.

---

* Although perhaps considered trivial, neither this formula (2.6) nor that for the error (2.8) are shown in the published methods, only the lower and upper ratio limits. Nevertheless, these formulae do follow standard practices e.g. as used in isotope ratio MS [noting its usage of *per mille* (‰) rather than percent] (Muccio and Jackson, 2009).

To illustrate the Monte Carlo simulation process, Figure 2.1 shows the results from a set of trials where two peaks, each with area RSDs[*] between 0% and 20%, were modelled, and the probabilities of their ratios exceeding the 15% tolerance calculated. E.g. with two peaks, each having a 10% RSD measurement error, there is ~29% chance of failing the 15% ratio criterion.

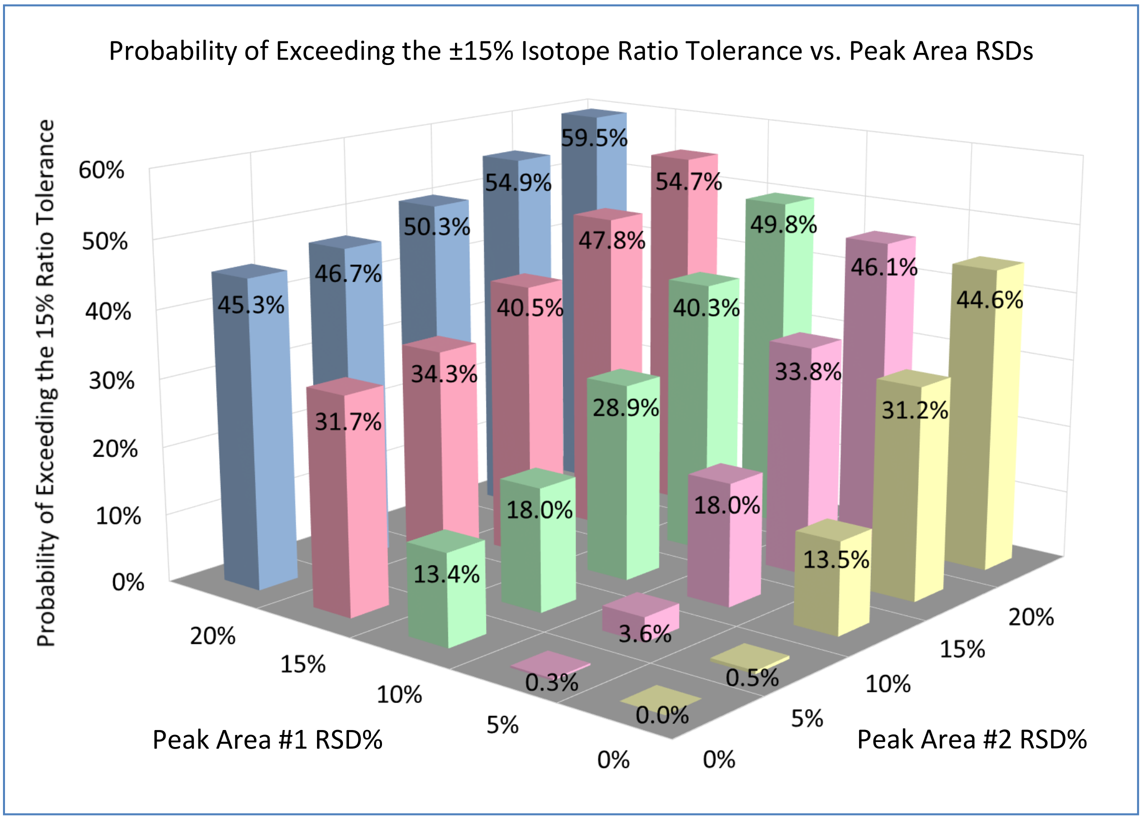

Figure 2.1 Probability of exceeding the ±15% isotope ratio tolerance as a function of the relative standard deviations (RSD) of two (Monte Carlo) simulated peaks' areas.

It is interesting to note that the chart shows a slight asymmetry (contrary to initial expectations); if the two peaks' RSDs are not equal, then for the probability of failure, $P_f$ of the two peaks' RSDs:

$$P_f\left(RSD_{peak\#1}, RSD_{peak\#2}\right) \neq P_f\left(RSD_{peak\#2}, RSD_{peak\#1}\right) \tag{2.8}$$

---

[*] It is often preferred to use the RSD (i.e. σ/mean) in these calculations since σ has limited meaning without knowing the mean to which it applies.

E.g. from the above chart, using RSDs of 15% and 5%: $P_f$ (15%, 5%) gives 34.3% whereas $P_f$ (5%, 15%) gives 33.8%. This arises from the simple fact that the first peak is always treated as the numerator in the ratio calculation. Consider the hypothetical example of two peaks with a theoretical isotope ratio of 1.0 and nominal responses (areas, counts, etc.) of 100. If the first peak is 10% lower than expected, the reported ratio is 90 / 100 = 0.9 and the ratio error is -10% (as expected); however, if the second peak is 10% lower – an equally likely situation – then the ratio is 100 / 90 ≈ 1.11, hence a ratio error of +11%.

To examine this asymmetry in more detail, a probability distribution histogram derived from Monte Carlo simulations of $10^6$ ratio estimates is shown in Figure 2.2. Each peak was modelled as a Gaussian with 8.5% RSD to give the probability vs. isotope ratio (black line, with the red line scaled x10). The results show that the proportion of estimates giving ratios within the ±15% tolerance is ~80% as shown by the green shading; the proportion that fall below -15% is ~8.3% (yellow shading), however the proportion above +15% is notably higher at ~11.7% (blue shading).

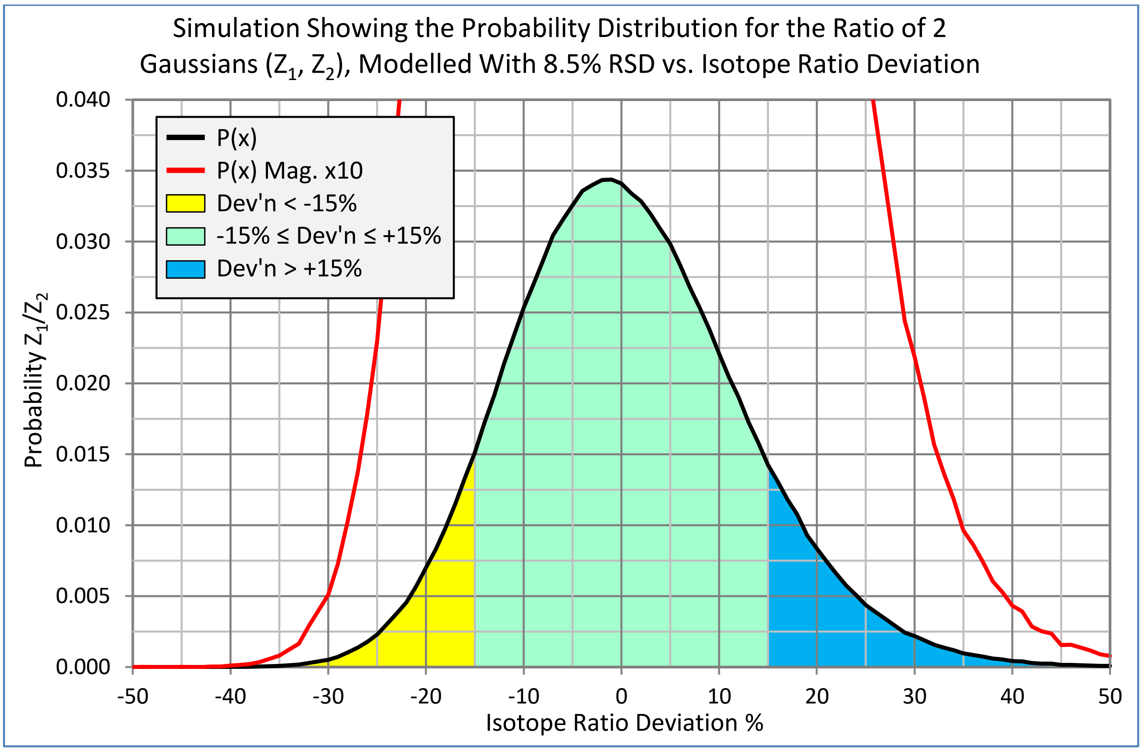

Figure 2.2 Histogram of the probability distribution from the modelled isotope ratio of 2 peaks generated using a Monte Carlo simulation with $10^6$ iterations.

The ratio of two normal (Gaussian) distributions can be represented by the Cauchy[*] distribution (Marsaglia, 1965) as shown by the equation in (2.9). This can be used to examine the modelling process for ratios based on Poisson (Figure 2.3) and normal distribution simulations (Figure 2.4) – both yielding good correlations to theoretical with $r^2$ values of 0.9996 and 0.9999 respectively. An unusual property of the Cauchy distribution is that it has no mean or variance (although it does possess a median and mode, both zero in these examples) since its integral is undefined. The distribution's heavy tails also lead to non-convergence of the averaged data.

$$C(x) = \frac{\gamma}{\pi\,[(x - x_0)^2 + \gamma^2]} \tag{2.9}$$

Where $x$ is the ratio ($z_1/z_2$) from the 2 distributions, and $x_0$ and $\gamma$ (gamma) are the location and scale parameters respectively (0 and 1 in these examples).

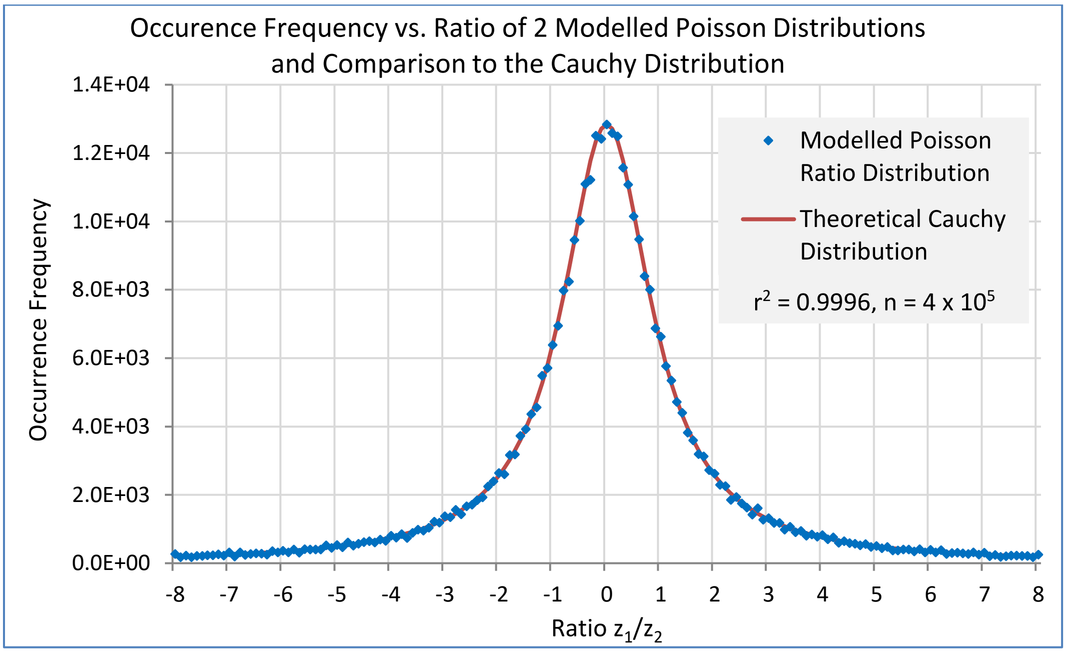

Figure 2.3 Histogram showing the occurrence frequency from the ratios of 2 modelled Poisson distributions ($z_1$, $z_2$) compared with the theoretical Cauchy distribution.

---

[*] Also known as the Lorenz distribution.

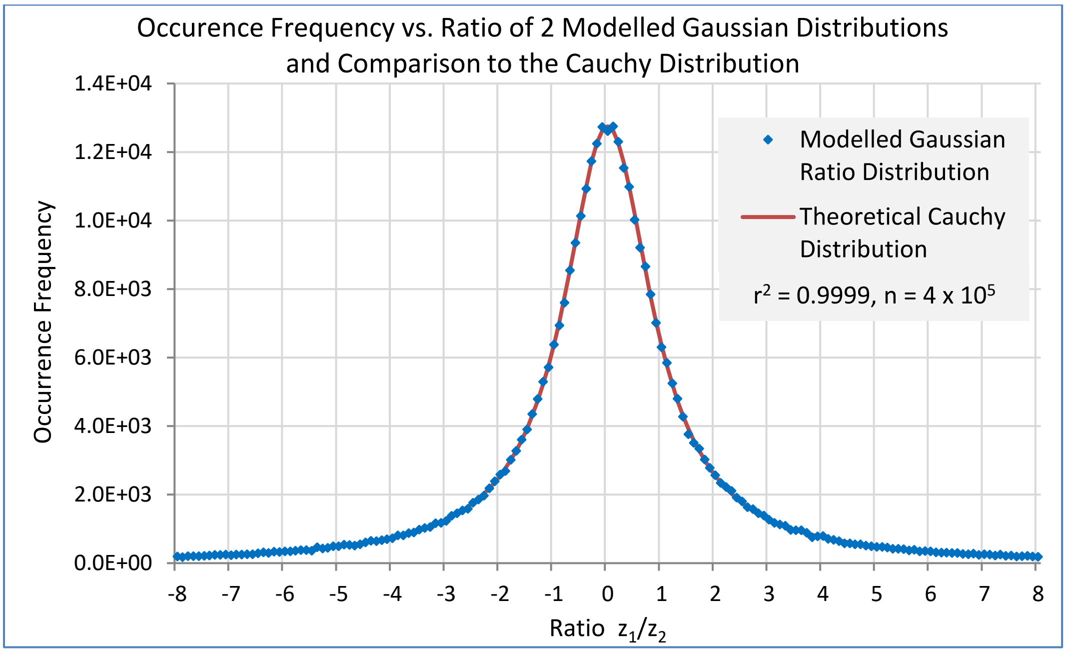

Figure 2.4 Histogram showing the occurrence frequency from the ratios of 2 modelled Gaussian (normal) distributions ($z_1$, $z_2$) with the theoretical Cauchy distribution.

## 2.3 SIM experimental setup

All magnetic sector HRMS data described in this chapter were acquired using an AutoSpec-Ultima (Waters, Wilmslow, UK) instrument operating in positive ion, electron ionisation mode at 34 eV electron energy. The instrument was tuned to a resolution of ~12,000 at 8 kV accelerating voltage.

The HRMS instrument was coupled to a 6890 GC (Agilent, Santa Clara, CA, USA), fitted with a 30 m (length) x 0.25 mm (internal diameter) x 0.25 µm (film thickness) SPB-Octyl column (Supelco, Bellefonte, PA, USA). Splitless injections were made using a GC-PAL auto-sampler (CTC Analytics, Zwingen, Switzerland) with a 1 µl injection volume.

Data were acquired in the voltage SIM mode using MassLynx V4.1 software (Waters, Wilmslow, UK) with post-processing done using UltraTrace-Pro V4.9 (SGS, Wilmington, NC, USA). Further details of the GC-HRMS parameters used are given in Appendix D.1.

## 2.4 SIM operation, ion detection and related calculations

The rationale for using SIM as the acquisition method was described in Chapter 1.7 together with an example of a typical function setup (Table 1.2); this section outlines the associated ion detection process, and subsequent data acquisition and processing – as needed for later statistics calculations. During a SIM experiment, ions generated in the source (from the various compounds eluting from the GC column) are sequentially selected by *m/z* and transmitted through to the instrument's detector according to the function descriptors. Figure 2.5 shows the basic schematic of the detector system (the circled numbers referring to the following stages):

1. Positive ions, with nominal 8 kV ion energy (from the instrument's mass analyser) impact the negatively charged conversion dynode.
2. Secondary electrons, liberated from the dynode's surface, are then accelerated towards the positively charged phosphor disc where their impacts produce photons.
3. Photons emanating from the phosphor disc are detected and amplified by the photomultiplier (with a typical gain of ~$10^5$).
4. The resultant signal is then passed to the head amplifier for current-to-voltage conversion giving an output with a 0 to 10-volt range (the "main beam").

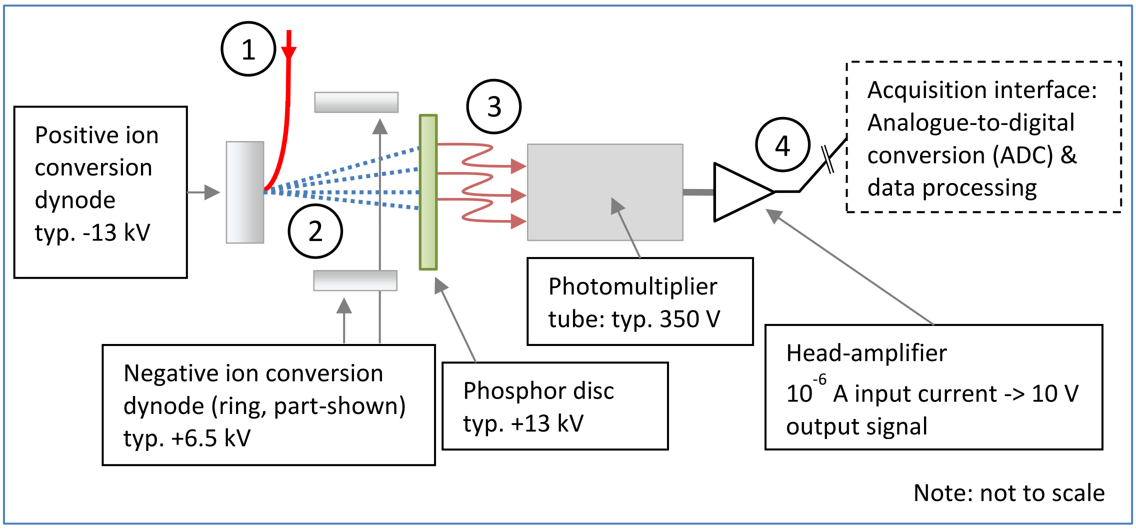

Figure 2.5 HRMS (Waters AutoSpec-Ultima) detector system schematic illustrating positive ion operation.

The detected main beam signal is then applied to the input of the instrument's acquisition interface where digitisation occurs using a 16-bit analogue-to-digital convertor (ADC) operating at 400 kHz. The ADC's output values, created throughout a *m/z* channel's dwell time, are then averaged. E.g. a typical channel time of 50 ms will result in the average from 20,000 digitisations. This allows average ion currents that correspond to less than a single ADC bit to be recorded and extends the dynamic range far beyond the ~65,000:1 nominally achievable with a 16-bit system.

Prior to data storage, the averaged values are then scaled[*] by a factor of $2^{14}$ such that SIM mass chromatograms have a y-axis maximum of ~$1.07 \times 10^9$ corresponding to the detector's head amplifier full-scale (10-volt) output. Since the chromatogram's x-axis represents time, any chromatographic peak area measurements are in units of "bits (or counts) seconds".

## 2.5 Testing the data modelling theory

To test the data modelling theory, a sample from a low-level (nominally 0.5 pg/µl) PCB calibration standard was analysed using GC-HRMS in the SIM mode and mass chromatograms for the pentachlorobiphenyl (PeCB) traces generated. Following peak integration and targeting, the rates of observed and modelled isotope ratio errors were compared. Figure 2.6 shows the chromatographic data: the native PeCB M+0 and M+2 ions (*m/z* 323.8834, 325.8804) are displayed in the upper two traces and the labelled $^{13}C_{12}$-PeCB M+2 ion (*m/z* 337.9207) in the lower trace[†]. There are 32 discrete PeCB

---

[*] The need for the scaling dates to an earlier design of acquisition interface used on VG Analytical's HRMS instruments in the mid-1980s. At that time, an instrument's available computing power was insufficient for real-time processing and storage of the acquired data using floating-point calculations. Integer based processing was therefore required, but to avoid the loss of precision in peak intensities that would result by limiting the numeric range to that of the 16-bit ADC (i.e. $2^{16}$ - 1 or 65,535), the values were scaled by $2^{14}$ (16,384) and hence the $2^{30}$ - 1 (~$10^9$) range.

When the HRMS instruments' acquisition systems were redesigned in the mid-to-late 1990s that limitation no longer existed, however, it was decided to retain the scaling so that users – especially those with systems from both generations – would benefit from a common, and familiar, range of peak intensities.

[†] The associated $^{13}C_{12}$-PeCB M+4 ion (*m/z* 339.9177) trace has been omitted from these chromatograms for clarity.

peaks in the native traces, but these include 5 coeluters, e.g. the peak pair of PCB-100 and PCB-93 at RT 24.89, and the multiple (6 peak) group at RT 28.12.

For the initial peak calculations, PCB-114 (RT 31.83) was chosen as a model since it represents one of the WHO toxic PCBs, does not coelute and its response is within 10% of the average (of the 27 single peaks). From the peak areas, and the following instrument and fundamental parameters, equation (2.10) can be used to calculate the ion counts at the detector, as shown in (2.11) and (2.12):

- Head amplifier input current at full-scale (FS) = $10^{-6}$ amps [FSA]
- Chromatogram y-axis (counts/bits) at FS = $1.07 \times 10^{9}$ [FSB]
- Head amplifier output* at FS = 10 volts [FSV]
- Detector† (multiplier) gain = $10^{5}$ [G]
- The elementary charge = $1.602 \times 10^{-19}$ coulombs [$e$]
- Peak duty cycle = 6% [DC]

$$\#\, charges = \frac{area\ (bits.sec) \times FSA\ (amps.volt^{-1}) \times DC\ (n)}{FSB\ (bits.volt^{-1}) \times e\ (amps.sec) \times G\ (n)} \tag{2.10}$$

Therefore, for PCB-114 (1st peak), area = $2.79 \times 10^{4}$:

$$\#\, charges = \frac{2.79\ \times 10^{4} \times 10^{-6} \times 0.06}{1.07\ \times 10^{9} \times 1.602\ \times 10^{-19} \times 10^{5}} \tag{2.11}$$
$$= 98$$

---

[*] For reference only, this parameter is not used in the calculation since the actual amplifier full-scale output voltage would equally apply to the FSA and FSB values and cancel out.

[†] Commonly referred to as “multiplier gain” – alluding to earlier HRMS designs where the ion detection system consisted of an electron multiplier, typically on-axis to the ion beam (i.e. without the use of conversion dynodes).

Similarly, for PCB-114 ($2^{nd}$ peak), area = $3.78 \times 10^4$:

$$\# \, charges = \frac{3.78 \times 10^4 \times 10^{-6} \times 0.06}{1.07 \times 10^9 \times 1.602 \times 10^{-19} \times 10^5} \tag{2.12}$$

$$= 132$$

Since this is a Poisson distribution, the values calculated for the number of charges are also equal to their variances, hence the peaks' σ are $\sqrt{98}$ and $\sqrt{132}$, and their RSD[*]:

$$RSD_1 = \frac{1}{\sqrt{98}} \approx 10\% \text{ and } RSD_2 = \frac{1}{\sqrt{132}} \approx 8.7\% \tag{2.13}$$

The RaStats (Monte Carlo) simulation program was then run using these RSD values: after $10^6$ trials it was determined that the probability of failing the 15% tolerance was ~26%. This compares to 19% in the observed data, i.e. due to 5 of the 27 singly eluting peaks being out-of-ratio.

This was repeated using data from the same sample, and for the same PeCBs, but from an alternate pair of *m/z* (M+2 and M+4 rather than M+0 and M+2). As shown in Figure 2.7 a similar proportion (22%, i.e. 6 of 27) of peaks are marked as out-of-ratio: however, with two exceptions (PCB-95 at RT 24.7 and PCB-99 at RT 27.7), these are different isomers to those identified as being out-of-ratio in the previous example. Since in both cases, these were the same isomers being analysed – and at the same time – any changes to their in- or out-of-ratio assessments are solely based on the choice of which isotopes are measured: such differences can therefore *only* be attributed to the statistical nature of the data.

---

[*] Since the number of charges (n) is the mean, and the variance is also n, therefore σ = √n and the RSD = √n / n, which simplifies to 1 / √n.

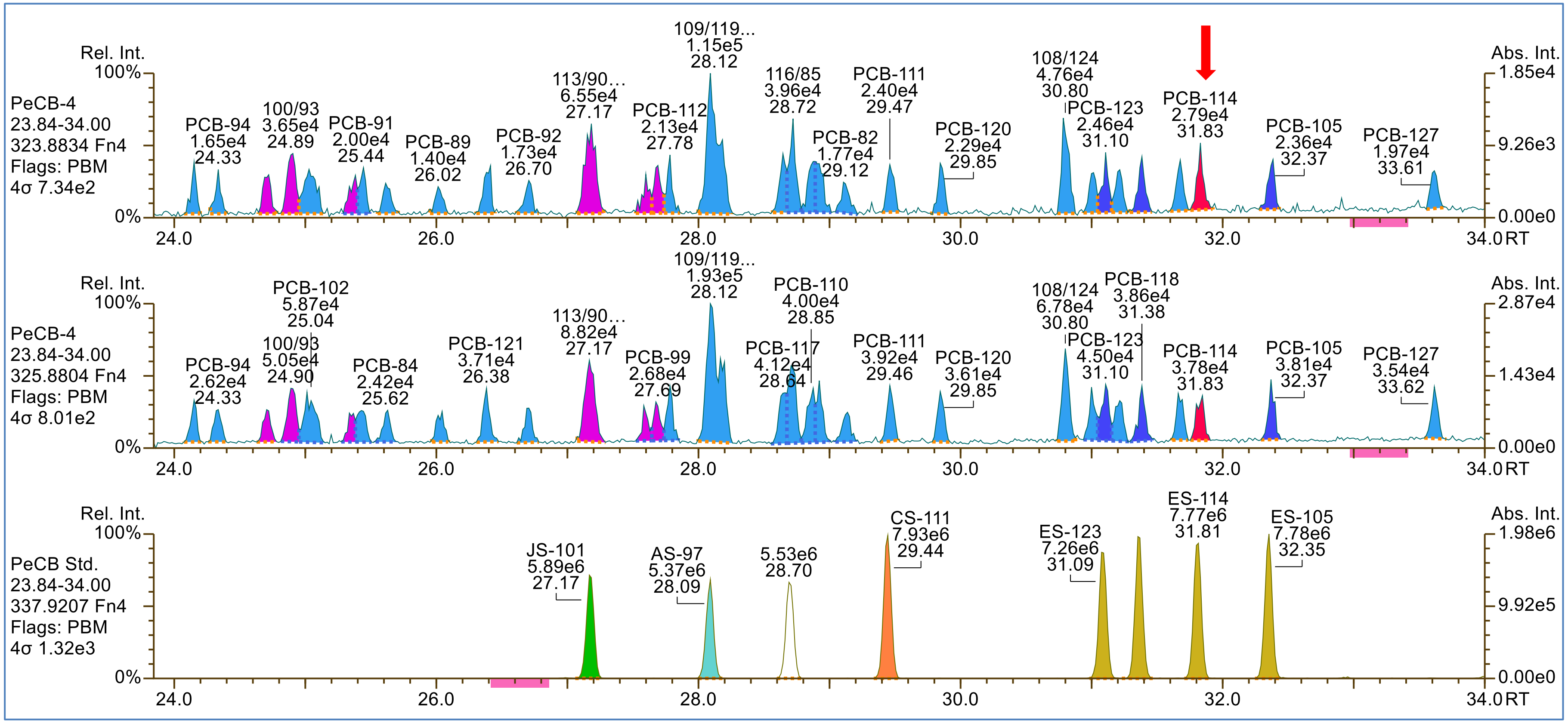

Figure 2.6 Chromatograms for the native PeCB M+0 (*m/z* 323.8834) and M+2 (*m/z* 325.8804) ions and the fully-labelled $^{13}C_{12}$-PeCB M+2 (*m/z* 337.9207) ion showing the incidence of peaks passing or failing the isotope ratio criterion.

Data acquired using an AutoSpec-Ultima GC-HRMS instrument at a mass resolution of 10,000 using the experimental conditions described in section 2.3.

The arrow marks PCB-114, that here, using the M+0 and M+2 data, exceeds the isotope ratio tolerance; c.f. the opposite result obtained from the M+2 and M+4 data shown in Figure 2.7.

Peak colour code: dark blue - WHO (toxic) PCB; light blue - other (non-toxic) PCB; red - WHO PCB (out-of-ratio); magenta - other PCB (out-of-ratio).

The pink x-axes markings show the RT ranges over which the background noise levels were calculated (and shown as the 4σ value in the trace headers).

[The $^{13}C_{12}$ labelled PCB M+2 standards (lower trace) are colour-coded according to their function and are shown for completeness but these are not referenced in this discussion. The $^{13}C_{12}$ M+4 ion trace is not shown for clarity.]

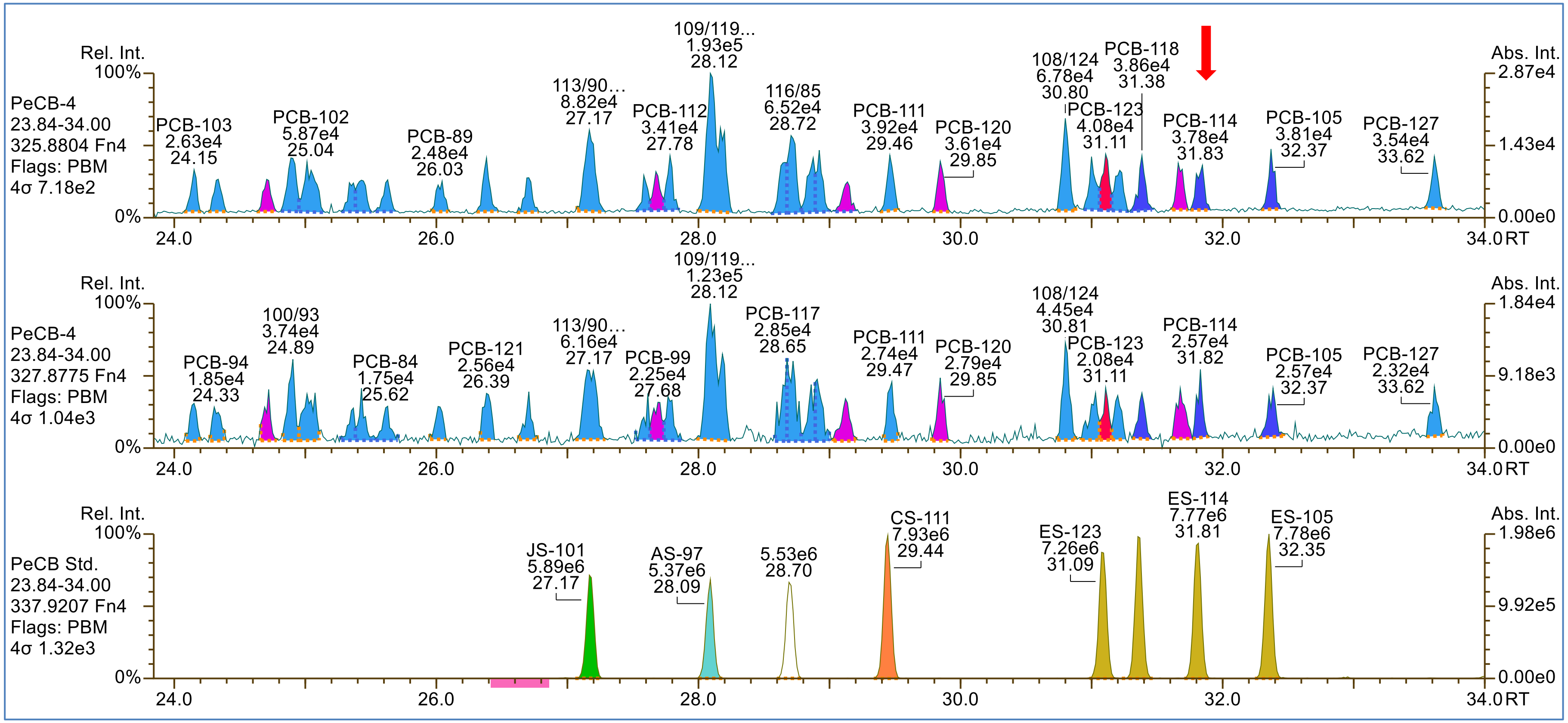

Figure 2.7 Chromatograms for the native PeCB M+2 (*m/z* 325.8804) and M+4 (*m/z* 327.8775) ions and the fully-labelled $^{13}C_{12}$-PeCB M+2 (*m/z* 337.9207) ion showing the incidence of peaks passing or failing the isotope ratio criterion.

Data acquired using an AutoSpec-Ultima GC-HRMS instrument at a mass resolution of 10,000 using the experimental conditions described in section 2.3.

The arrow marks PCB-114, that here, using the M+2 and M+4 data, is within the isotope ratio tolerance; c.f. the opposite result obtained from the M+0 and M+2 data shown in Figure 2.6.

Peak colour code: dark blue - WHO (toxic) PCB; light blue - other (non-toxic) PCB; red - WHO PCB (out-of-ratio); magenta - other PCB (out-of-ratio)

The pink x-axes markings show the RT ranges over which the background noise levels were calculated (and shown as the 4σ value in the trace headers).

[The $^{13}C_{12}$ labelled PCB M+2 standards (lower trace) are colour-coded according to their function and are shown for completeness but these are not referenced in this discussion. The $^{13}C_{12}$ M+4 ion trace is not shown for clarity.]

In these examples, the peaks are from a (low-level) calibration standard and are therefore unequivocally known to be the PCBs as annotated. Although both ion-pair combinations would not normally be processed, here we would have (amongst other examples) the paradoxical case of PCB-114 (highlighted by the arrows in both Figure 2.6 and Figure 2.7) being simultaneously reported both as a non-detect and as a confirmed positive within the same sample.

In a normal analysis (i.e. per the method) the data would only be acquired and processed from a single ion pair, and thus such contradictory results could not occur – or alternatively, an analyst would be unaware that such a result could occur given a different experiment setup.

The results from these data, together with those from analyses of tetra- to octa-chlorinated biphenyls at 4x greater concentration – the higher levels allowing additional comparisons at lower 10% and 5% isotope ratio tolerances – are shown in Table 2.1 and graphed in Figure 2.8. The experimental and modelled data would appear to show a good correlation with r = 0.94 ($r^2$ = 0.88).

| **Test Homologues** | **n** | **Test ratio tolerance** | **Modelled failure rate** | **Experimental failure rate** |
|---|---|---|---|---|
| TeCB (M, M+2) | 15 | 15% | 1% | 7% |
| TeCB (M, M+2) | 15 | 10% | 8% | 7% |
| TeCB (M, M+2) | 15 | 5% | 37% | 27% |
| [1]PeCB (M, M+2) | 27 | 15% | 26% | 20% |
| [2]PeCB (M+2, M+4) | 27 | 15% | 26% | 24% |
| PeCB (M, M+2) | 27 | 15% | 5% | 0% |
| PeCB (M, M+2) | 27 | 10% | 18% | 16% |
| PeCB (M, M+2) | 27 | 5% | 50% | 56% |
| HxCB (M+2, M+4) | 23 | 15% | 3% | 4% |
| HxCB (M+2, M+4) | 23 | 10% | 14% | 22% |
| HxCB (M+2, M+4) | 23 | 5% | 46% | 39% |
| HpCB (M+2, M+4) | 13 | 15% | 15% | 8% |
| HpCB (M+2, M+4) | 13 | 10% | 33% | 46% |
| HpCB (M+2, M+4) | 13 | 5% | 63% | 69% |
| OcCB (M+2, M+4) | 7 | 15% | 11% | 14% |
| OcCB (M+2, M+4) | 7 | 10% | 28% | 43% |
| OcCB (M+2, M+4) | 7 | 5% | 59% | 71% |

Table 2.1 Comparison of isotope ratio failure rates derived from Monte Carlo simulations and experimental results.
[1]Corresponds to the data shown in Figure 2.6; [2]corresponds to the data shown in Figure 2.7.

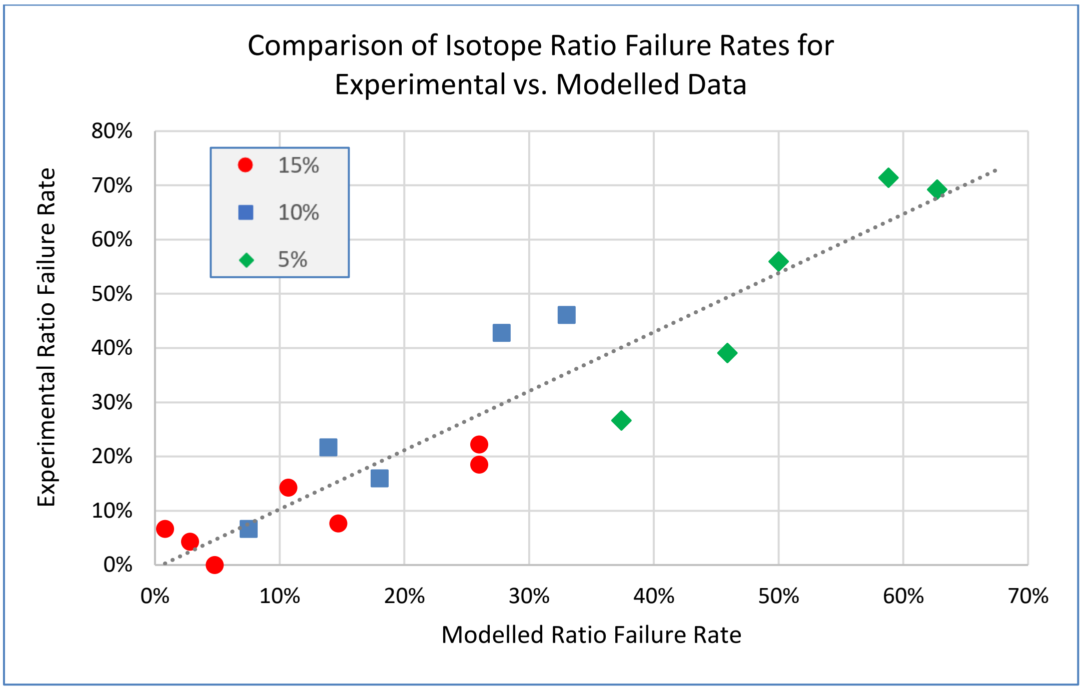

Figure 2.8 Chart showing experimental vs. Monte Carlo simulations of isotope ratio failure rates at 15%, 10% and 5% tolerances.
Pearson’s correlation coefficient, r = 0.94 ($r^2$ = 0.88).

## 2.6 Determination of the detector gain

Throughout this chapter, references have been made to detector gain, i.e. the degree of amplification applied to the input ion current presented to the detector system to give the resultant output ion current provided to the head amplifier (and hence to the subsequent detection processing hardware and software). Its value is a key parameter in the calculations relating to the statistical work described and can be determined using tools within the instrument’s peak display and tuning software – but is an instantaneous on-screen only value and is not recorded.

Conveniently, during HRMS data acquisition, a reference compound such as PFK is continually admitted to the ion source to provide suitable *m/z* for mass drift correction. The signal intensities from these reference ions are nominally at a constant level and these data can also be used to estimate multiplier gain. An example using the PFK ion at *m/z* 366.9292 ($C_{10}F_{13}$) was previously shown in Figure 1.11 (p. 24) as the trace labelled “QC Check”; a 1-minute section of these data was extracted into Excel as shown in Figure 2.9.

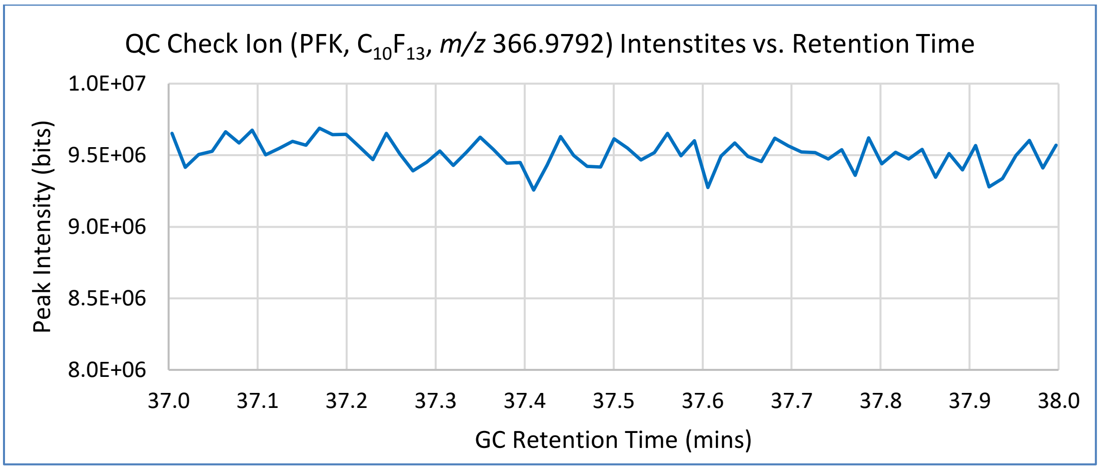

Figure 2.9 QC check ion data from PFK, $C_{10}F_{13}$ (*m/z* 366.9792), for detector gain calculations. $\sigma = 9.98 \times 10^4$, mean = $9.51 \times 10^6$.

From these statistics, and the ion detection and processing parameters, the detector gain can be estimated. The gain, G, is defined as the ratio of detector's output current to its input current as shown in (2.14):

$$G = \frac{I_{out}}{I_{in}} \tag{2.14}$$

The output current ($I_{out}$, amps) can be determined from the mean intensity (M, bits) and the head-amplifier (FSA) and chromatogram (FSB) full-scale parameters (from section 2.4):

$$I_{out} = \frac{M \ \times FSA}{FSB} \tag{2.15}$$

Therefore:

$$I_{out} = \frac{9.51 \ \times 10^6 \times 10^{-6}}{1.07 \times 10^9} = 8.89 \times 10^{-9} \ A \tag{2.16}$$

The input current can be determined by first estimating the mean number of ions, n, in each data point from the set of N measurements. From the RSD of the observed data, and the equivalence of the mean and variance of a Poisson distribution:

$$RSD = \frac{\sigma}{mean(N)} = \frac{\sqrt{var(N)}}{mean(N)} = \frac{\sqrt{n}}{n} \tag{2.17}$$

Therefore:

$$n = \frac{1}{RSD^2} \tag{2.18}$$

Incorporating the elementary charge, e (coulombs), and the dwell time (DT, seconds) (of the PFK *m/z* channel being monitored) into the equation yields the overall input current, $I_{in}$ (amps):

$$I_{in} = \frac{e}{RSD^2 \times DT} \tag{2.19}$$

From the above data:

$$I_{in} = \frac{1.602 \ \times 10^{-19}\, C}{1.10 \ \times 10^{-4} \times 0.020\, s} = 7.28 \times 10^{-14}\, A \tag{2.20}$$

Hence:

$$G = \frac{8.89 \times 10^{-9}\, A}{7.28 \times 10^{-14}\, A} = 1.2 \times 10^{5} \tag{2.21}$$

It is convenient to merge the two parts into a single equation for detector gain:

$$G = \frac{M \ \times FSA \times DT \ \times RSD^2}{FSB \times e} \tag{2.22}$$

This method is therefore useful in estimating the detector gain if no other record was made during instrument setup. It is unnecessary to know the actual flow rate of PFK entering the source to perform these calculations, however a caveat of this approach is that the variance in the PFK data, i.e. the peak-to-peak (p/p) noise, must be sufficiently greater than any systematic variations in level over the measurement period; if this is not the case then the calculated RSD will not accurately reflect the underlying Poisson variance and thus lead to elevated estimates of detector gain. Since the PFK level is principally set by the requirements for the instrument's lock-mass operation, an appropriate *m/z* and/or channel dwell time must be selected – e.g. the p/p noise should ideally be 5%–20% of its mean intensity.

Figure 2.10 shows data from the PFK reference compound with 3 channels concurrently recording the signal at *m/z* 219 ($C_4F_9$) with dwell times of 100, 50 and 10 ms. The RSDs of these data are 1.02%, 1.28% and 2.50% respectively (n = 1,000), however the factor between the 50 ms and 10 ms RSDs is 1.96, ~13% lower than the expected 2.24 (i.e. √5). However, taking a succession of sub-samples (n = 50) from the raw data shows a mean (n = 20) ratio (of RSDs) of 2.29, which is close (Δ ~2.3%) to the expected value. This is therefore suggestive of bias in the data that can be observed as a slight (~2%) overall positive slope.

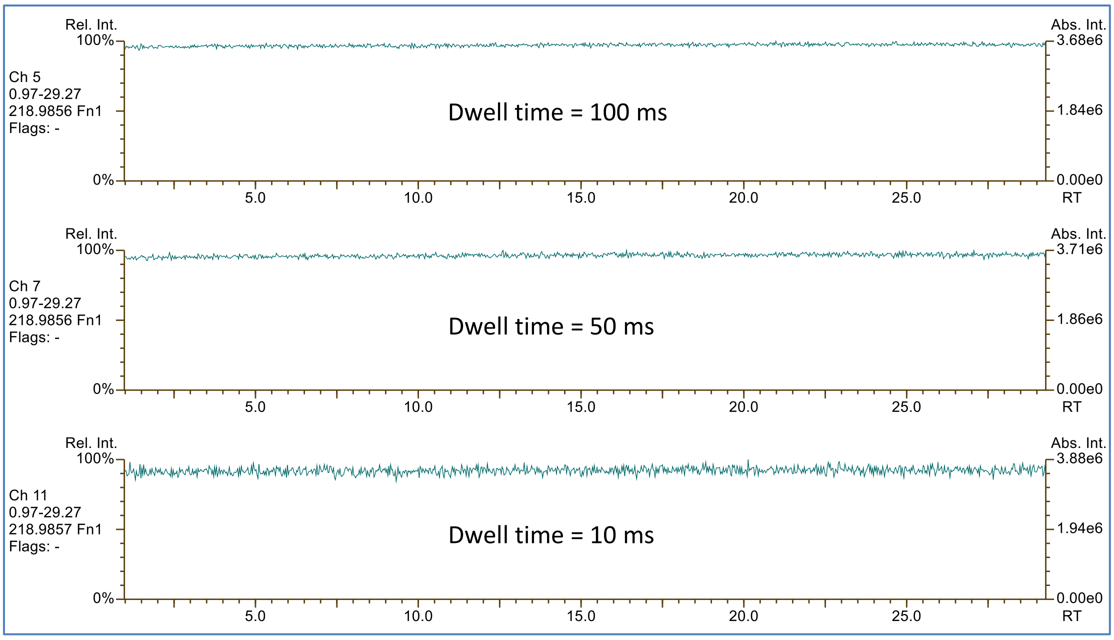

Figure 2.10 Chromatogram traces of the PFK reference compound at *m/z* 219 ($C_4F_9$) recorded using channel dwell times of 100, 50 and 10 ms.

Comparing the mean σ from the sub-samples with those from the full (n = 1,000) data shows differences of ~3%, ~18% and ~23% for the 10, 50 and 100 ms data respectively. This indicates that, in the absence of any prior knowledge of bias, the 10 ms data would give a truer representation of the noise level for any detector gain[*] calculations. This matches with the observation that the noise (4 σ) in the 10 ms data, being ~10% of the mean trace intensity, better masks the ~2% slope in the data than the 50 ms data with its noise level of ~5%. (The complete table of statistics for these data is shown in Appendix B.2)

## 2.7 Improving the odds: optimisation of acquisition dwell times

As shown in the previous section, the variance in a peak's response is reduced with increased dwell time: given the different relative intensities of the monitored ions, can the probability of being within the isotope ratio tolerance be improved by spending proportionately more time on those of lower intensity?

E.g. the isotope ratio of the monochlorobiphenyl (MoCB) M/M+2 ions ($C_{12}H_9{}^{35}Cl$, *m/z* 188 and $C_{12}H_9{}^{37}Cl$, *m/z* 190) is 3.06, so it might be expected that setting the dwell times to a 25:75 ratio[†] would result in fewer failures relative to using the default case of equal times. To test this theory, the data was modelled for MoCB and 4 other compounds covering a wide range of theoretical isotope ratios:

- TCDD and PeCB (both already discussed in this thesis), Ra 0.78 and 0.62.
- Methoxychlor (an organochlorine insecticide, $C_{16}H_{15}Cl_3O_2$, now banned in the US and EU): although this is a trichlorinated compound, the molecular ion is very weak due to the loss of the $CCl_3$ group and therefore the ions monitored are due to $C_{15}H_{15}O_2$ and $C_{14}{}^{13}CH_{15}O_2$, with a theoretical isotope ratio of 6.13.
- Malathion (an organophosphate insecticide, $C_{10}H_{19}O_6PS_2$, classified by the IARC as a probable, group 2A, carcinogen): as with methoxychlor, the molecular ion is weak due because of the loss of $C_2H_6O$ and therefore the ions monitored are due to $C_8H_{13}O_5PS_2$ and $C_7{}^{13}CH_{13}O_5PS_2$, with a theoretical isotope ratio of 9.51.

---

[*] The 50 ms data would have yielded a gain ~30% greater than that from the 10 ms data.

[†] From 1/(1+3.06) and 3.06/(1+3.06), i.e. more exactly 24.6% and 75.4%.

The results from the isotope ratio modelling using the Gaussian* distribution, with 500 ions in the molecular ion cluster and a combined dwell time for the 2 ions of 120 ms, processed over $10^5$ iterations, is shown in Figure 2.11 and summarised in Table 2.2.

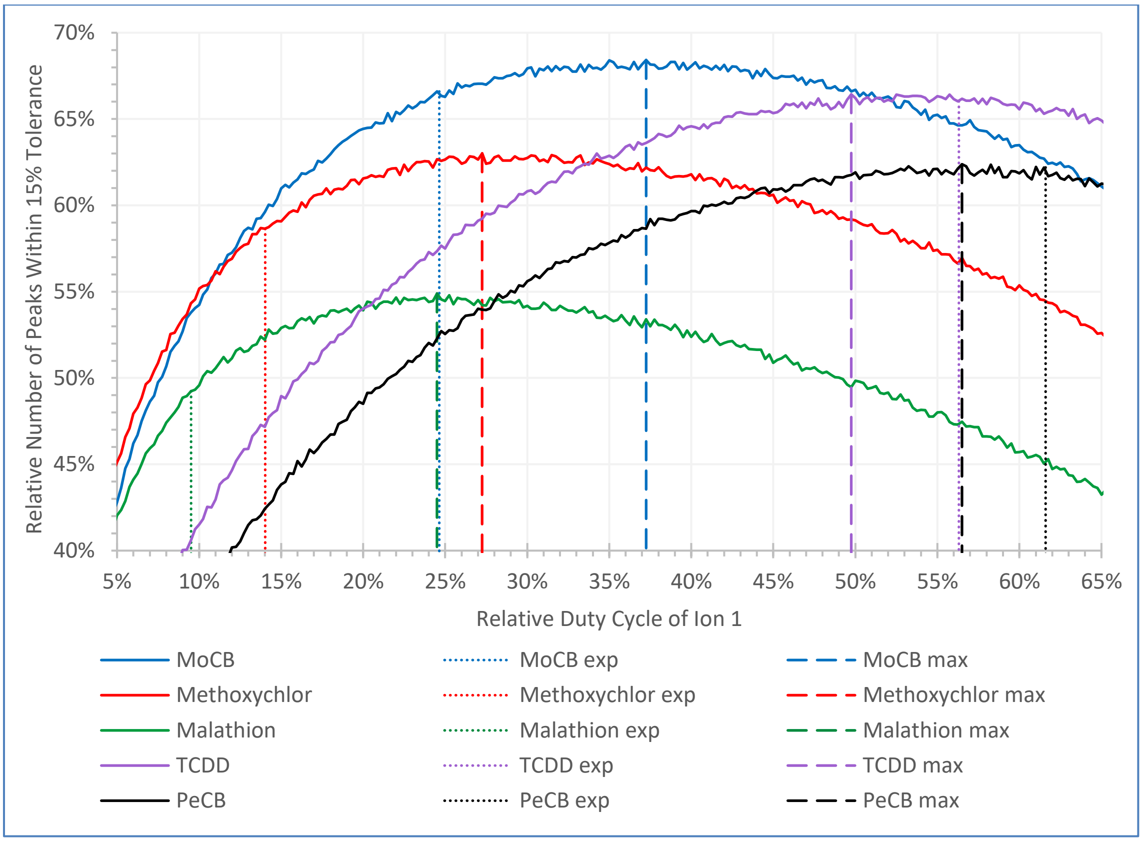

Figure 2.11 Modelled data showing the relative number of peaks within 15% of the theoretical isotope ratio vs. relative duty cycle for MoCB, Methoxychlor, Malathion, TCDD and PeCB. Also shown are the expected maxima (dotted lines) and actual maxima (dashed lines).

These data show that a small, 2.6%, improvement can be obtained for MoCB with primary and secondary ion dwell time proportions of 37.3% and 62.7% (equating to 45 ms and 75 ms) respectively, though not at the 24.6% and 75.4% that were initially expected. This is due to the greater overall number of ions obtained at the higher primary ion dwell time. At lower ion currents the benefit would increase, e.g. 4.4% at 100 ions. For methoxychlor and malathion, with their larger isotope ratios (6.13 and 9.51) the gains are more significant at 6.6% and 10.1% respectively, whereas for TCDD and PeCB with isotope ratios nearer to unity, the gains, at < 1%, are minimal.

---

* For comparison, data modelled using the Poisson distribution is shown in Appendix B.1.

|  | MoCB | Methoxy-chlor | Malathion | TCDD | PeCB |
|---|---|---|---|---|---|
| Theoretical isotope ratio | 3.06 | 6.13 | 9.51 | 0.78 | 0.62 |
| Expected optimum duty cycle (ion 1) | 24.6% | 14.0% | 9.5% | 56.3% | 61.6% |
| Modelled duty cycle for maximum pass rate (ion 1) | 37.3% | 27.3% | 24.5% | 49.8% | 56.5% |
| Pass rate at 50% duty cycle | 66.7% | 59.1% | 49.8% | 66.2% | 61.9% |
| Maximum pass rate | 68.4% | 63.0% | 54.9% | 66.4% | 62.4% |
| Increase | 2.6% | 6.6% | 10.1% | 0.3% | 0.8% |

Table 2.2 Summary of the data from Figure 2.11 showing the optimum duty cycle and increases in the "pass rate" for 5 different compounds.

This modelling process can also be used to indicate optimisation options for low vs. high-level peaks in the experiment setup. Figure 2.12 shows the relative variations in pass rates for a scenario with peaks at a nominal low-level signal (5 x $10^4$, red trace), compared to those at higher level ($10^6$, blue trace), as might be encountered for a labelled standard. For the high-level signal, the measurable performance is constant until the dwell times are reduced to < 20 ms, with a 1% drop at 10 ms; in contrast, the low-level signal shows significant changes as the dwell times are increased, e.g. showing 44.7% of peaks in ratio with dwell times of 10 ms, and 85.3% in ratio with times of 60 ms.

To equate the modelled data with real-world concentrations, Figure 2.13 shows the probabilities of PeCBs being within the 10%, 15% and 20% tolerances vs. amount injected. The peak areas used for the modelling program were extrapolated from actual sample data (50 pg on column, 2.5 x $10^5$ detector gain and 60 ms channel dwell times).

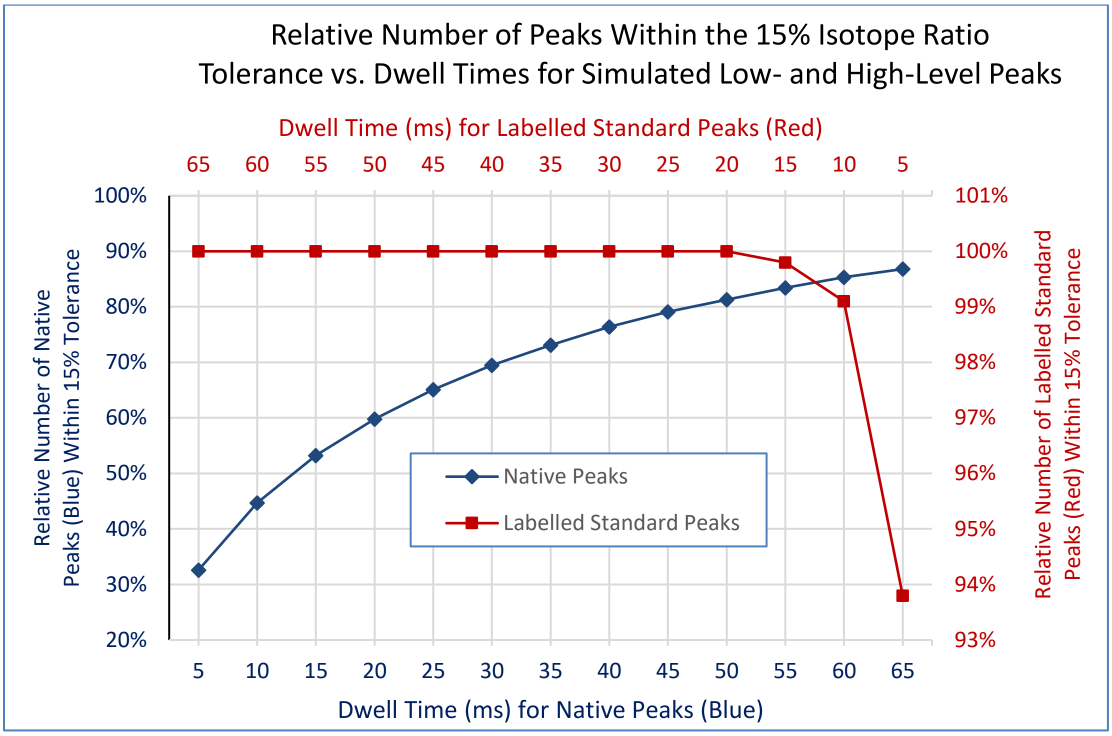

Figure 2.12 Relative number of peaks within the 15% isotope ratio tolerance vs. channel dwell times of the low- and high-level peaks.
Low-level (native) peak intensity = 5 x $10^4$; high-level (standard) peak intensity = $10^6$, isotope ratio = 1.0; detector gain = $10^5$.

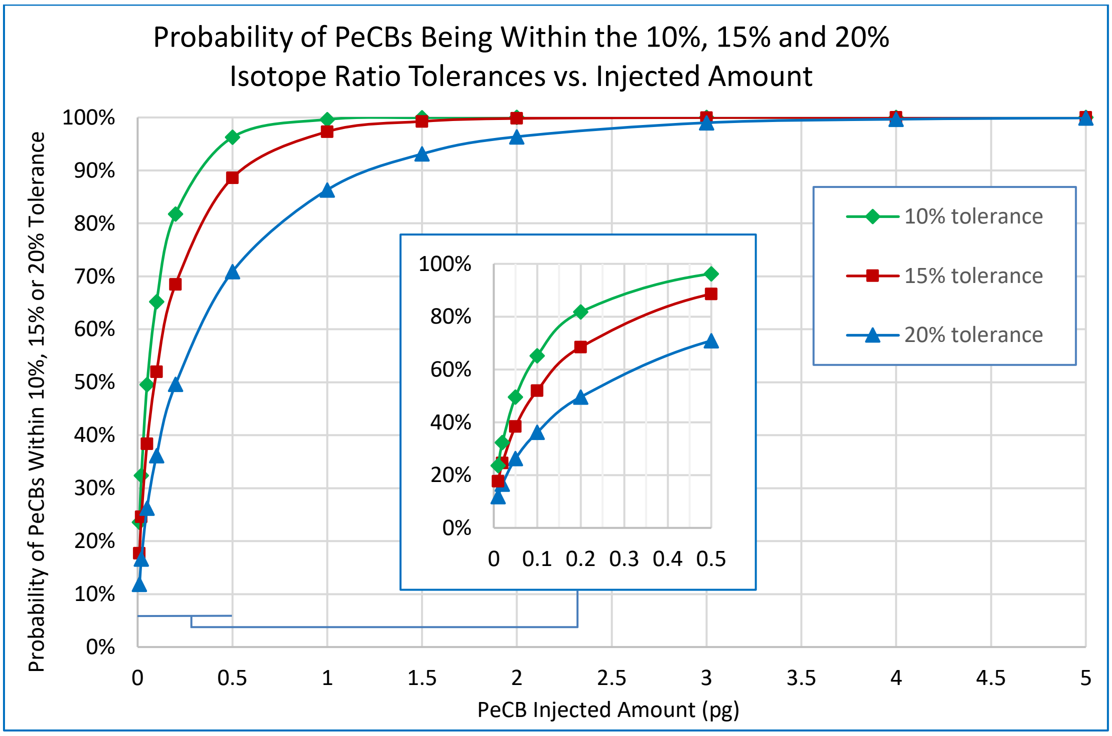

Figure 2.13 Modelled probability of PeCB peaks being within the 10%, 15% or 20% isotope ratio tolerances vs. injected amount of sample (10 fg to 5 pg).
Inset shows detail from the low concentration range (10 fg to 0.5 pg).

## 2.8 Implementing the dynamic isotope ratio criterion

A key theme of this work is that the isotope ratio tolerance defined by the current analytical methods is arbitrary and should be progressed from a static parameter to a dynamic one that reflects the actual data at the time of analysis. The chart in Figure 2.14 shows the 95% probabilities of being within certain ratio tolerances for various peak intensities for 4 different isotope ratios. E.g. using the curve for PeCB (shown in red) with its theoretical isotope ratio of 0.62, to achieve 95% of peaks being within a target tolerance of 15%, would require the sum of the two peak areas to be ~2.1 x $10^5$ (as shown by the dashed purple lines).

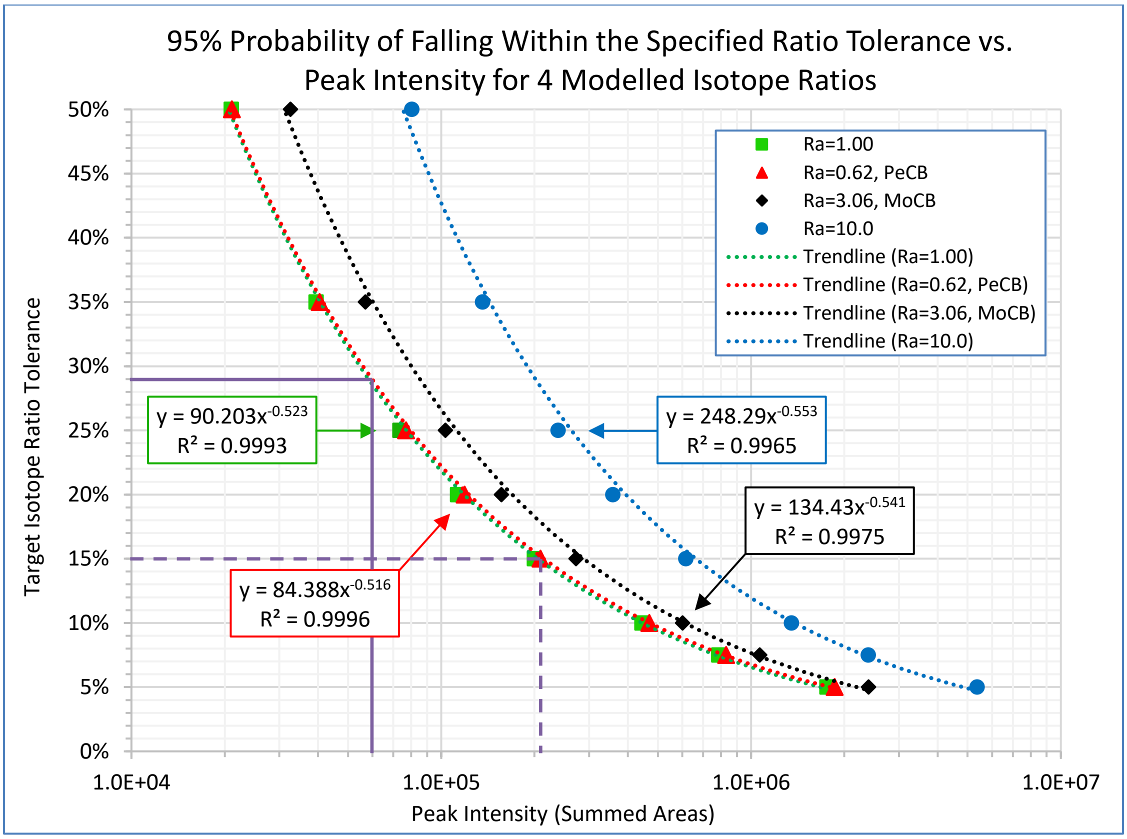

Figure 2.14 Chart showing the 95% probability of being within a specified ratio tolerance against peak intensity for 4 modelled isotope ratios.
Data modelling based on a detector gain of $10^5$ and peak duty cycles of 6%. The additional solid and dashed purple lines refer to example data referenced in the main text.

The above model can be applied to the PeCB data previously shown in Figure 2.6 (p. 50): the average response for a singly eluting peak was ~6.0 x $10^4$, on this basis the expectation is that 95% of peaks would fall within 29% of theoretical (as shown by the solid purple lines); this compares favourably with the actual figure of 92% (n = 25). Given these data, a ratio tolerance of 30% or 35% might be considered more appropriate than the method's 15% tolerance.

In addition to the PeCB curve, the modelled data show the probabilities for MoCB (Ra 3.06) and for Ra 1.0 and Ra 10. In this context, any of these curves would be equivalent to that of its reciprocal ratio, e.g. the curve for Ra 10 (blue line) is equally applicable to Ra 0.1. Implicitly, no other data can exist to the left of the curve showing Ra 1.0 (green line) under the same conditions (i.e. with a detector gain of $10^5$ and peak duty cycles of 6%).

The formulae from the trend lines produced by Excel are a useful alternative to using the chart, e.g. for the Ra 1.0 curve, the expected probability (P) that should encompass 95% of peaks of intensity (I) can be found from:

$$P = 90.2 \times I^{-0.523} \quad (r^2 = 0.9993) \tag{2.23}$$

As the power term is close to -0.5, this was simplified (using the curve fitting tool in MATLAB version R2018b) to:

$$P = \frac{72.1}{\sqrt{I}} \quad (r^2 = 0.995) \tag{2.24}$$

As a cross-check, applying this approximation (2.24) to the PeCB data from above: $P = 72.1/\sqrt{(6.0 \text{ x } 10^4)} = 29\%$ , which agrees with the graphical result. This formula can simply be reversed to give the required intensity for a given ratio expectation:

$$I = \left(\frac{72.1}{P}\right)^2 \tag{2.25}$$

Except for MoCB, all other PCBs and PCDD/Fs would fall between the curves of Ra 1.0 and that of PeCB; since the latter practically overlays the former, the Ra 1.0 curve could be considered a good approximation for any of these compounds. These curves are readily extensible for different instrument or experiment conditions[*]: e.g. for other detector gains (G), the values on the x-axis would be multiplied by G / $10^5$; for other duty cycles (DC), the x-axis values would be divided by DC / 0.06. The formula shown in (2.24) can also be revised using the square root of these values, e.g. the numerator would be multiplied by $\sqrt{G/10^5}$.

Further testing was performed on some high-level data: Figure 2.15 shows a TeCB chromatogram from a 50 pg per component mix. Using the formula from (2.24), revised for a detector gain of 2.5 x $10^5$ and an average summed peak intensity of 4.1 x $10^7$, yields the expectation that 95% of the singly[†] eluting peaks should have ratio errors ≤ 1.8% (i.e. $P = 114/\sqrt{4.1 \times 10^7}$) – which is in good agreement with the actual data where all peak ratio errors are ≤ 1.8% (n = 16).

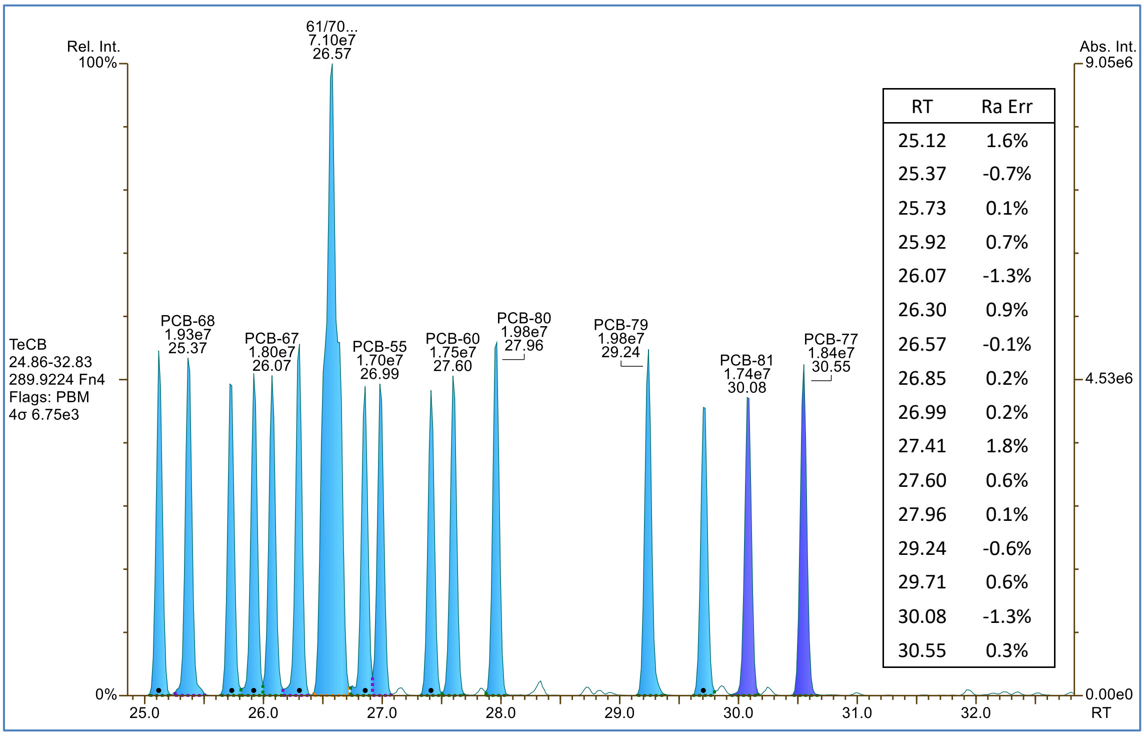

| RT | Ra Err |
|---|---|
| 25.12 | 1.6% |
| 25.37 | -0.7% |
| 25.73 | 0.1% |
| 25.92 | 0.7% |
| 26.07 | -1.3% |
| 26.30 | 0.9% |
| 26.57 | -0.1% |
| 26.85 | 0.2% |
| 26.99 | 0.2% |
| 27.41 | 1.8% |
| 27.60 | 0.6% |
| 27.96 | 0.1% |
| 29.24 | -0.6% |
| 29.71 | 0.6% |
| 30.08 | -1.3% |
| 30.55 | 0.3% |

Figure 2.15 TeCB chromatograms from a high-level, 50 pg per component, sample showing all isotope ratios within 1.8% of theoretical (0.78).
Mean error = 0.2%, RSD = 0.9%.

---

[*] It would, of course, be necessary to adapt the x-axis values for other instrument types with different electronics and data processing schemas.

[†] The 4-component coelution of PCB-61, 70, 74 and 76 at RT 26.57 is ignored here.

An additional set of data, acquired using the same 50 pg sample on the same instrument (but on a different day), produced the chromatogram shown in Figure 2.16. All peak ratio errors were within the method's 15% tolerance but showed an overall bias ranging from -9.4% to -7.2% (mean -8.6%, σ = 0.57%).

However, from (2.24) and the average summed intensities (3.1 x $10^7$), the expectation – due to statistical variance – was that the errors should have been no more than ±2%, which is clearly not in agreement with the actual data[*]. Applying the dynamic ratio in this case would have flagged this as a problem – believed to be due to an operational error during mass calibration – that could otherwise easily go unnoticed[†], potentially leading to subsequent identification errors.

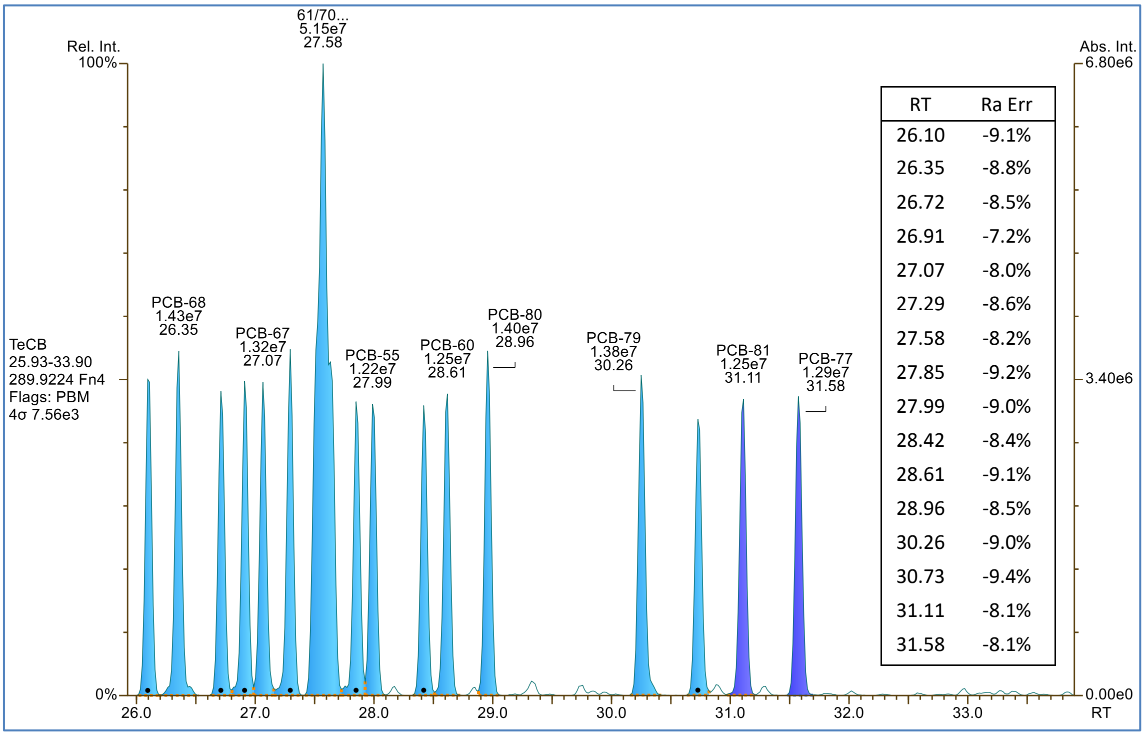

| RT | Ra Err |
|---|---|
| 26.10 | -9.1% |
| 26.35 | -8.8% |
| 26.72 | -8.5% |
| 26.91 | -7.2% |
| 27.07 | -8.0% |
| 27.29 | -8.6% |
| 27.58 | -8.2% |
| 27.85 | -9.2% |
| 27.99 | -9.0% |
| 28.42 | -8.4% |
| 28.61 | -9.1% |
| 28.96 | -8.5% |
| 30.26 | -9.0% |
| 30.73 | -9.4% |
| 31.11 | -8.1% |
| 31.58 | -8.1% |

Figure 2.16 TeCB chromatograms from a high-level, 50 pg per component, sample showing a systematic bias of measured isotope ratios relative to the theoretical value.
Theoretical ratio for TeCB = 0.78, mean error = -8.6%, RSD = 0.63%.

---

[*] However, the errors relative to the mean (i.e. accounting for its bias) are within the expected range.

[†] Calibration data often contains only 1 or 2 PCB peaks in any one function (rather than the 16 in this example), therefore systematic errors such as this may not be as obvious.

## 2.9 A statistical evaluation of signal-to-noise measurement

A peak's signal-to-noise (s/n) ratio is an important performance related parameter in the various POPs methods; with minimum values required for any peak to be considered valid for processing. In addition to various minimum s/n criteria, the related background noise value is also used as the basis for limit-of-detection (LOD) and limit-of-quantification (LOQ) calculations.

Figure 2.17 shows a segment of the PeCB trace used earlier in this chapter for the ion statistics study, with the peaks annotated with their s/n ratios. E.g. PCB-114 at RT 31.83 has a s/n of ~11, based on the background noise taken over 30 data points and calculated as 4σ (as shown in the magnified x5 section). However, we know from equation (2.13) that the estimated RSD of this peak is ~10%; this would give an "internal" s/n of ~10, based on 1σ, or ~2.5 using 4σ. Although this is ~4x lower than the conventional s/n figure it raises a question of whether this, statistically based, noise estimate would be a useful complement to the background-based value?

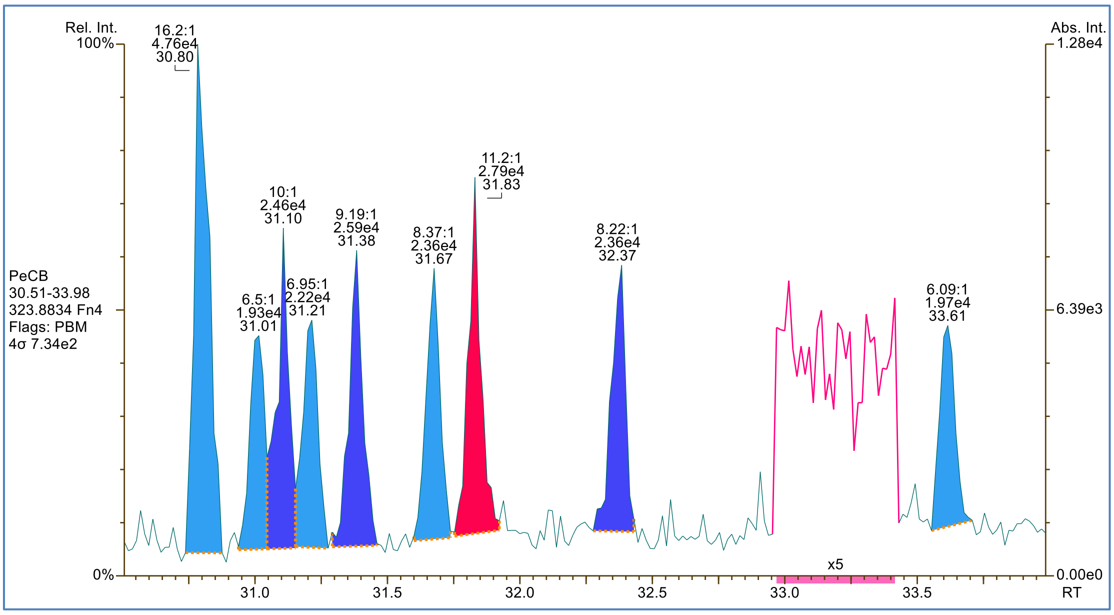

Figure 2.17 Chromatogram extract showing PeCBs annotated with their signal-to-noise ratios, peak areas and retention times.
The x5 magnified region (denoted by the pink marking in the x-axis) indicates the data range from which the noise was determined: 4σ = 7.34e2.

The current EPA HRMS methods for POPs, e.g. EPA-1668C (USEPA, 2010), specify that detected chromatographic peaks must have a minimum s/n ≥ 10 for calibration standards and ≥ 2.5 for sample analytes, however there are no references as to how the noise is defined, nor whether any data smoothing may be applied.

More recently, the EU's "*Guidance Document on the Estimation of LOD and LOQ for Measurements in the Field of Contaminants in Feed and Food"* (Wenzl *et al.*, 2016) and *"Estimation of LOQ for the Analysis of Persistent Organic Pollutants, in particular PCDD/Fs and PCBs*" (Schaechtele *et al.*, 2016), defined noise (N) as 2σ with a s/n requirement ≥ 3 for all peaks. The LOQ was then defined as 3N (i.e. 6σ) – approximately peak-to-peak since that would theoretically include 99.7% of the noise data points. The EU methods also permit the use of data smoothing, but if used, it must be used consistently; i.e. if required for sample data then it must also be used for the associated calibration data, it cannot be used selectively.

Early work in this area indicated that the prevalent noise source was the instrument's detector system and (head) amplifier (Hass and Friesen, 1979), however this is no longer the case. As the performance of the HRMS instrumentation has improved[*], resulting in greater ion currents reaching the detector, chemical noise – whether from the GC column, injector, reference compounds, sample matrix or contaminants, etc. – is now the dominant background noise source. However, chemical noise sources exhibit far greater variability than background electronic noise[†], hence dependent results such as LOQ are implicitly subject to that same variability. The US Centers for Disease Control and Prevention (Atlanta, GA, USA) report a typical factor of 2x higher detection limits in serum samples, compared to standards, due to chemical noise and matrix effects (Turner *et al.*, 2004).

The use of the background noise levels to determine such metrics can also be problematical with high-resolution TOF instruments where creating mass chromatograms using small (≤ 10 mDa) windows can result in the near (sometimes

---

[*] The base sensitivity of HRMS instrumentation has increased from 2 x $10^{-8}$ C/µg (methyl stearate) in the early 1980s to $10^{-6}$ C/µg today. Concurrently, transmission at 10,000 resolution has increased from 5% to 10%.

[†] The detector system itself is a source of noise, e.g. the dark current from the photomultiplier, but, under normal operating conditions, these are negligible in a modern instrument.

complete) absence of measurable noise. Although issues such as these can significantly affect LOD and LOQ determinations from background noise, their effect on the detected peaks' statistics are minimal.

Data smoothing is a useful tool that can be used to improve s/n and to aid the peak detection process. Irrespective of whether simple digital filtering (i.e. moving average) or more advanced processes, e.g. using polynomial methods (Savitzky and Golay, 1964), are used, the effect is to substantially reduce the background noise in comparison to the effect on any peak heights. A 2-fold improvement in s/n is readily achievable using data smoothing, and although this equates to a proportionally lower LOD, it is questionable as to whether the LOQ should be similarly reduced.

Again, the peak statistics are unchanged since, although a peak's height may be affected by the smoothing process, its area is nominally unaltered[*]. Similar concerns can also apply to the use of "fast" chromatography, particularly 2D-GC, where the very narrow peak widths (< 100 ms), can lead to remarkably high s/n ratios that can be inappropriately extrapolated to correspondingly low LOD and LOQ values.

## 2.10 Conclusions

In addition to the peak retention time (or relative retention time) the isotope ratio measurement is a key parameter in determining whether compounds such as dioxins or PCBs are positively identified. The 15%[†] tolerance employed by the current methods appears to be arbitrary and, as confirmed by the findings in this chapter, can be both too restrictive to allow for the variance found at low signal levels, and too broad to flag potentially problematic peaks at higher levels. The paradoxical example where PCB-114 was shown to be simultaneously both within and outside the method's ratio tolerance

---

[*] Minor area changes can occur due to slight differences in a peak's baseline start- and end-point determinations, but the fundamental process of smoothing does not affect a peak's area.

[†] It has also been noted that the ratio tolerances have been increased to 25% and 35% for the organochlorine pesticides in EPA Method 1699 (USEPA, 2007b), and although the reasoning behind this is not stated (and again, no references are offered), these too seem to be arbitrary limits and therefore subject to the same problems noted for the PCB and PCDD/F methods.

demonstrates a fundamental flaw in the use of the isotope ratio as a measurement parameter without proper consideration of the underlying statistics.

When the high-resolution methods were first published, it would not have been practical to use anything other than a fixed tolerance, but the dynamic approach introduced here could now be readily accommodated – including all necessary documentation and associated QC data – using off-the-shelf spreadsheet and/or database programs or added to commercial quantification software. Provision could also be made for the asymmetric nature of the ratio test in these calculations.

The methods should therefore consider – perhaps as part of their performance-based measurement system (PBMS) strategy – extending their scope to include such dynamically assigned isotope ratio tolerances. Reporting requirements would need to be extended to include both in and out-of-ratio data from both existing, static, tolerance(s) and any dynamic counterparts, so that the incidence and significance of this criterion can be comprehensively assessed and included in any measurement uncertainty reporting.

Ironically, an extant problem (particularly with large-scale projects) is that many end-users no longer work directly with the laboratories' reports, instead they are supplied with database generated summaries. Whilst this may be necessary, given the amount of data involved, any parameters that do not fit exactly with the methods' criteria – or a data managers' interpretation of them – can be lost. Although data qualifiers *should* indicate if an analyte was not reported due to the isotope ratio tolerance not being met, or its concentration being below the reporting or calibration limit, this may not be consistently or correctly applied.

A related, often contentious, issue concerns the reporting of undetected peaks – either because no measurable response was found, or the tentative compound is deemed to be a non-detect due to it failing the isotope ratio test: should the concentration simply be reported as zero, or as the detection limit (DL) (since a peak could have been present but not detected due to background noise), or DL/2 as a mid-point compromise between these values? This has been a longstanding problem with the current ultratrace methods and, since it is not uncommon for data from these analyses to be used in litigation, it presents more than just an academic problem. Some regard an out-of-ratio peak as simply not meeting the positive identification requirements and it should therefore be treated like any other non-detect; others argue that if the peak is at least at the correct retention time, then its concentration should be considered from a risk assessment perspective.

The use of ion statistics in environmental MS data processing can be a useful tool to help migrate existing analytical methods from their traditional HRMS roots to those based on newer technologies, e.g. using MS/MS and TOF instrumentation, where the current use of background data for signal-to-noise assessment is not viable. As with the isotope ratio proposals, the use of these statistics directly in LOD/LOQ determination would need thorough validation prior to approaching any regulatory authority. It was also shown that existing HRMS acquisition methods can be improved by optimising the channel dwell times according to the expected ion ratios.

It is understood that there will be many challenges to changing the “rules of the game”; previous personal communications with US based stakeholders of current HRMS analyses suggested that, since much of their work could be ultimately subject to litigation, there would be a certain reluctance – despite the methods being nominally performance-based – to adopting any variations to those methods that were not explicitly promulgated from the regulators (e.g. the EPA). The situation within the EU is likely to be more accommodating – as has already been seen by the acceptance of GC-MS/MS as a valid alternative to GC-HRMS for regulatory food and feed testing – as there exists a far closer coupling between its laboratories and legislators (i.e. a true performance-based approach).

As stated in the aims and objectives of Chapter 1, producing accurate and reliable data is of the utmost importance: considerable effort (and cost) is expended in project design, sample collection, laboratory analysis, data processing and reporting, and yet, minor shortcomings in the analytical methods can potentially lead to significant errors in the reported data – these should be addressed.

# Chapter 3

# Molecular Ion Cluster Calculations

## 3.1 Introduction

Throughout the work in this thesis it has been necessary to know the true theoretical isotope ratios for the comparisons to the measured and simulated data. This has highlighted several differences between the published ratios taken from the various dioxin and PCB methods, and the corresponding values obtained using the isotope calculation program included in the mass spectrometer's software (MassLynx).

Since no references were available to show how the published ratios were calculated, or to the source(s) of the exact masses or abundances used, it was considered prudent to create an *ab initio* program where all parameters and the calculation methods would be known. This has resulted in "PureIso", a Windows based isotope modelling program, written in Visual Basic using Visual Studio (Microsoft, Redmond, WA, USA). The key algorithms used by the program are given in Appendix A.4.2 and copies of this program are available to any interested parties on request.

Masses were obtained from IUPAC's Technical Report "*Atomic weights of the elements 2013*" (Meija *et al.*, 2016a), and abundances from both the companion document, "*Isotopic compositions of the elements 2013*" (Meija *et al.*, 2016b) and its predecessor "*Isotopic compositions of the elements 2009*" (Berglund and Wieser, 2011) for comparison purposes. A complete list of the masses and abundances used is given in Appendix C.2.

The primary aim of this chapter is to document the differences between the calculated ratios and those in the published methods, and whether changes to those values – that play a key role in determining a sample's toxicity and other attributes – should be considered. Certain new capabilities of the PureIso program: addressing the degree of purity in $^{13}C$ and other labelled standards, and abundance calculations over a specific mass window are also introduced. Finally, the effect on measured isotope ratios due to mixed, charge exchange and protonation, modes in atmospheric pressure ionisation is discussed.

## 3.2 Isotope cluster calculations: software design considerations

The calculation of a molecule's isotopic distribution can, depending on the numbers of atoms and isotopes in each element involved, and whether exact masses are required, lead to considerable memory and processing requirements. To overcome these issues, various strategies have been developed to filter and/or otherwise limit the results to create practically viable programs (Valkenborg *et al.*, 2012).

To avoid any uncertainty due to such reduction mechanisms, this software was designed solely for small molecules (< 1,000 Da) with a very limited range of elements – C, H, N, O, Br, Cl, F, P, Si and S – hence it was unnecessary to apply any such practices as the calculation of all possible isotopic contributions is well within the power of a current desktop computer. Although these restrictions would render the program unsuitable for general purpose applications, it is ideal for the POPs considered here (and many other small molecules) that are wholly within its capabilities.

For a monoisotopic element* (e.g. F, P), there is implicitly only one possible contribution to the calculation, for elements with 2 isotopes (e.g. C, H, N, Cl, Br) there are n + 1, and for those with 3 isotopes (e.g. O, Si, S†) there are (n + 1) x (n + 2) / 2.

Examples:

- Hexachlorobenzene ($C_6Cl_6$) gives (6+1) x (6+1) = 49 combinations.
- TCDD ($C_{12}H_4Cl_4O_2$) =>

  (12+1) x (4+1) x (4+1) x [(2+1) x (2+2)]/2 = 1,950 combinations.
- Malathion ($C_{10}H_{19}O_6PS_2$) =>

  (10+1) x (19+1) x [(6+1) x (6+2)]/2 x 1 x [(2+1) x (2+2)]/2 = 36,960 combinations.

---

* Only stable isotopes are considered in this program.

† Excluding the minor (~0.015%) $^{36}S$ isotope.

Even the last case is readily computable, although from a practical perspective, a post-calculation threshold filter is a worthwhile addition since the display of masses such as the M+45 ($^{13}C_{10}{}^{2}H_{19}{}^{18}O_{6}P^{34}S_{2}$) at a probability of ~3.5 x $10^{-114}$ is unlikely to be useful!

## 3.3 Abundance calculations of enriched isotopes

Although the isotope calculators embedded within MassLynx or found online allow the inclusion of enriched isotopes, e.g. as required for carbon-13, deuterium or chlorine-37 labelled compounds, they all assume 100% isotopic purity. This is a limitation as it does not allow for correct modelling of commercial, stable isotopically labelled, standards as used in these analyses where the purities are typically 99% for carbon-13 and 96% for chlorine-37 labelled compounds[*]. This program therefore includes $^{13}C$, $^{2}H$ and $^{37}Cl$ as independent pseudo-elements whose purities can be set to any value. E.g. the 'element' $^{13}C$ would have two isotopes with masses 13.003355 and 12.0 and default abundances of 99% and 1% respectively – essentially the converse of the natural carbon composition.

The seemingly high purity values of these labelled standards perhaps belie certain shortcomings, as demonstrated in the following calculations of the fully carbon-13 labelled PeCB ($^{13}C_{12}H_{5}Cl_{5}$): Figure 3.1 shows the modelled molecular ion cluster based on a carbon-13 purity of 100% and Figure 3.2 shows the same compound based on the manufacturers' assigned 99% purity. In the former, the minor ions (odd *m/z* values) are minimally existent and, in total, account for < 0.06% of the isotopic distribution; in the latter, these ions are clearly present and account for 10.8% of the distribution.

---

[*] Based on the published suppliers' catalogue data from Cambridge Isotope Laboratories Inc. (Tewksbury, MA, USA) and Wellington Laboratories Inc. (Guelph, Ontario, Canada).

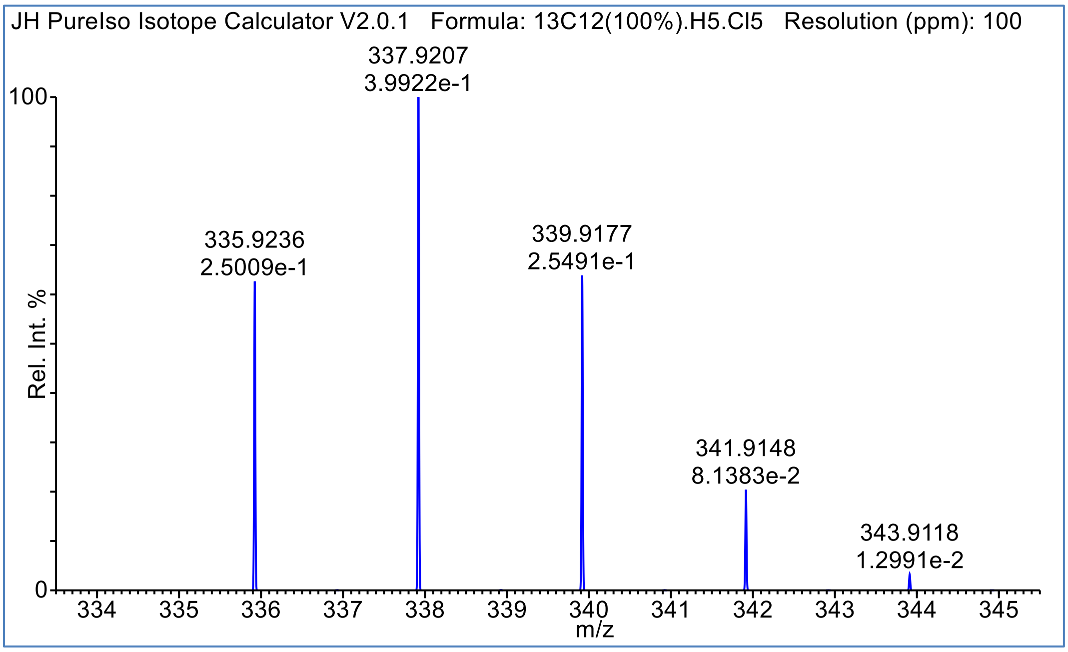

Figure 3.1 Modelled isotope distributions for the molecular ion cluster of carbon-13 labelled PeCB ($^{13}C_{12}H_5Cl_5$) showing exact *m/z* and abundances, assuming a $^{13}C$ purity of 100%.

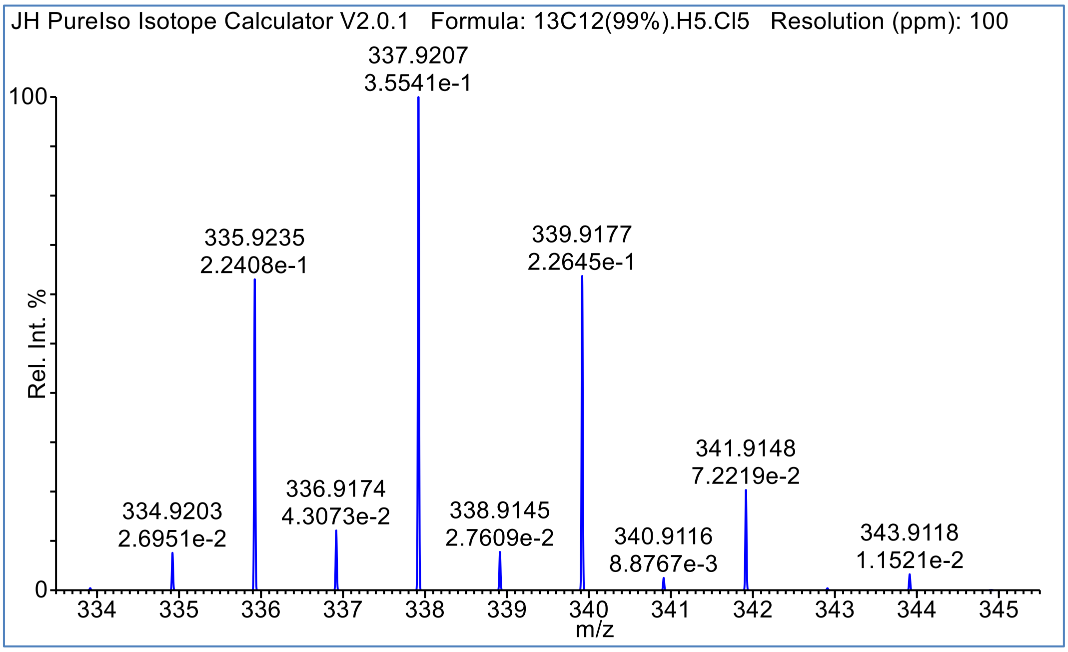

Figure 3.2 Modelled isotope distributions for the molecular ion cluster of carbon-13 labelled PeCB ($^{13}C_{12}H_5Cl_5$) showing exact *m/z* and abundances, assuming a $^{13}C$ purity of 99.0%.

## 3.4 Isotope cluster analysis: experimental data

For a comparison of actual vs. modelled $^{13}C_{12}$ molecular ion clusters, data were acquired on a G2-S Synapt, Q-IMS-TOF mass spectrometer (Waters, Wilmslow, UK) using positive AP ionisation with the TOF analyser operating at a resolution of ~18,000 (50% valley definition). The mass spectrometer was coupled to a 7890 GC with 7693 auto-sampler (Agilent, Santa Clara, CA, USA), fitted with a 30 m (length) x 0.25 mm (internal diameter) x 0.25 µm (film thickness) SPB-Octyl column (Supelco, Bellefonte, PA, USA). Splitless injections of PCB standards (Wellington Labs., Guelph, ON, Canada) were made using a 0.7 µl injection volume. Data acquisition and processing were done using MassLynx Versions 4.1. Further details of the GC-MS parameters used are given in Appendix D.2.

The molecular ion region from an averaged, centroided, spectrum of the acquired data is shown in Figure 3.3. These data show a better match to the modelled cluster using a $^{13}C$ purity of 99% (Figure 3.2) with similar contributions of minor ions, 10.1% cf. 10.8%, compared to < 0.6% from the model based on a purity of 100% (Figure 3.1) The $r^2$ values for the 99% and 100% purity models are 0.997 and 0.980 respectively.

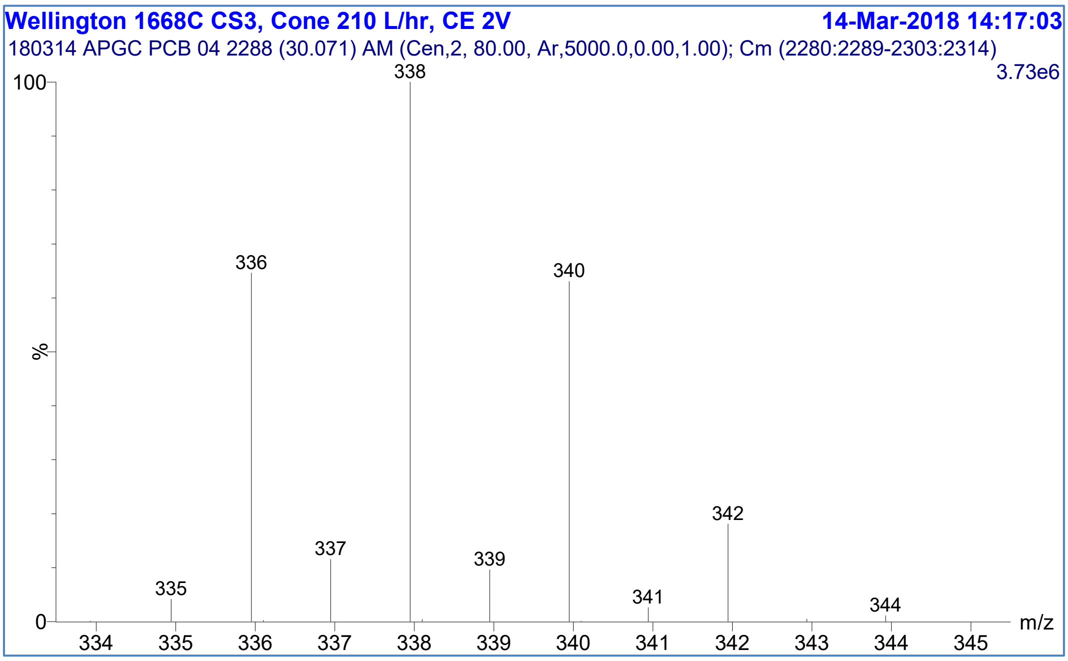

Figure 3.3 Mass spectrum of carbon-13 labelled PCB-101 (2,2',4,5,5'-PeCB, $^{13}C_{12}H_5Cl_5$) acquired on the Synapt G2-S in TOF-MS mode.

## 3.5 A comparison of abundance ratios given by PureIso, other isotope calculation programs and from published EPA methods

Table 3.1 shows the M/M+2 isotope ratios of TeCB and TCDD calculated using PureIso as compared with the published values from the EPA-1668C (USEPA, 2010) and EPA-1613B (USEPA, 1994) methods and those calculated by the MassLynx isotope utility (Ver. 4.2, Waters, Wilmslow, UK), and online programs from Chemcalc[*], Eawag[†] (Loos *et al.*, 2015) and SIS[‡].

Two sets of abundances were used for the PureIso calculations: in (1) 0.9894 for $^{12}$C and 0.7580 for $^{35}$Cl, these being the mid-points of the representative isotopic abundances' ranges from the latest 2013 IUPAC Technical Report (Meija *et al.*, 2016b); in (2) the respective values were 0.9893 and 0.7576 from the previous 2009 report (Berglund and Wieser, 2011). The abundances of H and O were unchanged between the two versions.

| Source | TeCB M/(M+2) ratio | Abs. diff. from consensus | TCDD M/(M+2) ratio | Abs. diff. from consensus |
|---|---|---|---|---|
| **PureIso (1)** | 0.7784 | 0.19% | 0.7757 | 0.16% |
| **PureIso (2)** | 0.7766 | 0.04% | 0.7741 | 0.04% |
| **MassLynx** | 0.7765 | 0.06% | 0.7740 | 0.05% |
| **Chemcalc** | 0.7766 | 0.04% | 0.7741 | 0.04% |
| **Eawag** | 0.7766 | 0.04% | 0.7741 | 0.04% |
| **SIS** | 0.7671 | 1.27% | 0.7689 | 0.71% |
| **EPA** | 0.77 | 0.89% | 0.77 | 0.57% |
| **Consensus (1-5)** | 0.7770 | | 0.7744 | |

Table 3.1 Comparison of calculated and published isotope ratios of M/M+2 for TeCB ($C_{12}H_6Cl_4$) and TCDD ($C_{12}H_4O_2Cl_4$), and the absolute differences from the consensus ratios. The PureIso program was ran using two different sets of C and Cl abundances – see main text. The EPA ratios are from the 1668C and 1613B methods (identical in these cases) and were only given to 2 decimal places. The consensus values are the average M/M+2 isotope ratios from the first 5 results, i.e. disregarding the SIS outlier value (~2 σ from the mean ratio). The magnitudes of the absolute differences from consensus values are also highlighted by the gradient shading.

---

[*] Silesian University of Technology & University of Lausanne. https://www.chemcalc.org/main

[†] Eawag/ETH, Dübendorf, Switzerland. https://www.envipat.eawag.ch/index.php

[‡] Scientific Instrument Services, NJ, USA. https://www.sisweb.com/mstools/isotope.htm

The ratios determined by PureIso match well with those from MassLynx, Chemcalc and Eawag, although the differences are clearly less with the 2009 isotopic abundances that would appear to be used in each of those programs. However, the SIS results showed differences of ~2 σ from the overall mean ratios, and these were therefore excluded in the determination of the consensus mean ratios. Compared to those consensus ratios, the EPA methods' ratios are low by ~0.9% and ~0.6% for TeCB and TCDD respectively. Whilst the latter is acceptable if reporting the ratios to 2 decimal places, the former should be revised. Furthermore, for the $^{13}$C-labelled TeCB, the calculated (PureIso) ratio is 0.786, yet the EPA-1668C value is unchanged at 0.77, i.e. an error of ~2%.

A further complication not addressed by the commercially available programs concerns mass resolution. Although parameters exist for peak separation and/or resolution, these determine the grouping and centroiding calculations for multiple isotopes within a mass window, but do not consider the partial contributions from minor isotopes made at certain exact *m/z* as monitored by the mass spectrometer at a given resolution.

In Table 3.1 above, the ratios were determined using contributions from all isotopes present at each nominal mass; e.g. for TeCB, the ratio was calculated from the sum of probabilities at mass 290 (1 contribution) and 292 (4 contributions); this is shown in detail in Table 3.2, i.e. 2.9030e-1 / 3.7294e-01 = 0.7784.

| M | Mass | Formula | Probability | Δm (ppm) | Σ probs. |
|---|---|---|---|---|---|
| M+0 | 289.9224 | $C_{12}H_6Cl_4$ | 2.9030e-1 | - | 2.9030e-1 |
| M+2 | 291.9194 | $C_{12}H_6Cl_3{}^{37}Cl$ | 3.7072e-1 | 0.0 | 3.7294e-01 |
| M+2 | 291.9291 | $C_{10}{}^{13}C_2H_6Cl_4$ | 2.1991e-3 | 33.1 | |
| M+2 | 291.9320 | $C_{11}{}^{13}CH_5{}^2HCl_4$ | 2.5755e-5 | 43.1 | |
| M+2 | 291.9349 | $C_{12}H_4{}^2H_2Cl_4$ | 5.7601e-8 | 53.1 | |

Table 3.2 Isotopologue contributions (probabilities) for TeCB ($C_{12}H_6Cl_4$) at *m/z* 290 and 292, relative mass differences of the M+2 fine isotopes and the overall M and M+2 probabilities.

However, according to the EPA-1668C method, the ions monitored for TeCB are *m/z* 289.9224 and 291.9194, therefore the 3 minor isotope peaks at *m/z* 292 that are separated in mass by ~33, 43 and 53 ppm from the main M+2 ions do not fully contribute to the overall abundance when using HRMS at the specified mass resolution of 10,000 (and hence 100 ppm peak width). The PureIso program addresses this with an option to calculate abundance ratios from the summed intensities of all isotopologue peak profiles present at each mass over a mass window defined by this (or any other) peak width; the modelled peaks assume a Gaussian distribution with a width of ca. ±2.45 σ (i.e. at 5% height), thus reasonably mimicking the acquired HRMS peak profiles. This modelling schema was then used for comparisons to the EPA-1668C method's published ratios, and the corresponding lower and upper quality control (QC) limits that must be met for positive compound identification, with the results shown for the native PCBs in Table 3.3 and for the carbon-13 labelled PCBs in Table 3.4.

| | **EPA-1668C Values** | | | **Calculated Values** | | | **Errors** | | |
|---|---|---|---|---|---|---|---|---|---|
| **PCB** | **Ra** | **-15%** | **+15%** | **Ra** | **-15%** | **+15%** | **Ra** | **-15%** | **+15%** |
| MoCB | 3.13 | 2.66 | 3.60 | 3.089 | 2.626 | 3.553 | -1.3% | -1.3% | -1.3% |
| DiCB | 1.56 | 1.33 | 1.79 | 1.550 | 1.318 | 1.783 | -0.6% | -0.9% | -0.4% |
| TrCB | 1.04 | 0.88 | 1.20 | 1.036 | 0.880 | 1.191 | -0.4% | 0.0% | -0.8% |
| TeCB | 0.77 | 0.65 | 0.89 | 0.778 | 0.661 | 0.894 | 1.0% | 1.7% | 0.5% |
| PeCB | 1.55 | 1.32 | 1.78 | 1.553 | 1.320 | 1.786 | 0.2% | 0.0% | 0.3% |
| HxCB | 1.24 | 1.05 | 1.43 | 1.244 | 1.057 | 1.431 | 0.3% | 0.7% | 0.0% |
| HpCB | 1.05 | 0.89 | 1.21 | 1.037 | 0.882 | 1.193 | -1.2% | -0.9% | -1.4% |
| OcCB | 0.89 | 0.76 | 1.02 | 0.890 | 0.756 | 1.023 | 0.0% | -0.5% | 0.3% |
| NoCB | 0.77 | 0.65 | 0.89 | 0.779 | 0.662 | 0.895 | 1.1% | 1.8% | 0.6% |
| DeCB | 1.16 | 0.99 | 1.33 | 1.168 | 0.993 | 1.343 | 0.7% | 0.3% | 1.0% |

Table 3.3 EPA-1668C native ($^{12}C_{12}$) PCB method ratios and ±15% limits of acceptance compared with calculated (PureIso) values using Gaussian modelled peak profiles with 100 ppm widths.
Absolute errors ≥1% are highlighted in yellow.

| | EPA-1668C Values | | | Calculated Values | | | Errors | | |
|---|---|---|---|---|---|---|---|---|---|
| **$^{13}$C-PCB** | **Ra** | **-15%** | **+15%** | **Ra** | **-15%** | **+15%** | **Ra** | **-15%** | **+15%** |
| MoCB | 3.13 | 2.66 | 3.60 | 3.130 | 2.660 | 3.599 | 0.0% | 0.0% | 0.0% |
| DiCB | 1.56 | 1.33 | 1.79 | 1.566 | 1.331 | 1.801 | 0.4% | 0.1% | 0.6% |
| TrCB | 1.04 | 0.88 | 1.20 | 1.045 | 0.888 | 1.202 | 0.5% | 1.0% | 0.2% |
| TeCB | 0.77 | 0.65 | 0.89 | 0.785 | 0.667 | 0.903 | 1.9% | 2.6% | 1.4% |
| PeCB | 1.55 | 1.32 | 1.78 | 1.566 | 1.331 | 1.800 | 1.0% | 0.8% | 1.1% |
| HxCB | 1.24 | 1.05 | 1.43 | 1.253 | 1.065 | 1.441 | 1.0% | 1.4% | 0.8% |
| HpCB | 1.05 | 0.89 | 1.21 | 1.045 | 0.888 | 1.201 | -0.5% | -0.2% | -0.7% |
| OcCB | 0.89 | 0.76 | 1.02 | 0.896 | 0.761 | 1.030 | 0.7% | 0.2% | 1.0% |
| NoCB | 0.77 | 0.65 | 0.89 | 0.784 | 0.667 | 0.902 | 1.8% | 2.5% | 1.3% |
| DeCB | 1.16 | 0.99 | 1.33 | 1.174 | 0.998 | 1.350 | 1.2% | 0.8% | 1.5% |

Table 3.4 EPA-1668C labelled ($^{13}C_{12}$) PCB method ratios and ±15% limits of acceptance compared with calculated (PureIso) values using Gaussian modelled peak profiles with 100 ppm widths.
Absolute errors ≥1% are highlighted in yellow and those ≥2% in orange.

Similarly, comparisons were made to the EPA-1613B method's ratios as shown in Table 3.5 for PCDDs and PCDFs, and in Table 3.6 for their $^{13}$C-labelled analogues.

| | EPA-1613B Values | | | Calculated Values | | | Errors | | |
|---|---|---|---|---|---|---|---|---|---|
| **PCDD** | **Ra** | **-15%** | **+15%** | **Ra** | **-15%** | **+15%** | **Ra** | **-15%** | **+15%** |
| TCDD | 0.77 | 0.65 | 0.89 | 0.775 | 0.659 | 0.891 | 0.6% | 1.3% | 0.1% |
| PeCDD | 1.55 | 1.32 | 1.78 | 1.547 | 1.315 | 1.779 | -0.2% | -0.4% | 0.0% |
| HxCDD | 1.24 | 1.05 | 1.43 | 1.240 | 1.054 | 1.426 | 0.0% | 0.4% | -0.3% |
| HpCDD | 1.05 | 0.89 | 1.21 | 1.035 | 0.880 | 1.190 | -1.4% | -1.2% | -1.6% |
| OCDD | 0.89 | 0.76 | 1.02 | 0.888 | 0.755 | 1.021 | -0.2% | -0.7% | 0.1% |
| **PCDF** | | | | | | | | | |
| TCDF | 0.77 | 0.65 | 0.89 | 0.776 | 0.660 | 0.893 | 0.8% | 1.5% | 0.3% |
| PeCDF | 1.55 | 1.32 | 1.78 | 1.550 | 1.318 | 1.783 | 0.0% | -0.2% | 0.1% |
| HxCDF | 1.24 | 1.05 | 1.43 | 1.242 | 1.056 | 1.428 | 0.2% | 0.5% | -0.1% |
| HpCDF | 1.05 | 0.89 | 1.21 | 1.036 | 0.881 | 1.192 | -1.3% | -1.0% | -1.5% |
| OCDF | 0.89 | 0.76 | 1.02 | 0.889 | 0.756 | 1.022 | -0.1% | -0.6% | 0.2% |

Table 3.5 EPA-1613B native ($^{12}C_{12}$) PCDD and PCDF method ratios and ±15% limits of acceptance compared with calculated (PureIso) values using Gaussian modelled peak profiles with 100 ppm widths.
Absolute errors ≥1% are highlighted in yellow.

|  | EPA-1613B Values |  |  | Calculated Values |  |  | Errors |  |  |
|---|---|---|---|---|---|---|---|---|---|
| **$^{13}$C-PCDD** | **Ra** | **-15%** | **+15%** | **Ra** | **-15%** | **+15%** | **Ra** | **-15%** | **+15%** |
| TCDD | 0.77 | 0.65 | 0.89 | 0.783 | 0.665 | 0.900 | 1.6% | 2.3% | 1.1% |
| PeCDD | 1.55 | 1.32 | 1.78 | 1.560 | 1.326 | 1.794 | 0.6% | 0.5% | 0.8% |
| HxCDD | 1.24 | 1.05 | 1.43 | 1.249 | 1.062 | 1.437 | 0.8% | 1.1% | 0.5% |
| HpCDD | 1.05 | 0.89 | 1.21 | 1.042 | 0.886 | 1.198 | -0.8% | -0.5% | -1.0% |
| OCDD | 0.89 | 0.76 | 1.02 | 0.894 | 0.760 | 1.028 | 0.4% | 0.0% | 0.8% |
| **$^{13}$C-PCDF** |  |  |  |  |  |  |  |  |  |
| TCDF | 0.77 | 0.65 | 0.89 | 0.784 | 0.666 | 0.901 | 1.8% | 2.5% | 1.3% |
| PeCDF | 1.55 | 1.32 | 1.78 | 1.563 | 1.328 | 1.797 | 0.8% | 0.6% | 1.0% |
| HxCDF | 0.51 | 0.43 | 0.59 | 0.524 | 0.445 | 0.602 | 2.7% | 3.6% | 2.1% |
| HpCDF | 0.44 | 0.37 | 0.51 | 0.450 | 0.382 | 0.517 | 2.2% | 3.3% | 1.4% |
| OCDF | 0.89 | 0.76 | 1.02 | 0.895 | 0.761 | 1.029 | 0.5% | 0.1% | 0.9% |

Table 3.6 EPA-1613B labelled ($^{13}C_{12}$) PCDD and PCDF method ratios and ±15% limits of acceptance compared with calculated (PureIso) values using Gaussian modelled peak profiles with 100 ppm widths.
Absolute errors ≥1% are highlighted in yellow, ≥2% in orange and ≥3% in red.

Differences between the calculated[*] and methods' values ≥ 1% are highlighted in yellow, ≥ 2% in orange and ≥ 3% in red. Notwithstanding the issues previously discussed in Chapter 2 (regarding ion statistics in these assessments) these errors, although small, could lead to misrepresentation of the data due to the binary choice of accepting or rejecting peaks based on these QC limits: the methods[†] should therefore be revised accordingly.

---

[*] Using abundances of 0.9893 for $^{12}$C and 0.7576 for $^{35}$Cl.

[†] Similar re-evaluations should also be performed on other POPs methods that use the same identification criteria.

## 3.6 MS/MS isotope ratio calculations

For MS/MS analyses, the determination of the isotope ratios of product ions needs to consider the proportion of the relevant isotopes present in the precursor ion and the chosen mass loss. E.g. for TCDD, the most intense fragments are due to the loss of COCl, therefore the experiment would include the multiple reaction monitoring (MRM) transitions:

> *m/z* 319.9 > 256.9 and *m/z* 321.9 > 258.9
>
> In both cases, $\Delta m \approx 63$ Da from (specifically) $^{12}C^{16}O^{35}Cl$.

As shown in Table 3.7, the first transition has just one possible pathway as the *m/z* 319.9 ion of TCDD can only be formed by a single combination of the available isotopes, however there are 8 contributors to the loss from *m/z* 321.9 ion, although one of these – albeit an extremely minor ($< 10^{-5}$ %) contributor – cannot lose the COCl *m/z* 63 since it does not contains any $^{16}O$ atoms, hence there are 7 viable transition pathways.

| **Precursor ion** | ***m/z*** | **Precursor abundance** | **Product ion from the loss of $^{12}C^{16}O^{35}Cl$** | ***m/z*** |
|---|---|---|---|---|
| $^{12}C_{12}{}^{1}H_{4}{}^{16}O_{2}{}^{35}Cl_{4}$ | 319.8965 | 2.88e-01 | $^{12}C_{11}{}^{1}H_{4}{}^{16}O_{1}{}^{35}Cl_{3}$ | 256.9328 |
| $^{12}C_{12}{}^{1}H_{4}{}^{16}O_{2}{}^{35}Cl_{3}{}^{37}Cl_{1}$ | 321.8936 | 3.69e-01 | $^{12}C_{11}{}^{1}H_{4}{}^{16}O_{1}{}^{35}Cl_{2}{}^{37}Cl_{1}$ | 258.9298 |
| $^{12}C_{12}{}^{1}H_{4}{}^{16}O_{1}{}^{18}O_{1}{}^{35}Cl_{4}$ | 321.9008 | 1.18e-03 | $^{12}C_{11}{}^{1}H_{4}{}^{18}O_{1}{}^{35}Cl_{3}$ | 258.9370 |
| $^{12}C_{10}{}^{13}C_{2}{}^{1}H_{4}{}^{16}O_{2}{}^{35}Cl_{4}$ | 321.9032 | 2.22e-03 | $^{12}C_{9}{}^{13}C_{2}{}^{1}H_{4}{}^{16}O_{1}{}^{35}Cl_{3}$ | 258.9395 |
| $^{12}C_{11}{}^{13}C_{1}{}^{1}H_{4}{}^{16}O_{1}{}^{17}O_{1}{}^{35}Cl_{4}$ | 321.9041 | 2.85e-05 | $^{12}C_{10}{}^{13}C_{1}{}^{1}H_{4}{}^{17}O_{1}{}^{35}Cl_{3}$ | 258.9403 |
| $^{12}C_{12}{}^{1}H_{4}{}^{17}O_{2}{}^{35}Cl_{4}$ | 321.9050 | 4.18e-08 | no viable loss of $^{12}C^{16}O^{35}Cl$ | |
| $^{12}C_{11}{}^{13}C_{1}{}^{1}H_{3}{}^{2}H_{1}{}^{16}O_{2}{}^{35}Cl_{4}$ | 321.9062 | 1.72e-05 | $^{12}C_{10}{}^{13}C_{1}{}^{1}H_{3}{}^{2}H_{1}{}^{16}O_{1}{}^{35}Cl_{3}$ | 258.9424 |
| $^{12}C_{12}{}^{1}H_{3}{}^{2}H_{1}{}^{16}O_{1}{}^{17}O_{1}{}^{35}Cl_{4}$ | 321.9070 | 1.01e-07 | $^{12}C_{11}{}^{1}H_{3}{}^{2}H_{1}{}^{17}O_{1}{}^{35}Cl_{3}$ | 258.9433 |
| $^{12}C_{12}{}^{1}H_{2}{}^{2}H_{2}{}^{16}O_{2}{}^{35}Cl_{4}$ | 321.9091 | 2.29e-08 | $^{12}C_{11}{}^{1}H_{2}{}^{2}H_{2}{}^{16}O_{1}{}^{35}Cl_{3}$ | 258.9453 |

Table 3.7 Precursor and product ion formulae, exact *m/z* and abundances for the loss of COCl (specifically $^{12}C^{16}O^{35}Cl$) from the molecular ion of TCDD (M+0 and M+2) in an MS/MS (MRM) experiment.
Due to the nature of this discussion, all superscripts and subscripts are shown, including unity.

For each pathway, there is an associated probability that the atoms are those required for the specific mass loss. E.g. of the 4 Cl atoms in the precursor TCDD molecule for the [M+2] > [M+2 -$^{12}C^{16}O^{35}Cl$] transition, [$^{12}C_{12}{}^{1}H_{4}{}^{16}O_{2}{}^{35}Cl_{3}{}^{37}Cl_{1}$] > [$^{12}C_{11}{}^{1}H_{4}{}^{16}O_{1}{}^{35}Cl_{2}{}^{37}Cl_{1}$], 3 are $^{35}Cl$ and 1 is $^{37}Cl$; since the required mass loss must include $^{35}Cl$ there is a 75% probability of this occurring. These probabilities can be similarly calculated for the remaining transitions as shown in Table 3.8; although many of these transitions result in minor contributions, they are nevertheless included for completeness.

The effective ratio can then be calculated by taking the M+0 abundance divided by the total of M+2 abundances, yielding 1.031. Using just the major M+2 contribution (0.277) would have given a reasonable approximation (difference < 1%) to this with a ratio of 1.041. This matches the 1.04 given by Kotz *et al* where their calculations used only this single value for the M+2 abundance (Kotz *et al.*, 2014).

| **M** | **Precursor ion** | **Precursor abundance** | **Product ion from the loss of $^{12}C^{16}O^{35}Cl$** | **Occurrence probability** | **Product ion abundance** |
|---|---|---|---|---|---|
| M+0 | $^{12}C_{12}{}^{1}H_{4}{}^{16}O_{2}{}^{35}Cl_{4}$ | 2.88e-01 | $^{12}C_{11}{}^{1}H_{4}{}^{16}O_{1}{}^{35}Cl_{3}$ | 100% | 2.88e-01 |
| M+2 | $^{12}C_{12}{}^{1}H_{4}{}^{16}O_{2}{}^{35}Cl_{3}{}^{37}Cl_{1}$ | 3.69e-01 | $^{12}C_{11}{}^{1}H_{4}{}^{16}O_{1}{}^{35}Cl_{2}{}^{37}Cl_{1}$ | 75% | 2.77e-01 |
| | $^{12}C_{12}{}^{1}H_{4}{}^{16}O_{1}{}^{18}O_{1}{}^{35}Cl_{4}$ | 1.18e-03 | $^{12}C_{11}{}^{1}H_{4}{}^{18}O_{1}{}^{35}Cl_{3}$ | 50% | 5.90e-04 |
| | $^{12}C_{10}{}^{13}C_{2}{}^{1}H_{4}{}^{16}O_{2}{}^{35}Cl_{4}$ | 2.22e-03 | $^{12}C_{9}{}^{13}C_{2}{}^{1}H_{4}{}^{16}O_{1}{}^{35}Cl_{3}$ | 83% | 1.84e-03 |
| | $^{12}C_{11}{}^{13}C_{1}{}^{1}H_{4}{}^{16}O_{1}{}^{17}O_{1}{}^{35}Cl_{4}$ | 2.85e-05 | $^{12}C_{10}{}^{13}C_{1}{}^{1}H_{4}{}^{17}O_{1}{}^{35}Cl_{3}$ | 46% | 1.31e-05 |
| | $^{12}C_{12}{}^{1}H_{4}{}^{17}O_{2}{}^{35}Cl_{4}$ | 4.18e-08 | n/a | 0% | 0.00e+00 |
| | $^{12}C_{11}{}^{13}C_{1}{}^{1}H_{3}{}^{2}H_{1}{}^{16}O_{2}{}^{35}Cl_{4}$ | 1.72e-05 | $^{12}C_{10}{}^{13}C_{1}{}^{1}H_{3}{}^{2}H_{1}{}^{16}O_{1}{}^{35}Cl_{3}$ | 92% | 1.58e-05 |
| | $^{12}C_{12}{}^{1}H_{3}{}^{2}H_{1}{}^{16}O_{1}{}^{17}O_{1}{}^{35}Cl_{4}$ | 1.01e-07 | $^{12}C_{11}{}^{1}H_{3}{}^{2}H_{1}{}^{17}O_{1}{}^{35}Cl_{3}$ | 50% | 5.05e-08 |
| | $^{12}C_{12}{}^{1}H_{2}{}^{2}H_{2}{}^{16}O_{2}{}^{35}Cl_{4}$ | 2.29e-08 | $^{12}C_{11}{}^{1}H_{2}{}^{2}H_{2}{}^{16}O_{1}{}^{35}Cl_{3}$ | 100% | 2.29e-08 |

Table 3.8 Precursor ion abundances and probabilities of product ion formation for the loss of COCl (specifically $^{12}C^{16}O^{35}Cl$) from the molecular ion of TCDD (M+0 and M+2) and the resultant product ion abundances.

## 3.7 MS/MS fragmentation: experimental

In the following experiment, a mix of 4 Aroclors[*]: 1016, 1232, 1248 and 1260 [Supelco, Bellefonte, PA, USA (catalogue number 4-8861)] was analysed using a Quattro MS/MS triple-quadrupole instrument (Micromass, Manchester, UK). The source was operated in positive electron ionisation (EI) at 34 eV, and data acquisition performed in the MRM mode.

The MS/MS instrument was coupled to a 6890 GC (Agilent, Santa Clara, CA, USA), fitted with a 30 m (length) x 0.25 mm (internal diameter) x 0.25 µm (film thickness) DB-5ms column (Agilent, Santa Clara, CA, USA). Manual injections of 1 µl were made with a 10:1 split ratio.

Argon was used as the collision gas at a pressure of ~$10^{-3}$ mbar with a collision energy of 20 eV. Further details of the key GC-MS/MS parameters used are given in Appendix D.3.

## 3.8 MS/MS fragmentation: results and discussion

MRM chromatograms were generated, and peak detection performed, for the *m/z* 323.9 > 253.9, *m/z* 325.9 > 255.9 and *m/z* 325.9 > 253.9 transitions, as shown in Figure 3.4. Although the MS/MS analysis of PeCBs, as per the current EU PCB method (European Commission, 2017), only requires the first 2 transitions to be monitored for the mass loss of 70 Da ($2^{35}Cl$), the loss of 72 Da ($^{35}Cl^{37}Cl$) from *m/z* 325.9 > 253.9 is included here for additional confirmation.

---

[*] See section 1.3 (p. 5) for background information on the Aroclor PCB mixes.

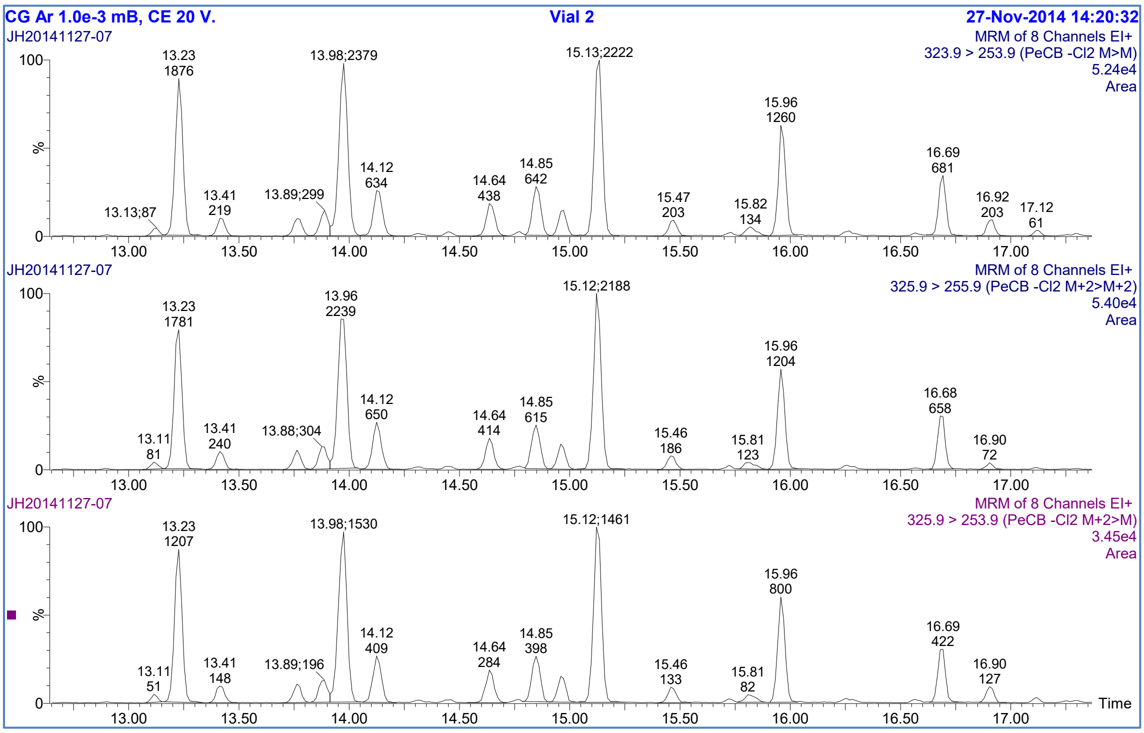

Figure 3.4 Peak-detected MRM chromatograms for the *m/z* 323.9 > 253.9 (-70 Da), *m/z* 325.9 > 255.9 (-70 Da) and *m/z* 325.9 > 253.9 (-72 Da) transitions for a set of PeCB congeners.

The expected abundance ratios can be determined using the same approach described in the previous section, resulting in the values shown in Table 3.9. The expected ion abundance ratios for peaks from the *m/z* 325.9 > 255.9 and *m/z* 325.9 > 253.9 transitions, relative to those of *m/z* 323.9 > 253.9, can therefore be calculated from the summed product ion abundances:

2.192e-1 / 2.121e-1 = 1.033

2.192e-1 / 1.403e-1 = 1.563

| M | Precursor ion | Precursor abundance | Mass loss | Product ion | Prob. | Product ion abundance | Sum of abundances |
|---|---|---|---|---|---|---|---|
| M+0 | $^{12}C_{12}{}^{1}H_{5}{}^{35}Cl_{5}$ | 2.192e-1 | 70 | $^{12}C_{12}{}^{1}H_{5}{}^{35}Cl_{3}$ | 100% | 2.192e-1 | 2.192e-1 |
| M+2 | $^{12}C_{12}{}^{1}H_{5}{}^{35}Cl_{4}{}^{37}Cl_{1}$ | 3.507e-1 | 70 | $^{12}C_{12}{}^{1}H_{5}{}^{35}Cl_{2}{}^{37}Cl_{1}$ | 60% | 2.104e-1 | 2.121e-1 |
| M+2 | $^{12}C_{10}{}^{13}C_{2}{}^{1}H_{5}{}^{35}Cl_{5}$ | 1.693e-3 | 70 | $^{12}C_{10}{}^{13}C_{2}{}^{1}H_{5}{}^{35}Cl_{3}$ | 100% | 1.693e-3 | |
| M+2 | $^{12}C_{11}{}^{13}C_{1}{}^{1}H_{4}{}^{2}H_{1}{}^{35}Cl_{5}$ | 1.636e-5 | 70 | $^{12}C_{11}{}^{13}C_{1}{}^{1}H_{4}{}^{2}H_{1}{}^{35}Cl_{3}$ | 100% | 1.636e-5 | |
| M+2 | $^{12}C_{12}{}^{1}H_{3}{}^{2}H_{2}{}^{35}Cl_{5}$ | 2.900e-8 | 70 | $^{12}C_{12}{}^{1}H_{3}{}^{2}H_{2}{}^{35}Cl_{3}$ | 100% | 2.900e-8 | |
| M+2’ | $^{12}C_{12}{}^{1}H_{5}{}^{35}Cl_{4}{}^{37}Cl_{1}$ | 3.507e-1 | 72 | $^{12}C_{12}{}^{1}H_{5}{}^{35}Cl_{3}$ | 40% | 1.403e-1 | 1.403e-1 |

Table 3.9 Probabilities of formation of product ions from the loss of 2Cl from the M+0 and M+2 ions of PeCB and the resultant product ion abundances.
The data in the last row (M+2’) correspond to the loss of $^{35}Cl^{37}Cl$ (72 Da), for all other rows the loss is of $2^{35}Cl$ (70 Da).

The results from the acquired data of the 10 most intense peaks are summarised in Table 3.10 and show consistent ion abundance ratios (RSD < 3%) and good agreement with theoretical values (mean error < 1%).

| RT | Peak area 324 > 254 (A) | Peak area 326 > 256 (B) | Peak area 326 > 254 (C) | Abundance ratio A/B | Abundance ratio A/C |
|---|---|---|---|---|---|
| 13.23 | 1876 | 1781 | 1207 | 1.054 | 1.554 |
| 13.89 | 299 | 304 | 196 | 0.982 | 1.522 |
| 13.98 | 2379 | 2239 | 1530 | 1.062 | 1.555 |
| 14.13 | 634 | 650 | 409 | 0.977 | 1.552 |
| 14.64 | 438 | 414 | 284 | 1.057 | 1.545 |
| 14.85 | 642 | 615 | 398 | 1.044 | 1.613 |
| 14.97 | 318 | 314 | 215 | 1.012 | 1.481 |
| 15.13 | 2222 | 2188 | 1461 | 1.016 | 1.521 |
| 15.96 | 1260 | 1204 | 800 | 1.047 | 1.576 |
| 16.69 | 681 | 658 | 422 | 1.036 | 1.613 |
| | | | **Mean:** | 1.029 | 1.553 |
| | | | **RSD:** | 2.99% | 2.63% |
| | | | **Theoretical abundance:** | 1.033 | 1.563 |
| | | | **Deviation from theoretical:** | -0.45% | -0.60% |

Table 3.10 Summary of the PeCB MRM data shown in the chromatograms of Figure 3.4, showing peak retention times (RT), areas, calculated abundance ratios and comparisons to theoretical values.

## 3.9 Mass and intensity errors due to mixed AP ionisation modes

To date, all published methods relating to the analysis of the POPs discussed in this thesis have been based on the use of HRMS and EI; as GC-MS/MS is now permitted for certain regulated analyses (as previously discussed in section 1.13), any mass or intensity artefacts arising from atmospheric pressure (AP) ionisation – commonly used as an alternative to EI with such instruments – should be examined.

A schematic of the AP ion source region for the Synapt G2-S GC-MS/MS (Q-TOF) instrument (Waters, Wilmslow, UK) used in the following experiments is shown in Figure 3.5. The GC column is carried through a heated interface to within ~5 mm of the corona pin to maximise ionisation of its eluent.

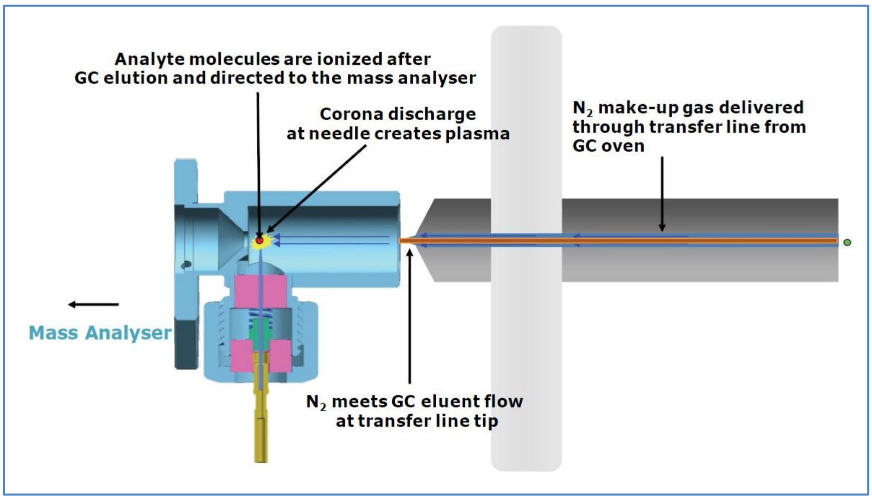

Figure 3.5 Schematic outline of the GC interface and atmospheric pressure (AP) ion source region found in the Waters' Synapt G2-S (Q-TOF) and Xevo (triple-quad) instruments. (Image courtesy of Waters, Wilmslow, UK)

AP ionisation nominally operates in either charge transfer or protonation mode based on the mechanisms shown in Figure 3.6. In the former, a high voltage (~5 kV) is applied to the source corona pin causing corona discharge ionisation of the nitrogen gas present in the source; these $N_2^{+\bullet}$ cations then react with the analyte molecules and the resulting charge transfers form positive ions ($M^{+\bullet}$). In protonation mode, the corona discharge ionisation initiates a reaction with a suitable reagent, e.g. water as in this example, that is admitted into the ion source; intermediate cations of $H_2O^{+\bullet}$ and $H_3O^{+\bullet}$ are created and provide the protons that lead to formation of the $[M+H]^+$ ions. Although this might be desirable for some compounds, it is less likely to benefit the relatively non-polar dioxins or PCBs.

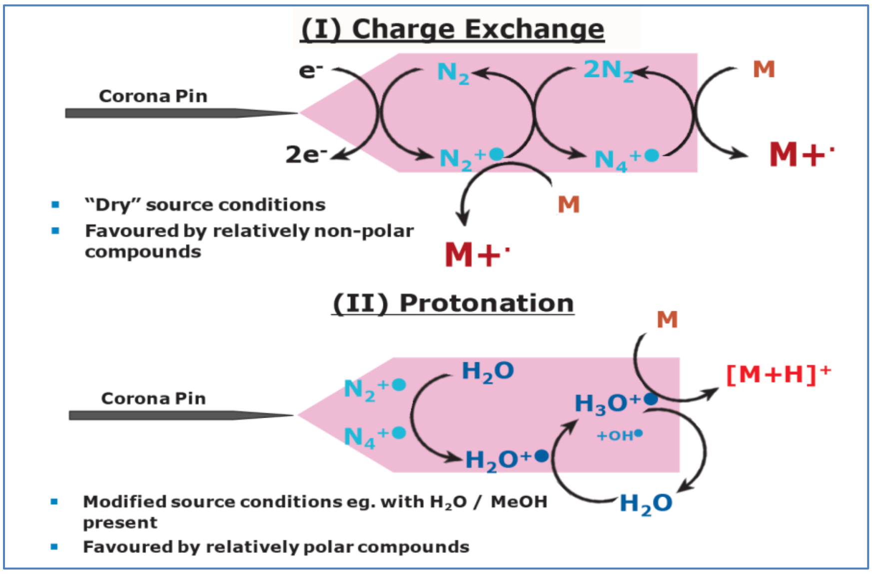

Figure 3.6 Illustration of the atmospheric pressure ionisation mechanisms for charge exchange and protonation.
(Image courtesy of Waters, Wilmslow, UK)

Although an instrument may be nominally operating in the charge transfer mode, some degree of protonation can occur due to the ubiquitous presence of background water in the ion source and/or sample introduction systems resulting in mixed ionisation modes. This was observed in the molecular ion region of the TeCB spectrum shown in Figure 3.7 where intensities of the minor ions – those due to naturally occurring $^{13}C$ isotope peaks – were clearly higher than expected.

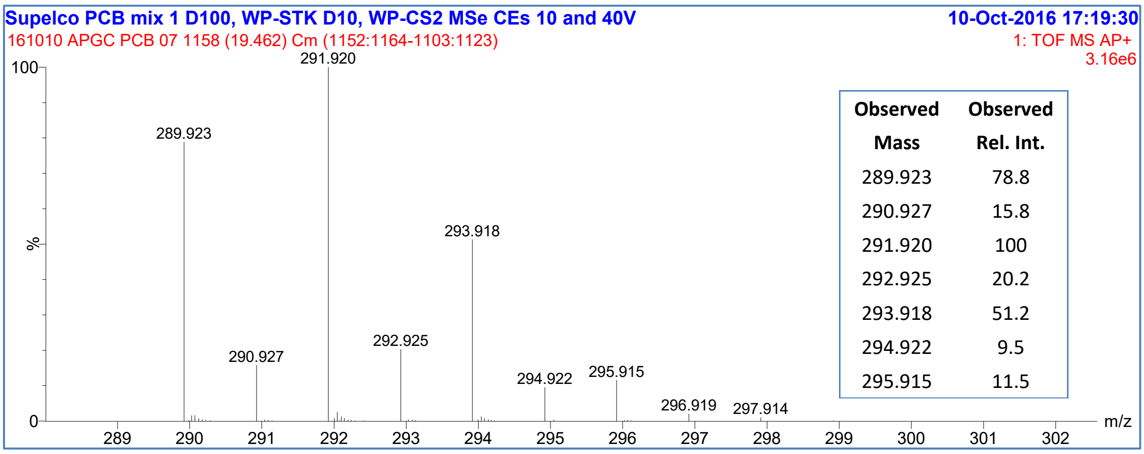

| Observed Mass | Observed Rel. Int. |
|---|---|
| 289.923 | 78.8 |
| 290.927 | 15.8 |
| 291.920 | 100 |
| 292.925 | 20.2 |
| 293.918 | 51.2 |
| 294.922 | 9.5 |
| 295.915 | 11.5 |

Figure 3.7 Acquired spectrum from the molecular ion region of TeCB ($C_{12}H_6Cl_4$) indicating mixed ionisation from both charge transfer and protonation modes.

A comparison with the modelled isotope cluster distribution, as shown in Figure 3.8, confirmed this: e.g. the ion recorded at *m/z* 293 showed a relative intensity of ~20% compared to its theoretical value of ~13%. In addition, the measured *m/z* of these ions showed errors ~1 mDa greater than those of the major ions.

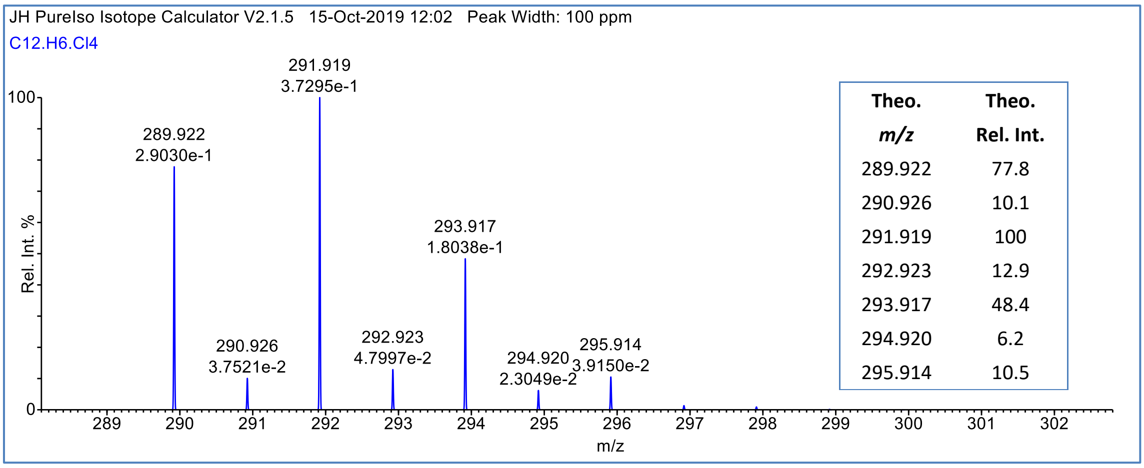

| Theo. *m/z* | Theo. Rel. Int. |
|---|---|
| 289.922 | 77.8 |
| 290.926 | 10.1 |
| 291.919 | 100 |
| 292.923 | 12.9 |
| 293.917 | 48.4 |
| 294.920 | 6.2 |
| 295.914 | 10.5 |

Figure 3.8 Modelled molecular ion cluster of TeCB ($C_{12}H_6Cl_4$) showing exact *m/z* and abundances.

These data are summarised in Table 3.11 with the *m/z* and intensities shown for the theoretical (Columns B, C) and measured (Columns D, E) data, and their corresponding differences (Columns F, G). These data suggest that the observed errors may be due to the formation of protonated molecules that, given the *m/z* differences between the protonated and non-protonated species of ~15 ppm, would not have been resolved on the instrument in use.

| A | B | C | D | E | F | G | H | I | J | K | L | M |
|---|---|---|---|---|---|---|---|---|---|---|---|---|
| **TeCB** | **Theo.** | **Theo.** | **Obs.** | **Obs.** | **Δ *m/z*** | **Int.** | **Theo.** | **Adj.** | **Int.** | **[M+H]** | **Adj.** | **Adj.** |
| **Ion** | ***m/z*** | **Rel. Int.** | ***m/z*** | **Rel. Int.** | **mDa** | **Error** | **[M+H]** | **Rel. Int.** | **RPD** | **% (est.)** | ***m/z*** | **Δ mDa** |
| M+0 | 289.922 | 77.8 | 289.923 | 78.8 | 0.6 | 1% | | | | | 289.923 | 0.6 |
| M+1 | 290.926 | 10.1 | 290.927 | 15.8 | 1.3 | 57% | 290.930 | 15.8 | 0% | 36% | 290.926 | 0.1 |
| M+2 | 291.920 | 100 | 291.920 | 100 | 0.5 | 0% | 291.934 | 100 | 0% | 0% | 291.920 | 0.5 |
| M+3 | 292.923 | 12.9 | 292.925 | 20.2 | 2.2 | 57% | 292.927 | 20.2 | 0% | 36% | 292.924 | 1.4 |
| M+4 | 293.917 | 48.4 | 293.918 | 51.2 | 1.4 | 6% | 293.931 | 49.0 | 5% | 1% | 293.918 | 1.2 |
| M+5 | 294.920 | 6.2 | 294.922 | 9.5 | 2.1 | 54% | 294.924 | 9.7 | 2% | 37% | 294.921 | 1.2 |
| M+6 | 295.914 | 10.5 | 295.915 | 11.5 | 1.2 | 10% | 295.928 | 10.9 | 6% | 4% | 295.915 | 0.8 |
| | | | RMS error (mDa) | | 1.46 | | [M+H] % | 7.5% | | RMS error (mDa) | | 0.93 |

Table 3.11 The *m/z* and intensity errors due to mixed AP ionisation in the analysis of TeCB ($C_{12}H_6Cl_4$), and the results from applying corrections to account for the degree of protonation.

Although these *m/z* differences could be partially or fully resolved on other mass spectrometers that also support APCI, such as Orbitraps[*] and Fourier-transform ion cyclotron resonance (FTICR) instruments[†], other performance limitations, practical considerations and/or high cost restrict their use for routine analysis.

To test this idea, the theoretical protonated *m/z* have been added to the table (Column H) and the overall intensities at each *m/z* calculated (Column I) based on the "degree-of-protonation" factor shown as [M+H] %. From these, the relative percent difference (RPD) in intensity for each *m/z* is calculated (Column J). The average RPD value was then used as the target for minimisation using the Excel solver function – this yielded an estimate for the degree-of-protonation of ~7.5%. The relative contributions due to the protonated *m/z* can now be calculated (Column K) and used to determine corrected *m/z* (Column L). The *m/z* errors (Column M) show an overall reduction with an RMS error of 0.93 mDa compared to 1.46 mDa in the uncorrected data, though an overall bias in the reported *m/z* is still evident.

---

[*] E.g. Q-Exactive Orbitrap (Thermo Scientific); resolution specification > 50,000 (FWHM)

[†] E.g. solariX FTICR-MS (Bruker Daltonics); resolution specification > $10^7$ (FWHM)

The above process was then repeated using PeCB data from the same sample with the results summarised in Table 3.12. The results show a similar pattern to the TeCB data above, with an estimate for the degree-of-protonation of ~6.5%.

| A | B | C | D | E | F | G | H | I | J | K | L | M |
|---|---|---|---|---|---|---|---|---|---|---|---|---|
| **PeCB** | **Theo.** | **Theo.** | **Obs.** | **Obs.** | **Δ *m/z*** | **Int.** | **Theo.** | **Adj.** | **Int.** | **[M+H]** | **Adj.** | **Adj.** |
| **Ion** | ***m/z*** | **Rel. Int.** | ***m/z*** | **Rel. Int.** | **mDa** | **Error** | **[M+H]** | **Rel. Int.** | **RPD** | **% (est.)** | ***m/z*** | **Δ mDa** |
| M+0 | 323.883 | 62.3 | 323.884 | 65.0 | 0.6 | 4% | | | | | 323.884 | 0.6 |
| M+1 | 324.887 | 8.1 | 324.887 | 12.4 | 0.2 | 54% | 324.891 | 12.0 | 3% | 33% | 324.886 | -1.2 |
| M+2 | 325.881 | 100 | 325.881 | 100 | 0.5 | 0% | 325.895 | 100 | 0% | 0% | 325.881 | 0.5 |
| M+3 | 326.884 | 12.9 | 326.885 | 19.3 | 1.2 | 50% | 326.888 | 19.3 | 0% | 33% | 326.884 | 0.1 |
| M+4 | 327.878 | 64.3 | 327.878 | 66.3 | 0.4 | 3% | 327.892 | 64.8 | 2% | 1% | 327.878 | 0.3 |
| M+5 | 328.881 | 8.2 | 328.882 | 11.6 | 1.1 | 41% | 328.885 | 12.4 | 6% | 33% | 328.881 | 0.0 |
| M+6 | 329.875 | 20.8 | 329.875 | 22.1 | 0.2 | 6% | 329.889 | 21.2 | 4% | 2% | 329.875 | -0.1 |
| | | | RMS error (mDa) | | 0.71 | | [M+H] % | 6.5% | | RMS error (mDa) | | 0.55 |

Table 3.12 The *m/z* and intensity errors due to mixed AP ionisation in the analysis of PeCB ($C_{12}H_5Cl_5$), and the results from applying corrections to account for the degree of protonation.

To verify that these proposed protonation effects were not due to peak (intensity) saturation – that would have similarly resulted in elevated isotopic abundances of the minor peaks, though not their corresponding *m/z* shifts – a further study was made using $^{13}C$-labelled TeCB.

As shown by the data in Table 3.13, the M-1/M+1 ratio is elevated due to protonation of M+0; any saturation effects would have led to a decreased ratio. (A similar proof can also be seen in the subsequent MoCB data with its increased M+1/M+2 ratio.)

| A | B | C | D | E | F | G | H | I | J | K | L | M | |
|---|---|---|---|---|---|---|---|---|---|---|---|---|---|
| **TeCB** | **Theo.** | **Theo.** | **Obs.** | **Obs.** | **Δ *m/z*** | **Int.** | **Theo.** | **Adj.** | **Int.** | **[M+H]** | **Adj.** | **Adj.** | **Weighted** |
| **Ion** | ***m/z*** | **Rel. Int.** | ***m/z*** | **Rel. Int.** | **mDa** | **Error** | **[M+H]** | **Rel. Int.** | **RPD** | **% (est.)** | ***m/z*** | **Δ mDa** | **errors** |
| M-1 | 300.959 | 9.5 | 300.960 | 9.9 | 0.8 | 4% | 300.964 | | | | 300.960 | 0.8 | 0.1 |
| M+0 | 301.963 | 78.7 | 301.964 | 79.2 | 1.2 | 1% | 301.967 | 78.7 | 1% | 0% | 301.964 | 1.2 | 0.9 |
| M+1 | 302.956 | 12.1 | 302.960 | 17.1 | 4.0 | 41% | 302.970 | 16.8 | 2% | 28% | 302.958 | 1.2 | 0.1 |
| M+2 | 303.960 | 100 | 303.961 | 100 | 1.3 | 0% | 303.964 | 100.0 | 0% | 0% | 303.961 | 1.3 | 1.3 |
| M+3 | 304.954 | 5.9 | 304.961 | 11.4 | 7.8 | 95% | 304.968 | 11.9 | 4% | 51% | 304.958 | 4.7 | 0.3 |
| M+4 | 305.957 | 47.8 | 305.958 | 47.7 | 1.4 | 0% | 305.961 | 47.8 | 0% | 0% | 305.958 | 1.4 | 0.7 |
| M+5 | 306.951 | 1.3 | 306.960 | 4.2 | 9.1 | 234% | 306.965 | 4.1 | 2% | 70% | 306.957 | 5.8 | 0.1 |
| M+6 | 307.954 | 10 | 307.955 | 10 | 1.2 | -5% | 307.959 | 10.2 | 5% | 0% | 307.955 | 1.2 | 0.1 |
| | | | RMS error (mDa) | | 4.57 | | [M+H] % | 6.10% | | RMS error (mDa) | | 2.84 | 0.63 |

Table 3.13 The *m/z* and intensity errors due to mixed AP ionisation in the analysis of carbon-13 labelled TeCB ($^{13}C_{12}H_6Cl_4$), and the results from applying corrections to account for the degree of protonation.

The above examples have focussed on the effect on minor ions – as these are the most apparent – though the primary ions are also affected as evident in the MoCB data shown in Table 3.14 where the M/M+2 ratio is ~9% lower than expected.

| A | B | C | D | E | F | G | H | I | J | K | L | M |
|---|---|---|---|---|---|---|---|---|---|---|---|---|
| **MoCB** | **Theo.** | **Theo.** | **Obs.** | **Obs.** | **Δ *m/z*** | **Int.** | **Theo.** | **Adj.** | **Int.** | **[M+H]** | **Adj.** | **Adj.** |
| **Ion** | ***m/z*** | **Rel. Int.** | ***m/z*** | **Rel. Int.** | **mDa** | **Error** | **[M+H]** | **Rel. Int.** | **RPD** | **% (est.)** | ***m/z*** | **Δ mDa** |
| M+0 | 188.039 | 100 | 188.041 | 100 | 1.7 | 0% | | 100 | | | 188.041 | 1.7 |
| M+1 | 189.043 | 13.1 | 189.045 | 17.7 | 2.3 | 35% | 189.047 | 17.7 | 0% | 26% | 189.044 | 1.8 |
| M+2 | 190.037 | 32.4 | 190.038 | 35.5 | 1.4 | 10% | 190.051 | 33.0 | 7% | 2% | 190.038 | 1.2 |
| M+3 | 191.040 | 4.2 | 191.042 | 5.6 | 2.2 | 33% | 191.044 | 5.7 | 2% | 26% | 191.041 | 1.6 |
| | | | RMS error (mDa) | | 1.94 | | [M+H] % | 4.6% | | RMS error (mDa) | | 1.57 |

Table 3.14 The *m/z* and intensity errors due to mixed AP ionisation in the analysis of MoCB ($C_{12}H_9Cl$), and the results from applying corrections to account for the degree of protonation.

## 3.10 Conclusions

The discussion on ion statistics in the previous chapter stressed the importance of ion abundance ratios in compound identification and proposed the use of dynamic tolerances rather than the fixed, ±15%, value of the existing methods. Irrespective of this choice, having the correct ratio as the point around which any ratio is established is fundamental in ensuring the creation of irrefutable data and hence the findings here have shown that the current methods should, subject to review and validation, be revised accordingly.

Although this work has focussed on the EPA-1613B (USEPA, 1994) and EPA-1668C methods (USEPA, 2010) for PCDD/Fs and PCBs respectively, these are directly referenced, in regard to *m/z* and expected isotope ratios, by the EU method for food and feed analysis (European Commission, 2017). Furthermore, since the scope of the EU method extends to MS/MS, any revisions would also affect the MRM isotope ratios as these are derived from the precursor ions' ratios with factors applied according to the relative proportions of $^{35}$Cl vs. $^{37}$Cl in the precursor and the selected mass loss. The study of the determination of MS/MS ratios is also instructive in showing that not all contributors to the fine isotope structure are involved in a specific mass loss transition. An MS/MS study using a triple-quadrupole instrument to investigate the fragmentation losses from a set of PeCBs was performed, with the results showing close agreement between the measured and calculated isotope ratios for the conventional transition involving the loss of 2[$^{35}$Cl] and also for the alternative loss of $^{35}$Cl$^{37}$Cl.

The ability of the PureIso program to model molecular ion clusters containing enriched isotopes at purities other than 100% has been shown to be valuable in validating the manufacturers' claims of their standards' purities. This was demonstrated with the analysis of a commercially available $^{13}$C-labelled PeCB standard and comparison of the acquired molecular ion cluster data with its modelled equivalent at an assumed 99% isotopic purity. It also, more importantly, fully characterises the additional (M+1, M+3, etc.) peaks in the labelled standards' spectra that might otherwise be misconstrued as other analyte peaks or as protonated artefacts in AP ionisation analyses.

The work using the modelled peak profiles has highlighted issues concerning the peak separation and resolution parameters in the various isotope calculators and that those studied may not accurately reflect the peak intensities detected by HRMS; in contrast, the PureIso program calculates the isotope ratios by summing the intensities of the various isotopologues, modelled as a set of Gaussian peaks, at the *m/z* and resolution specified.

The issue with mixed charge exchange ionisation and protonation has highlighted another unexpected cause of possible isotope ratio error. Although such effects are minimal in many instances and/or only affect minor peaks, there exists the possibility of incorrect peak acceptance or rejection. Furthermore, any shift away from the ionisation conditions present during the (concentration) calibration phase could also lead to quantification errors for any compound that does not have its own labelled standard. With full-scan[*] data, as in the above examples, and the ability to examine additional ions over those used for the ratio assessment, such effects would be identifiable. For SIM or MRM analyses the use of additional *m/z* or transitions would be required over those specified by the method to provide the information needed to evaluate whether this is occurring.

---

[*] TOF data is considered "full-scan" in this context even though it is not a scanning instrument in the conventional sense.

# Chapter 4

# Analytical Effects of PCB Fragmentation

## 4.1 Introduction

The EPA-1668C method (USEPA, 2010) has been widely adopted for the analysis of all 209 PCB congeners, both for regulatory measurements within the US and as a prototype for PCB analyses in other territories, including the EU. In addition to the use of HRMS instrumentation at a resolution of ≥ 10,000 with EI at an energy between 28 and 40 eV, it specifies a proprietary GC column, the SPB-Octyl[*], for its ability to adequately resolve all (current) WHO toxic PCBs with the exception of PCB-156 (2,3,3',4,4',5-HxCB) and PCB-157 (2,3,3',4,4',5'-HxCB). However, these two isomers, that differ only in the ring position of one of the meta Cl atoms (5 or 5'), have the same toxic equivalency factor (TEF, ref. Table 1.5) and hence their need for separation is considered unnecessary.

Other GC columns with less polar stationary phases, e.g. 100% dimethyl polysiloxane or 5% diphenyl / 95% dimethyl polysiloxane – the latter type being routinely used in PCDD/F analyses – do resolve PCB-156 and 157, but not the toxic congener PCB-118 (due to its coelution with the non-toxic PCB-106) and are therefore ruled out from use in this application.

In contrast to the analysis of PCDDs and PCDFs, where, with one minor exception[†], the various congeners are separated into distinct retention time (RT) windows for each level of chlorination, routine PCB analysis – irrespective of the GC column choice – exhibits overlaps of the RT windows of the di- to nona-chlorinated biphenyls and is particularly significant for the tetra- to hepta-chlorinated homologues that also contain the toxic PCBs.

---

[*] 30 m (length) x 0.25 mm (ID) x 0.25 µm (film thickness) (Supelco, Bellefonte, PA, USA).

[†] With the commonly used, low polarity, "5ms" phase GC columns (e.g. DB-5ms, ZB-5ms, etc.), the first two pentachlorofuran isomers (1,3,4,6,8 and 1,2,4,6,8-PeCDF) elute before the last tetrachlorofuran isomer (1,2,8,9-TCDF) and therefore must be acquired as part of the TCDD/F, rather than the PeCDD/F, function. Although the latter would be preferred to avoid inter-function referencing of the PeCDF labelled standards and any ensuing response-factor errors, it is considered acceptable practice due to the non-toxicity of these isomers.

A consequence of these RT overlaps is the potential problem of interferences from product ions, due to the loss of 1 or 2 chlorine atoms from coeluting, higher chlorinated congeners, leading to errors in peak identification and concentration measurements.

To illustrate the cause of these fragment ion interferences, the modelled molecular ion cluster for TeCB ($C_{12}H_6Cl_4$) is shown in Figure 4.1 and that resulting from PeCB losing a Cl ($C_{12}H_5Cl_4$) in Figure 4.2; the PeCB - Cl cluster has an almost identical pattern (as predicated by the same $Cl_4$ distribution) but is nominally 1 *m/z* unit lower.

The issue of interfering peaks affecting the TeCB data principally[*] arises due to the naturally occurring $^{13}C$ isotopes present in the fragment ion cluster, at *m/z* 289.9179 ($C_{11}{}^{13}CH_5{}^{35}Cl_4$) and *m/z* 291.9150 ($C_{11}{}^{13}CH_5{}^{35}Cl_3{}^{37}Cl$), being very close in mass ($\Delta m$ ~15 ppm) to those of the TeCB major ions at *m/z* 289.9224 ($C_{12}H_6{}^{35}Cl_4$) and *m/z* 291.9195 ($C_{12}H_6{}^{35}Cl_3{}^{37}Cl$). Separation of these ions would require a mass resolution of ~65,000 – far higher than the 10,000 normally used for HRMS (EI) analysis.

Furthermore, the relative abundance of these $^{13}C$ isotope ions is 0.782, which at the measurement precision available in routine GC-MS analyses – either using HRMS or MS/MS – is indistinguishable from the 0.778 of the primary (M, M+2) ions of TeCB and hence their presence would only be detectable through any differences in their chromatographic RTs. Since the acceptable RT window in EPA-1668C is -1 to +3 seconds for toxic PCBs and -3 to +3 seconds for individual non-toxic PCBs (relative to their respective $^{13}C$-labelled standards) many interferences could pass unnoticed. This is even more likely if there is a partial interference, i.e. the target compound is present *and* has additive contributions from the product ions.

---

[*] Other fragmentation mechanisms that can also lead to interfering ions affecting the [M - Cl] cluster, e.g. loss of HCl and Cl/H exchange, will be discussed later in the chapter.

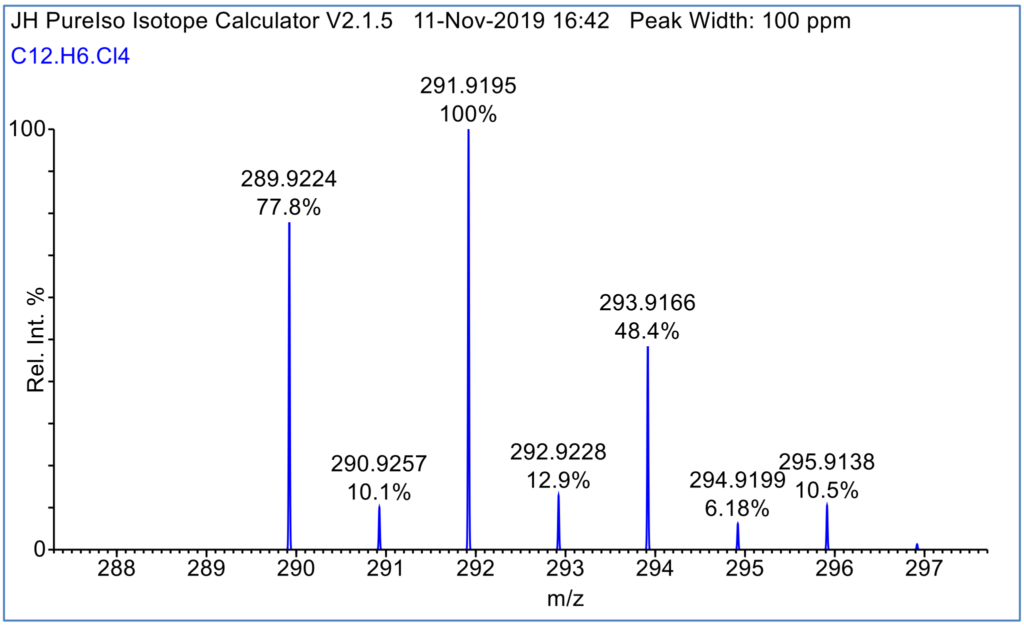

Figure 4.1 Modelled isotope cluster of the molecular ion of TeCB ($C_{12}H_6Cl_4$) showing exact *m/z* and relative abundances.

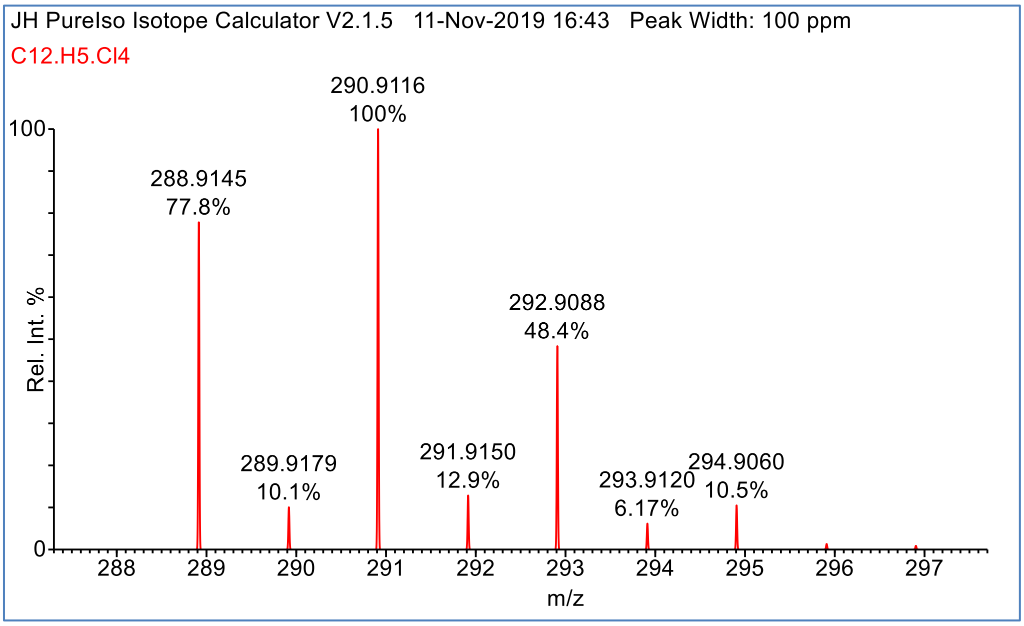

Figure 4.2 Modelled isotope cluster of product ions ($C_{12}H_5Cl_4$) formed from the loss of Cl from PeCB ($C_{12}H_5Cl_5$) showing a ~1 *m/z* unit (negative) displacement relative to TeCB ($C_{12}H_6Cl_4$). The peaks are annotated with their exact *m/z* and relative abundances.

The problem of interferences due to product ions from the fragmentation loss of 2 chlorines also exists, but, as shown in the example of Figure 4.3, the situation is distinctly different since the HxCB product ions' isotope cluster pattern is displaced by ~2 *m/z* units relative to that of TeCB. These ions are further separated in mass (Δm ~63 ppm, relative to TeCB) than the product ions due to the loss of Cl from PeCB but would still be unresolved using the method's standard resolution (10,000).

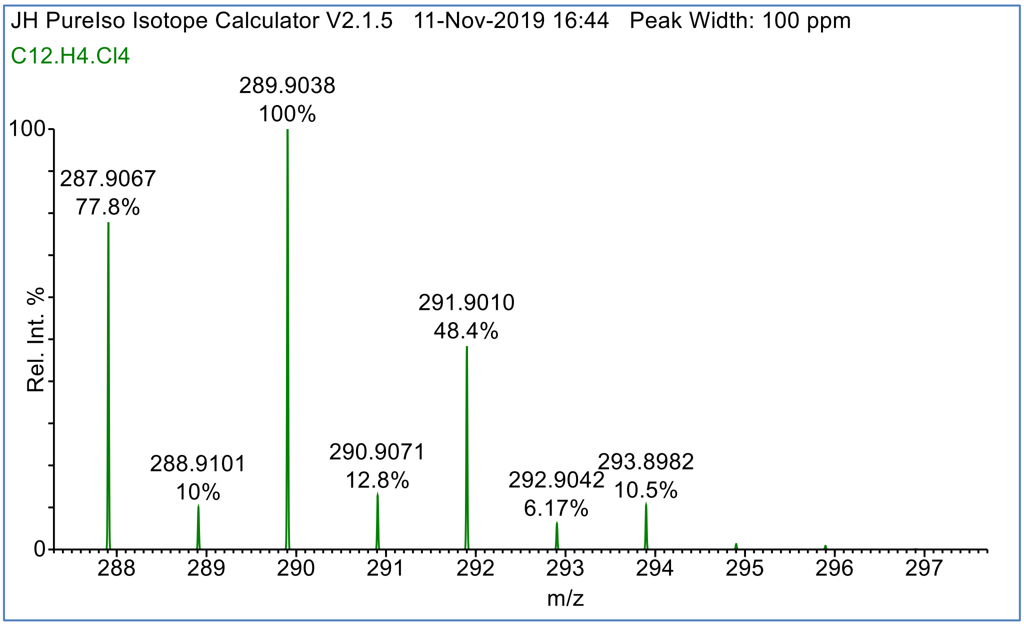

Figure 4.3 Modelled isotope cluster of the product ions ($C_{12}H_4Cl_4$) formed due to the loss of 2Cl from HxCB ($C_{12}H_4Cl_6$) showing a ~2 *m/z* units (negative) displacement relative to TeCB ($C_{12}H_6Cl_4$).
The peaks are annotated with their exact *m/z* and relative abundances.

These *m/z* differences are clearly depicted in Figure 4.4 with the superimposed modelled peak profiles from TeCB (*m/z* 291.9195, $C_{12}H_6{}^{35}Cl_3{}^{37}Cl$), the M+1 interference due to the loss of Cl from PeCB (*m/z* 291.9150, $C_{11}{}^{13}CH_5{}^{35}Cl_3{}^{37}Cl$) and the M+2 due to the loss of 2Cl from HxCB (*m/z* 291.9010, $C_{12}H_4{}^{35}Cl_2{}^{37}Cl_2$). Each peak is annotated with its exact *m/z* and the mass difference, in ppm, relative to TeCB. The peak intensities are normalised to their corresponding isotopes at *m/z* 290 to reflect their relative ion abundances.

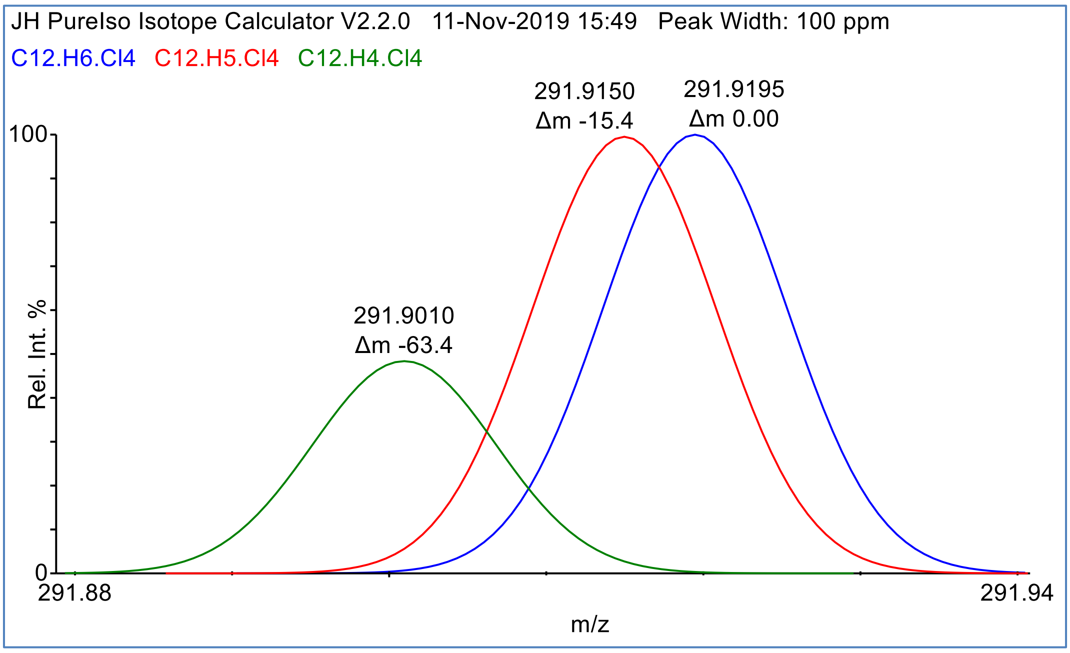

Figure 4.4 Modelled peaks showing the base peak of TeCB (*m/z* 291.9195, $C_{12}H_6{}^{35}Cl_3{}^{37}Cl$) and product ion interferents due to the loss of Cl from PeCB (*m/z* 291.9150, $C_{11}{}^{13}CH_5{}^{35}Cl_3{}^{37}Cl$) and 2Cl from HxCB (*m/z* 291.9010, $C_{12}H_4{}^{35}Cl_2{}^{37}Cl_2$).
TeCB (blue trace), PeCB - Cl (red) and HxCB - 2Cl (green); calculated mass differences in ppm. Intensities were normalised to the peaks at (nominal) *m/z* 290 such that the displayed peaks indicate the relative isotope contributions at *m/z* 292: the PeCB - Cl product ions' ratio differs by just ~0.5% whereas the HxCB - 2Cl product ions' isotope ratio is 2.07 (cf. 0.78 for TeCB).

Although EPA-1668C includes several (partially repeated) references to this potential problem, they are not comprehensive and there are no specific guidelines as to when any corrective actions should be taken, as shown by these quoted sections:

> *[From 10.3.1.1] "The laboratory must also monitor exact m/z's for congeners at higher levels of chlorination to determine if fragments will compromise measurement of congeners at lower levels of chlorination."*
>
> *[From 14.3.2] "Where warranted, monitor m/z's associated with congeners at higher levels of chlorination to assure that fragments are not interfering with the m/z's for congeners at lower levels of chlorination. Also where warranted, monitor m/z's associated with interferents expected to be present."*
>
> *[From 18.1] "Fragment ions from congeners at higher levels of chlorination may interfere with determination of congeners at lower levels of chlorination."*

> *[From 18.5] "Interferences may pose a problem in the determination of congeners 81, 123, 126, and 169 in some environmental samples. Loss of one or more chlorines from a highly chlorinated congener may inflate or produce a false concentration for a less-chlorinated congener that elutes at the same retention time. If, upon inspection of the chromatogram, the possibility of interferences is evident (e.g., high concentrations of fragments from loss of one or two chlorines from higher chlorinated closely eluting congeners), carbon column fractionation (Section 13.4) and analysis is recommended."*

Considering the above 4 points: section 10.3.1.1 is redundant since if congeners from a higher level of chlorination are present, then those *m/z* would be implicitly recorded as part of a method's core requirements. This similarly applies to the first part of section 14.3.2, although the second part regarding the monitoring of interferents' *m/z* has some merit (and will be discussed further later in this chapter). The statement in section 18.1 only repeats the cautionary note but does not suggest any solutions.

The last point, section 18.5, in referring to only PCBs 81, 123, 126 and 169 being affected, ignores other known toxic PCBs that are, as will be shown, potential candidates for interferences due to fragmentation, and to the fact that many other PCBs – although non-toxic – may also be subject to these effects. In addition to the risk of misreporting any individual congener's concentration (and its associated homologue total concentration), its TEQ and the overall sample TEQ, the congener distribution profiles could be altered thus undermining any pattern matching based comparisons, e.g. as used in environmental forensics. Additional sample clean-up using a carbon-column is an option for the toxic PCBs but not any others; coupled with the additional analytical costs this is therefore only a partial solution to the problem.

Although (surprisingly) not referenced in the current version of the EPA-1668C (HRMS) PCB method or its predecessors, it is interesting to note that a much earlier method for the low-resolution mass spectrometry (LRMS) analysis of PCBs (and pesticides), EPA Method 680 (Alford-Stevens *et al.*, 1985), did offer a correction strategy. It explicitly specified the *m/z* to be monitored to identify interfering coeluters, their corresponding fragment *m/z* and correction factors that could be applied to the peak areas of those fragment ions that, if detected, could be subtracted from the areas of the corresponding target PCBs.

There are some weaknesses to this approach: it does not consider partially or multiple coeluting peaks, the factors assume an exact overlap of the *m/z* of the fragment ions and of the affected ions that is only directly applicable to a unit-mass resolution instrument, and it assumes that all fragments are from a simple loss of Cl or 2Cl, thereby incorrectly accounting for errors due to, for example, the loss of HCl[*]. Despite these issues in the context of the HRMS analyses of PCBs, it would seem to have been useful foundation to build upon.

There have been few published studies focussed on PCB fragmentation and none (that the author is aware of) with experimental data from all 209 congeners. Greaves *et al* reported on the correlation between the degree of fragmentation, calculated internal energies and the number of ortho substitutions, but their data was limited to that acquired using electron capture negative chemical ionisation from a subset (n = 49) of TeCB, PeCB and HxCB congeners (Greaves, Harvey and MacIntyre, 1994). Laušević *et al* compared the fragmentation responses for a limited number (n = 13) of non-, mono- and di-ortho substituted PCBs using a quadrupole ion trap mass spectrometer with collision induced dissociation (CID) under various resonant excitation conditions (Laušević, Splendore and March, 1996). In both cases, the proportionally greater fragmentation observed for di-ortho, relative to that of non- or mono-ortho, PCBs was mirrored in the experimental data reported here.

The aims of this chapter are to characterise the PCB fragmentation losses of Cl and 2Cl at all levels[†] of chlorination, and to examine the correlation, if any, between these data and currently assessed toxicity values. In addition to the use of traditional EI HRMS analyses, this study will also examine the fragmentation results obtained from GC-MS/MS data acquired at various collision energies (CE) using a Q-TOF type instrument with AP ionisation.

---

[*] The EPA 680 Method notes that some MoCBs and DiCBs can lose HCl, however none of these coelute with any other PCB.

[†] Clearly there is no viable loss of 2Cl from a MoCB.

## 4.2 Materials and methods

### 4.2.1 GC-HRMS (EI)

GC-HRMS data were acquired using an AutoSpec-Ultima (Waters, Wilmslow, UK) magnetic sector[*] instrument tuned to a resolution of ~12,000 at its nominal 8 kV accelerating voltage. The HRMS instrument was coupled to a 6890 GC (Agilent, Santa Clara, CA, USA) fitted with a GC-PAL auto-sampler (CTC Analytics, Zwingen, Switzerland). Positive ion, electron ionisation (EI) was used at 34 eV electron energy. Archived AutoSpec-Ultima data obtained at the same laboratory (SGS/Analytical Perspectives, Wilmington, NC, USA) were also used with permission.

SIM acquisition was used to record data from 2 ions for the native ($^{12}C_{12}$) PCBs, 2 ions for $^{13}C_{12}$-labelled PCBs, and a lock-mass and lock-mass check channel in each function. Additional *m/z* representing the losses of Cl and 2Cl were included as needed. In total, 7 functions were required to accommodate the overlapping retention time windows of the various PCB homologues as summarised in Table 4.1.

| Function # | PCBs monitored | Fragments monitored |
|---|---|---|
| 1 | MoCB, DiCB | - |
| 2 | DiCB, TrCB, TeCB | TrCB - 2Cl, TeCB - Cl |
| 3 | TrCB, TeCB, PeCB | PeCB - 2Cl, TeCB - Cl |
| 4 | TeCB, PeCB, HxCB, HpCB | HxCB - 2Cl, PeCB - Cl, HpCB - 2Cl, HxCB - Cl |
| 5 | PeCB, HxCB, HpCB, OcCB | HpCB - 2Cl, HxCB - Cl, OcCB - 2Cl, HpCB - Cl, OcCB - Cl |
| 6 | HpCB, OcCB, NoCB | NoCB - 2Cl, OcCB - Cl, NoCB - Cl |
| 7 | DeCB | - |

Table 4.1 Summary of the PCB homologues monitored in each acquisition function for the HRMS PCB fragmentation data.

The GC column used was a SPB-Octyl (Supelco, Bellefonte, PA, USA) with dimensions 30 m (length) x 0.25 mm (internal diameter) x 0.25 µm (film thickness). Auto-injections of 1 µl of the standards' mixtures were made in the splitless mode with helium as the carrier gas at a constant flow rate of 1.2 ml/min. Full details of the relevant GC and MS parameters are provided in Appendix D.1.

---

[*] The AutoSpec HRMS instruments have an EBE geometry, i.e. first electrostatic analyser (ESA, E), magnet (B) and 2nd ESA.

Native and $^{13}$C-labelled PCB reference standards were manufactured by Cambridge Isotope Laboratories (Tewksbury, MA, USA), Wellington Laboratories (Guelph, ON, Canada) and AccuStandard (New Haven, CT, USA). Full details of the various PCB mixes are provided in Appendix C.3.

### 4.2.2 GC-MS/MS (APCI)

GC-MS/MS data were acquired using a Synapt G2-S hybrid Q-IMS-TOF (Waters, Wilmslow, UK). Atmospheric pressure chemical ionisation (APCI) was used in the positive ion mode at a mass resolution of ~18,000 (FWHM). The instrument was coupled to a 7890A GC with a 7693A auto-sampler (Agilent, Santa Clara, CA, USA).

Figure 4.5 shows the instrument's schematic with the collision cell (trap) located between the quadrupole and the ion mobility cell. Fragmentation occurs via CID with argon used as the collision gas in these experiments. The gas pressure and collision energies (CE) used are described in the results and discussion section. For the experiments discussed in this chapter, there was no mass selection in the quadrupole mass analyser and the ion mobility cell was inactive.

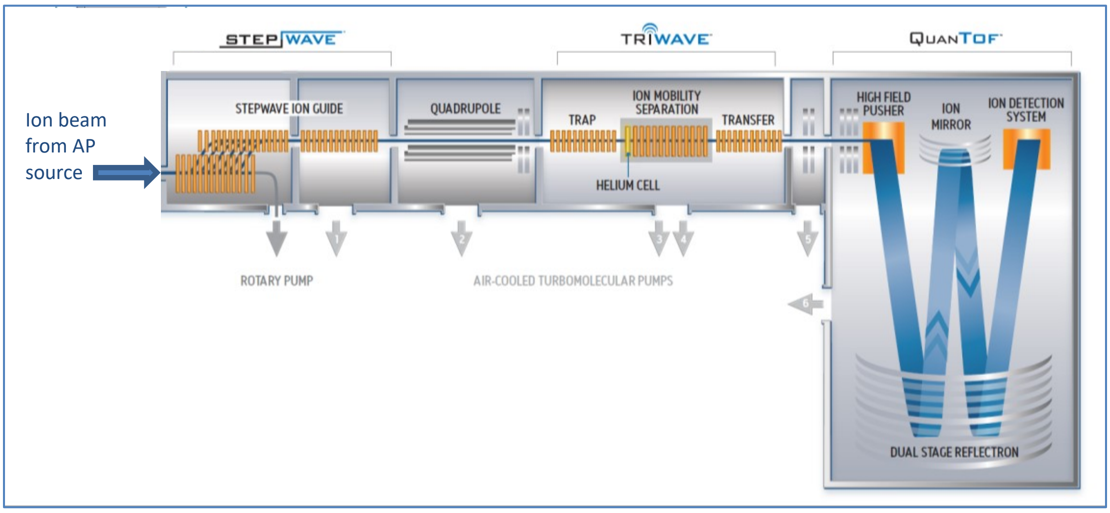

Figure 4.5 Schematic outline of the Waters' Synapt G2-S MS/MS (Q-IMS-TOF) analyser ion optics.
(Image courtesy of Waters, Wilmslow, UK)

The GC columns used were the SPB-1 and SPB-Octyl (Supelco, Bellefonte, PA, USA), both with dimensions 30 m (length) x 0.25 mm (internal diameter) x 0.25 µm (film thickness). For the SPB-1 column, splitless mode auto-injections were made using a volume of 1 µl with helium as the carrier gas at a flow rate of 1.4 ml/min; for the SPB-Octyl column, these figures were 0.7 µl and 1.7 ml/min respectively. Full details of the relevant GC and MS parameters are provided in Appendix D.2.

Native and $^{13}$C-labelled PCB reference standards were manufactured by Ultra Scientific (North Kingstown, RI, USA) and Wellington Laboratories (Guelph, ON, Canada). Full details of the various PCB mixes used are provided in Appendix C.3.

### 4.2.3 GC-TOF (EI)

Accurate mass scan data were acquired using a GCT-Premier (Waters, Wilmslow, UK) TOF mass spectrometer coupled to a 6890 GC (Agilent, Santa Clara, CA, USA) fitted with a GC-PAL auto-sampler (CTC Analytics, Zwingen, Switzerland). The GCT was operated in positive ion, electron ionisation (EI) mode with an electron energy of 34 eV. Data were acquired over a mass range of *m/z* 50–650 at a resolution of ~7,500 (FWHM). The archived GC-TOF data were obtained from SGS/Analytical Perspectives (Wilmington, NC, USA) and used with permission.

The GC column and conditions used were as described for the GC-HRMS data above and full details of the relevant GC and MS parameters are given in Appendix D.4. The native PCB reference standards used were manufactured by AccuStandard (New Haven, CT, USA) with full details given in Appendix C.3.

### 4.2.4 MS data acquisition and processing

Data from all instruments were acquired using MassLynx V4.1 and processed using MassLynx V4.2 software (Waters, Wilmslow, UK); additional MS data processing was done using UltraTrace-Pro V4.9 and V5.0 (SGS, Wilmington, NC, USA). Further calculations used Excel 365 (Microsoft, Redmond, WA, USA) and MATLAB R2018b (MathWorks, Natick, MA, USA) was used for the principal component analysis (PCA).

### 4.2.5 Molecular modelling

To obtain 3-dimensional structural information of the PCBs – required to obtain comparable values of published dihedral angles for the work in this chapter, and for subsequent use with the ion-mobility work in Chapter 5 – molecular modelling was performed using the “Orca” program (Version 4.0.1.2) (Neese, 2012) to determine the structural configurations of the most stable conformers.

2-dimensional structures of each PCB were created using the molecular editing software, “Avogadro” (Version 1.2.0) (Hanwell *et al.*, 2012); these were initially optimised using its integrated universal force field methods (Rappe *et al.*, 1992) prior to export in Orca format. These files include the functional and basis set parameters, and the x, y, z coordinates (in ångströms) for all atoms; Figure 4.6 shows an example Orca input file for the modelling of PCB-126.

There is much discussion in the literature as to the most suitable modelling mechanisms for biphenyl and its halogenated compounds (Grein, 2002; Johansson and Olsen, 2008; Popelier *et al.*, 2018), and these have led to the use of the ‘6-31G*’ basis set in the above calculations together with the restricted Hartree-Fock (RHF) functional method. Other options included the use of the latest atomic masses of the most abundant isotopes and parallel processing with 6 processor cores as specified by the ‘Mass2016’ and ‘PAL6’ parameters respectively.

```
# Auto modified by JH's Orca Input Editor 15-Dec-2019 09:23:03
! RHF OPT 6-31G* TightSCF SmallPrint
!Mass2016
!PAL6
%scf
      MaxIter 250
end

* xyz 0 1
   C        1.72760        2.24070        0.81764
   C        3.09436        2.48742        0.63903
   C        4.01714        1.43417        0.41030
   C        3.48781        0.11928        0.37137
   C        2.12389       -0.12259        0.55002
   C        1.24040        0.93027        0.77295
   C        5.50024        1.70125        0.21642
   C        6.03063        3.01459        0.25749
   C        7.78614        0.89201       -0.19311
   C        6.42002        0.64840       -0.01429
   C        7.39623        3.26146        0.07907
   C        8.28141        2.20068       -0.14728
  Cl        7.96977        4.92457        0.14558
   H        5.41422        3.87927        0.42666
   H        6.11482       -0.38158       -0.06292
  Cl       -0.46883        0.57878        0.99251
  Cl       10.00332        2.50989       -0.37246
   H        1.75371       -1.13973        0.51420
  Cl        8.85833       -0.47558       -0.47484
   H        3.39655        3.51833        0.68596
  Cl        0.64603        3.60046        1.09676
   H        4.09720       -0.75105        0.20496
*
```

Figure 4.6 Example Orca input file for PCB-126 (3,3’,4,4’,5-PeCB, $C_{12}H_5Cl_5$)

Since Orca is normally invoked from the command line, a simple front-end program was created, “OrcaControl”, to manage its operation and allow entries to be interactively added to the process queue – a particular benefit given the lengthy processing time[*] of some calculations that would often require batched operations to be run overnight. Figure 4.7 shows a screenshot of the program in operation.

---

[*] E.g. PCB-54 optimisation, including frequency calculations, required a run time of ~50 minutes using 6 (of 8 available) cores of an Intel® i7-2600 processor running at 3.4 GHz.

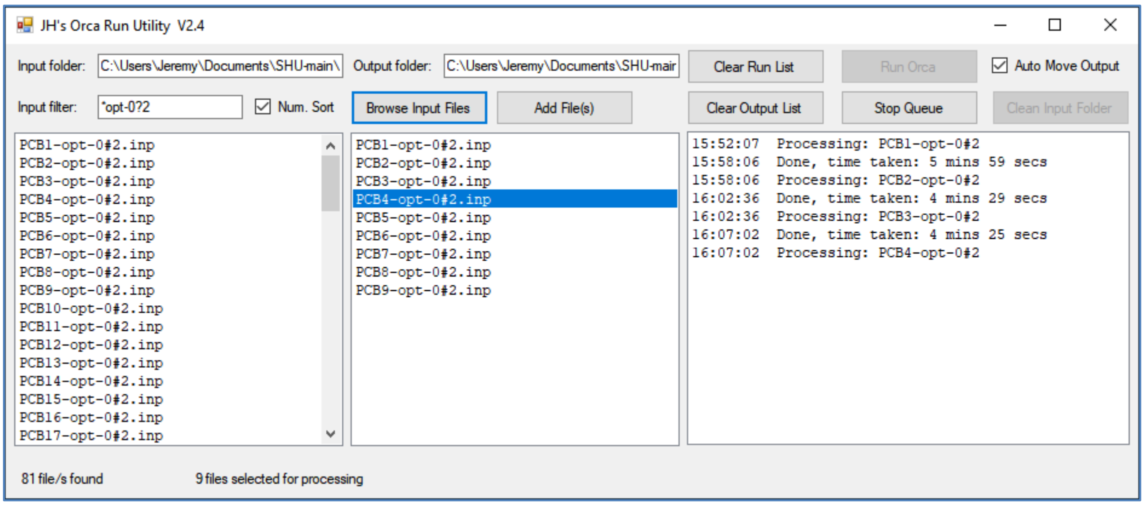

Input folder: C:\Users\Jeremy\Documents\SHU-main\

Output folder: C:\Users\Jeremy\Documents\SHU-mair

Input filter: *opt-0?2

☑ Num. Sort

☑ Auto Move Output

```
PCB1-opt-0#2.inp
PCB2-opt-0#2.inp
PCB3-opt-0#2.inp
PCB4-opt-0#2.inp
PCB5-opt-0#2.inp
PCB6-opt-0#2.inp
PCB7-opt-0#2.inp
PCB8-opt-0#2.inp
PCB9-opt-0#2.inp
PCB10-opt-0#2.inp
PCB11-opt-0#2.inp
PCB12-opt-0#2.inp
PCB13-opt-0#2.inp
PCB14-opt-0#2.inp
PCB15-opt-0#2.inp
PCB16-opt-0#2.inp
PCB17-opt-0#2.inp
```

```
PCB1-opt-0#2.inp
PCB2-opt-0#2.inp
PCB3-opt-0#2.inp
PCB4-opt-0#2.inp
PCB5-opt-0#2.inp
PCB6-opt-0#2.inp
PCB7-opt-0#2.inp
PCB8-opt-0#2.inp
PCB9-opt-0#2.inp
```

```
15:52:07  Processing: PCB1-opt-0#2
15:58:06  Done, time taken: 5 mins 59 secs
15:58:06  Processing: PCB2-opt-0#2
16:02:36  Done, time taken: 4 mins 29 secs
16:02:36  Processing: PCB3-opt-0#2
16:07:02  Done, time taken: 4 mins 25 secs
16:07:02  Processing: PCB4-opt-0#2
```

81 file/s found

9 files selected for processing

Figure 4.7 Screenshot showing the OrcaControl program in operation.

The results created by Orca are also text files and can be visualised using the program "ChemCraft" (Version 1.8) as shown by the example for PCB-126 (3,3',4,4',5-PeCB) in Figure 4.8. This program also provided the tools for determining the dihedral angle (and other measurements).

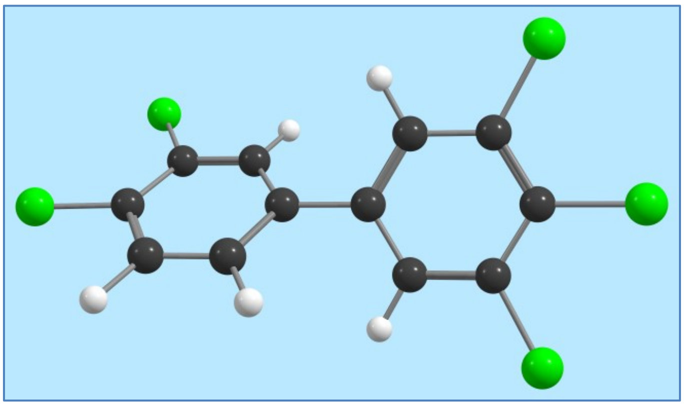

Figure 4.8 Depiction of the 3-D structure of PCB-126 (3,3',4,4',5-PeCB).
Image generated using ChemCraft from the Orca computed structure conformation based on the parameters given in Figure 4.6.

## 4.3 Results and discussion

### 4.3.1 The scope of the fragmentation problem in PCB analyses

To illustrate the scope of the problem, a solution containing all 209 PCB congeners at nominally equal concentrations (50 pg/µl) was analysed using GC-HRMS with the conditions specified by the EPA-1668C method (including the use of the SPB-Octyl GC column). The chromatograms showing the molecular ion M+0 peak intensities due to the MoCB ($Cl_1$) to PeCB ($Cl_5$) congeners are shown in Figure 4.9, and the M+2 intensities for HxCB ($Cl_6$) to NoCB ($Cl_9$) and M+4 for DeCB ($Cl_{10}$) congeners are shown in Figure 4.10. The peak annotations in the TeCB to HpCB traces refer to the WHO toxic PCB congeners (as indicated by the red shading).

For the DiCB ($Cl_2$) to OcCB ($Cl_8$) congeners, the traces shown are composites of data acquired from either 2 or 3 functions as required to address the HRMS mass range limitations (as previously described in section 1.9), hence the repeated *m/z* labels shown in those chromatograms' y-axes.

The overlapping elution time windows of certain PCB homologues are readily apparent [note: the same RT range (x-axes) has been used for all traces] with, for example, the PeCB group being potentially affected by HxCB fragmentation (loss of Cl) from RT ~30.4 onwards and HpCB fragmentation (loss of 2Cl) from RT ~35.2 onwards. MoCB, OcCB, NoCB and DeCB are unaffected as there are no coeluting, higher-chlorinated, congeners present – implicitly so in the case of DeCB since it is at the highest level of chlorination possible for biphenyls.

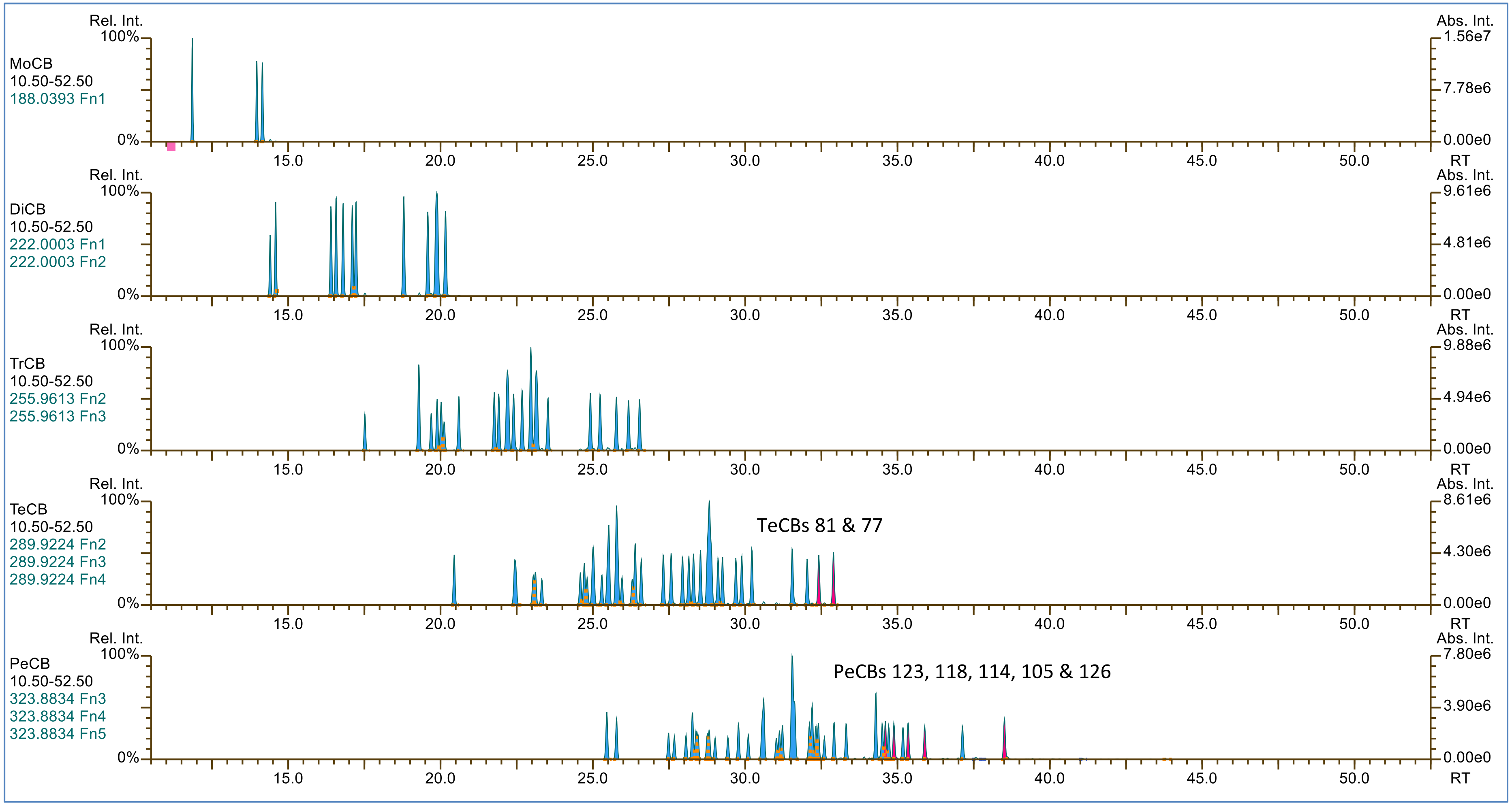

TeCBs 81 & 77

PeCBs 123, 118, 114, 105 & 126

Figure 4.9 Chromatograms showing the homologue windows for mono- to penta-chlorinated biphenyls illustrating the overlap in retention times under the analytical conditions of the EPA-1668C method.

The peak annotations refer to the WHO toxic congeners (highlighted in red).

[The pink markings in certain x-axes show ranges over which the background noise was determined – not used in these data.]

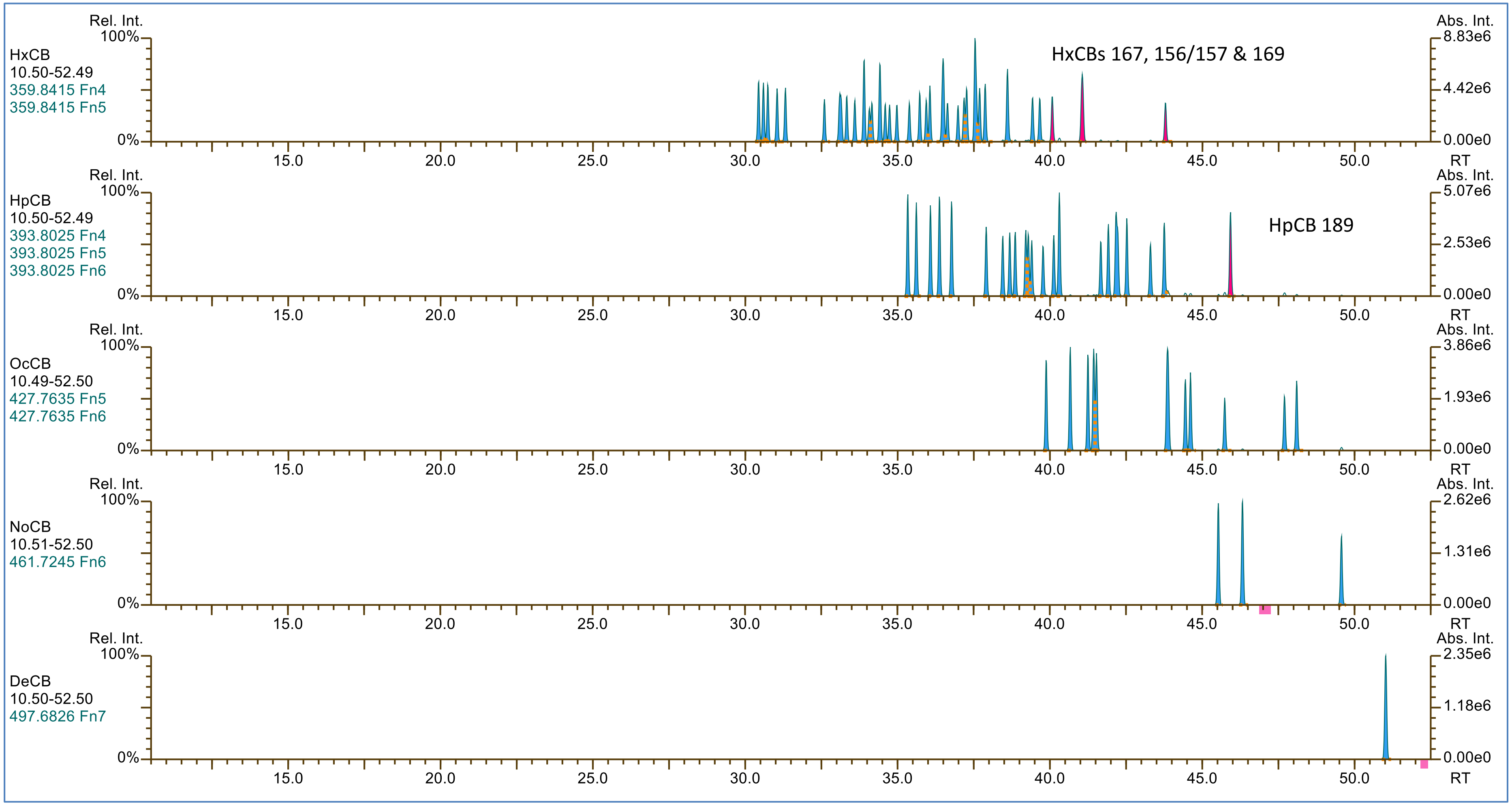

Figure 4.10 Chromatograms showing the homologue windows for hexa- to deca-chlorinated biphenyls illustrating the overlap in retention times under the analytical conditions of the EPA-1668C method.
The peak annotations refer to the WHO toxic congeners (highlighted in red).
[The pink markings in certain x-axes show ranges over which the background noise was determined – not used in these data.]

### 4.3.2 Artefact peak formation in PCB analyses

To demonstrate the formation of artefact peaks due to fragmentation in GC-HRMS analysis, data from a sample containing a limited number of PCB congeners was examined. Figure 4.11 shows the resulting chromatograms: the upper trace shows the peaks due to the M+0 molecular ion of PeCB ($C_{12}H_5{}^{35}Cl_5$, $m/z$ 323.8834), those due to the loss of Cl from PeCB ($C_{12}H_5{}^{35}Cl_4$, $m/z$ 288.9145, centre trace) and those due to the M+0 molecular ion of TeCB ($C_{12}H_6{}^{35}Cl_4$, $m/z$ 289.9224, lower trace).

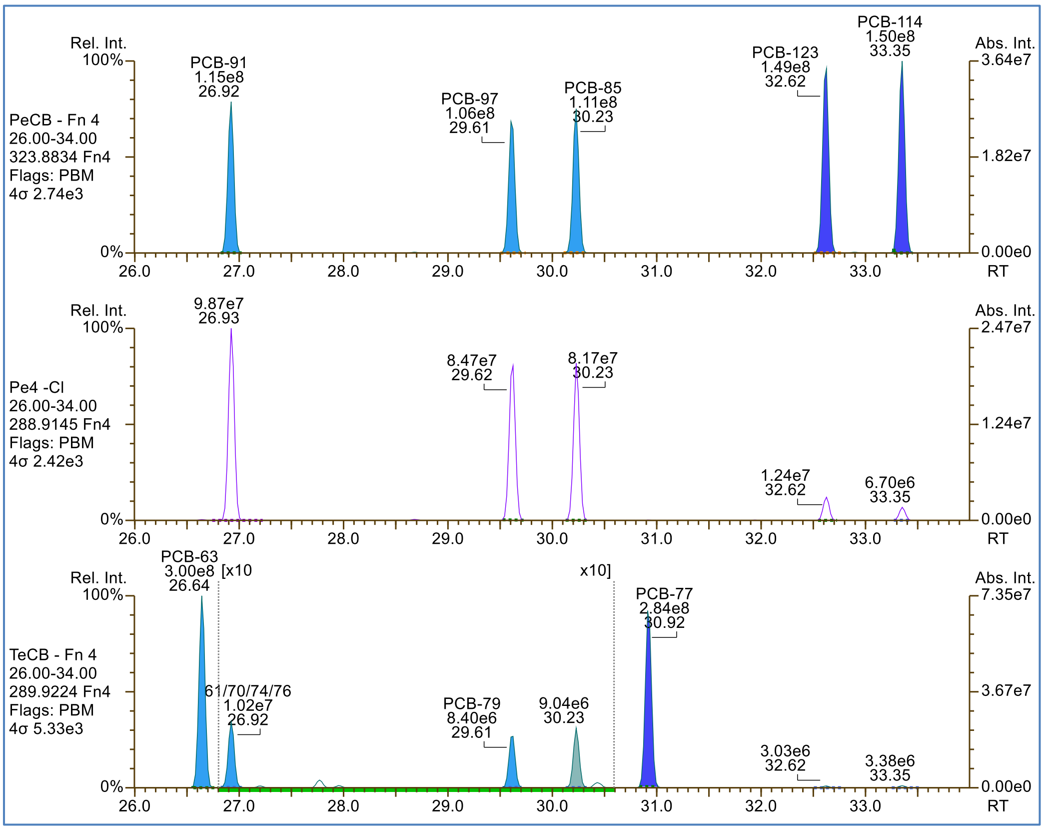

Figure 4.11 HRMS (EI) chromatograms showing PeCB congeners (upper trace), their fragment ions due to a loss of Cl (centre trace) and TeCB congeners (lower trace).
Of the TeCBs, only PCB-63 and PCB-77 were present in the mix – the other peaks, including those annotated as [PCB-]61/70/74/76 and PCB-79 are artefacts of PeCB fragmentation.
A x10 magnification has been applied to the lower trace over the RT range 26.8–30.6.

The PeCBs present in the sample (upper trace) include PCB-91, 97, 85, 123 and 114 – the latter two being WHO toxic PCBs. The 5 fragment ion peaks due to the loss of Cl from these PeCBs are shown in the centre trace and are clearly aligned with their precursors. In addition to the PeCBs, the sample included two TeCBs: PCB-63 and 77 (lower trace), as identified by the peaks at RT 26.64 and 30.92. However, the peaks annotated as 61/70/74/76[*] and PCB-79 were not actually present in the sample mix but are artefacts due to the fragment ions caused by the loss of Cl[†] from PCB-91 (2,2',3,4',6-PeCB) and PCB-97 (2,2',3,4',5'-PeCB) respectively: they are nevertheless indistinguishable from the true TeCB peaks since both their isotope ratios and RTs match. The peaks at RT 30.23, 32.62 and 33.35 are similarly also artefact peaks (with valid isotope ratios), but none of these RTs match that of an actual TeCB.

An EI spectrum obtained from TOF-MS data (acquired using the same, 34 eV, ionisation energy as the HRMS data) of PCB-97 is shown in Figure 4.12. This shows the molecular ion cluster region and those for the losses of Cl and 2Cl, and clearly illustrates the minor isotope peaks in the -Cl cluster that would cause the artefact identified as PCB-79. It is important to note that PCB-79's structure – 3,3',4,5'-TeCB – is not one that would be actually formed due to this fragmentation process and this assignment is purely due to the arbitrary alignment of the two PCBs' retention times.

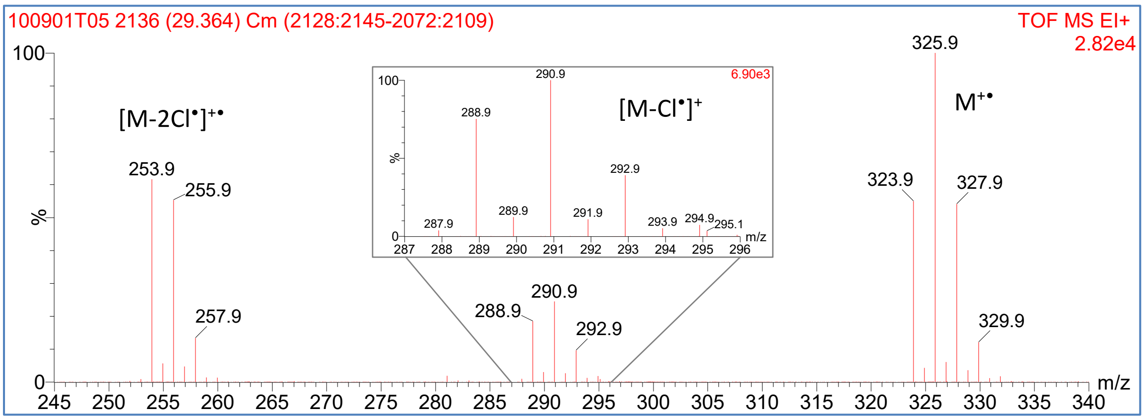

Figure 4.12 Mass spectrum of PCB-97 (2,2',3,4',5'-PeCB) obtained in positive EI at 34 eV showing the molecular ion region and those principally from the losses of Cl and 2Cl. The minor peaks at *m/z* 289.9 and 291.9 (expanded in the inset) being the contributors to the false artefact identified as PCB-79.

---

[*] There are 4 possible coeluting isomers at this retention time; per the EPA-1668C method they are therefore reported as the quadruplet "61/70/74/76".

[†] More specifically from mass interferences of the M+1 and M+3 isotope ions, as discussed in the introduction (section 4.1).

To examine this effect with AP ionisation, the Synapt G2-S instrument was used with a CE of 15 eV and argon as the collision gas at a pressure of ~2.4 x $10^{-2}$ mbar. As with the EI data, a subset of PeCBs were present in the sample mix, here including PCB-102, 109, 115 and 123 as shown by the acquired data chromatograms in Figure 4.13. The upper trace shows the peaks due to the M+0 molecular ion of PeCB ($C_{12}H_5{}^{35}Cl_5$, *m/z* 323.8834), the loss of Cl from PeCB ($C_{12}H_5{}^{35}Cl_4$, *m/z* 288.9145, centre trace) and for the M+0 molecular ion of TeCB ($C_{12}H_6{}^{35}Cl_4$, *m/z* 289.9224, lower trace).

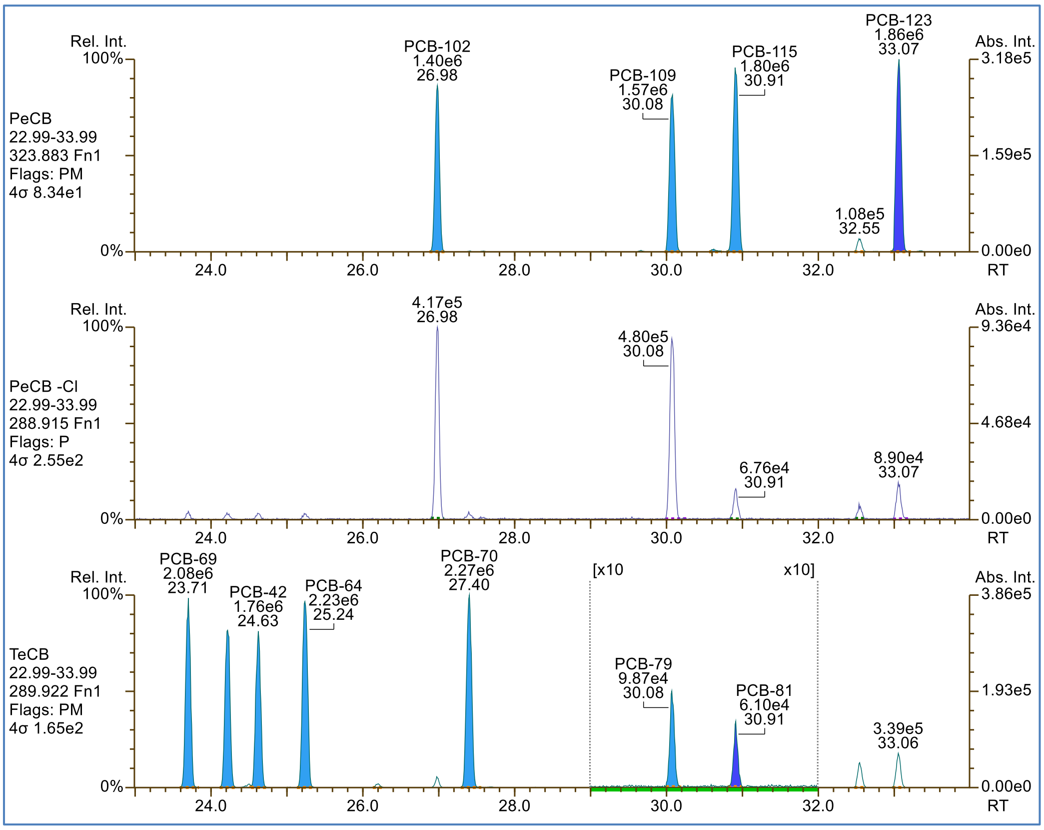

Figure 4.13 APCI-MS chromatograms showing 4 PeCB congeners (upper trace), their fragment ions due to a loss of Cl (centre trace) and TeCB congeners (lower trace).
Of the identified TeCBs, only the first 5: PCB-69, 47*, 42, 64 and 70 were present in the mix; those annotated as PCB-79 and PCB-81 are fragment artefacts due to loss of Cl from PCB-109 and PCB-115 respectively.
A x10 magnification has been applied to the lower trace over the RT range 29.0–32.0
* PCB-47 was not annotated by the software due to space limitations: RT 24.22, area 1.84e6

The 5 TeCB congeners shown in the RT 23–28 region, PCB-69, 47, 42, 64 and 70, were present in the sample mix, however this is not the case for PCB-79 and PCB-81; these peaks, similarly to those in the previous EI example, are artefacts, here due to the loss of Cl from PCB-109 and PCB-115 respectively. It is important to note that the latter artefact, incorrectly assigned as PCB-81, would in the case of a real-world sample be of special concern due to it being one of the 12 WHO toxic PCBs.

This potential problem extends to many other PCBs: Table 4.2 lists the precursors and corresponding close eluting product PCBs due to the loss of a single Cl, and their respective RTs and RT differences.

| **Precursor Congener** | **RT** | **Product Target Congener (-Cl)** | **RT** | **Δ RT (s)** |
|---|---|---|---|---|
| PCB-27 TrCB | 19.89 | PCB-13/12 DiCB | 19.88 | 0.76 |
| PCB-16 TrCB | 20.12 | PCB-15 DiCB | 20.16 | -2.49 |
| PCB-50/53 TeCB | 22.45 | PCB-25 TrCB | 22.40 | 2.96 |
| PCB-51 TeCB | 23.11 | PCB-21/33 TrCB | 23.14 | -1.99 |
| PCB-96 PeCB | 25.77 | PCB-59/62/75 TeCB | 25.79 | -0.70 |
| PCB-100/93 PeCB | 28.27 | PCB-67 TeCB | 28.30 | -2.00 |
| PCB-91 PeCB | 28.82 | PCB-61/70/74/76 TeCB | 28.82 | -0.23 |
| PCB-152 HxCB | 30.59 | PCB-113/90/101 PeCB | 30.58 | 0.61 |
| PCB-136 HxCB | 31.04 | PCB-83 PeCB | 31.02 | 1.22 |
| PCB-109/119/86/97/125/87 PeCB | 31.56 | PCB-79 TeCB | 31.54 | 1.24 |
| PCB-115 PeCB | 32.39 | **PCB-81 TeCB** | 32.41 | -1.03 |
| PCB-148 HxCB | 32.60 | PCB-82 PeCB | 32.59 | 0.10 |
| PCB-111 PeCB | 32.91 | **PCB-77 TeCB** | 32.89 | 1.09 |
| PCB-154 HxCB | 33.33 | PCB-120 PeCB | 33.31 | 1.07 |
| PCB-131 HxCB | 34.59 | **PCB-123 PeCB** | 34.60 | -0.47 |
| PCB-142 HxCB | 34.73 | PCB-106 PeCB | 34.71 | 1.54 |
| PCB-133 HxCB | 35.38 | **PCB-114 PeCB** | 35.34 | 2.34 |
| PCB-146 HxCB | 35.94 | **PCB-105 PeCB** | 35.89 | 3.03 |
| PCB-184 HpCB | 36.08 | PCB-161 HxCB | 36.06 | 1.06 |
| PCB-137 HxCB | 37.18 | PCB-127 PeCB | 37.13 | 2.81 |
| PCB-178 HpCB | 37.91 | PCB-158 HxCB | 37.87 | 1.95 |
| PCB-174 HpCB | 39.40 | PCB-159 HxCB | 39.43 | -1.67 |
| PCB-181 HpCB | 40.13 | **PCB-167 HxCB** | 40.08 | 2.86 |
| PCB-190 HpCB | 43.76 | **PCB-169 HxCB** | 43.80 | -2.38 |

Table 4.2 Precursor PCBs that present potential interferences due to the loss of Cl and their corresponding target PCBs.
The congeners are sorted in RT order with the WHO toxic PCBs highlighted in bold type. The list is limited to the 25 closest eluting PCBs and their fragmentation products with a maximum RT difference of ~3 seconds using the GC conditions required for the EPA-1668C method.

Similarly, Table 4.3 lists the precursors and corresponding close eluting product PCBs due to the loss of 2Cl, and their respective RTs and RT differences. Although it shows far fewer instances than for the loss of Cl, it includes 3 WHO toxic PCBs. Of these, PCB-126 and 169, with their TEFs of 0.1 and 0.03 respectively, are the 2 most toxic congeners and hence of particular importance in these analyses.

| **Precursor Congener** | **RT** | **Product Target Congener (-2Cl)** | **RT** | **Δ RT (s)** |
|---|---|---|---|---|
| PCB-96 PeCB | 25.77 | PCB-38 TrCB | 25.77 | 0.00 |
| PCB-188 HpCB | 35.33 | **PCB-114 PeCB** | 35.34 | -0.60 |
| PCB-175 HpCB | 38.45 | **PCB-126 PeCB** | 38.51 | -3.60 |
| PCB-198/199 HpCB | 43.87 | **PCB-169 HxCB** | 43.80 | 4.20 |

Table 4.3 Precursor PCBs that present potential interferences due to the loss of 2Cl and their corresponding target PCBs.
The congeners are sorted in RT order with the WHO toxic PCBs highlighted in bold type. The GC conditions used were as required for the EPA-1668C method.

Nevertheless, there is a fundamental difference in the isotope ratio measurement from any resultant peaks of these fragment interferences (compared to those from the loss of a single chlorine) due to the fragment ion cluster *m/z* being ~2 Da lower than those of the molecular ion cluster being affected. E.g. in the case of a HpCB affecting a PeCB, it is the fragment M+4 and M+6 ions that affect the M+2 and M+4 ions being monitored. Since the theoretical isotopic abundance ratios of these two peak pairs are ~3.10 and ~1.55 respectively, any peaks formed through this mechanism would not, in isolation, be identified as a PeCB; however, if present in addition to the true compound, their contribution could lead to an out-of-ratio assessment and hence a false negative result being reported.

### 4.3.3 PCB fragmentation in GC-HRMS (EI) analyses

To illustrate the variability in the degree of fragmentation exhibited by different isomers, GC-HRMS data was acquired from a mix containing all HxCB isomers at equal (50 pg/µl) concentrations. The experimental conditions for the GC-HRMS analyses using EI at 34 eV and the GC program used in conjunction with the SPB-Octyl GC column were as described earlier in section 4.2.1 with full details in Appendix D.1.

The chromatographic data are shown in Figure 4.14 where the upper trace shows the detected peaks from the M+2 ion of the HxCB molecular ion cluster, with the toxic PCBs highlighted in red, and the lower trace shows the corresponding fragment peaks due to the loss of Cl.

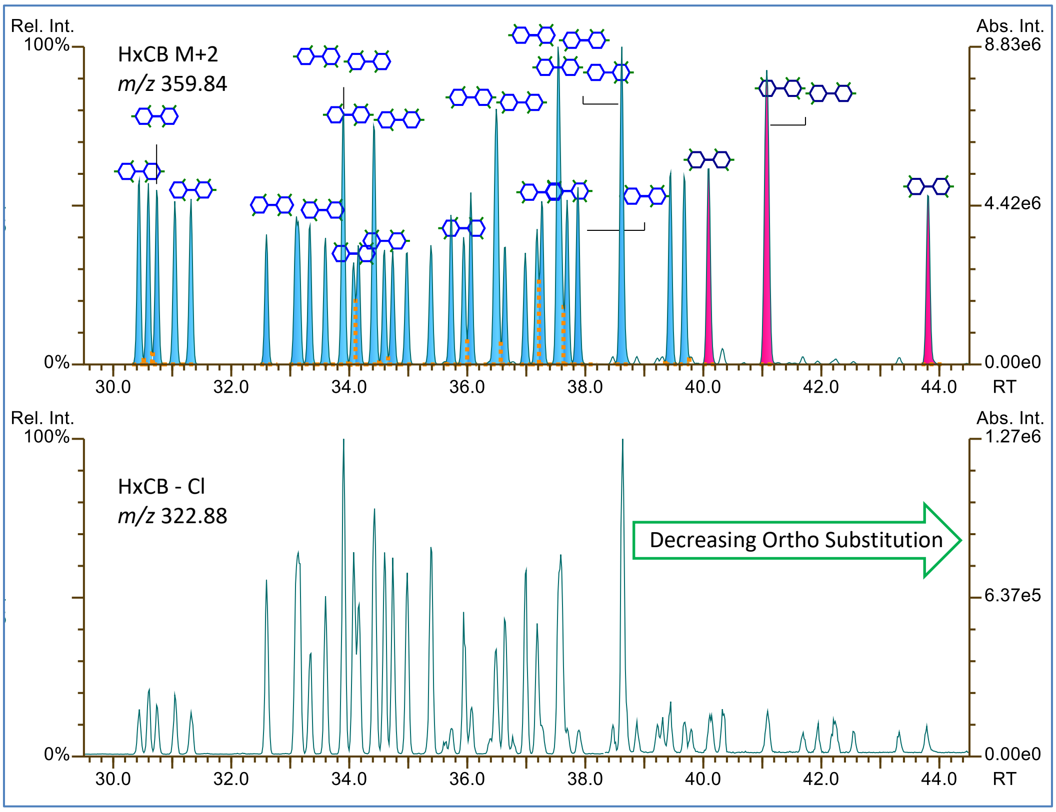

Figure 4.14 Chromatograms from data acquired (HRMS/EI) from a mix of all 42 HxCB congeners. The upper trace shows peaks due to the M+2 molecular ion, with the WHO toxic PCBs highlighted in red, and the lower trace shows the fragment peaks due to the loss of Cl. Structures are shown for selected HxCBs to indicate the transition from the tetra-ortho substituted congeners in the lower RT range through to the mono- and non-ortho substituted congeners at higher RTs.
Note: there are 34 discrete peaks shown as these include 6 coeluting doublets and 1 triplet. The additional peaks in the HxCB - Cl trace, e.g. at RT ~42, are due to the loss of 2Cl from HpCB.

There is clearly considerable variability in the degree of fragmentation of the various isomers, and there would appear to be some coupling between this and the number of Cl atoms in ortho positions: the group of tetra-ortho substituted congeners at the beginning of the retention time (RT) window, and the mono-ortho and non-ortho congeners at higher RTs, show markedly less fragmentation than the di- and tri-ortho peaks that fall in the central RT band. This observation is however confounded by the existence of the various coeluting congeners.

To resolve this, data from 9 separate PCB mixes were obtained where each mix contained a subset of the 209 PCBs such that no coeluting peaks were present, either at the same chlorination level or that would result in interferences due to fragmentation. A table listing the PCB contents of each mix is shown in Appendix C.3. The same experimental conditions as above were used, i.e. to meet the requirements of the EPA-1668C method, with full details provided in Appendix D.1.

The results for the relative fragmentation responses due to the loss of Cl are charted in Figure 4.15 for TeCB, Figure 4.16 for PeCB, Figure 4.17 for HxCB and Figure 4.18 for HpCB – these being the 4 homolog groups that, between them, contain the 12 WHO toxic PCBs. For the remaining homologues, Appendix B.3 shows the data due to the loss of Cl from MoCB, DiCB and TrCB in Figure B.2, and from OcCB, NoCB and DeCB in Figure B.3.

In each case, the most intense fragment responses are due to PCBs that are at least di-ortho substituted with Cl atoms in positions 2 and 2’ (i.e. on each ring), with lower responses (i.e. less fragmentation) for mono-ortho substituted congeners and the lowest responses for the mono- and non-ortho substituted toxic PCBs[*]. This would appear to correlate with the steric hindrance introduced by the Cl ortho substitutions in opposing rings that constrain rotation about the biphenyl’s central C-C bond. It is important to note that such hindrance would also inhibit a congener’s ability to adopt a sufficiently planar conformation required for AhR binding and its ensuing toxicity effects (McFarland and Clarke, 1989).

---

[*] Of the 209 PCBs: there are 20 non-ortho, 48 mono-ortho, 36 di-ortho (2,6 – i.e. same ring), 36 di-ortho (2,2’ – i.e. opposite rings), 48 tri-ortho and 21 tetra-ortho substituted biphenyls; therefore 105 PCBs contain at least the 2,2’ ortho substitutions.

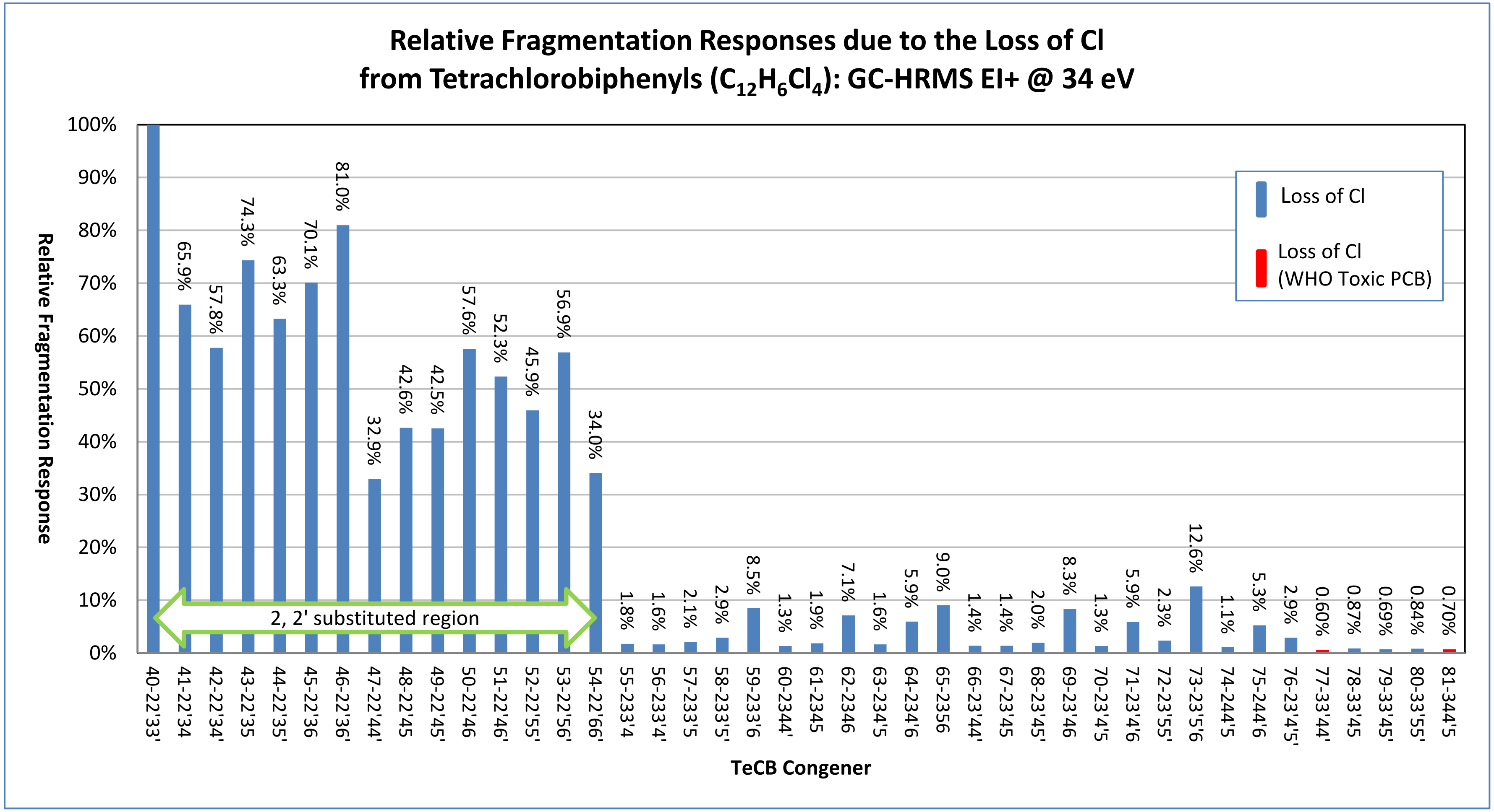

Figure 4.15 Chart showing the relative fragmentation responses due to the loss of Cl from TeCB ($C_{12}H_6Cl_4$) congeners using GC-HRMS EI+ @ 34 eV. The x-axis labels indicate the congener number and the chlorine substitution pattern.

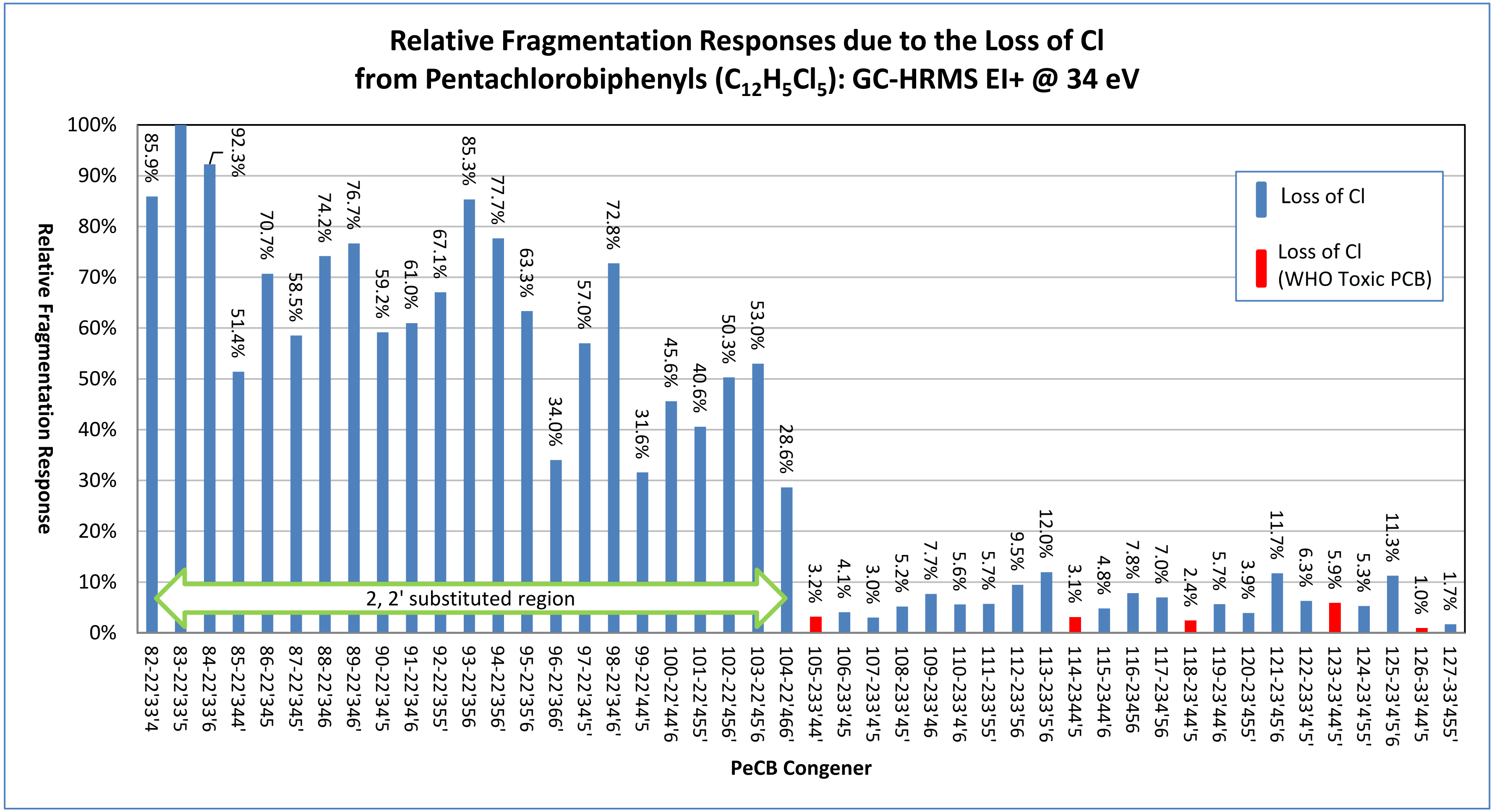

Figure 4.16 Chart showing the relative fragmentation responses due to the loss of Cl from PeCB ($C_{12}H_5Cl_5$) congeners using GC-HRMS EI+ @ 34 eV. The x-axis labels indicate the congener number and the chlorine substitution pattern.

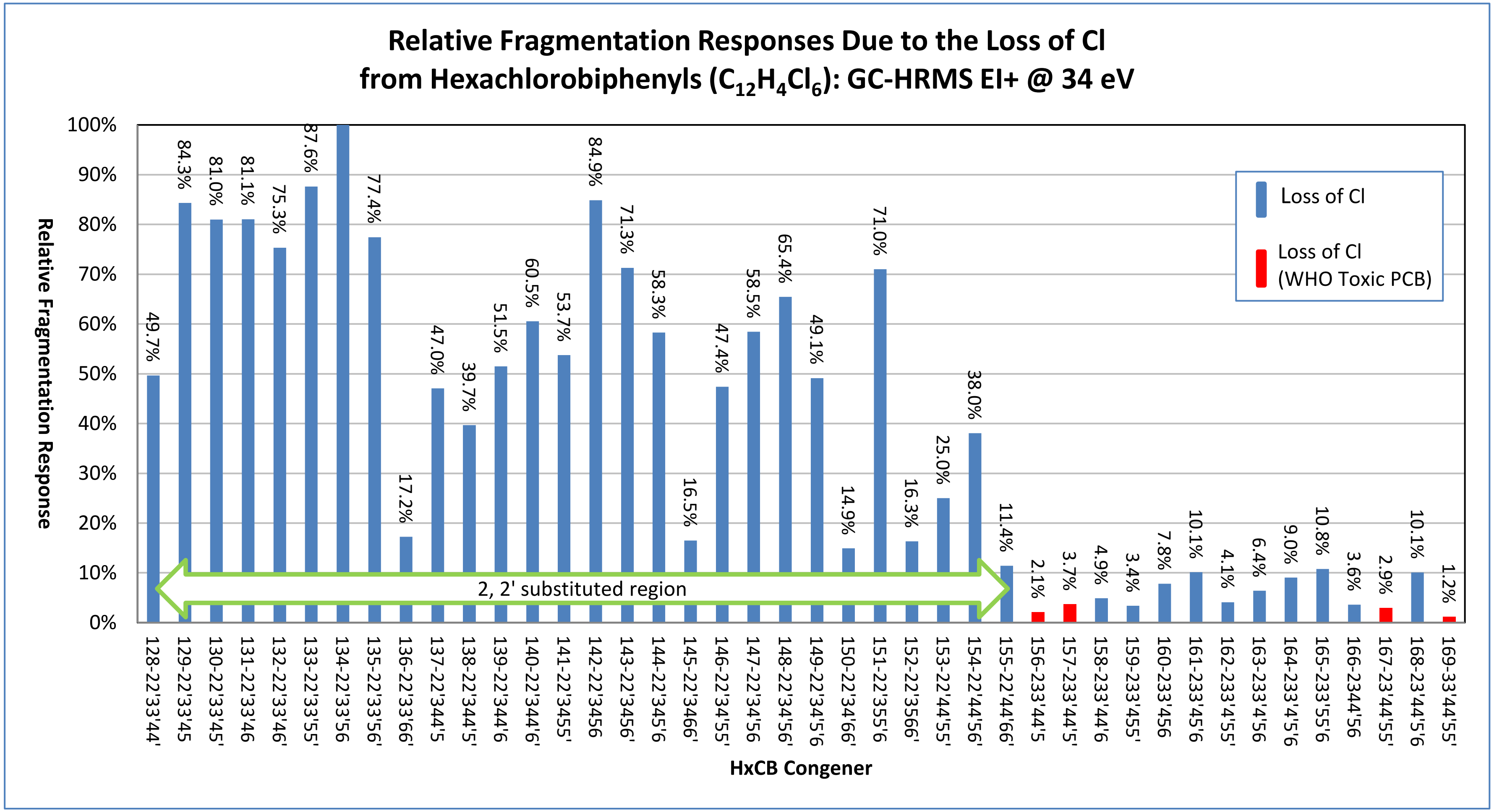

Figure 4.17 Chart showing the relative fragmentation responses due to the loss of Cl from HxCB ($C_{12}H_4Cl_6$) congeners using GC-HRMS EI+ @ 34 eV. The x-axis labels indicate the congener number and the chlorine substitution pattern.

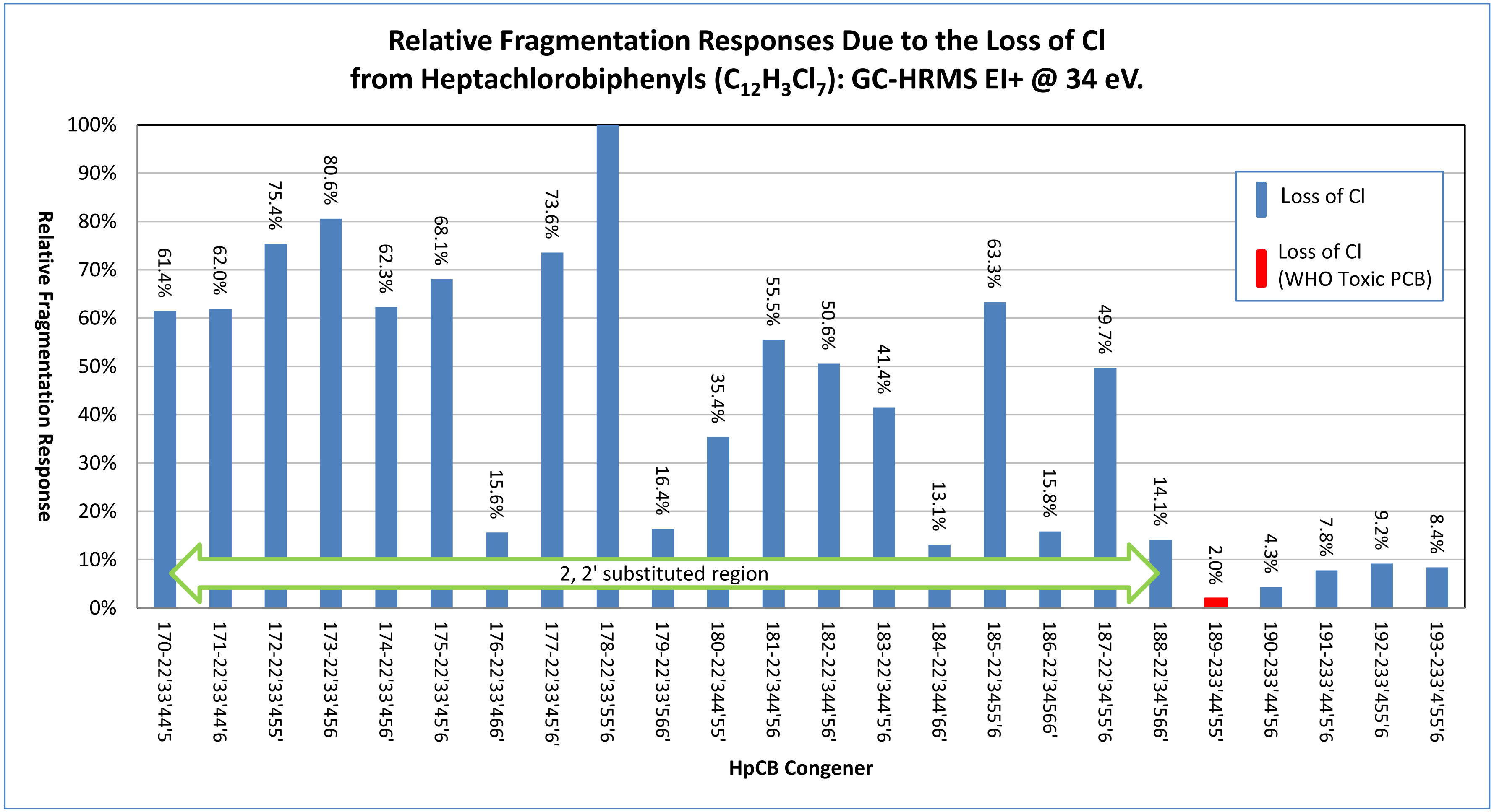

Figure 4.18 Chart showing the relative fragmentation responses due to the loss of Cl from HpCB ($C_{12}H_3Cl_7$) congeners using GC-HRMS EI+ @ 34 eV. The x-axis labels indicate the congener number and the chlorine substitution pattern.

### 4.3.4 Variation of HxCB fragmentation with collision energy in GC-MS/MS (APCI) analyses

For the initial study to investigate the variation in PCB fragmentation with collision energy (CE) a solution of 5 $^{13}$C-labelled HxCBs (listed in Table 4.4) was analysed using the Synapt G2-S instrument at CE from 0 to 30 eV with argon as the collision gas at a pressure of 7.7 x 10$^{-3}$ mbar. Other experimental conditions were as described in section 4.2.2 with the SPB-1 GC column installed.

| PCB | Structure | RT |
|---|---|---|
| $^{13}$C-PCB-138 | 2,2’,3,4,4’,5’-HxCB | 30.73 |
| $^{13}$C-PCB-167 | 2,3’,4,4’,5,5’-HxCB | 32.41 |
| $^{13}$C-PCB-156 | 2,3,3’,4,4’,5-HxCB | 33.47 |
| $^{13}$C-PCB-157 | 2,3,3’,4,4’,5’-HxCB | 33.70 |
| $^{13}$C-PCB-169 | 3,3’,4,4’,5,5’-HxCB | 35.60 |

Table 4.4 The $^{13}$C-labelled HxCBs ($^{13}C_{12}H_4Cl_6$) used for the initial fragmentation experiments with their structures and GC retention times (RT).
The SPB-1 GC column, unlike the SPB-Octyl column used to meet the EPA-1668C method’s chromatographic requirements, does completely resolve PCB-156 and 157.

Figure 4.19, Figure 4.20 and Figure 4.21 show a series of extracted ion chromatograms due to the $^{13}$C-labelled HxCB M+0 molecular ion ($^{13}C_{12}H_4{}^{35}Cl_6$, *m/z* 369.8846), the loss of Cl ($^{13}C_{12}H_4{}^{35}Cl_5$, *m/z* 334.9157) and of 2Cl ($^{13}C_{12}H_4{}^{35}Cl_4$, *m/z* 299.9469) at CE of 0, 15 and 30 eV respectively.

The data obtained with the CE at 0 eV (Figure 4.19) show similar responses for each of the M+0 peaks (RSD < 7%), and only weak responses for the M-Cl (avg. ~1.3%) and M-2Cl (avg. ~2.8%) product ion peaks.

At a CE of 15 eV (Figure 4.20) the M+0 peaks show a greater variation (RSD ~11%) in their areas; there are also notable increases in the responses of both the M-Cl and M-2Cl product ion peaks, particularly for PCB-138, those being ~18% and ~13% compared to ~7.2% and ~7.4% for the averages of the 4 toxic isomers respectively.

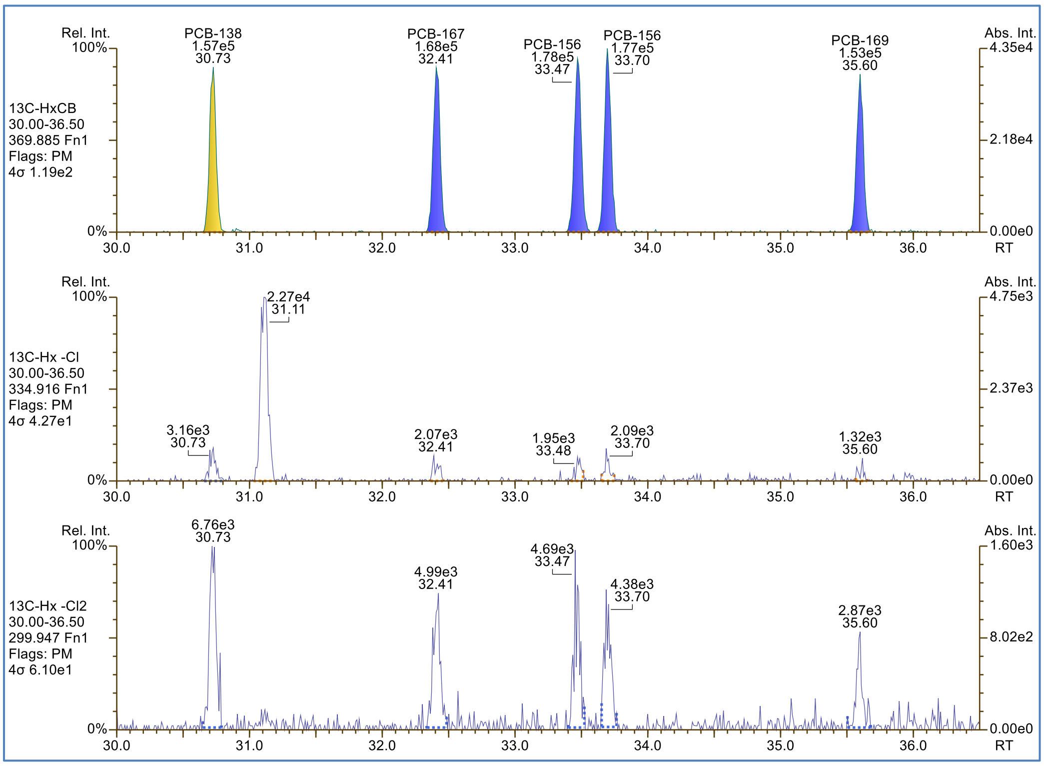

Figure 4.19 Chromatograms from data acquired (Synapt, APCI) from a mix of 5 $^{13}$C-labelled HxCBs showing peaks due to the M+0 ions, and from the losses of Cl and 2Cl at 0 eV CE.

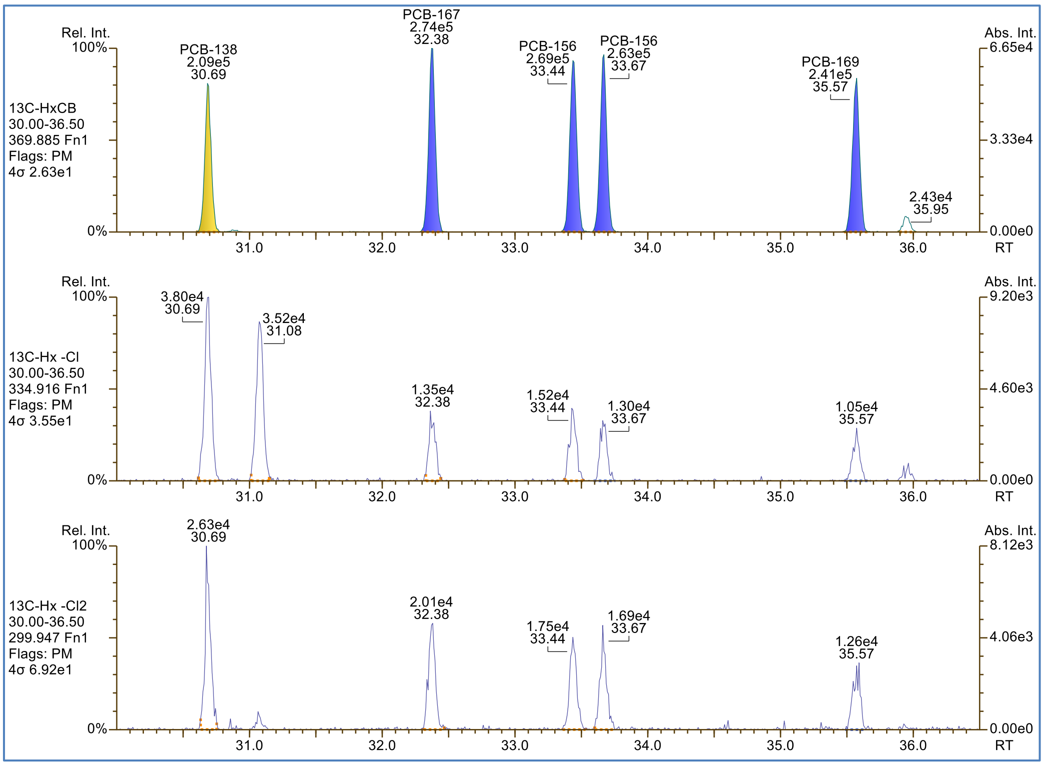

Figure 4.20 Chromatograms from data acquired (Synapt, APCI) from a mix of 5 $^{13}$C-labelled HxCBs showing peaks due to the M+0 ions, and from the losses of Cl and 2Cl at 15 eV CE.

At a CE of 30 eV (Figure 4.21), the M+0 response of PCB-138 has been significantly (> 90%) reduced and there is some (~25%) reduction in the response of the 3 mono-ortho HxCBs relative to PCB-169. In this context, it should be noted that the current, WHO-2005, TEF of the non-ortho PCB-169 is 1000x that of any of the mono-ortho HxCBs.

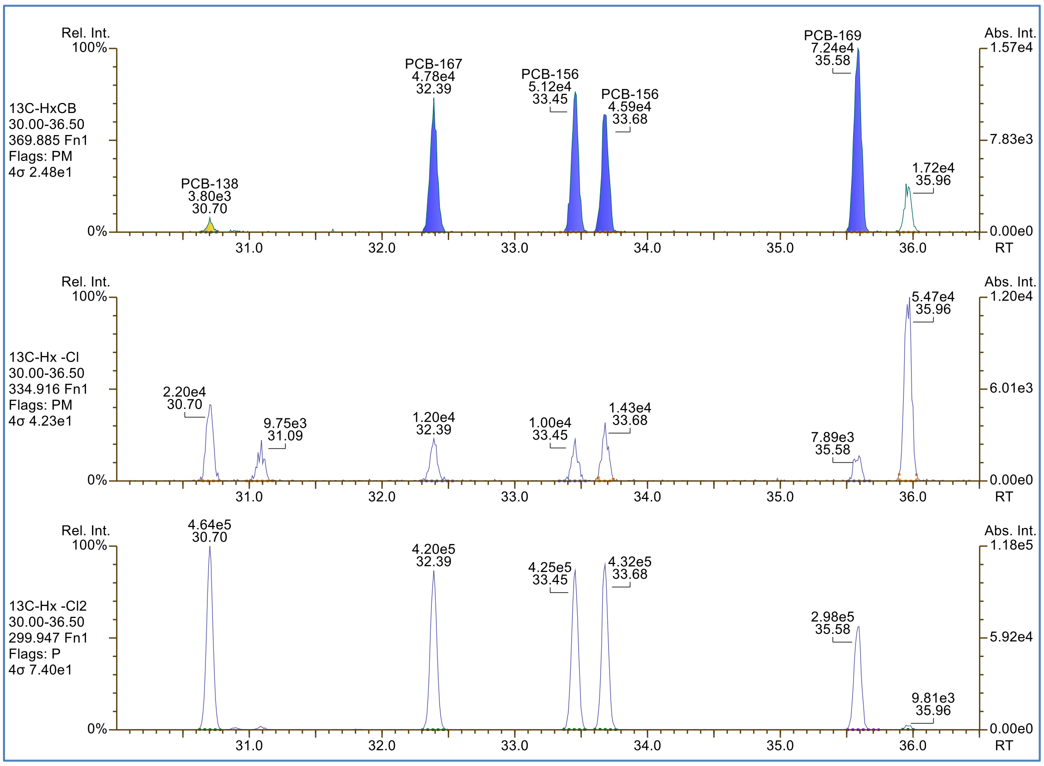

Figure 4.21 Chromatograms from data acquired (Synapt, APCI) from a mix of 5 $^{13}$C-labelled HxCBs showing peaks due to the M+0 ions, and from the losses of Cl and 2Cl at 30 eV CE.

Additional data were then acquired at CE of 10, 20 and 25 eV (chromatograms not shown) to provide intermediate values. For the loss of Cl data, in addition to the peaks' responses at *m/z* 334.9157 ($^{13}C_{12}H_3{}^{35}Cl_5$) – as shown in the above chromatograms – contributions due to the loss of HCl at *m/z* 333.9079 ($^{13}C_{12}H_3{}^{35}Cl_5$) and 335.9050 ($^{13}C_{12}H_3{}^{35}Cl_4{}^{37}Cl$) were also included*.

---

* The latter, given the instrument's mass resolution and the data processing mass window, would also include any contributions due to Cl/H exchange giving rise to PeCB ions at *m/z* 335.9235 ($^{13}C_{12}H_5{}^{35}Cl_5$). This will be discussed in more detail later in this chapter.

The intensities of the precursor ions relative to those of the loss of Cl (and HCl) fragment ions against CE were calculated and plotted for each of the 5 HxCBs as shown in Figure 4.22.

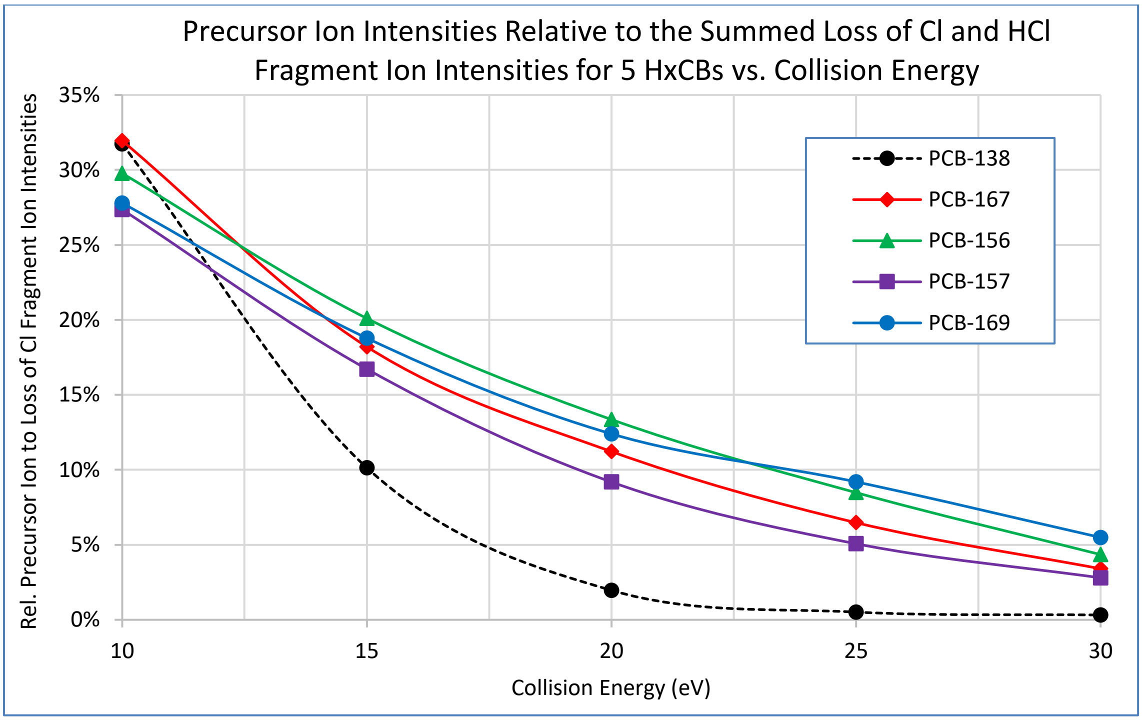

Figure 4.22 Chart showing the intensities of 5 HxCB precursor (molecular) ions relative to the summed fragment ion intensities due to the losses of Cl and HCl vs. CE of 10 to 30 eV. Data were normalised to values obtained at CE = 0 eV and line smoothing applied.

These data reflect the initial observations and show a similar trend for each of the mono-ortho substituted PCB-167, 156 and 157, and the non-ortho substituted PCB-169 congeners, with only minor variances across the CE range as seen by the cross-overs in their response curves. In contrast, the di-ortho substituted PCB-138 (dashed line) exhibits a distinctly different response curve that, for example, shows a relative response of ~2% at 20 eV CE compared to the ~12% averaged response of the other 4 PCBs.

The acquired data were similarly processed for the loss of 2Cl as shown in Figure 4.23. In addition, the comparative losses of Cl and 2Cl were plotted in Figure 4.24 and show a rise in the relative losses of Cl to those of 2Cl at a CE of 15 eV.

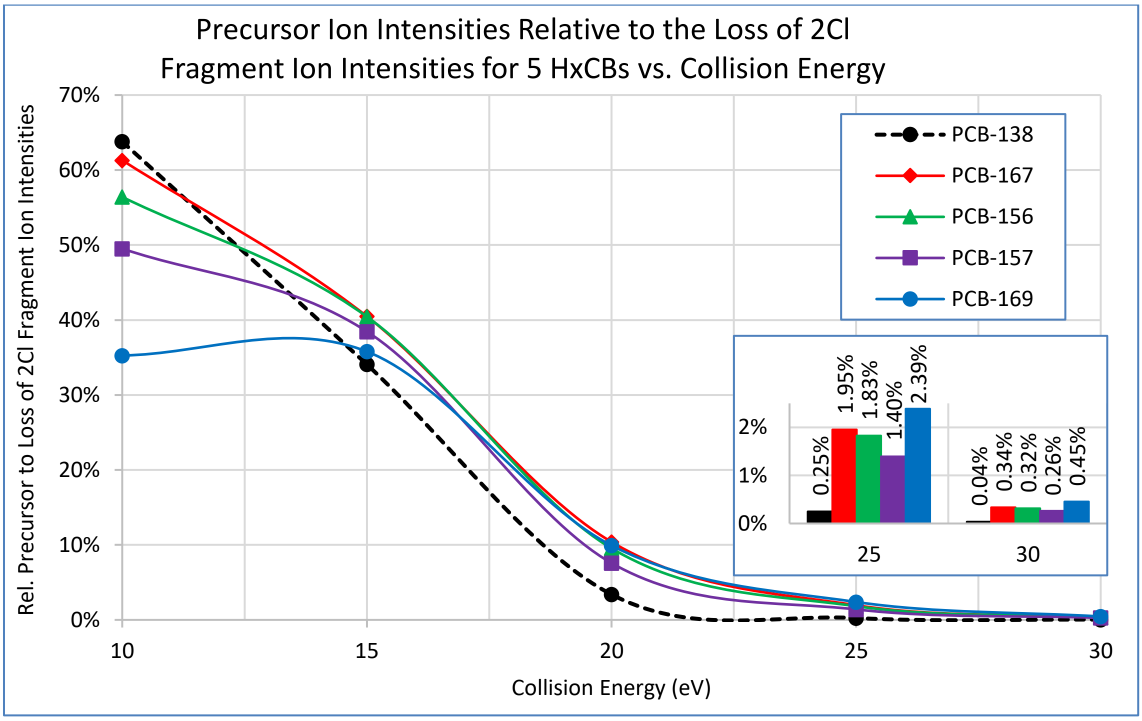

Figure 4.23 Chart showing the intensities of 5 HxCB precursor (molecular) ions relative to the fragment ion intensities due to the loss of 2Cl vs. CE of 10 to 30 eV.
Data were normalised to values obtained at CE = 0 eV and line smoothing applied. The inset bar chart shows detail for the 25 and 30 eV CE data.

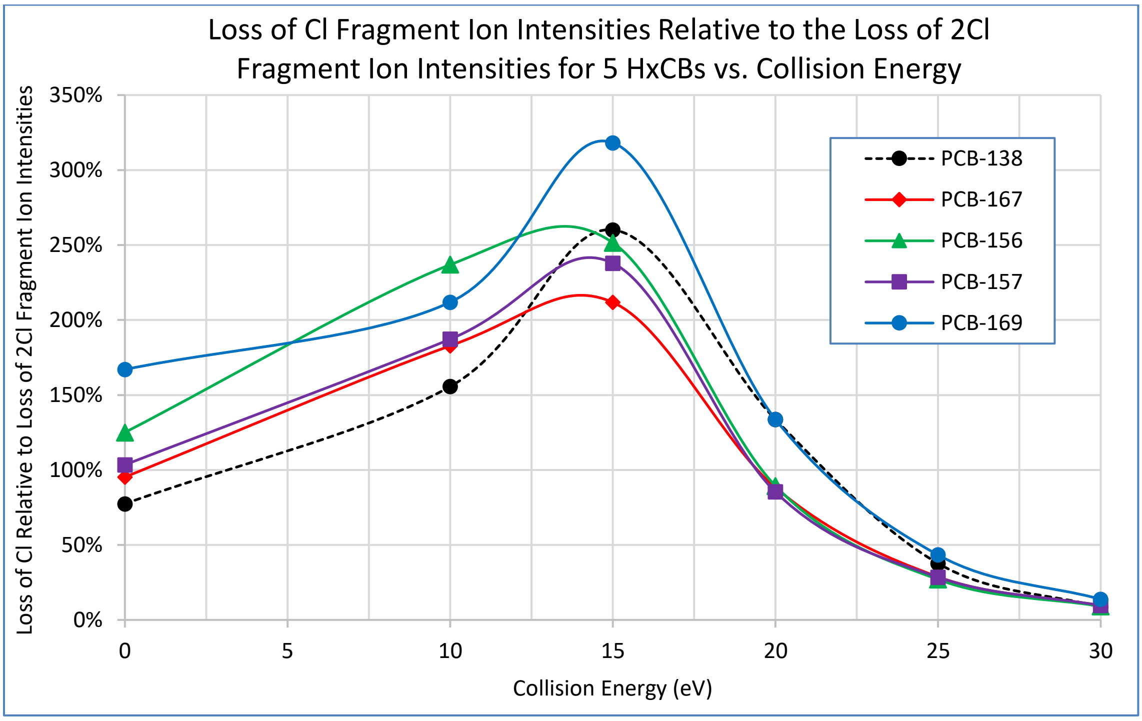

Figure 4.24 Chart showing the fragment ion intensities due to loss of Cl relative to those due loss of 2Cl for 5 HxCBs vs. CE of 0 to 30 eV.
Note: line smoothing applied.

Of these 5 HxCB isomers, only PCB-138 is considered non-toxic per the current WHO assessment: a key attribute (as previously discussed in section 4.3.3) being that it has di-ortho (2, 2’) chlorine substitutions, whereas the remainder are either mono-ortho (PCB-167, 156 and 157) or non-ortho (PCB-169) substituted.

In considering the gas-phase structural differences between these 5 PCBs, a key parameter is the dihedral angle between the two ring planes (i.e. the twist, or torsion, angle about the central C-C bond) that is predominately governed by the presence of ortho substituted Cl atoms. The dihedral angles obtained from published data (Dorofeeva *et al.*, 2005), as shown in Table 4.5, are suggestive of a possible relationship with the degree of fragmentation. This, as also shown in Table 4.5, is similarly seen with the internal barrier to rotation energy, a parameter closely related to the dihedral angle with 3 distinct energy levels of ~65, ~32 and ~10 kJ/mol corresponding to the di-, mono and non-ortho substitution respectively of these PCBs (Andersson, Haglund and Tysklind, 1997).

It was however noted that the angle given for PCB-169 – and for several other PCBs – was lower than the accepted ~45° value (Popelier *et al.*, 2018) for the (non-chlorinated) biphenyl molecule; this led to an alternate set of values being derived from the *ab initio* molecular modelling methods (as described in section 4.2.5). These have been included in Table 4.5, and although showing higher values than those published, exhibit a similar trend. Noting these differences, a further set of published values (Bureš, Pekárek and Ocelka, 2007) was then obtained for comparison purposes; these values also differ but exhibit the same basic pattern.

| **Congener** | **Structure** | **Cl ortho substitution** | **Dihedral angle$^1$** | **Dihedral angle$^2$** | **Dihedral angle$^3$** | **$E_{rot}$ kJ/mol** |
|---|---|---|---|---|---|---|
| PCB-138 | 2,2’,3,4,4’,5’-HxCB | Di-ortho | 83.1° | 71° | 87.7° | 65.2 |
| PCB-167 | 2,3’,4,4’,5,5’-HxCB | Mono-ortho | 55.2° | 51° | 68.1° | 29.6 |
| PCB-156 | 2,3,3’,4,4’,5-HxCB | Mono-ortho | 59.2° | 53° | 68.1° | 33.5 |
| PCB-157 | 2,3,3’,4,4’,5’-HxCB | Mono-ortho | 59.0° | 54° | 69.7° | 33.7 |
| PCB-169 | 3,3’,4,4’,5,5’-HxCB | Non-ortho | 37.9° | 47° | 45.9° | 9.61 |

Table 4.5 The dihedral angles of PCB-138, 167, 156, 157 and 169, and their internal barrier of rotation energies ($E_{rot}$).
Dihedral angles obtained from Dorofeeva *et al* (1), Bureš *et al* (2) and from values calculated herein (3).

### 4.3.5 PCB fragmentation in GC-MS/MS (APCI) analyses

To replicate the previous fragmentation (EI) study using APCI, the Synapt G2-S GC-MS/MS instrument was used with the experimental conditions as described in section 4.2.2 (with full details in Appendix D.2) and the SPB-Octyl GC column installed. Argon was used as the collision gas at a pressure of 7.8 x $10^{-3}$ mbar, but no voltage was applied to the collision cell.

For these data, a set of 5 native (unlabelled) PCB mixes was available that contained all 209 congeners between them, distributed such that no coeluting isomers (i.e. at the same level of chlorination) would be present in any single mix when using the EPA-1668C GC conditions. Full details of the PCBs found in each mix are given in Appendix C.3.

The results for the relative fragmentation responses due to the loss of Cl are charted in Figure 4.25 for TeCB, Figure 4.26 for PeCB, Figure 4.27 for HxCB and Figure 4.28 for HpCB. At each level of chlorination, the greatest degree of fragmentation occurs for congeners with di- and tri-ortho Cl substitution and the least for those with non-, mono- and tetra-ortho substitution. (For the remaining homologues, Appendix B.3 shows the data due to the loss of Cl from MoCB, DiCB and TrCB in Figure B.4, and from OcCB, NoCB and DeCB in Figure B.5.)

These fragmentation profiles are broadly similar to the corresponding EI data shown previously (Figure 4.15 to Figure 4.18) – with $r^2$ of 0.88, 0.91, 0.93 and 0.93 for the $Cl_4$ to $Cl_7$ homologues respectively – though the degree of fragmentation of the tetra-ortho substituted congeners is significantly greater in the APCI data, e.g. the average relative response of the loss of Cl fragments from the 2,2’,*,*,*,6,6’-HpCBs is ~15% for EI and ~4.6% for the APCI data.

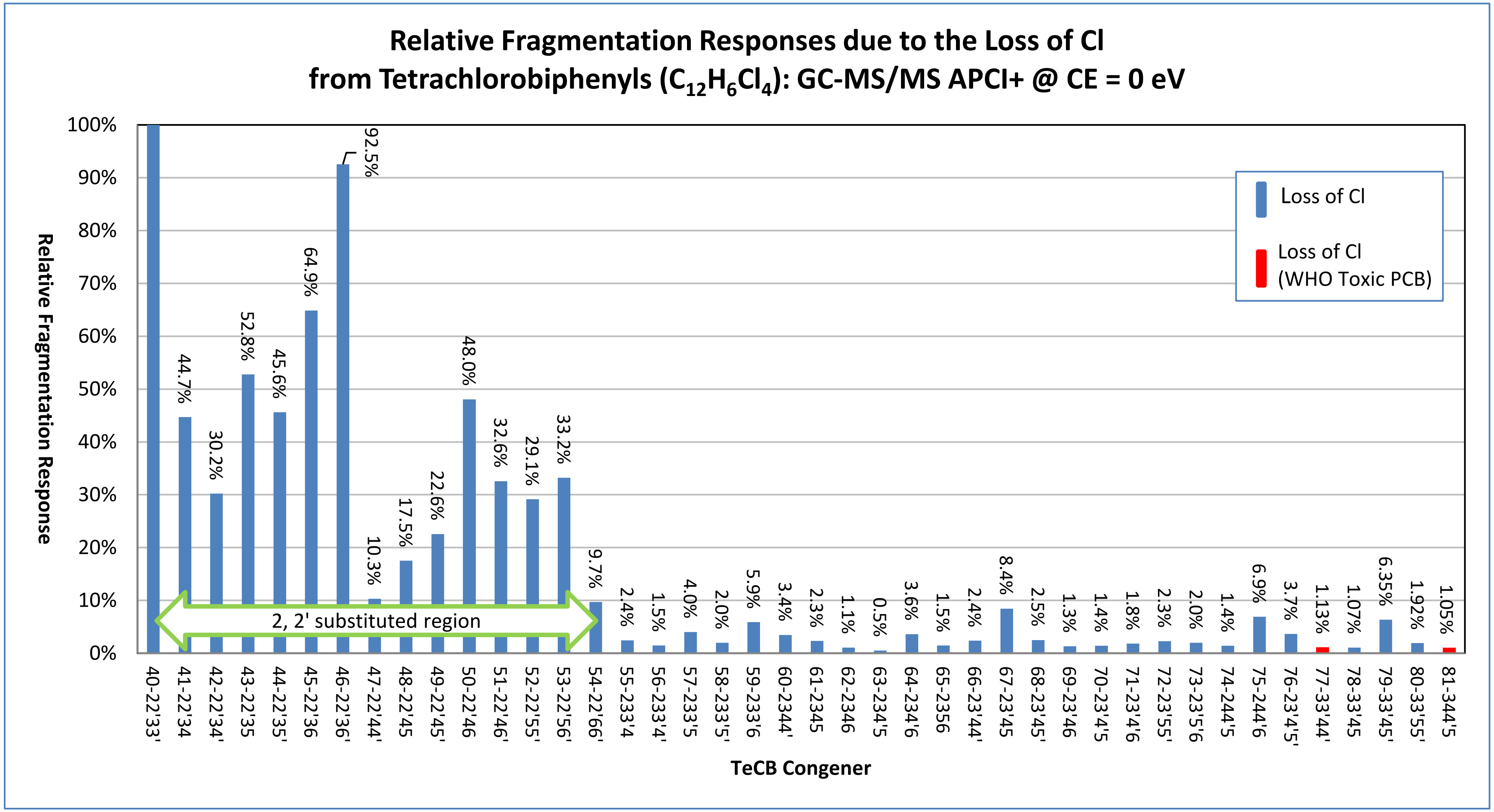

Figure 4.25 Chart showing the relative fragmentation responses due to the loss of Cl from TeCB ($C_{12}H_6Cl_4$) congeners using GC-MS/MS APCI+. Data acquired using a CE of 0 eV. The x-axis labels indicate the congener number and the chlorine substitution pattern.

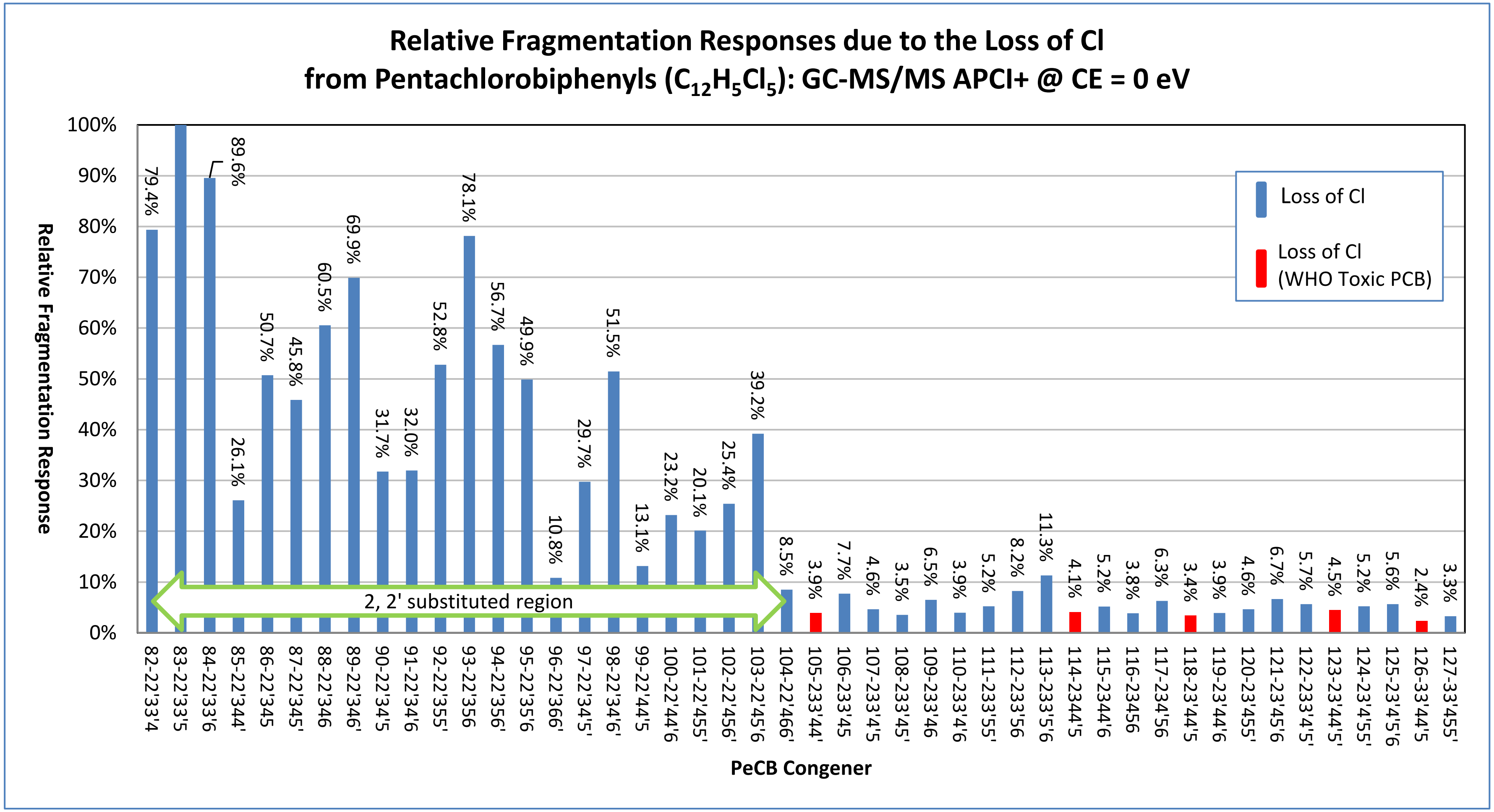

Figure 4.26 Chart showing the relative fragmentation responses due to the loss of Cl from PeCB ($C_{12}H_5Cl_5$) congeners using GC-MS/MS APCI+. Data acquired using a CE of 0 eV. The x-axis labels indicate the congener number and the chlorine substitution pattern.

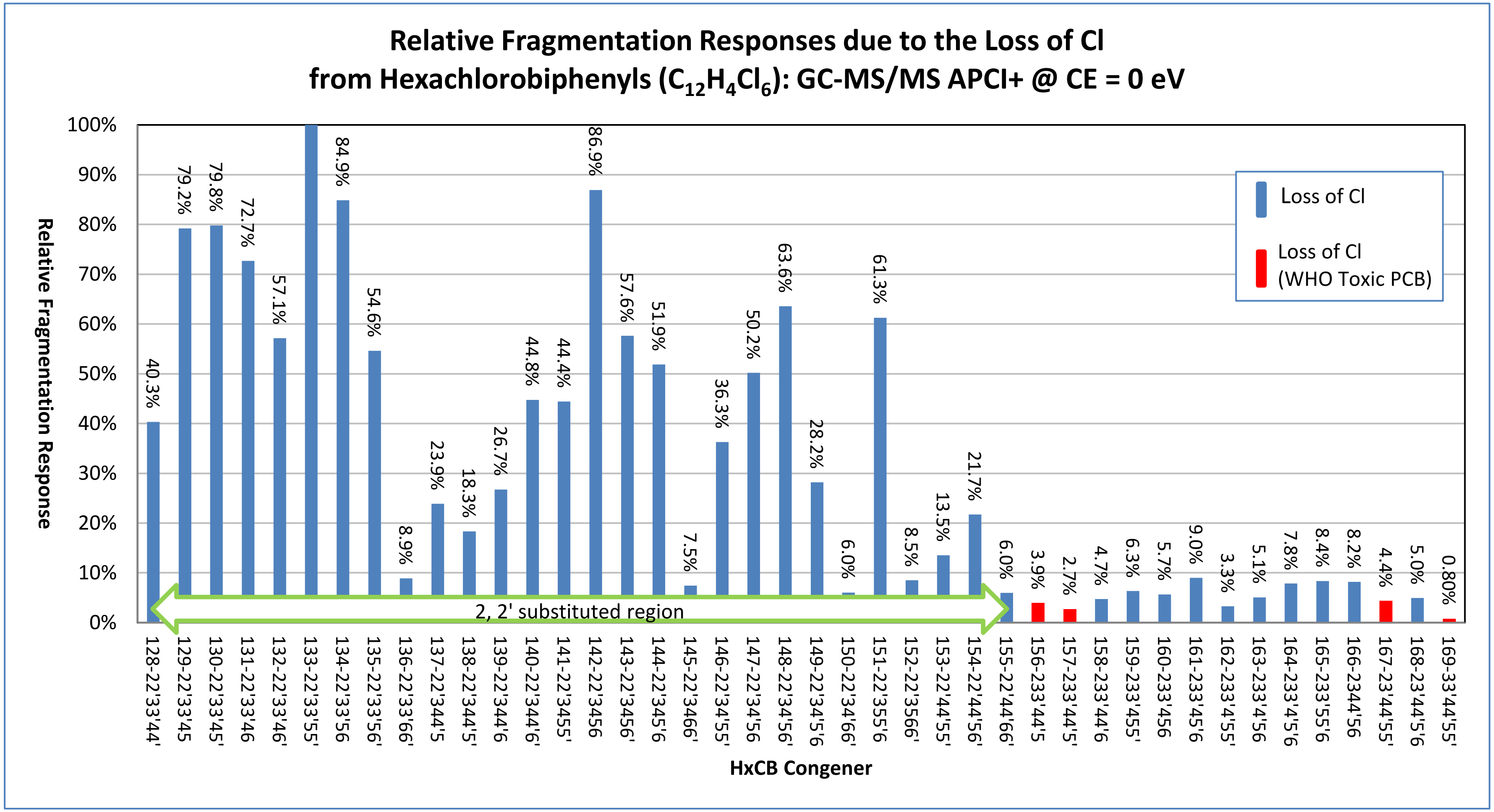

Figure 4.27 Chart showing the relative fragmentation responses due to the loss of Cl from HxCB ($C_{12}H_4Cl_6$) congeners using GC-MS/MS APCI+. Data acquired using a CE of 0 eV. The x-axis labels indicate the congener number and the chlorine substitution pattern.

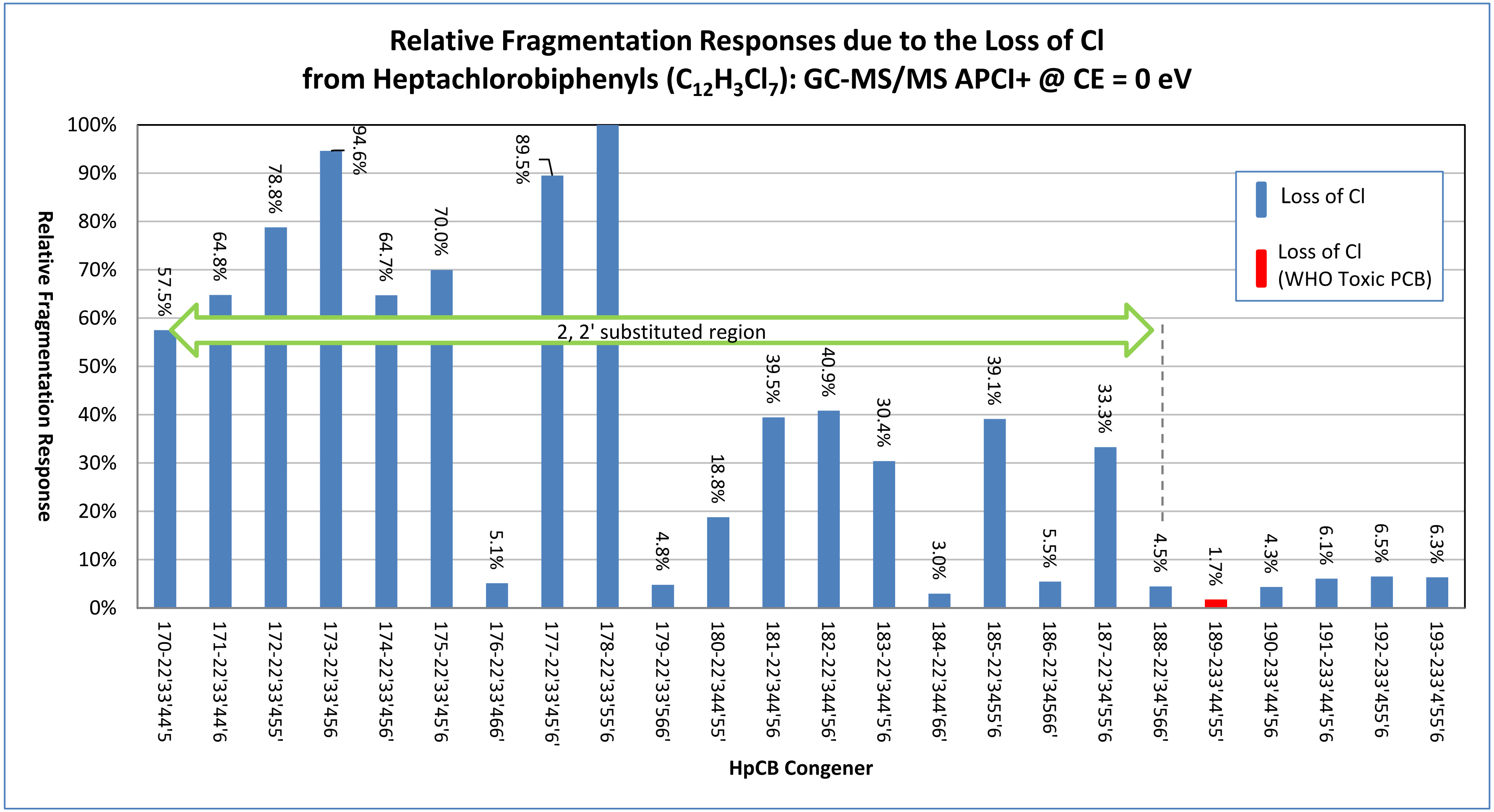

Figure 4.28 Chart showing the relative fragmentation responses due to the loss of Cl from HpCB ($C_{12}H_3Cl_7$) congeners using GC-MS/MS APCI+. Data acquired using a CE of 0 eV. The x-axis labels indicate the congener number and the chlorine substitution pattern.

### 4.3.6 Variation of PCB fragmentation with collision energy in GC-MS/MS (APCI) analyses

The following work expands on the earlier HxCB fragmentation vs. CE study by using the 209 PCB congener mixes and experimental conditions of the previous section with data acquired at CE of 0, 10, 20 and 30 eV. Initially, spectra corresponding to each of the 5 HxCBs previously analysed were examined, though these are now from the native, rather than $^{13}$C-labelled, congeners. The spectra from the data acquired at 20 eV CE (each averaged over their GC peak and background subtracted) are shown in Figure 4.29 and were obtained from 3 separate sample analyses due to the make-up of the congener-specific solutions – e.g. PCB-156 and 157 could not be in the same mix as they would otherwise coelute on the SPB-Octyl GC column.

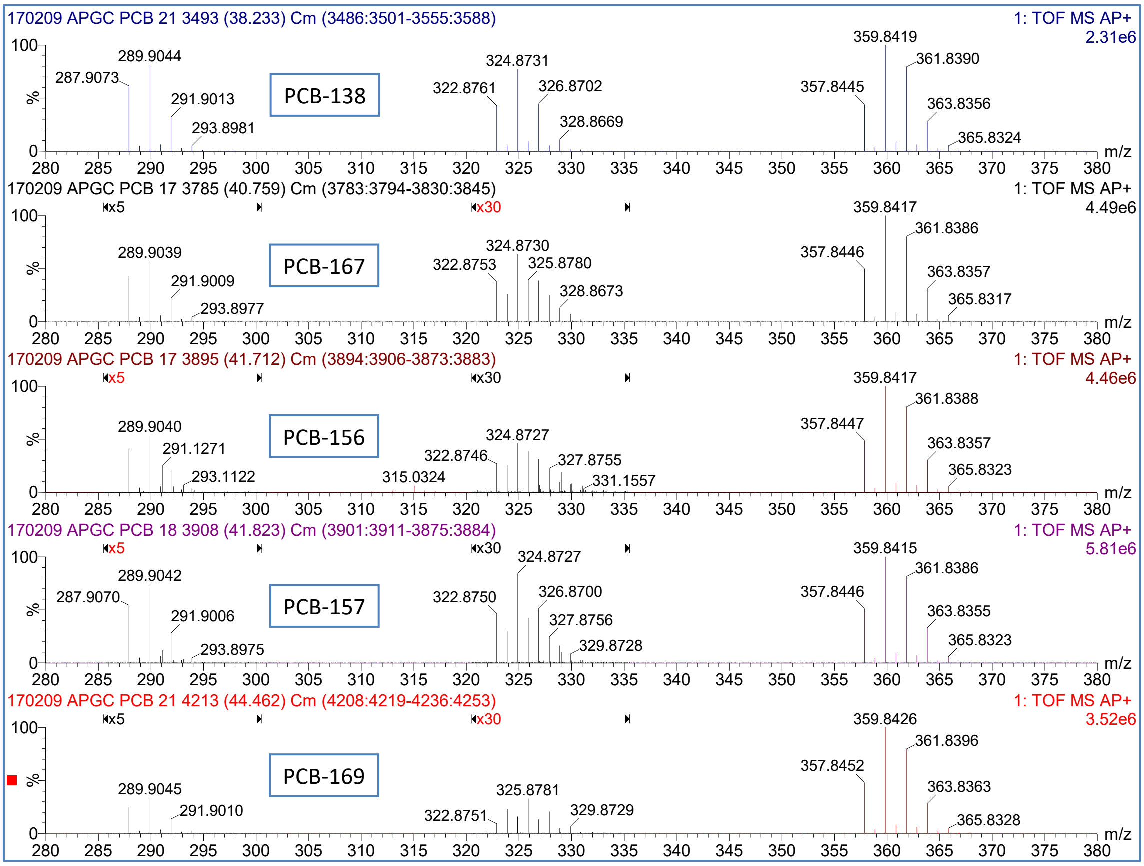

Figure 4.29 Mass spectra showing the molecular ion, loss of Cl and loss of 2Cl regions for the HxCBs (from top): PCB-138 (2,2',3,4,4',5'), 167 (2,3',4,4',5,5'), 156 (2,3,3',4,4',5), 157 (2,3,3',4,4',5') and 169 (3,3',4,4',5,5'). Data acquired using AP+ ionisation at a CE of 20 eV. Note the x5 and x30 magnified sections in all spectra except PCB-138.

Each of the molecular ion clusters appear, as expected, to be practically identical as are the loss of 2Cl regions around *m/z* 290. However, the clusters corresponding to the loss of Cl (ca. *m/z* 325) show some notable differences in each spectrum – these are shown in detail in Figure 4.30.

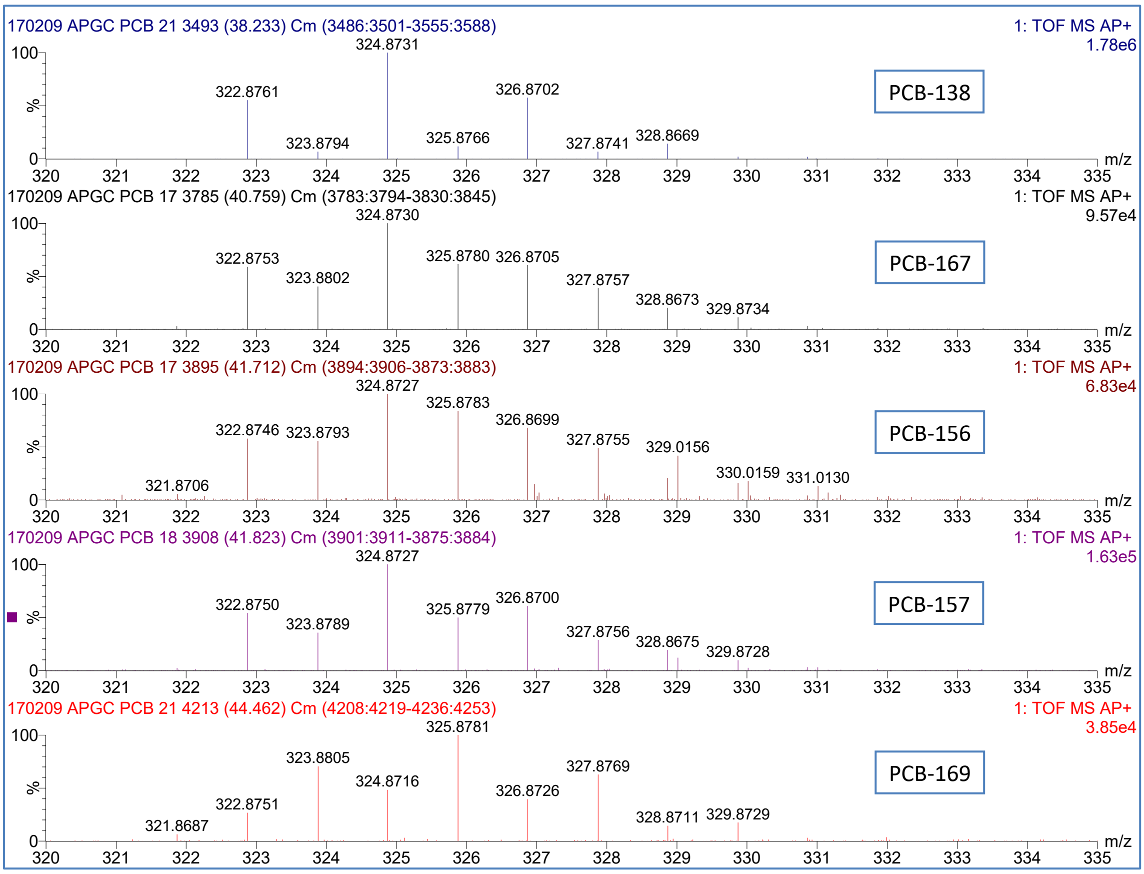

Figure 4.30 Mass spectra showing the loss of Cl region for the HxCBs (from top): PCB-138 (2,2’,3,4,4’,5’), 167 (2,3’,4,4’,5,5’), 156 (2,3,3’,4,4’,5), 157 (2,3,3’,4,4’,5’) and 169 (3,3’,4,4’,5,5’). Data acquired using AP+ ionisation at a CE of 20 eV.

The upper spectrum of Figure 4.30 shows the loss of Cl region from PCB-138 (2,2’,3,4,4’,5’-HxCB) with an isotope distribution that appears similar to the theoretical model for $C_{12}H_4Cl_5$ and confirmed by the comparison shown in Figure 4.31 ($r^2 = 0.993$). However, the remaining spectra show other features: the minor peak at *m/z* 321.9 appears to be due to the (not unexpected) loss of HCl although the series of peaks at *m/z* 323.9, 325.9, etc. show significantly higher than expected intensities but with isotopic ratios that still match the $Cl_5$ distribution pattern. This could indicate that one of the chlorine atoms has been replaced by a hydrogen – as will be further examined using the accurate mass data.

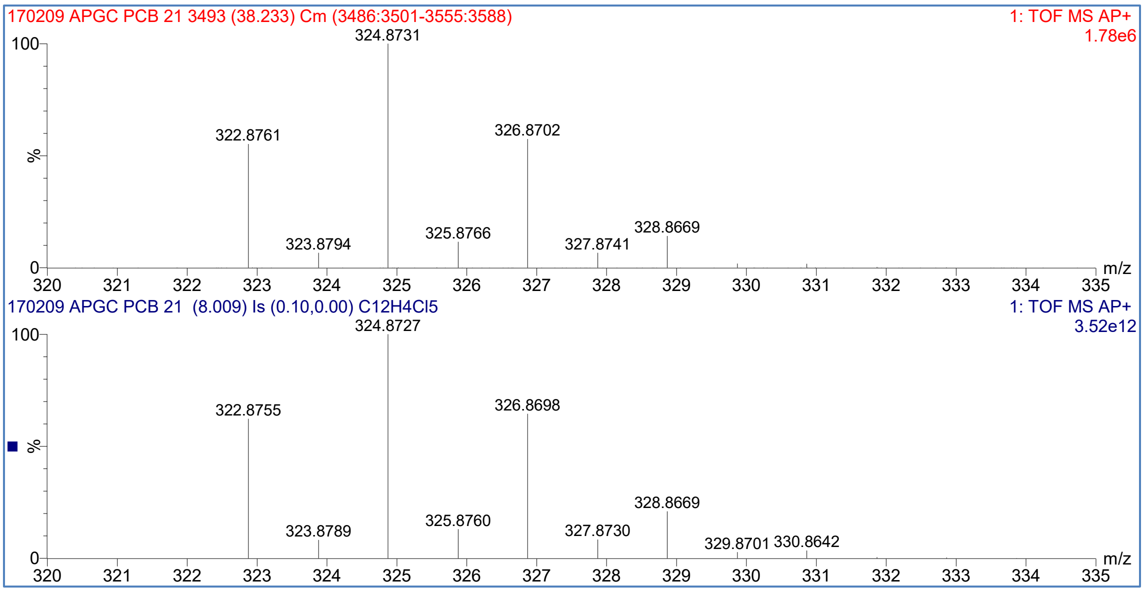

Figure 4.31 Comparison spectra showing the loss of Cl region from the acquired data of PCB-138 (2,2',3,4,4',5'-HxCB, upper trace) and the theoretical isotope model of $C_{12}H_4Cl_5$ (lower trace) giving an $r^2$ value of 0.993.

The results from the elemental composition calculations using MassLynx for ions in the loss of Cl region from PCB-138 are given in Table 4.6. These data show that all product ions in the cluster are due to the direct loss of Cl and are even-electron ions, as expected for MS/MS fragmentation of the molecular ion (Eckers, Monaghan and Wolff, 2005).

| **Measured *m/z*** | **Relative Abun. %** | **Calculated *m/z*** | **Error mDa** | **Error ppm** | **DBE** | **Electron state** | **Formula** | **Comments** |
|---|---|---|---|---|---|---|---|---|
| 322.8761 | 55.2 | 322.8756 | 0.5 | 1.5 | 8.5 | Even | $C_{12}H_4{}^{35}Cl_5$ | Loss of Cl |
| 323.8794 | 6.64 | 323.8789 | 0.5 | 1.5 | 8.5 | Even | $C_{11}{}^{13}CH_4{}^{35}Cl_5$ | Loss of Cl ($^{13}C$) |
| 324.8731 | 100 | 324.8726 | 0.5 | 1.5 | 8.5 | Even | $C_{12}H_4{}^{35}Cl_4{}^{37}Cl$ | Loss of Cl |
| 325.8766 | 11.6 | 325.8760 | 0.6 | 1.8 | 8.5 | Even | $C_{11}{}^{13}CH_4{}^{35}Cl_4{}^{37}Cl$ | Loss of Cl ($^{13}C$) |
| 326.8702 | 57.5 | 326.8697 | 0.5 | 1.5 | 8.5 | Even | $C_{12}H_4{}^{35}Cl_3{}^{37}Cl_2$ | Loss of Cl |
| 327.8741 | 6.63 | 327.873 | 1.1 | 3.4 | 8.5 | Even | $C_{11}{}^{13}CH_4{}^{35}Cl_3{}^{37}Cl_2$ | Loss of Cl ($^{13}C$) |
| 328.8669 | 14.1 | 328.8667 | 0.2 | 0.6 | 8.5 | Even | $C_{12}H_4{}^{35}Cl_2{}^{37}Cl_3$ | Loss of Cl |

Table 4.6 Elemental composition calculations for ions in the loss of Cl cluster from PCB-138 (2,2',3,4,4',5'-HxCB; $C_{12}H_4Cl_6$).

The elemental composition results for ions from the PCB-169 (3,3',4,4',5,5'-HxCB) loss of Cl cluster are shown in Table 4.7. The odd (integer *m/z*) product ions at *m/z* 322.9, 324.9, etc. show comparable results to those observed for PCB-138 above, however, other than the minor peak due to the loss of HCl at *m/z* 321.9, the remaining even ions at *m/z* 323.9, 325.9, etc. (highlighted in bold type) indicate a possible mix of two contributions: one in each case being the expected (even electron) Cl loss and the other that would match that of a prototypical PeCB radical cation (odd electron).

Since a PeCB ion has one additional H and there is no evidence of protonation of the molecular ion, it could not have been directly formed from fragmentation. Although the source of H or $H_2$ is unknown, this suggests either[*] a Cl/H exchange process or $H_2$ adduct formation with the HCl loss ion – the latter having been observed in chemical ionisation experiments using $H_2$ (Harrison, Onuska and Tsang, 1981). As will be shown in Chapter 5, the formation of a PeCB – and specifically PCB-126 (3,3',4,4',5-PeCB) – is further supported by data obtained from the ion mobility analysis of these fragments.

| **Measured *m/z*** | **Relative Abun. %** | **Calculated *m/z*** | **Error mDa** | **Error ppm** | **DBE** | **Electron state** | **Formula** | **Comments** |
|---|---|---|---|---|---|---|---|---|
| 321.8687 | 6.29 | 321.8677 | 1.0 | 3.1 | 9 | Odd | $C_{12}H_3{}^{35}Cl_5$ | Loss of HCl |
| 322.8751 | 26.6 | 322.8756 | -0.5 | -1.5 | 8.5 | Even | $C_{12}H_4{}^{35}Cl_5$ | Loss of Cl |
| **323.8805** | **70.3** | **323.8789** | **1.6** | **4.9** | **8.5** | **Even** | **$C_{11}{}^{13}CH_4{}^{35}Cl_5$** | **Loss of Cl ($^{13}C$)** |
| | | **323.8834** | **-2.9** | **-9.0** | **8** | **Odd** | **$C_{12}H_5{}^{35}Cl_5$** | **Cl -> H exchange** |
| 324.8716 | 48.2 | 324.8726 | -1.0 | -3.1 | 8.5 | Even | $C_{12}H_4{}^{35}Cl_4{}^{37}Cl$ | Loss of Cl |
| **325.8781** | **100** | **325.8760** | **2.1** | **6.4** | **8.5** | **Even** | **$C_{11}{}^{13}CH_4{}^{35}Cl_4{}^{37}Cl$** | **Loss of Cl ($^{13}C$)** |
| | | **325.8804** | **-2.3** | **-7.1** | **8** | **Odd** | **$C_{12}H_5{}^{35}Cl_4{}^{37}Cl$** | **Cl -> H exchange** |
| 326.8726 | 39.4 | 326.8697 | 2.9 | 8.9 | 8.5 | Even | $C_{12}H_4{}^{35}Cl_3{}^{37}Cl_2$ | Loss of Cl |
| **327.8769** | **62.6** | **327.8775** | **-0.6** | **-1.8** | **8** | **Odd** | **$C_{12}H_5{}^{35}Cl_3{}^{37}Cl_2$** | **Cl -> H exchange** |
| | | **327.8730** | **3.9** | **11.9** | **8.5** | **Even** | **$C_{11}{}^{13}CH_4{}^{35}Cl_3{}^{37}Cl_2$** | **Loss of Cl ($^{13}C$)** |
| 328.8711 | 14.2 | 328.8667 | 4.4 | 13.4 | 8.5 | Even | $C_{12}H_4{}^{35}Cl_2{}^{37}Cl_3$ | Loss of Cl |
| **329.8729** | **17.4** | **329.8745** | **-1.6** | **-4.9** | **8** | **Odd** | **$C_{12}H_5{}^{35}Cl_2{}^{37}Cl_3$** | **Cl -> H exchange** |
| | | **329.8701** | **2.8** | **8.5** | **8.5** | **Even** | **$C_{11}{}^{13}CH_4{}^{35}Cl_2{}^{37}Cl_3$** | **Loss of Cl ($^{13}C$)** |

Table 4.7 Elemental composition calculations for ions in the loss of Cl cluster from PCB-169 (3,3',4,4',5,5'-HxCB; $C_{12}H_4Cl_6$).
Entries in bold type indicate a possible mix of ions due to the loss of Cl and from the proposed Cl/H exchange; their *m/z* are separated by ~14 ppm and therefore cannot be resolved by the (available) mass spectrometer.

---

[*] For the remainder of the thesis, this will be referred to as a Cl/H exchange (since that is the effective outcome) even though the specific mechanism remains unknown.

Comparable patterns to the above were also observed in the PeCB data as shown by the examples in Figure 4.32; these spectra show the molecular ion and losses of Cl and 2Cl regions for PCB-109 (2,3,3’,4,6), PCB-117 (2,3,4’,5,6), PCB-111 (2,3,3’,5,5’) and PCB-114 (2,3,4,4’,5) acquired using AP+ ionisation at a CE of 20 eV. Of this group, only PCB-114 is regarded as a toxic congener. As with the previous HxCB data, the molecular ion and loss of 2Cl regions of all spectra show the same isotope distribution patterns, but this was not the case for the loss of Cl region.

PCB-109 shows a significantly (~50x) lower intensity of the molecular ion region compared to the other 3 congeners, and the cluster around *m/z* 290 shows loss of HCl, Cl and of Cl/H exchange. Loss of Cl and of Cl/H exchange were similarly also observed for PCB-111, 117 and 114, but the loss of HCl was only otherwise significant in the spectrum of PCB-114.

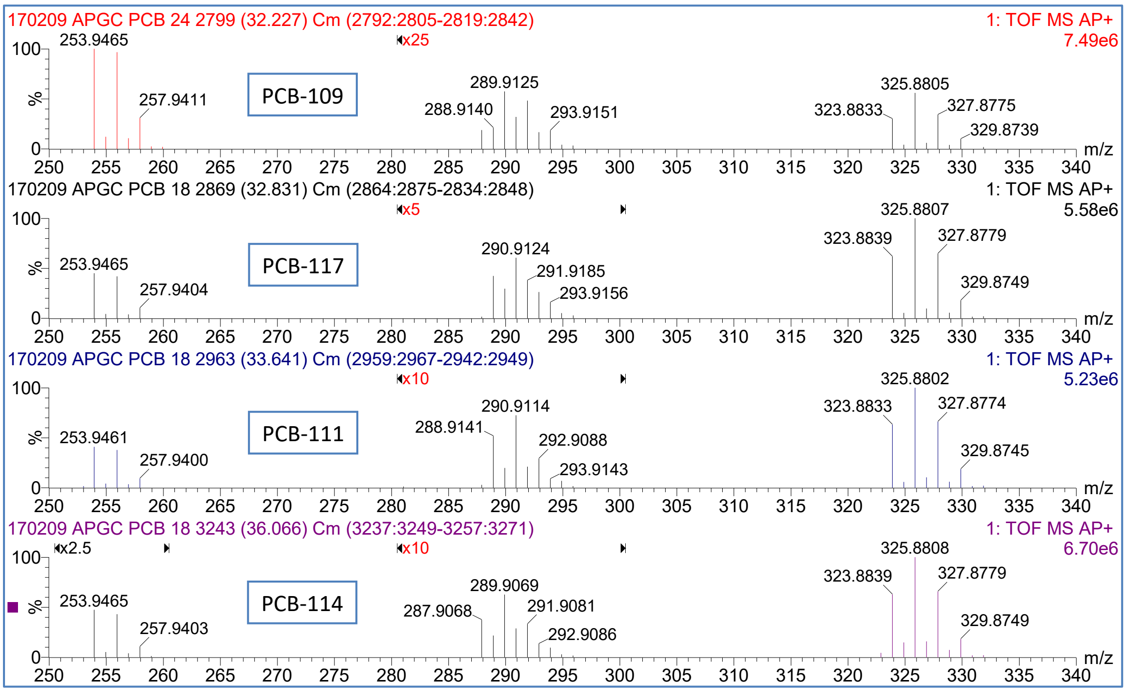

Figure 4.32 Mass spectra showing the molecular ion and loss of Cl regions for (from top): PCB-109 (2,3,3’,4,6-PeCB), PCB-117 (2,3,4’,5,6-PeCB), PCB-111 (2,3,3’,5,5’-PeCB) and PCB-114 (2,3,4,4’,5-PeCB). Data acquired using AP+ ionisation at a CE of 20 eV.
Note the different magnification regions and factors used within these spectra.

In addition to the congener-to-congener variation, the relative proportions of the losses of Cl, HCl, 2Cl and of the Cl/H exchange also vary with CE as shown in Figure 4.33 for PCB-114.

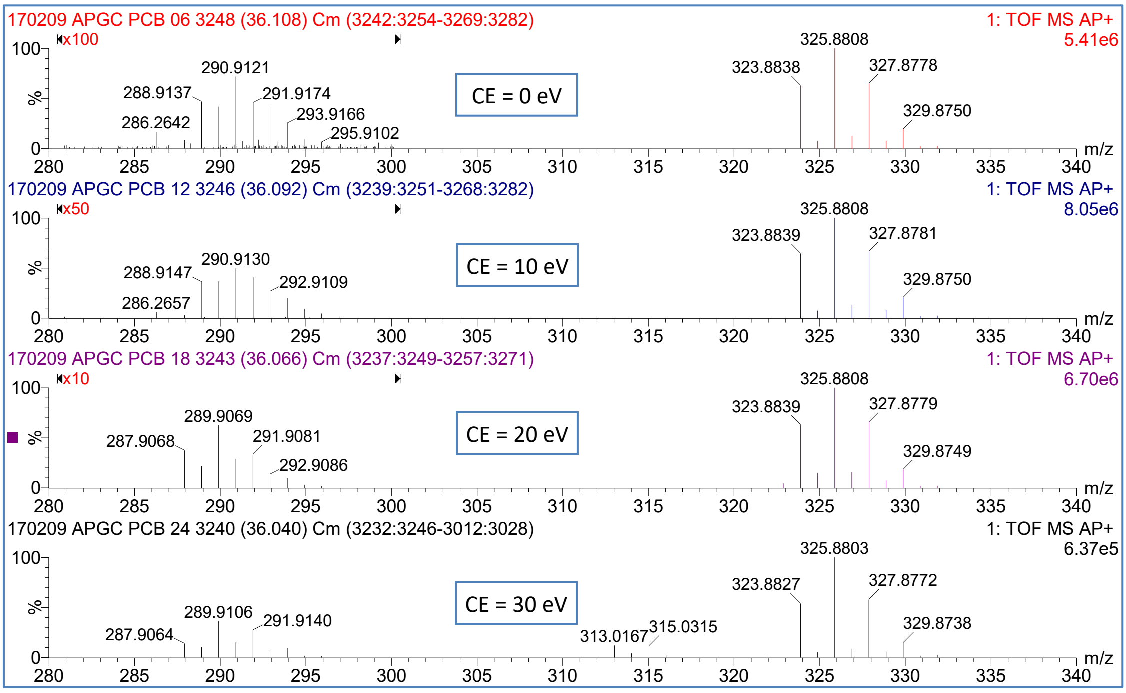

Figure 4.33 Mass spectra showing the molecular ion and loss of Cl regions for PCB-114 (2,3,4,4’,5-PeCB) acquired using AP+ ionisation at CE of (from top) 0, 10, 20 and 30 eV. Note: different magnifications for the loss of Cl region in these spectra.

### 4.3.7 Principal component analysis (PCA) of the fragmentation profiles from GC-MS/MS (APCI) data at various collision energies

The complex fragmentation trends of the above PeCB congeners at CE from 0 to 30 eV were calculated as normalised relative responses to create the profiles as shown in the graphs[*] of Figure 4.34 for PCB-109, Figure 4.35 for PCB-117, Figure 4.36 for PCB-111 and Figure 4.37 for PCB-114.

In each graph, the 6 series of points correspond to the ratios of intensities from:

- Mol. ion relative to the loss of Cl (green)
- Mol. ion relative to the loss of 2Cl (blue)
- Mol. ion relative to the loss of HCl (red)
- Mol. ion relative to the loss of 34[*] (black)
- Loss of Cl relative to the loss of 2Cl (magenta)
- Loss of Cl relative to the loss of 34[*] (orange)

[*] The M-34 ion could be due to the M+2 ($^{37}$Cl) isotope of the HCl loss, the M+1 ($^{13}$C) isotope of the loss of Cl, the Cl/H exchange process or any combination of these.

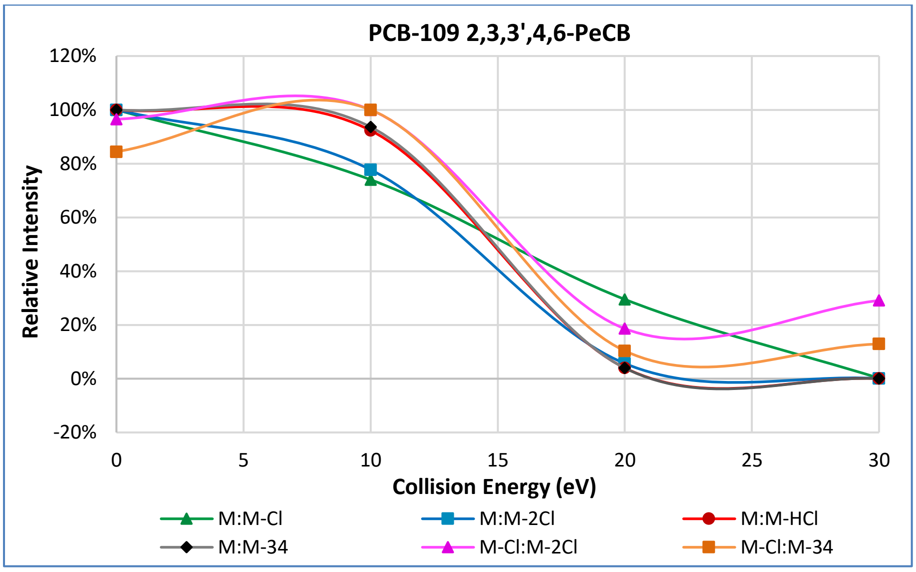

Figure 4.34 Fragmentation profile for PCB-109 (2,3,3',4,6-PeCB) based on the relative responses of selected mass losses vs. CE of 0 to 30 eV.

---

[*] These graphs, plotted in Microsoft Excel, used its built-in line smoothing function (based on a Bézier cubic-spline algorithm) hence the appearance of lines outside the data's 0 to 100% y-axis range.

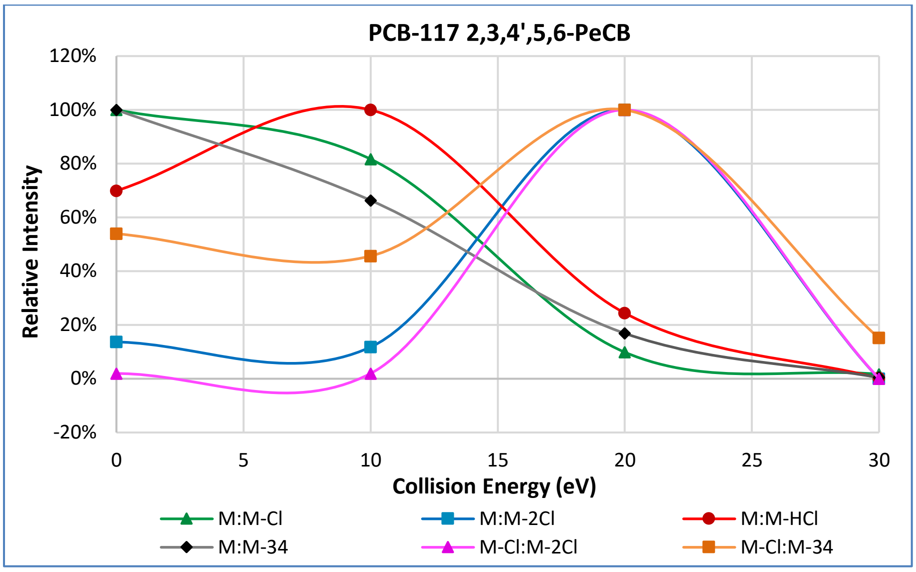

Figure 4.35 Fragmentation profile for PCB-117 (2,3,4',5,6-PeCB) based on the relative responses of selected mass losses vs. CE of 0 to 30 eV.

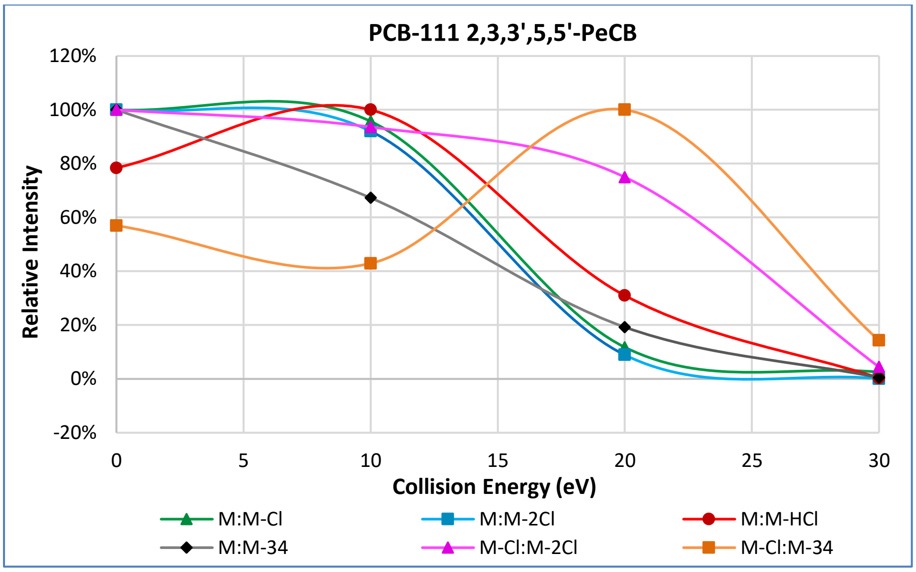

Figure 4.36 Fragmentation profile for PCB-111 (2,3,3',5,5'-PeCB) based on the relative responses of selected mass losses vs. CE of 0 to 30 eV.

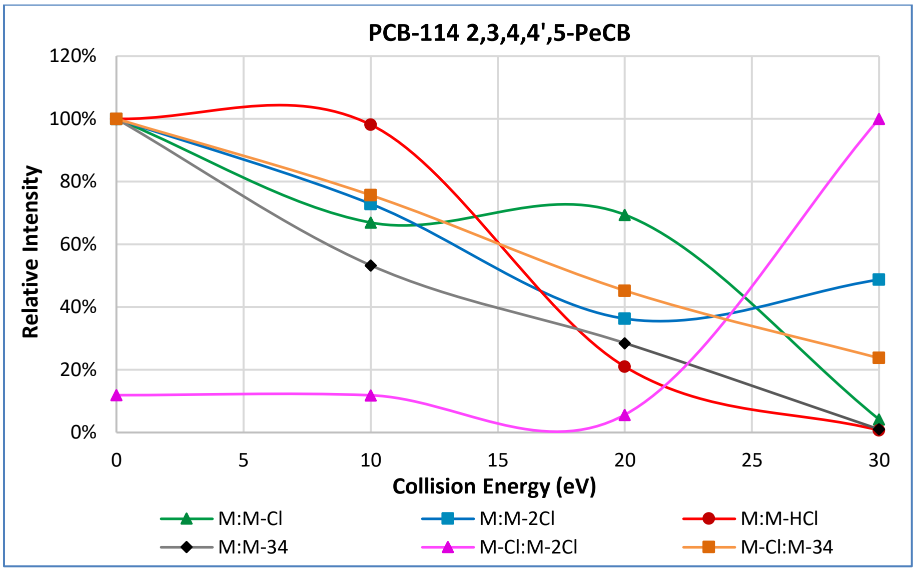

Figure 4.37 Fragmentation profile for PCB-114 (2,3,4,4',5-PeCB) based on the relative responses of selected mass losses vs. CE of 0 to 30 eV.

These profiles were also calculated for a wider range (n = 80*) of congeners as shown in profile charts in Appendix B.4. To investigate the correlation between these data, principal component analysis (PCA) was used. The data for each parameter (loss of Cl, loss of 2Cl, etc.) at each CE were normalised to their respective standard deviations and mean-centred prior to PCA.

PCA calculations were made using MATLAB and plotted as shown in Figure 4.38. The data for the non-ortho and mono-ortho substituted toxic PCBs are indicated by the red and blue star-shaped points respectively, together with their accompanying 95% confidence interval ellipses. The remaining non-toxic PCBs are divided into 6 further groups: non-ortho, mono-ortho, di-ortho on opposing rings (2, 2’), di-ortho on the same ring (2, 6), tri-ortho and tetra-ortho substituted.

The variance of the first principal component (PC1) accounts for ~25% of the total and ~17% for the second (PC2)†; this is perhaps reflected by the lack of grouping of PCBs other than those with non-ortho substitutions.

---

* It is important to note that, although the individual mixes were immune from isomeric coelutions, the problem of coeluting fragment ions persisted, thus significantly limiting the number of PCBs that could be comprehensively studied.

† PC3 ~15% and PC4 ~10%; all others < 10%.

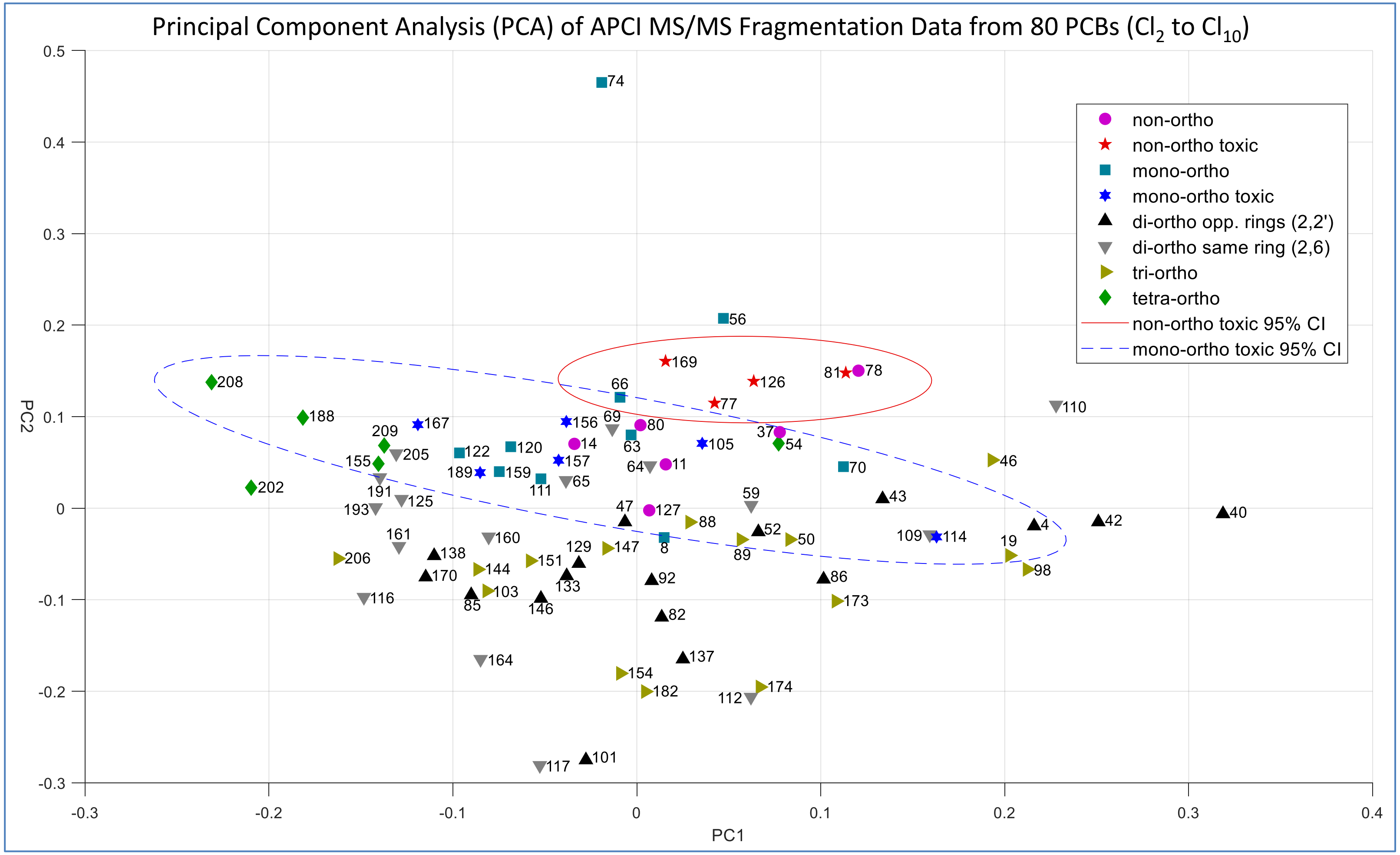

Figure 4.38 Chart showing the principal component analysis (PCA) of APCI fragmentation data from 80 di- to deca-chlorinated biphenyls with the 95% confidence interval ellipses for all (n = 4, solid red line) non-ortho and a subset (n = 6*, dashed blue line) mono-ortho WHO toxic PCBs.

* Of the 8 mono-ortho toxic congeners, PCB-118 and PCB-123 were excluded due to coeluting interferences from PCB-132 and PCB-131 respectively.

## 4.4 Conclusions

The data shown in this chapter have illustrated the inherent issues in PCB analysis due to fragmentation from co-eluting, higher-chlorinated congeners, particularly in the context of the EPA-1668C method. These are multiple concerns: artefact peaks can be formed that mimic true congeners that are not actually present in a sample but that share their retention time and have the correct isotope ratio (i.e. false positives); such artefacts can also increase the measured areas and hence reported concentrations of affected congeners (i.e. incorrect positives); conversely, and particularly for losses of 2Cl, they can lead to an out-of-ratio assessment of otherwise valid peaks (i.e. false negatives). It should also be realised that sample matrix effects can lead to differential retention time shifts such that peaks that are normally immune from fragmentation problems can then be affected and *vice-versa*.

Although any of the above could distort the congener profile and hence diminish the data quality in any forensic/pattern matching work, for the toxic PCBs these effects are clearly more significant as their measured concentrations are often at the core of regulatory reporting. A simple error correction scheme, as had been proposed in Method 680, is insufficient to address the various fragmentation mechanisms.

A calibration process is therefore suggested as the best option: here a series of mixes – similar to those used in these studies – would be analysed such that unequivocal responses from fragment ion formation can be determined and then used to identify, and in some cases correct, potential problems during sample data processing. Although this would still have limitations due to uncertainty with coeluting isomers and would not address differential retention time shifts (though the latter would invariably require further sample clean-up as the chromatography would inevitably be impaired in such cases) it could serve as a useful aid to analysis and one that could be semi-automated.

Given that MS/MS based analyses are likely to become more prominent in the future – as instrument manufacturers move away from magnetic sector HRMS – these findings could provide useful supplemental information to the current methods.

These data have also shown that varying collision energy in a GC-MS/MS instrument is a useful means of controlling the response of certain isomers. In the real-world analysis of compounds such as PCBs – particularly in environmental samples where concentrations can range over several orders of magnitude – the ability to attenuate non-toxic isomers could be advantageous in cases where their very high levels can inhibit accurate measurements of their (often low-level) toxic counterparts when adequate chromatographic separation cannot be achieved. The use of isotope dilution is also helpful here since the calculated concentration of any toxic congener should be invariant with collision energy as both its response, and that of its $^{13}$C-labelled standard, are equally affected by any fragmentation.

In the study of mass spectra obtained from PCBs at various collision energies, it was observed that in addition to the expected changes of specific (e.g. loss of Cl) fragment ions' intensities, there were also changes to the relative intensities of ions within the loss of Cl cluster (e.g. loss of Cl vs. loss of HCl). These variances in fragmentation were charted and submitted to PCA: although grouping of the non-ortho toxic PCB congeners can be recognised, the cluster is insufficiently separated from other non-toxic congeners for these data to be a definitive indicator of toxicity. The proximity of certain PCBs with suggested AhR related activity, such as PCB-11 (3,3'-DiCB) (Roy *et al.*, 2019) or PCB-37 (3,3',4-TrCB)[*] to the toxic group could therefore simply be due to their non-ortho structures rather than any implied toxicity.

Given the abrupt changes seen in the relative intensities of certain ions in the (nominal) loss of Cl cluster of some PCBs at certain collision energies, these data would benefit from additional points being acquired at intermediate energies. This should also be extended to all congeners using more extensive PCB mixes where coeluting fragments do not occur. The latter would also benefit a more detailed study of the accurate mass fragment data where the formation of molecular ion-like species within the loss of Cl fragment cluster, attributed to possible Cl/H exchange or $H_2$ adduct formation, was observed. Such experiments were beyond the scope of the current study but would form the basis of future work.

---

[*] PCB-37 is currently assessed as a non-toxic congener, but has been suggested for possible future inclusion in the WHO toxic list (Van den Berg *et al.*, 2006).

# Chapter 5

# Ion Mobility Separation – Mass Spectrometry of all 209 PCBs

## 5.1 Introduction

As described in the preceding chapters, PCBs have been extensively studied over many years using GC, GC-(HR)MS and GC-MS/MS based analyses for their identification and quantification; this research extends the scope of analysis by using ion mobility separation together with mass spectrometry (IMS-MS). Although conventional drift tube ion mobility spectrometry (DTIMS) has long existed as a standalone technique to separate molecules based on their size and shape, its combination with mass spectrometry in a practical and commercially available instrument is far more recent (May and McLean, 2015), notably the Synapt-HDMS[*] (Waters, Wilmslow, UK) system – based on travelling wave ion mobility spectrometry (TWIMS) technology – launched in 2006 (Giles *et al.*, 2004; Pringle *et al.*, 2007).

The focus of IMS-MS work to date has mostly concerned peptides, proteins and other biomolecules (Lanucara *et al.*, 2014), such analytes being commensurate with the electrospray ionisation sources [and their associated liquid-chromatography (LC) sample introduction systems] or matrix-assisted laser desorption/ionisation (Djidja *et al.*, 2009) that were intrinsic to the mass spectrometers from which the IMS-MS systems were derived. Initial work to open this technique to GC-based sample analyses – as required for the compounds of interest in this thesis – was seen with the development of a prototype Synapt instrument fitted with an EI source.

---

[*] "High-definition" mass spectrometry – a marketing, rather than formal MS, term.

Data from this instrument was shown in the 2011 ASMS poster presentation from Jones *et al*, "*Analysis of halogenated aromatic compounds by electron impact ionisation and ion mobility separation on a GC-EI-Q-IMS-ToF*", where, in conjunction with high-resolution TOF mass analysis, the arrival time distributions[*] (ATDs) from a series of 2,3,7,8-substituted PCDD/Fs were observed (Jones, Richardson and Green, 2011). Although this instrument variant never progressed to commercial production, concurrent advances in atmospheric pressure sources nevertheless enabled GC sample introduction on a Synapt Q-IMS-TOF[†].

There is currently very limited published data on IMS-MS of PCBs, and these only consider a small number (n = 26) of congeners (Zheng *et al.*, 2018) or their metabolites, hydroxy-PCBs (n = 9) (Adams *et al.*, 2018). Given the ability of IMS-MS to determine structural information in terms of an ion's rotationally averaged collisional cross section (CCS) area, the aim of this chapter is to complement the previous (fragmentation) study by investigating the relationship between these data and that of the modelled structures of all 209 PCBs. Since certain toxic effects, such as those associated with AhR binding, are principally a function of a PCB's structure (Safe *et al.*, 1985), this implicitly asks the question as to whether any correlation exists between the congeners' toxicities – whether known or suggested – and their measured CCS values.

---

[*] The term "arrival time distribution" (ATD) has recently been recommend for use in place of "drift time" (DT) to reflect the fact that the measured data includes time spent outside the actual drift region and other systematic delays (Gabelica *et al.*, 2019). This will be used where practicable, but the older term will persist for some existing graphs and software, e.g. for axis labelling, and this should be considered as being synonymous with ATD.

[†] With the additional benefits of avoiding the vacuum system and electronics requirements of an EI source and allowing the ready interchange between LC and GC inlets.

## 5.2 Ion mobility theory – a brief overview

In conventional DTIMS, the velocity of an ion through a gas filled cell is a function of the axial electric field intensity and the mobility coefficient, as shown in equation (5.1) (Revercomb and Mason, 1975).

$$v_d = KE \tag{5.1}$$

Where $v_d$ is the velocity through the drift gas, K is the ion mobility coefficient and E is the electric field intensity.

Hence, as shown in equation (5.2), the ion's mobility can be determined from the measured drift time (DT) through the cell.

$$K = \frac{l}{t_d E} \tag{5.2}$$

Where K is the ion mobility coefficient, l is the length of the drift cell, $t_d$ is the measured time to traverse the cell and E is the electric field intensity.

An analyte ion's CCS may then be determined from its mass and charge, the mass, number density and temperature of the buffer gas, Boltzmann's constant and the above mobility coefficient as expressed by the Mason-Schamp equation (5.3) together with that for the reduced mass (5.4) (Mason and MacDaniel, 1988).

$$\Omega = \frac{3ze}{16N}\left(\frac{2\pi)}{\mu k_B T}\right)^{0.5}\frac{1}{K} \tag{5.3}$$

Where Ω is the CCS, z is the number of charges, e is the elementary charge, μ is the reduced mass of the analyte ion and buffer (drift) gas masses [as shown in equation (5.4)], N and T are the number density and temperature of the buffer gas, $k_B$ is the Boltzmann constant and K is the mobility coefficient.

$$\mu = \frac{mM}{m + M} \tag{5.4}$$

Where μ is the reduced mass of the analyte ion mass (m) and buffer gas mass (M).

As noted, the above formulae apply to conventional ion mobility using a linear drift geometry and operating in the low (≤ 2 Td[*]) field region. This, however, is not the case for the analyses performed herein using the TWIMS-based Synapt G2-S instrument where, as implied by the travelling wave design, the electric field is not static and operates at much greater (> 100 Td) field strengths than linear mobility cells (Gabelica and Marklund, 2018): the net velocity through the gas cell is therefore no longer linear but approximates to quadratic function requiring empirical calibration to determine CCS (Shvartsburg and Smith, 2008).

Smith *et al* showed a reduced version of the CCS equation by replacing the non-mass dependent variables[†] with a constant, A, and including the power term, B, to account for the non-linear characteristics of the TWIMS device (Smith *et al.*, 2009). An offset parameter, C, has been added here to allow for the ion mobility wave delay as shown in equation (5.5).

$$\Omega = ze\left(\frac{m+M}{mM}\right)^{0.5} A\, {t_a}^{B} + C \tag{5.5}$$

Where A represents the combined non-mass dependent variables, $t_a$ is the ion arrival time, the power term, B, accounts for the non-linearity found in TWIMS and C allows for time-delay correction. Other parameters are as shown in (5.3) above.

The above parameters can then be determined from a calibration process where ion mobility arrival time distribution (ATD) data are obtained from the analyses of standard compounds of known CCS – and ideally with reasonably similar structures and mass range – using the same instrument and conditions as the analytes in question.

---

[*] Townsends – the reduced electric field corresponding to E/N; 1 Td = $10^{-21}$ V.m$^2$.

[†] If all ions are of the same charge state, e.g. singly charged as in this work, then *ze* could also be incorporated into the *A* coefficient.

## 5.3 Materials and methods

### 5.3.1 GC-Q/IMS/TOF

Travelling-wave ion-mobility mass spectrometry was performed using a Synapt G2-S hybrid Q-IMS-TOF (Waters, Wilmslow, UK) coupled to a 7890A GC fitted with a 7693A auto-injector (Agilent, Santa Clara, CA, USA). Atmospheric pressure chemical ionisation (APCI) was used in the positive ion mode. To meet the chromatographic requirements for PCB analysis, as specified in EPA-1668C, a 30 m x 0.25 mm x 0.25 µm SPB-Octyl capillary column (Supelco, Bellefonte, PA, USA) was installed in the GC with the injector operating in splitless mode. Helium was used as the carrier gas at a constant flow of 1.4 ml/min. The mobility cell used nitrogen as the buffer gas at a pressure of 3.29 mbar; the travelling wave velocity was 300 m/s. (A complete list of the relevant GC and MS parameters is provided in Appendix D.2)

To correctly identify each PCB congener, a set of 5 separate mixes (Ultra Scientific, North Kingstown, RI, USA) was used, each containing a subset of the 209 PCBs such that no coeluting isomers – at the same level of chlorination – were present in any individual analysis. For the analysis of certain fully ($^{13}C_{12}$) labelled PCBs, a mid-point calibration standard based on the EPA-1668C method was used (Wellington Laboratories Inc., Guelph, ON, Canada). A complete list of the PCB congeners used for these analyses is provided in Appendix C.3.

For CCS calibration, an 8-component mix (Waters, Wilmslow, UK) comprising: 1,2-dichlorobenzene, 2,3,7,8-TCDD, anthracene, benzo(*ghi*)perylene, endosulphan, hexachlorobenzene, octafluoronaphthalene and phenanthrene was used.

### 5.3.2 Data processing

As shown in the flow chart in Figure 5.1, TWIMS data were acquired using MassLynx (Waters, Wilmslow, UK), and this software was also used for the initial data checks, e.g. to verify chromatography, peak intensities, etc. Following this, there are 2 possible paths, the choice of which depends on the degree of detail required:

- Path 1 provides rapid processing of sets of *m/z* – e.g. all PCB congeners can be processed in a single pass – however there is limited control of the peak detection and review process.
- Path 2 provides a much greater level of control – e.g. allowing reintegration of the ion mobility ATD data – it is however limited to processing individual congeners and can thus be a more time-consuming process.

Both paths require the use of DriftScope (Waters, Wilmslow, UK) for initial processing of the raw IMS-MS data – although this software has some interactive processing capabilities, it cannot, for example, simultaneously display peaks from the multiple *m/z* as would be required for the comparison of PCB data – and therefore the data is exported from DriftScope into the format required for the selected path for subsequent processing.

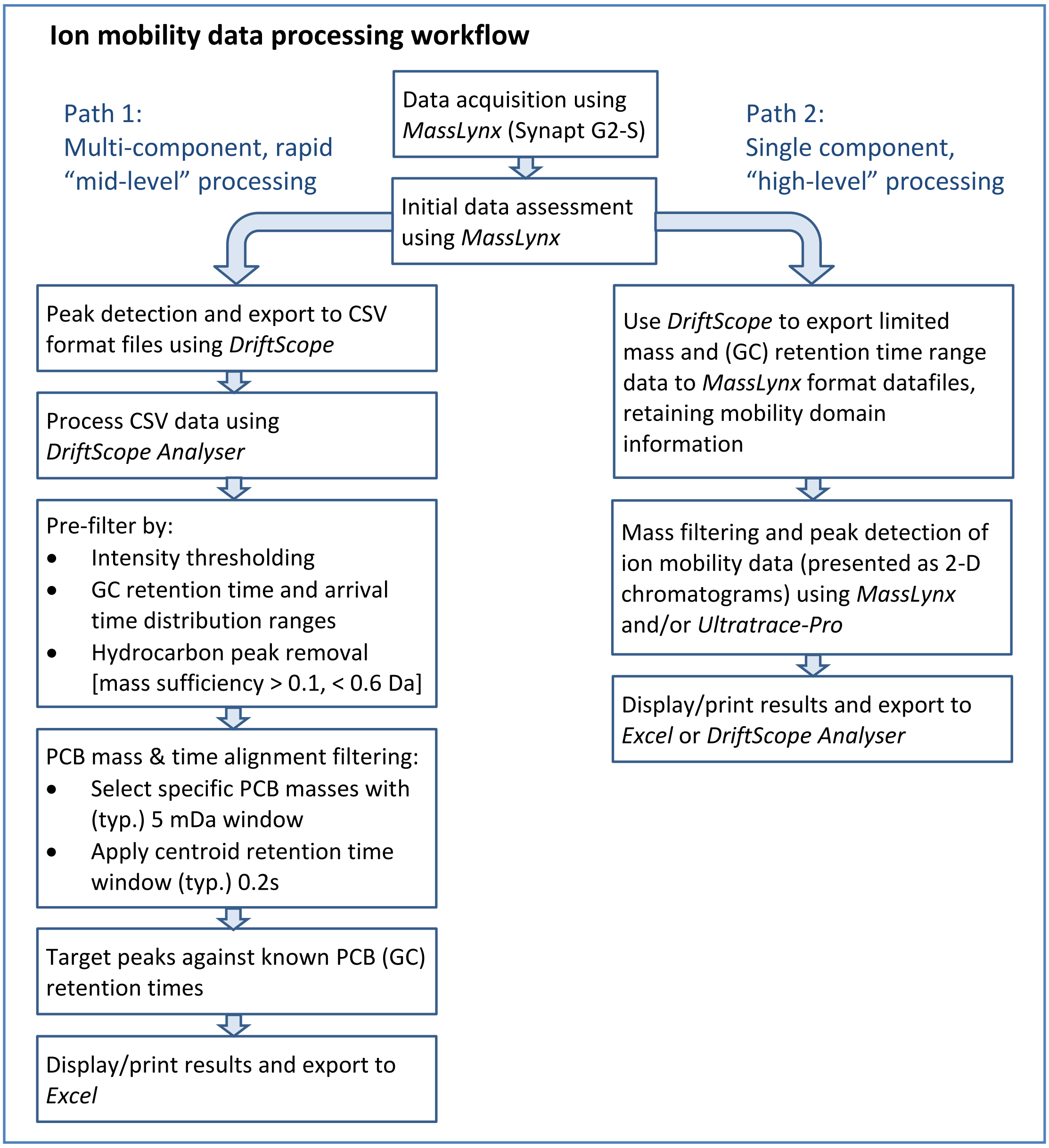

Figure 5.1 Ion mobility data processing flow chart showing the 2 processing paths used for these data.

For the first path, a peak list created by DriftScope is exported as a comma separated values (CSV) file. Due to the very large size of these files – more than 200,000 peaks in each of the datafiles considered here – it was decided to create a dedicated *ab initio* program, "*DriftScope Analyser*" to process these files with the relevant tools for PCB (and similar) content.

After reading the CSV file, DriftScope Analyser reduces the imported data using intensity, retention time (RT), ATD and mass filters – the latter to remove hydrocarbon and other interferences that are readily separable from the halogenated compounds of interest due to their mass sufficiency.

The resulting data are then subject to mass selection based on a pre-defined list with up to 8 masses specified for each homologue group and an appropriate mass window. Optionally, a centroiding time window can be applied to ignore peaks that are not coincident (in RT) with those from other *m/z* of the compound's molecular ion cluster. Finally, the peaks can be identified by matching their actual and expected RTs. The results are displayed, as shown by the example in the screenshot in Figure 5.2, as points on a 2-D (ATD vs. RT) graph with the point size indicating peak intensity.

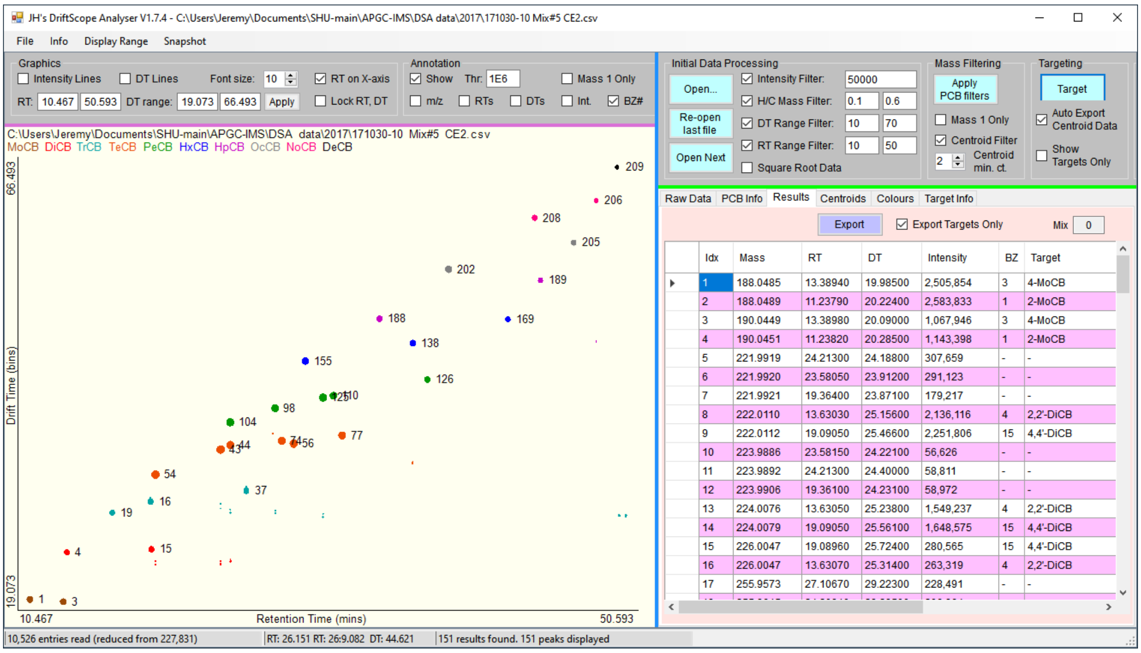

JH's DriftScope Analyser V1.7.4 - C:\Users\Jeremy\Documents\SHU-main\APGC-IMS\DSA data\2017\171030-10 Mix#5 CE2.csv

Graphics
☐ Intensity Lines ☐ DT Lines Font size: 10 ☑ RT on X-axis
RT: 10.467 50.593 DT range: 19.073 66.493 ☐ Lock RT, DT

Annotation
☑ Show Thr: 1E6 ☐ Mass 1 Only
☐ m/z ☐ RTs ☐ DTs ☐ Int. ☑ BZ#

Initial Data Processing
☑ Intensity Filter: 50000
☑ H/C Mass Filter: 0.1 0.6
☑ DT Range Filter: 10 70
☑ RT Range Filter: 10 50
☐ Square Root Data

Mass Filtering
☐ Mass 1 Only
☑ Centroid Filter
2 Centroid min. ct.

Targeting
☑ Auto Export Centroid Data
☐ Show Targets Only

☑ Export Targets Only Mix 0

| Idx | Mass | RT | DT | Intensity | BZ | Target |
|---|---|---|---|---|---|---|
| 1 | 188.0485 | 13.38940 | 19.98500 | 2,505,854 | 3 | 4-MoCB |
| 2 | 188.0489 | 11.23790 | 20.22400 | 2,583,833 | 1 | 2-MoCB |
| 3 | 190.0449 | 13.38980 | 20.09000 | 1,067,946 | 3 | 4-MoCB |
| 4 | 190.0451 | 11.23820 | 20.28500 | 1,143,398 | 1 | 2-MoCB |
| 5 | 221.9919 | 24.21300 | 24.18800 | 307,659 | - | - |
| 6 | 221.9920 | 23.58050 | 23.91200 | 291,123 | - | - |
| 7 | 221.9921 | 19.36400 | 23.87100 | 179,217 | - | - |
| 8 | 222.0110 | 13.63030 | 25.15600 | 2,136,116 | 4 | 2,2'-DiCB |
| 9 | 222.0112 | 19.09050 | 25.46600 | 2,251,806 | 15 | 4,4'-DiCB |
| 10 | 223.9886 | 23.58150 | 24.22100 | 56,626 | - | - |
| 11 | 223.9892 | 24.21300 | 24.40000 | 58,811 | - | - |
| 12 | 223.9906 | 19.36100 | 24.23100 | 58,972 | - | - |
| 13 | 224.0076 | 13.63050 | 25.23800 | 1,549,237 | 4 | 2,2'-DiCB |
| 14 | 224.0079 | 19.09050 | 25.56100 | 1,648,575 | 15 | 4,4'-DiCB |
| 15 | 226.0047 | 19.08960 | 25.72400 | 280,565 | 15 | 4,4'-DiCB |
| 16 | 226.0047 | 13.63070 | 25.31400 | 263,319 | 4 | 2,2'-DiCB |
| 17 | 255.9573 | 27.10670 | 29.22300 | 228,491 | - | - |

10,526 entries read (reduced from 227,831) | RT: 26.151 RT: 26:9.082 DT: 44.621 | 151 results found. 151 peaks displayed

Figure 5.2 Screenshot showing an example of the DriftScope Analyser program in operation.

For the second path, DriftScope is used to extract a datafile's ion mobility content from specified RT and *m/z* ranges[*], and to export this information to a new datafile in MassLynx format. The resulting files allow mass chromatograms to be created where the x-axis now represents the ATD (the y-axis still shows intensity); since the original RT data has been lost, the RT range used at the DriftScope export stage is therefore critical and is usually limited to that required to encompass a single congener.

---

[*] Optionally, ATD ranges may also be defined.

This is shown by the example in Figure 5.3 where the mobility data was extracted from a PCB sample mix from RT 37.7 to 38.0 and the ATDs for the M+0 to M+3 ions of PCB-126 displayed using the UltraTrace-Pro (SGS, Wilmington, NC) software. Although the ion mobility resolution is very low (~30, Ω/ΔΩ at FWHM), in the absence of mass interferences – due to the high resolution of the TOF analyser – the ion mobility centroids can be determined with sufficient precision to characterise the variations between isotopologue peaks.

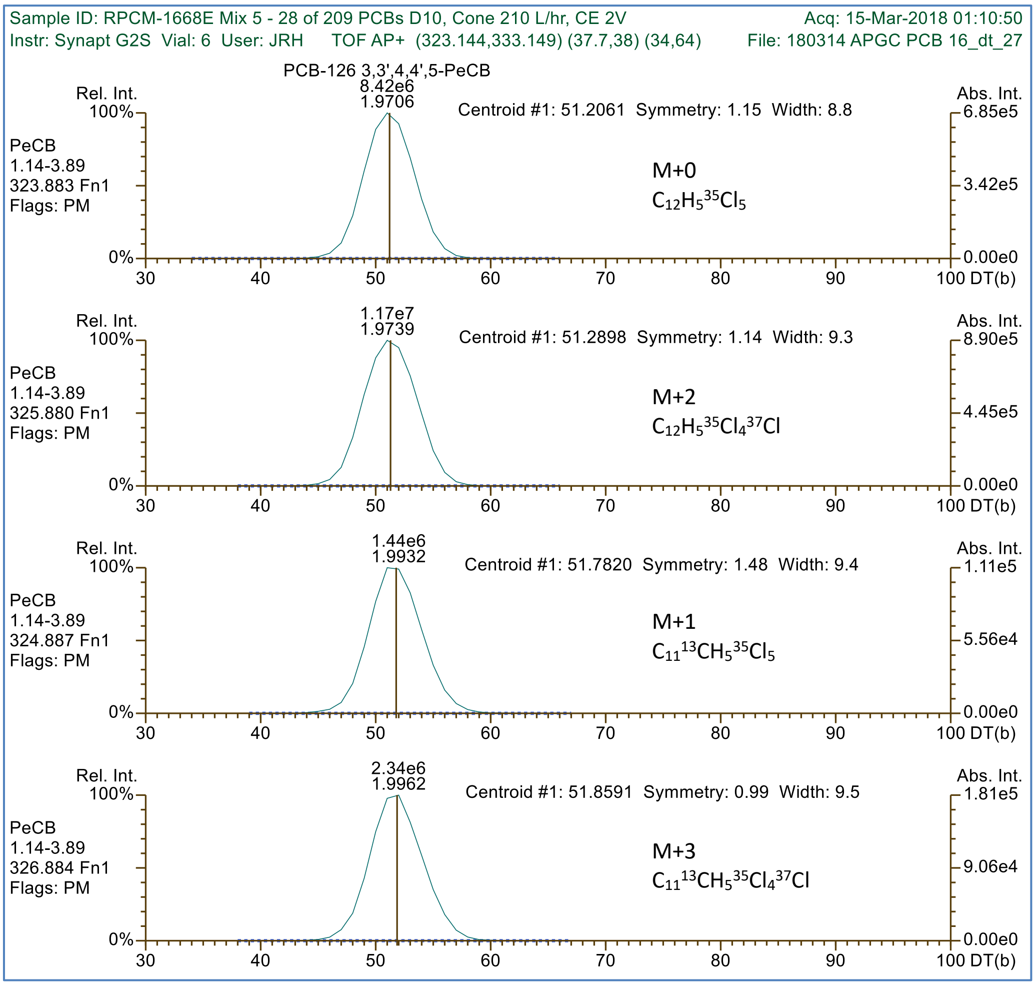

Figure 5.3 Example of ion mobility arrival time distributions (ATDs) for the M+0, M+2 and M+1, M+3 ions of PCB-126 (3,3',4,4',5-PeCB).
The peaks are annotated with their areas and arrival time distributions (ms); the x-axis and associated centroid values are based on the raw data bin numbers.

## 5.4 Results and discussion

### 5.4.1 Arrival time distribution variation with PCB chlorination level and structure

A chart of the ion mobility arrival time distribution (ATD) vs. GC retention time (RT) for all 209 PCBs obtained from the combined analyses of the 5 separate PCB mixes is shown in Figure 5.4. The ATDs show an increasing trend following the level of chlorination, though as with the RT data, there are several overlaps. In addition, the data exhibit distinct sub-groups according to the number of ortho substituted Cl atoms; this is particularly well-defined for the subset of the 46 PeCBs, as shown by the expanded detail in Figure 5.5.

Furthermore, the 12 PCB congeners that are known to be toxic – based on current WHO assessments – also appear to form a sub-group within the data as indicated by the points annotated in red (Figure 5.4). This is unsurprising given that structure is a key parameter to one of the accepted mechanisms of toxicity based on AhR binding. However, this is clearly not an exclusive metric since several other, nominally non-toxic congeners, such as PCB-106 and 122 (Figure 5.5) also fall within this grouping. There is nevertheless the possibility that these are potentially toxic and that the current list of toxic PCBs is incomplete: e.g. the trichlorinated PCB-37 (3,4,4’-TrCB) (annotated in purple) has been suggested by the WHO for possible future inclusion (Van den Berg *et al.*, 2006).

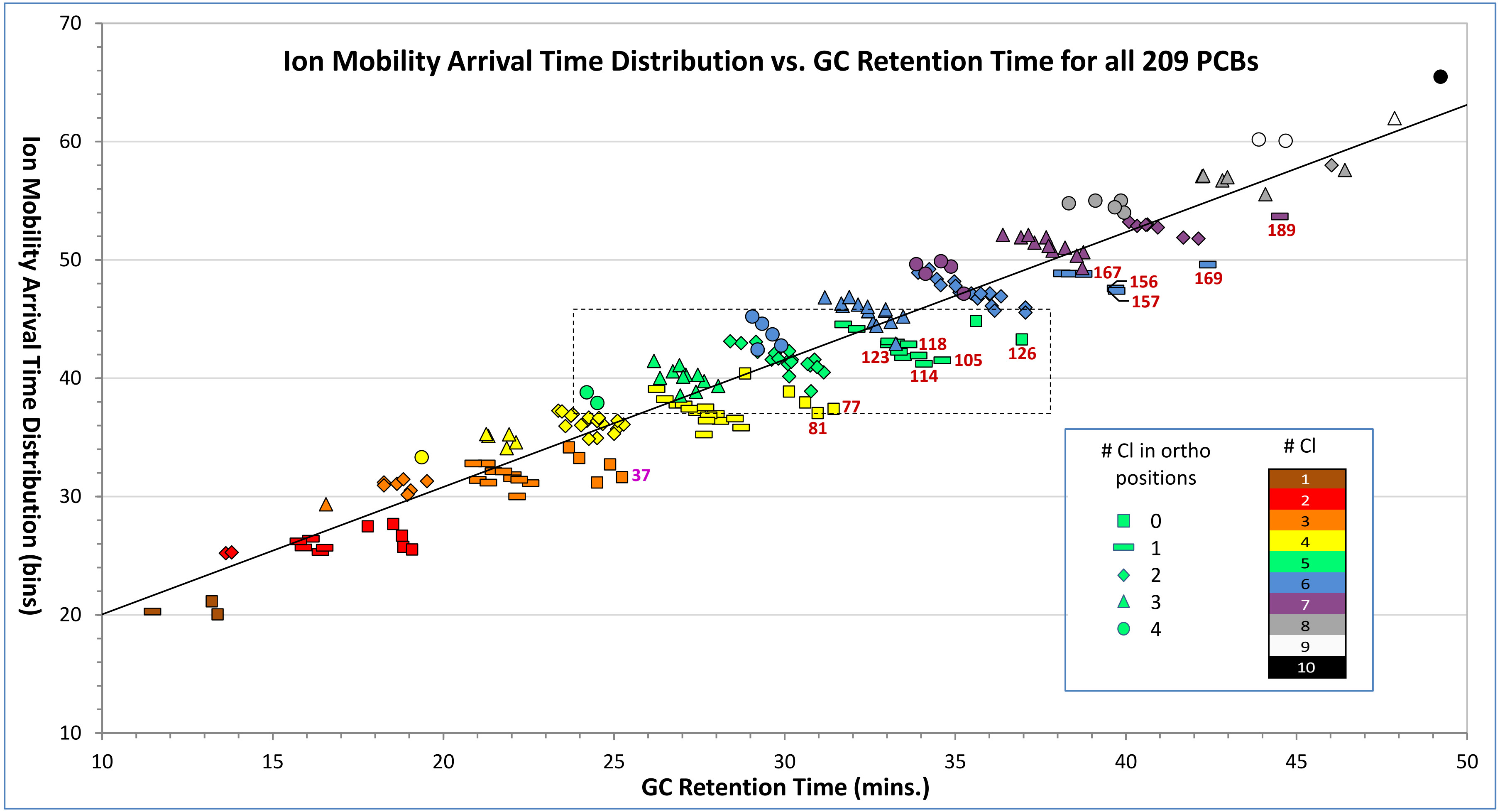

Figure 5.4 Synapt G2-S (GC-Q-IMS-TOF) ion mobility arrival time distribution vs. GC retention time for all 209 PCBs. Data acquired using the experimental details described in Appendix D.2. The data point colour-coding indicates the number of Cl atoms and shapes denote the number of Cl ortho substitutions as shown by the key. The PCB numbers for the WHO toxic compounds are annotated in red, and the tentative toxic PCB-37 in purple. The region outlined (dashed rectangle) is shown in detail for the PeCBs in Figure 5.5.

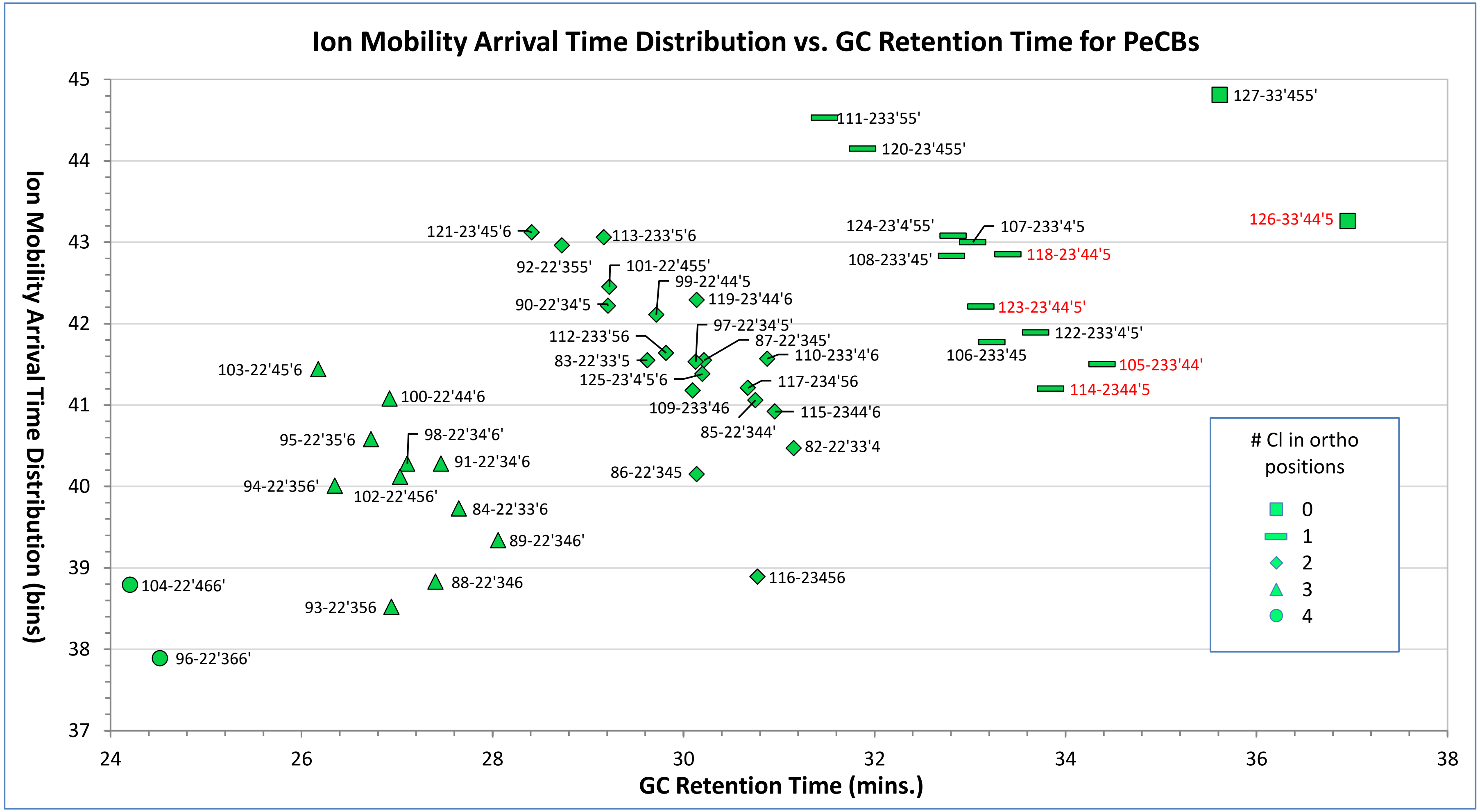

Figure 5.5 Synapt G2-S (GC-Q-IMS-TOF) ion mobility arrival (drift) time distribution vs. GC retention time for all 46 PeCBs. Data acquired using the experimental details described in Appendix D.2. The data points are annotated with the PCB number and structure (with the toxic congeners shown in red), and the shapes indicate the number of Cl ortho substituents as shown by the key.

### 5.4.2 Comparisons of modelled, experimental and published CCS data

Two, freely available, modelling programs were used to estimate the CCS values for all 209 PCB congeners to allow comparisons with those derived from the acquired ion mobility data and other published data:

- "*Impact*" (Univ. of Oxford) – using the projection approximation (PA) and trajectory (TJ) methods (Marklund *et al.*, 2015)
- "*CrossArea*" (Univ. of Leeds) used the PA method (Smith *et al.*, 2009).

Both programs required input files created in the Protein Database (PDB) format*; as all PCBs had been modelled and their optimum conformations determined for the previous fragmentation study [using the "Orca" program (Neese, 2012) and associated methods (as described in section 4.2.5)], these data were converted† to that format.

A summary‡ of the CCS data is shown in Table 5.1 for the first and last eluting PCBs at each level of chlorination, all toxic congeners (shown in bold type) and a subset of PCBs (n = 26) for which published data was available (Zheng *et al.*, 2018). The results columns show CCS data from the 3 modelled approaches, the experimental data acquired herein and the published data. Also shown are the deviations between the experimental and published data, and between experimental and TJ data.

The CCS calibration for the acquired Synapt mobility data was initially based on the 8-component mix described in section 5.3.1; this yielded RMS errors between the acquired and modelled data of 5.67%, 3.75% and 5.61% for the 3 methods (*Impact* PA and TJ, and *CrossArea* PA respectively) for all 209 congeners, and 3.83% between the acquired and published data from Zheng *et al*.

The latter was then used to recalibrate the acquired CCS data; this resulted in the respective errors being revised to 8.81%, 1.93% and 8.67% for the 3 methods, and 0.56% for the published data. Clearly the reduction in the latter value is not unexpected given

---

* This being indicative of their intended application rather than the small molecules considered here; nevertheless, the data shown suggest that their usage here is also appropriate.

† An *ab initio* program, "*PDBprocessor*", was developed to convert these files into PDB format and automatically submit them to the CCS modelling programs.

‡ The complete table of modelled and experimental data for all 209 PCBs is shown in Appendix B.5.

that its data was used as the basis for the calibration. With either calibration the TJ modelled CCS data showed lower RMS errors than the PA methods but were lowest with the revised calibration.

| **PCB** | ***Impact* PA (Å$^2$)** | ***Impact* TJ (Å$^2$)** | ***Cross-Area* PA (Å$^2$)** | **Zheng *et al.* (Å$^2$)** | **Synapt expt. data (Å$^2$)** | **Dev’n expt.-Zheng** | **Dev’n expt.-TJ** |
|---|---|---|---|---|---|---|---|
| PCB-1 2-MoCB | 117.9 | 126.9 | 116.8 | n/a | 134.9 | - | 6.3% |
| PCB-3 4-MoCB | 121.6 | 131.0 | 122.4 | n/a | 134.5 | - | 2.6% |
| PCB-4 2,2’-DiCB | 123.7 | 133.4 | 122.2 | n/a | 141.9 | - | 6.3% |
| PCB-15 4,4’-DiCB | 131.7 | 142.5 | 131.1 | n/a | 142.3 | - | -0.1% |
| PCB-16 2,2’,3-TrCB | 131.0 | 141.8 | 131.0 | n/a | 148.8 | - | 5.0% |
| PCB-28 2,4,4’-TrCB | 138.1 | 149.8 | 137.3 | 149.7 | 150.0 | 0.2% | 0.1% |
| PCB-29 2,4,5-TrCB | 135.7 | 147.0 | 133.6 | 150.7 | 149.6 | -0.7% | 1.7% |
| PCB-30 2,4,6-TrCB | 134.2 | 145.4 | 134.7 | 150.1 | 149.2 | -0.6% | 2.6% |
| PCB-39 3,4’,5-TrCB | 141.2 | 153.4 | 143.8 | n/a | 152.3 | - | -0.7% |
| PCB-40 2,2’,3,3’-TeCB | 138.5 | 150.3 | 139.0 | n/a | 155.1 | - | 3.2% |
| PCB-52 2,2’,5,5’-TeCB | 142.5 | 154.9 | 143.0 | 156.7 | 157.2 | 0.3% | 1.5% |
| PCB-70 2,3’,4’,5-TeCB | 144.5 | 157.1 | 148.4 | 155.6 | 157.5 | 1.2% | 0.2% |
| **PCB-77 3,3’,4,4’-TeCB** | **146.6** | **159.6** | **143.3** | **156.8** | **157.2** | **0.3%** | **-1.5%** |
| **PCB-81 3,4,4’,5-TeCB** | **146.3** | **159.2** | **146.8** | **158.6** | **156.7** | **-1.2%** | **-1.6%** |
| PCB-82 2,2’,3,3’,4-PeCB | 146.1 | 159.0 | 147.4 | n/a | 160.7 | - | 1.1% |
| PCB-101 2,2’,4,5,5’-PeCB | 149.9 | 163.3 | 149.2 | 162.6 | 163.0 | 0.3% | -0.2% |
| PCB-103 2,2’,4,5’,6-PeCB | 147.5 | 160.6 | 149.2 | 160.7 | 161.9 | 0.7% | 0.8% |
| **PCB-105 2,3,3’,4,4’-PeCB** | **150.5** | **163.9** | **154.2** | **161.6** | **161.8** | **0.1%** | **-1.3%** |
| **PCB-114 2,3,4,4’,5-PeCB** | **150.6** | **164.2** | **151.6** | **162.1** | **161.4** | **-0.4%** | **-1.7%** |
| **PCB-118 2,3’,4,4’,5-PeCB** | **152.5** | **166.3** | **153.5** | **n/a** | **163.4** | **-** | **-1.7%** |
| **PCB-123 2,3',4,4',5'-PeCB** | **152.2** | **165.9** | **154.6** | **n/a** | **163.0** | **-** | **-1.8%** |
| **PCB-126 3,3’,4,4’,5-PeCB** | **153.5** | **167.4** | **148.0** | **164.4** | **163.8** | **-0.4%** | **-2.2%** |
| PCB-127 3,3’,4,5,5’-PeCB | 155.4 | 169.6 | 152.7 | n/a | 165.6 | - | -2.4% |

Table 5.1 CCS values obtained from the “Impact” Projection Approximation (PA) and Trajectory (TJ) methods, the “CrossArea” PA method, published data (Zheng *et al.*, 2018) and from the Synapt experimental data.
*(Table continues overleaf)*

| **PCB** | ***Impact* PA (Å$^{2}$)** | ***Impact* TJ (Å$^{2}$)** | ***Cross-Area* PA (Å$^{2}$)** | **Zheng *et al.* (Å$^{2}$)** | **Synapt expt. data (Å$^{2}$)** | **Dev'n expt.-Zheng** | **Dev'n expt.-TJ** |
|---|---|---|---|---|---|---|---|
| PCB-128 2,2',3,3',4,4'-HxCB | 153.2 | 167.0 | 151.0 | n/a | 166.7 | - | -0.2% |
| PCB-138 2,2',3,4,4',5'-HxCB | 155.4 | 169.6 | 157.1 | 168.0 | 168.0 | 0.0% | -0.9% |
| **PCB-156 2,3,3',4,4',5-HxCB** | **157.1** | **171.6** | **161.2** | **168.2** | **168.5** | **0.1%** | **-1.8%** |
| **PCB-157 2,3,3',4,4',5'-HxCB** | **156.9** | **171.4** | **156.9** | **n/a** | **168.3** | **-** | **-1.8%** |
| **PCB-167 2,3',4,4',5,5'-HxCB** | **156.8** | **171.3** | **154.9** | **167.8** | **169.9** | **1.2%** | **-0.8%** |
| **PCB-169 3,3',4,4',5,5'-HxCB** | **161.3** | **176.4** | **164.3** | **170.0** | **170.7** | **0.4%** | **-3.2%** |
| PCB-170 2,2',3,3',4,4',5-HpCB | 159.8 | 174.6 | 161.2 | n/a | 173.1 | - | -0.9% |
| **PCB-189 233'44'55'-HpCB** | **163.8** | **179.3** | **163.4** | **173.9** | **175.0** | **0.6%** | **-2.4%** |
| PCB-190 2,3,3',4,4',5,6-HpCB | 160.2 | 175.1 | 159.0 | 173.3 | 172.9 | -0.2% | -1.2% |
| PCB-193 2,3,3',4',5,5',6-HpCB | 161.9 | 177.1 | 159.1 | 173.9 | 174.3 | 0.2% | -1.6% |
| PCB-194 2,2',3,3',4,4',5,5'-OcCB | 166.2 | 182.0 | 167.4 | 180.3 | 179.3 | -0.6% | -1.5% |
| PCB-195 2,2',3,3',4,4',5,6-OcCB | 162.3 | 177.5 | 164.4 | 178.0 | 176.8 | -0.7% | -0.4% |
| PCB-202 2,2',3,3',5,5',6,6'-OcCB | 161.4 | 176.5 | 160.1 | 176.9 | 176.2 | -0.4% | -0.2% |
| PCB-205 2,3,3',4,4',5,5',6-OcCB | 163.9 | 179.4 | 165.7 | n/a | 178.9 | - | -0.3% |
| PCB-206 2,2',3,3',4,4',5,5',6-NoCB | 168.6 | 184.8 | 171.0 | 183.5 | 183.1 | -0.2% | -0.9% |
| PCB-207 2,2',3,3',4,4',5,6,6'-NoCB | 166.2 | 182.1 | 168.4 | 181.7 | 181.2 | -0.2% | -0.5% |
| PCB-208 2,2',3,3',4,5,5',6,6'-NoCB | 165.7 | 181.5 | 165.2 | 182.1 | 181.5 | -0.3% | 0.0% |
| PCB-209 DeCB | 170.3 | 186.7 | 168.2 | 185.9 | 186.3 | 0.2% | -0.2% |
| | | | | | **RMS Error** | **0.56%** | **1.93%$^{*}$** |

Table 5.1 (continued) CCS values obtained from the "Impact" Projection Approximation (PA) and Trajectory (TJ) methods, the "CrossArea" PA method, published data (Zheng *et al.*, 2018) and from the Synapt experimental data.
The deviations between experimental and both the published and TJ method modelled data are also shown. *The RMS error for the TJ data is from all 209 congeners (as shown in Table B.3 of Appendix B.5). The WHO toxic congeners are indicated by bold type.

### 5.4.3 Artefacts in the arrival time distributions of PCB isotopologues

During the above analyses, an unusual observation was made concerning the relative ATDs of different *m/z* (isotopologues) within the molecular ion cluster of many PCBs. Figure 5.6 shows an example from 8 late eluting HpCBs: the individual primary ions (M+0, M+2…) (blue) have progressively increasing ATDs, as expected given their increasing masses, and this is similarly the case for the secondary ions (M+1, M+3…) (red). However, as groups of ions, although sometimes intermixed, the secondary ions' ATDs were often significantly displaced – both positively and negatively – relative to those of the primary ions.

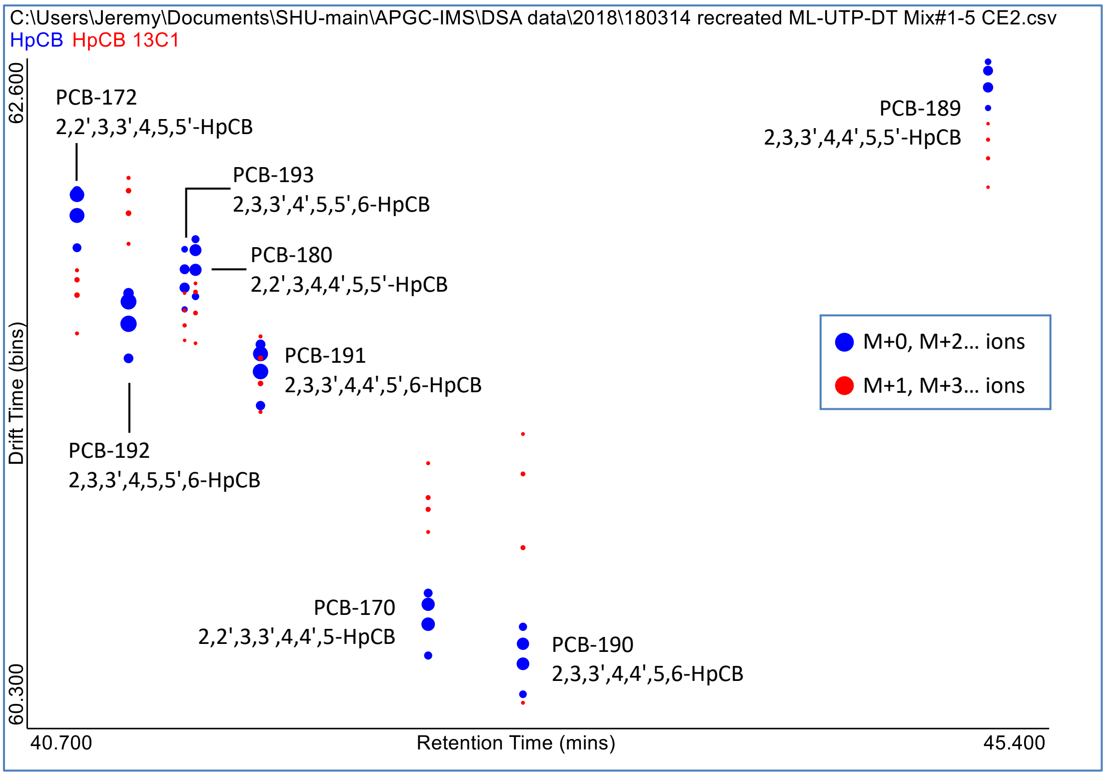

Figure 5.6 DriftScope Analyser plot of ion mobility ATD vs. RT for 8 late eluting HpCBs showing mixed positive, negative and overlapping ATDs of the groups of naturally occurring secondary ($^{13}$C) ions (red) relative to those of the primary ($^{12}$C) ions (blue).
For each HpCB, the primary and secondary ion group *m/z* (listed below) increase with ATD.
The marker sizes indicate the relative peak intensities.

| Primary ions (shown in blue) | Secondary ions (shown in red) |
|---|---|
| M+0, *m/z* 391.8054, $C_{12}H_3{}^{35}Cl_7$ | M+1, *m/z* 392.8088, $C_{11}{}^{13}CH_3{}^{35}Cl_7$ |
| M+2, *m/z* 393.8025, $C_{12}H_3{}^{35}Cl_6{}^{37}Cl$ | M+3, *m/z* 394.8059, $C_{11}{}^{13}CH_3{}^{35}Cl_6{}^{37}Cl$ |
| M+4, *m/z* 395.7996, $C_{12}H_3{}^{35}Cl_5{}^{37}Cl_2$ | M+5, *m/z* 396.8029, $C_{11}{}^{13}CH_3{}^{35}Cl_5{}^{37}Cl_2$ |
| M+6, *m/z* 397.7967, $C_{12}H_3{}^{35}Cl_4{}^{37}Cl_3$ | M+7, *m/z* 398.8000, $C_{11}{}^{13}CH_3{}^{35}Cl_4{}^{37}Cl_3$ |

E.g. the secondary ions of PCB-172 (2,2’,3,3’,4,5,5’-HpCB), 193 (2,3,3’,4’,5,5’,6-HpCB) and 189[*] (2,3,3’,4,4’,5,5’-HpCB) have ATDs that are negatively offset relative to the primary ions, with the M+7 ion (*m/z* 399) having a lower ATD than even the M+0 primary ion (*m/z* 392). Conversely, for PCB-192 (2,3,3’,4,5,5’,6-HpCB) and 170 (2,2’,3,3’,4,4’,5-HpCB), all secondary ions show a positive offset with the M+1 ion (*m/z* 393) having a higher ATD than the M+6 primary ion (*m/z* 398). In addition to the clearly separated ion groups, varying degrees of overlap are also seen, e.g. PCB-180 (2,2’,3,4,4’,5,5’-HpCB), 191 (2,3,3’,4,4’,5’,6-HpCB) and 190 (2,3,3’,4,4’,5,6-HpCB).

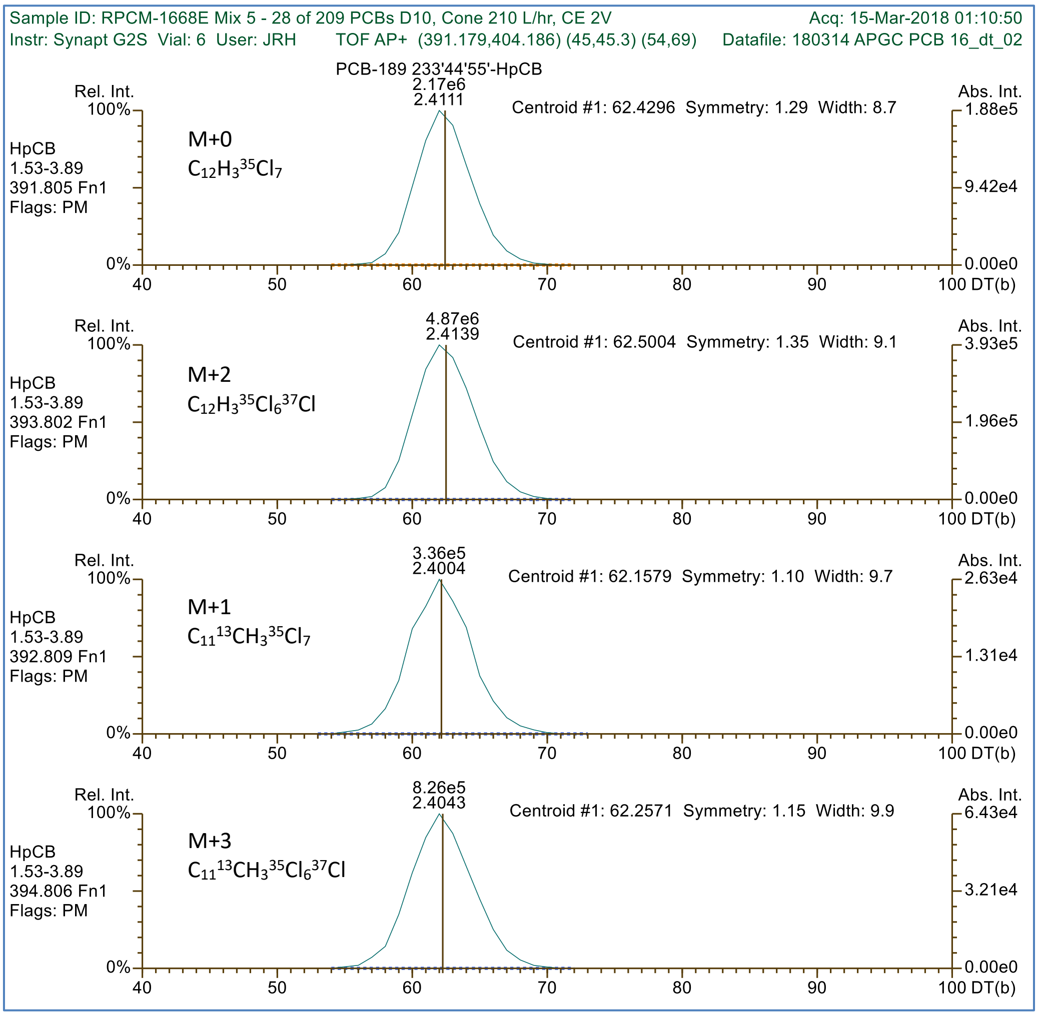

Figure 5.7 Ion mobility ATDs for the M+0, M+2 and M+1, M+3 ions of PCB-189 (2,3,3’,4,4’,5,5’-HpCB).
The peaks are annotated with their areas and arrival time distributions (ms); the x-axis and associated centroid values are based on the raw data bin numbers.

---

[*] The only WHO toxic PCB in this homologue group.

The corresponding raw ion mobility data for PCB-189 is shown in Figure 5.7; the detected peaks mirror the reported data above with lower ATDs for the M+1 and M+3 ions (upper 2 traces) relative to those of the M+0 and M+2 ions (lower 2 traces). It is important to note that the peak widths of the M+1 and M+3 ions are greater than for the M+0 and M+2 ions – this is also the case for the peaks of the M+5 and M+7 ions relative to the M+4 and M+6 ions (not shown).

The first 5 eluting HpCBs were then investigated – each having the common feature of Cl substitution in all 4 ortho positions (i.e. 2,2',6,6'): as shown by the data in Figure 5.8, all showed positive ATD offsets of the secondary ion groups; however, amongst these, PCB-186 (2,2',3,4,5,6,6'-HpCB) showed a much greater (weighted average) shift of ~4.6% compared to ~2.1% (average of the other 4).

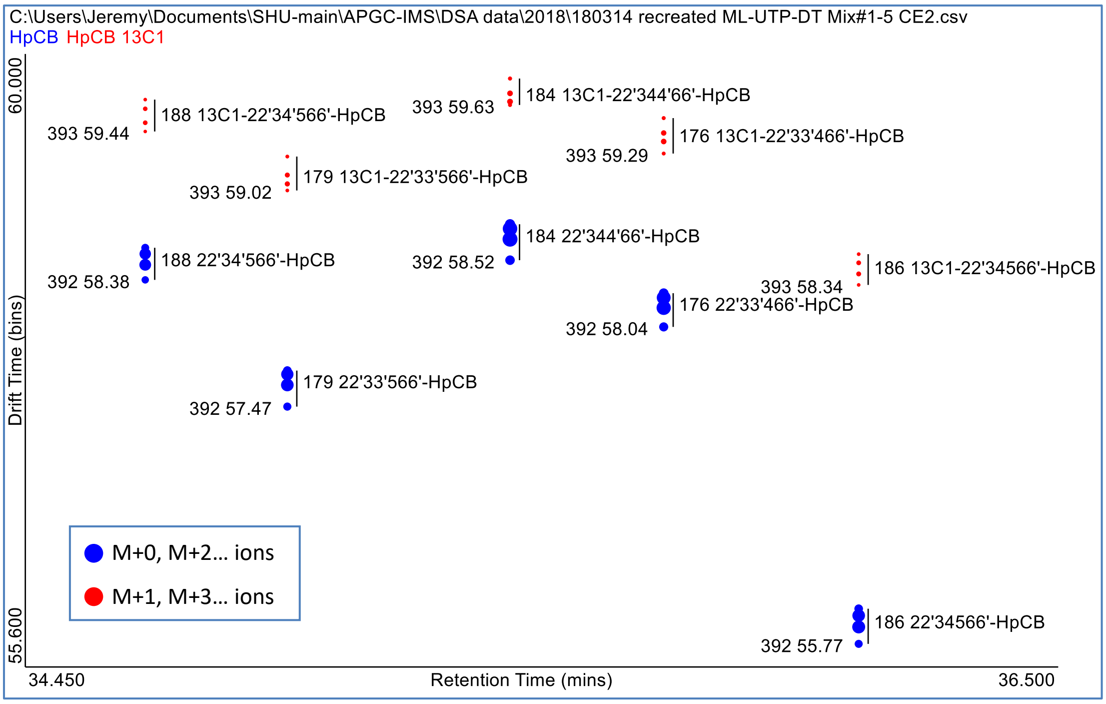

Figure 5.8 DriftScope Analyser plot of ion mobility ATD vs. RT for 5 early eluting HpCBs, PCB-188, 179, 184, 176 and 186, each showing positive arrival time offsets for the groups of secondary ($^{13}$C) ions (red) relative to those due to the primary ($^{12}$C) ions (blue).
The M+0 and M+1 peaks are annotated with their nominal *m/z* and ion arrival times (the remaining peaks in each series are not annotated for clarity) and the marker sizes indicate the relative peak intensities.

Examination of the PCB-186 raw data, as shown in Figure 5.9, reveals some distinctly different characteristics for the secondary ions, where a bimodal distribution is clearly seen but is not present in any of the primary ion traces. The centroid times of these doublets correspond to the data plotted in Figure 5.8 and explain the appearance – but not the underlying cause – of the secondary ions' excess ATD shifts.

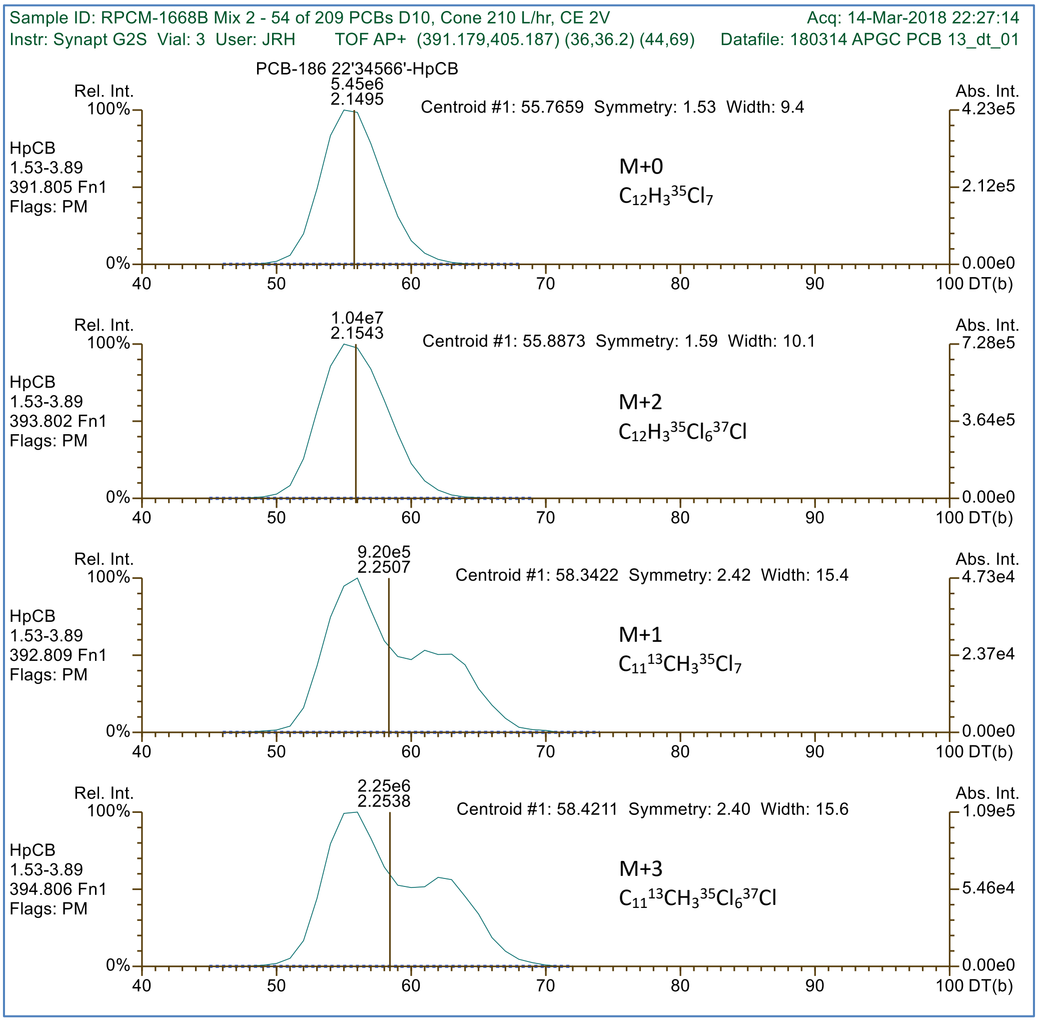

Figure 5.9 Ion mobility ATD for the M+0, M+2 and M+1, M+3 ions of PCB-186 (2,2',3,4,5,6,6'-HpCB) showing a bimodal distribution for the *m/z* 393 and 395 ions.

By reintegrating/splitting the doublets, as shown in Figure 5.10, the secondary ion ATD values were updated using the times from the first of the two peaks at each *m/z*. (The nature of the second of each of these doublets will be discussed later in the chapter.) The revised secondary ion group for PCB-186 now shows an ATD offset of ~0.4% – this is substantially lower than the other 4 tetra-ortho substituted HpCBs and closer to theoretical expectation (~0.02%).

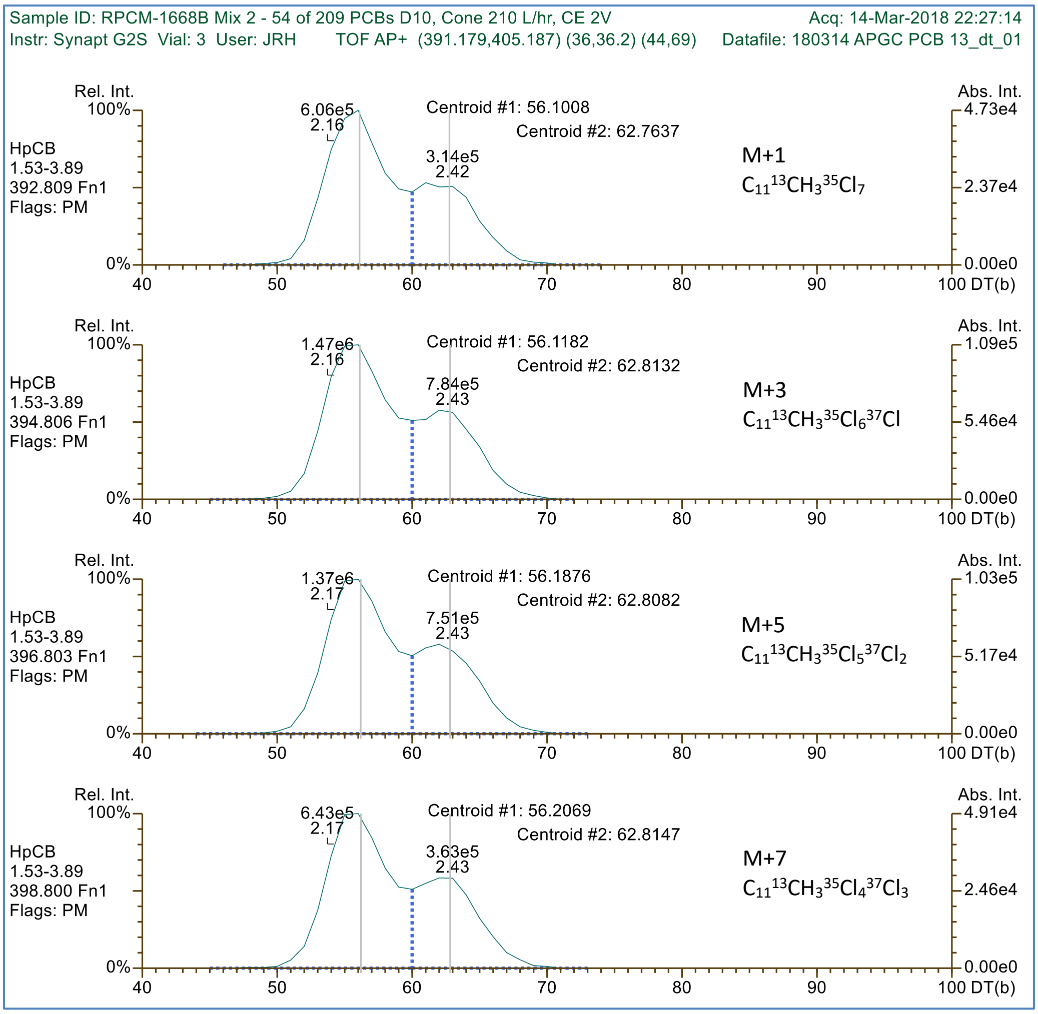

Figure 5.10 Ion mobility ATDs for the M+1, M+3, M+5 and M+7 ions of PCB-186 (2,2’,3,4,5,6,6’-HpCB). Each peak has been reintegrated to separate the 2 components of the bimodal distribution.

Clearly the splitting of these peaks can only provide an approximation to the true data; accurate measurement would require a higher resolution ion mobility device. The low IMS resolution may also be masking similar effects in other PCBs: as noted above (in the observations for PCB-189), the peak widths of the secondary ions are greater than those of the primary ions; this suggests that similar artefacts could also exist in these data but not to the extent as made apparent by the doublets of PCB-186. The greater widths of the secondary peaks affect ~90% of all PCBs irrespective of whether they show greater or lesser ATDs than the primary ions.

### 5.4.4 Ion mobility doublets and associated isomerisation

Further examination of the PCB-186 (2,2',3,4,5,6,6'-HpCB) data (Figure 5.10) showed an unusual feature of the secondary ion doublets: following reintegration/splitting, the averaged ATD from the first of the two peaks created at each *m/z* is reasonably well aligned with its (non-doublet) primary ion ATD; furthermore, examination of the second set of peaks, as shown for the M+3 ion in Figure 5.11, indicates close ATD alignment with the corresponding *m/z* of another congener, PCB-192 (2,3,3',4,5,5',6-HpCB).

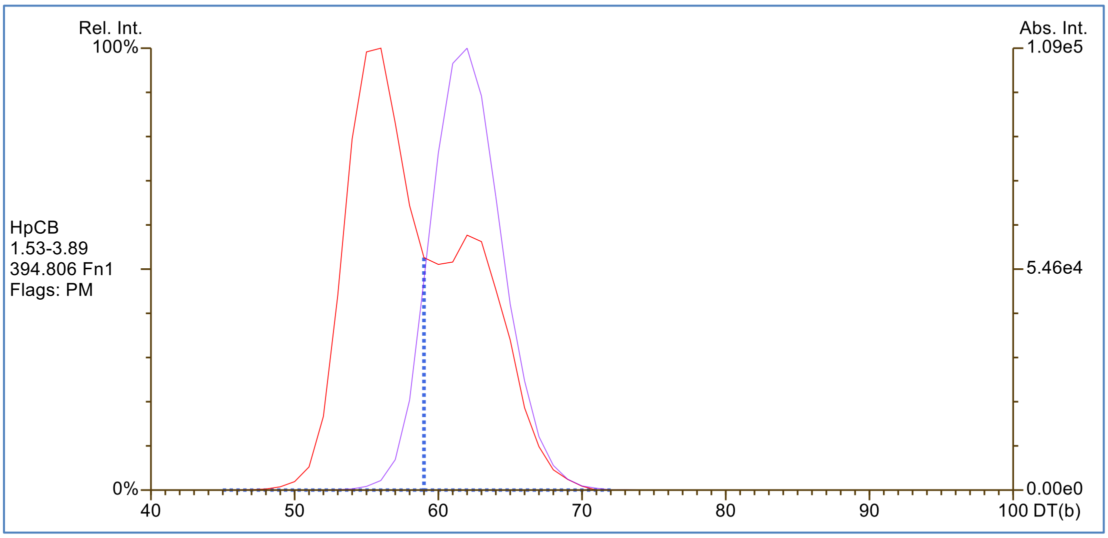

Figure 5.11 Ion mobility ATDs for the M+3 ion (*m/z* 394.8059, $C_{11}{}^{13}CH_3{}^{35}Cl_6{}^{37}Cl$) of PCB-186, (2,2',3,4,5,6,6'-HpCB) (red trace) and PCB-192 (2,3,3',4,5,5',6-HpCB) (purple trace).

The ATD of the higher split peak from PCB-186, based on the centroid data from the 4 secondary ions, is 62.3 (bins) as compared to 62.1 for PCB-192, a deviation of ~0.3%.

This could suggest that partial isomerisation is occurring: as shown in Figure 5.12, the structures of PCB-186 and PCB-192 have identical Cl substitutions on one ring, and rearrangement of the 2’ and 6’ ortho (Cl) positions to the 3’ and 5’ meta positions respectively on the other ring would be required for this to be achieved. The lower single point conformation energy of PCB-192 (relative to PCB-186) also suggests that this is a favoured rearrangement following the affected C-Cl and C-H bond breakages.

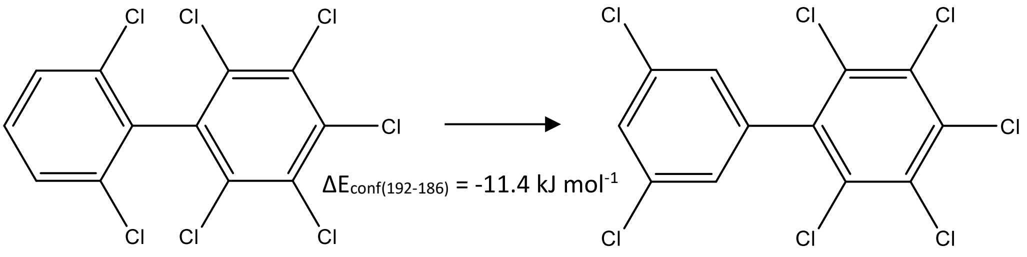

PCB-186 (2,2’,3,4,5,6,6’-HpCB) PCB-192 (2,3,3’,4,5,5’,6-HpCB)

Figure 5.12 Structures of PCB-186 and PCB-192 showing isomerisation via the rearrangement of the 2’ and 6’ ortho (Cl) positions to the 3’ and 5’ meta positions respectively.

To help identify further instances of bimodal distributions the relative peak widths of the M+1 to M+0 ions were calculated and plotted as shown in Figure 5.13 for the tri- to octa-chlorinated congeners (the lower vertical axis limit of 20% having effectively filtered any other congeners). For the 6 PCBs with the greatest relative peak widths at each level-of-chlorination, the peak profiles of the M+0 (blue traces) and M+1 (red traces) ions are also shown in the insets.

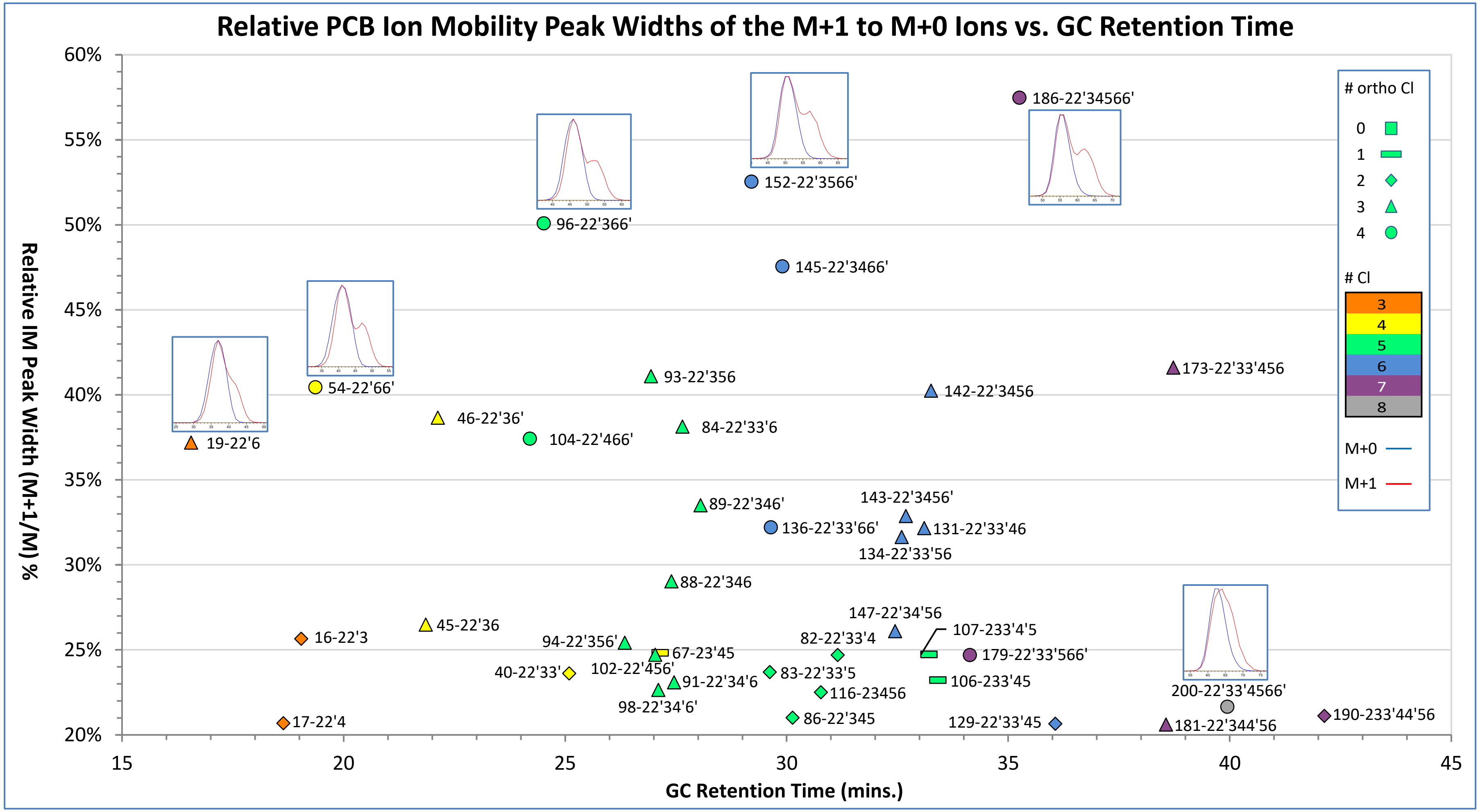

Relative PCB Ion Mobility Peak Widths of the M+1 to M+0 Ions vs. GC Retention Time

Figure 5.13 Relative PCB ion mobility peak widths of the M+1 to M+0 ions vs. GC retention time.
Data has been filtered to show only the PCBs with a relative peak width of the M+1 to M+0 ions greater than 20% (n = 39). The inset ion mobility spectra show the peak shapes of the M+0 (blue) and M+1 (red) ions for the tri- to octachlorinated biphenyls with the largest M+1 to M+0 ratios.

The 6 candidate PCBs identified in Figure 5.13 as having the largest relative M+1/M+0 ion mobility peak widths at each level-of-chlorination (including the aforementioned PCB-186) are:

- PCB-19 (2,2',6-TrCB)
- PCB-54 (2,2',6,6'-TeCB)
- PCB-96 (2,2',3,6,6'-PeCB)
- PCB-152 (2,2',3,5,6,6'-HxCB)
- PCB-186 (2,2',3,4,5,6,6'-HpCB)
- PCB-200 (2,2',3,3',4,5,6,6'-OcCB)

2 other PCBs – similarly containing the subset of 2,2',6,6' ortho substitutions – that also showed pronounced doublets in their secondary ion traces are:

- PCB-104 (2,2',4,6,6'-PeCB)
- PCB-145 (2,2',3,4,6,6'-HxCB)

The pre- and post-split ATDs for these 8 PCBs and the corresponding ATDs of PCBs suggested as being the target isomers are shown by the graph in Figure 5.14. In all cases, close alignment between the upper ATD from the split doublet peak and the corresponding ATD from the (non-doublet) target isomer was observed. The overall alignment RMS deviation of ~0.8% (n = 8) also strengthens the idea that partial isomerisation is occurring in these examples.

This effect was also observed for some other PCBs identified in Figure 5.13, such as PCB-93 (2,2',3,5,6-PeCB) and PCB-142 (2,2',3,4,5,6-HxCB) – unlike the above tetra-ortho substituted PCBs, these both have a subset of tri-ortho substitutions – but the doublet peaks formed were less definitive and therefore not included in these results.

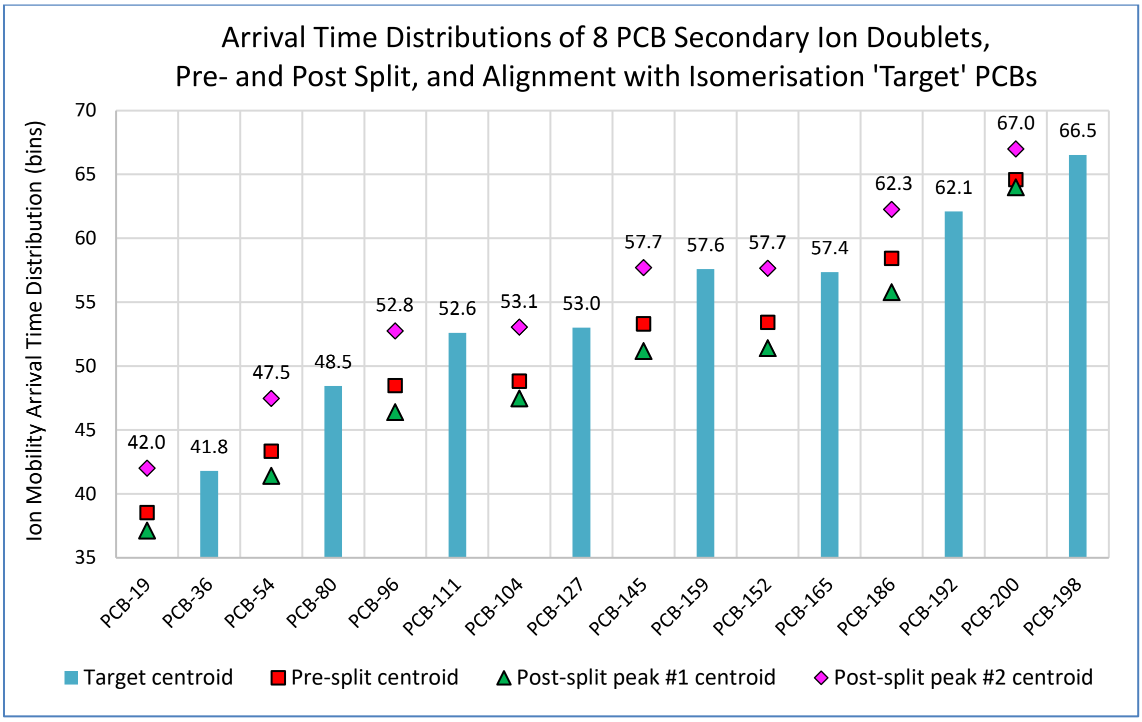

Figure 5.14 The ion mobility ATDs of the secondary ions of 8 PCBs, pre- and post-reintegration (splitting), and their alignment with possible isomerisation ‘targets’.
The PCBs are shown in pairs, e.g. PCB-19 and PCB-36: the first of each pair is the PCB showing doublet formation, where the central points (red squares) indicates the ATD centroids prior to splitting, and the lower (green triangles) and higher (purple diamonds) points show the ATD centroids created by the peak splitting; the second PCB of each pair (blue columns) has an ATD that closely aligns with the upper ATD from the first PCB’s split. For the 8 PCB pairs considered here the overall alignment RMS error is ~0.8%.

The structures for the remaining 7 PCBs[*] and their suggested isomerisation targets, as referenced in Figure 5.14, are shown in Figure 5.15 to Figure 5.21.

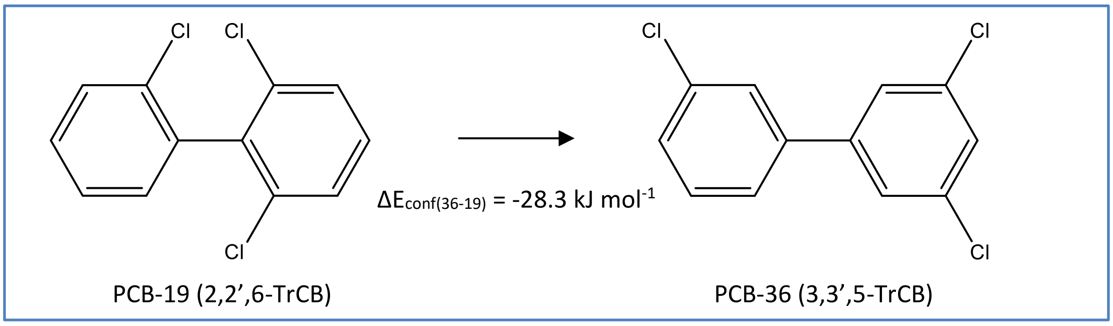

Figure 5.15 Structures of PCB-19 and PCB-36 showing isomerisation via the rearrangement of the 2, 2’ and 6 ortho (Cl) positions to the 3, 3’ and 5 meta positions respectively.

---

[*] The structures of PCB-186 and PCB-192 having been previously shown in Figure 5.12.

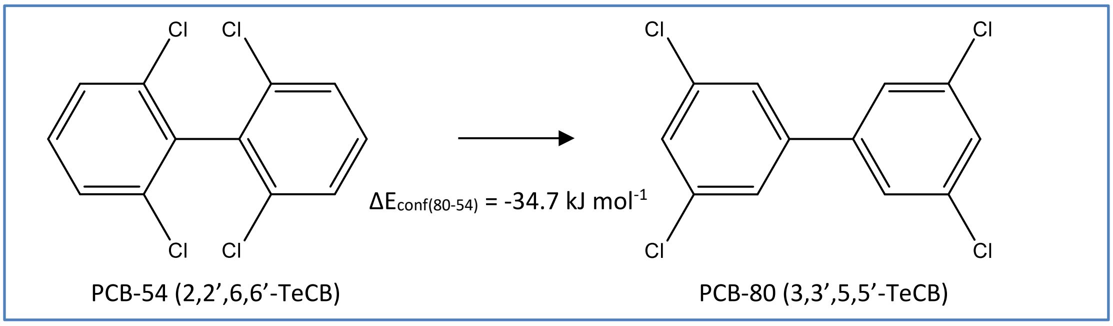

Figure 5.16 Structures of PCB-54 and PCB-80 showing isomerisation via the rearrangement of the 2, 2', 6 and 6' ortho (Cl) positions to the 3, 3', 5 and 5' meta positions respectively.

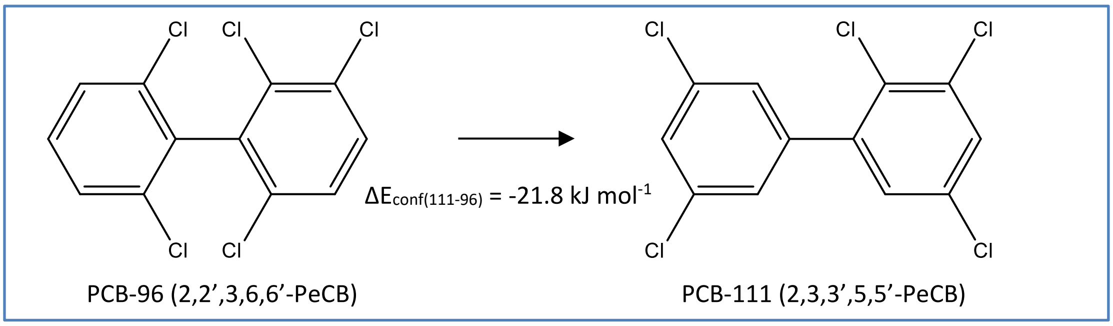

Figure 5.17 Structures of PCB-96 and PCB-111 showing isomerisation via the rearrangement of the 2', 6 and 6' ortho (Cl) positions to the 3', 5 and 5' meta positions respectively.

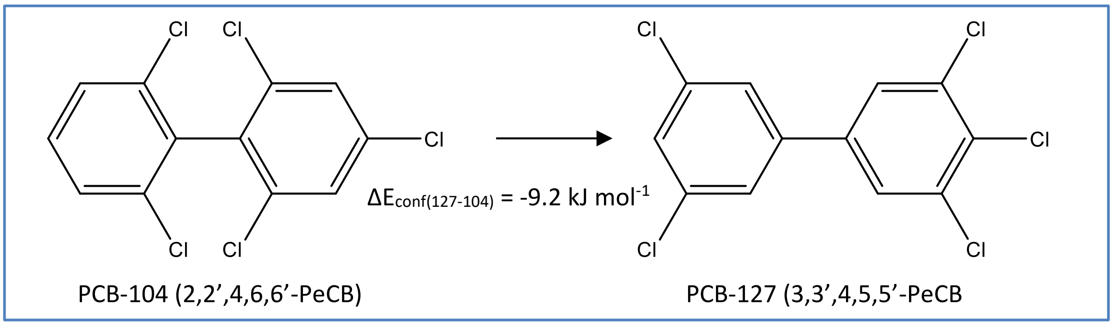

Figure 5.18 Structures of PCB-104 and PCB-127 showing isomerisation via the rearrangement of the 2, 2', 6 and 6' ortho (Cl) positions to the 3, 3', 5 and 5' meta positions respectively.

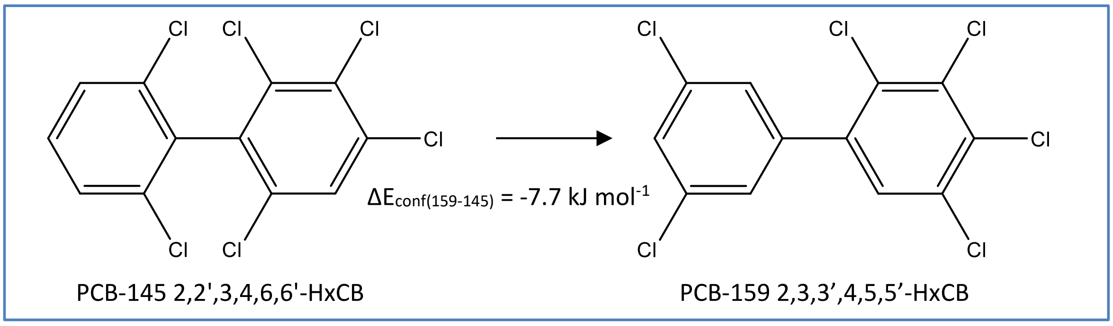

Figure 5.19 Structures of PCB-145 and PCB-159 showing isomerisation via the rearrangement of the 2’, 6 and 6’ ortho (Cl) positions to the 3’, 5 and 5’ meta positions respectively.

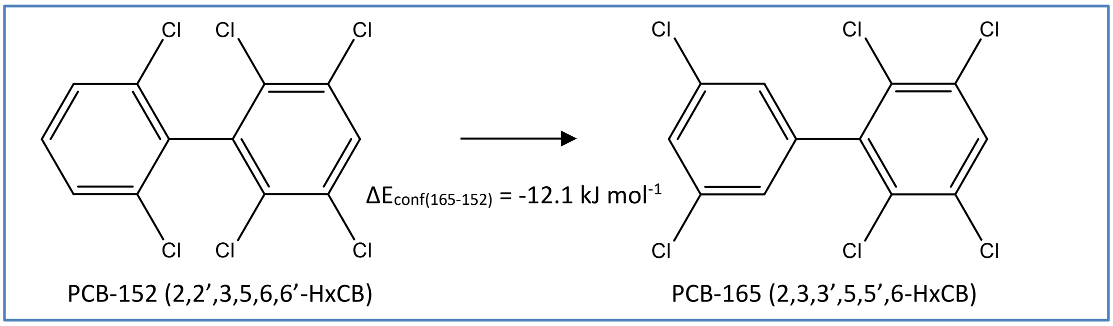

Figure 5.20 Structures of PCB-152 and PCB-165 showing isomerisation via the rearrangement of the 2’ and 6’ ortho (Cl) positions to the 3’ and 5’ meta positions respectively.

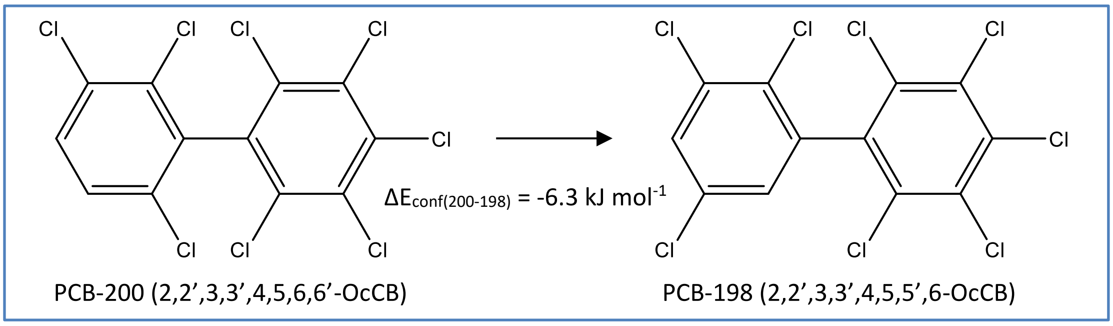

Figure 5.21 Structures of PCB-200 and PCB-198 showing isomerisation via the rearrangement of the 6’ ortho (Cl) positions to the 5’ meta position.

In all cases, isomerisation appears to occur from the rearrangement of one or more ortho substituted Cl atoms to a meta position, however, it is important to note that ortho substitution alone does not directly lead to this process. E.g. although PCB-104 (2,2’,4,6,6’-PeCB), as shown by the above data, is a convincing candidate, PCB-155 (2,2’,4,4’,6,6’-HxCB), with its additional para Cl, shows no evidence of peak broadening or doublet formation.

The process of PCB-155 isomerising to PCB-169 (3,3',4,4',5,5'-HxCB) – that would result from all 4 ortho Cl becoming meta – is depicted in Figure 5.22; however, unlike the rearrangements shown above, it is not favoured due to the difference in their single point conformation energies ($\Delta E_{conf}$ = 15.9 kJ mol$^{-1}$).

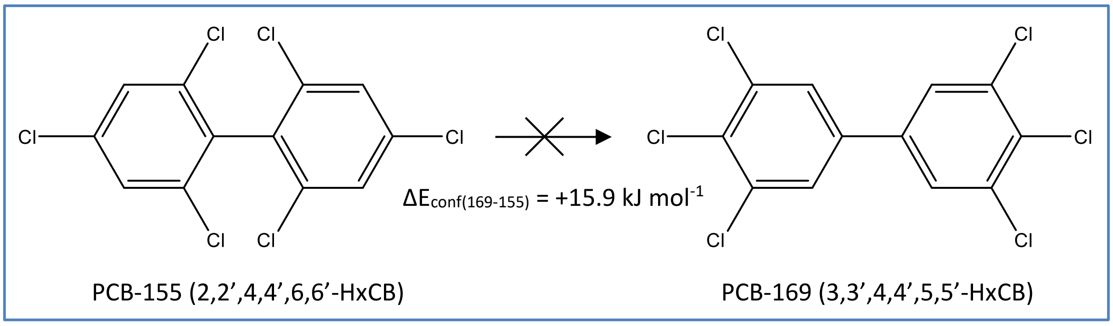

Figure 5.22 Structures of PCB-155 and PCB-169 indicating that although isomerisation could, in principle, occur via the rearrangement of all ortho Cl to meta positions, it is not energetically favoured by the processes realised in these experiments.

This is similarly the case for the other 4 PCBs that could, in principle, be formed via ortho -> meta rearrangements involving either 3 Cl atoms, 2 Cl on the same ring, 2 Cl on opposite rings or 1 Cl, respectively:

PCB-167 (2,3',4,4',5,5'-HxCB, $\Delta E_{conf}$ = 31.0 kJ mol$^{-1}$)
PCB-153 (2,2',4,4',5,5'-HxCB, $\Delta E_{conf}$ = 6.4 kJ mol$^{-1}$)
PCB-168 (2,3',4,4',5',6-HxCB, $\Delta E_{conf}$ = 27.2 kJ mol$^{-1}$)
PCB-154 (2,2',4,4',5,6'-HxCB, $\Delta E_{conf}$ = 3.5 kJ mol$^{-1}$).

### 5.4.5 Observations from fully-labelled ($^{13}C_{12}$) PCB data

To further examine the above effects related to the presence of $^{13}C$ atoms, IMS-MS was performed on a mix[*] containing several fully-labelled PCBs (i.e. where all $^{12}C$ atoms have been replaced by $^{13}C$) in addition to certain native, unlabelled, PCBs. Figure 5.23 shows the DriftScope Analyser plot for both PCB-188 (2,2’,3,4’,5,6,6’-HpCB) and PCB-189 (2,3,3’,4,4’,5,5’-HpCB)

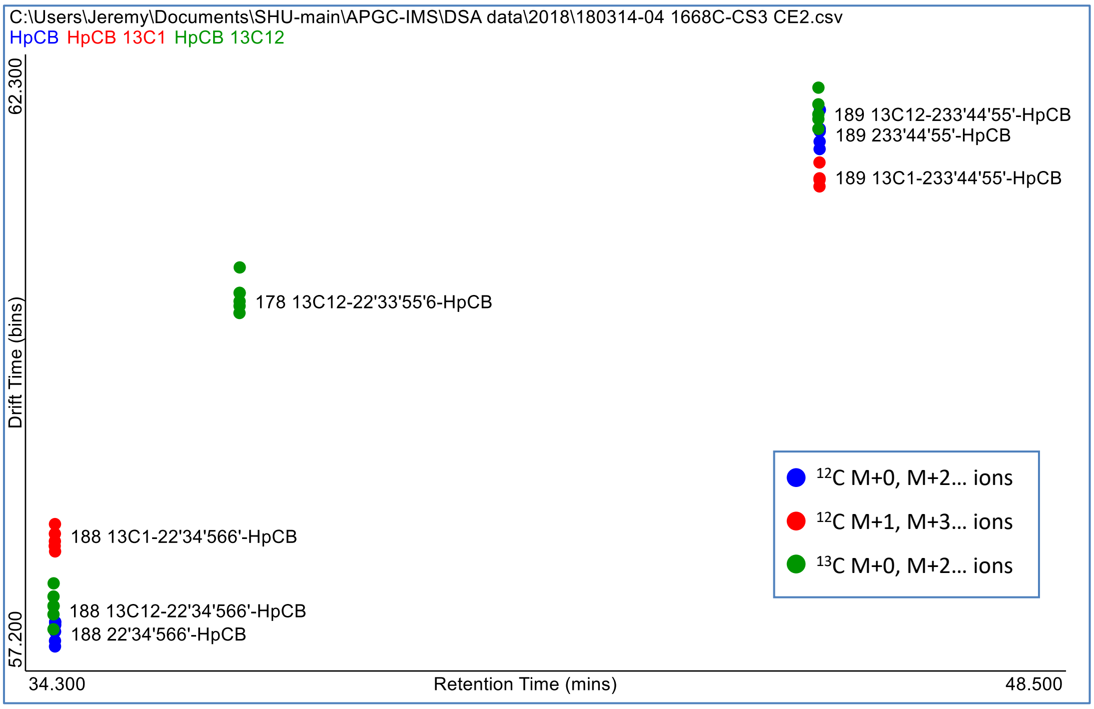

Figure 5.23 DriftScope Analyser plot of ion mobility ATD vs. RT for PCB 188 (2,2’,3,4’,5,6,6’-HpCB) and PCB 189 (2,3,3’,4,4’,5,5’-HpCB) showing data from the native primary ions (blue), native secondary ions (red) and the $^{13}C_{12}$-labelled primary ions (green).
(PCB-178, present as a $^{13}C_{12}$-labelled standard only, is not part of this study.)

As previously reported in section 5.4.3, PCB-188 showed a positive offset in the ATDs of its secondary ions (relative to the primary ions’ ATDs), whereas PCB-189 showed a negative offset; however, the fully-labelled ($^{13}C_{12}H_3Cl_7$) ions show a positive offset for both congeners.

---

[*] See Table C.4 (p. 243) for complete details.

Doublet formation, and hence possible isomerisation, was also observed in the data of certain $^{13}C$-labelled PCBs. The left panel of Figure 5.24 shows the ATDs for the native, M+0 to M+6, ions of PCB-54 (2,2′,6,6′-TeCB); the figure's right panel shows the ATDs for the corresponding $^{13}C_{12}$-labelled M-1 to M+5 ions. The secondary series of the labelled ions starts at M-1 due to the presence of a single $^{12}C$ in place of one of the $^{13}C$ atoms resulting from the $^{13}C$ isotopic purity[*] being less than 100%.

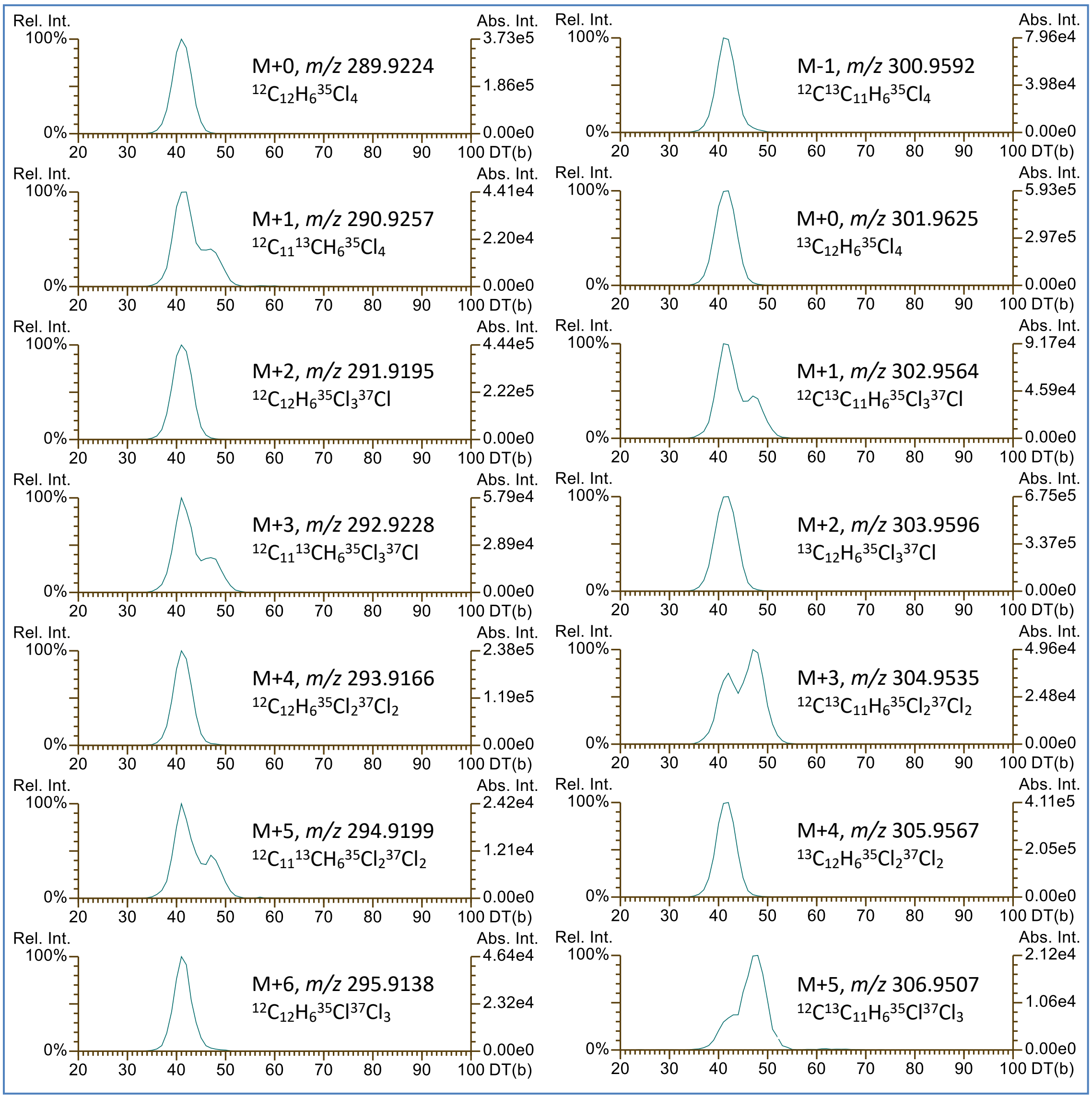

Figure 5.24 Ion mobility ATDs of native and $^{13}C$-labelled PCB-54 (2,2′,6,6′-TeCB, $C_{12}H_6Cl_4$). The native M+0 to M+6 ions are shown on the left and the $^{13}C$-labelled M-1 to M+5 ions on the right. Both sets exhibit bimodal distributions for their secondary ions but, while consistent for the native ions, the $^{13}C$-labelled ions' profiles vary with the degree of $^{37}Cl$ substitution.

---

[*] The purity of isotopically labelled standards was previously discussed in detail in Chapter 3.

The secondary native ions of PCB-54 each show similar doublet peaks, and their profiles are also reasonably like several of those noted in the previous section; however, this is not the case for the $^{13}$C-labelled ions where the profiles show distinct changes depending on the number of $^{37}$Cl atoms present.

No doublet is observed for the M-1 ion ($^{12}C^{13}C_{11}H_6{}^{35}Cl_4$) where only $^{35}$Cl are present; for M+1 ($^{12}C^{13}C_{11}H_6{}^{35}Cl_3{}^{37}Cl$), with its single $^{37}$Cl, a doublet is formed that resembles one from the native secondary ion series. As the $^{35}$Cl atoms are subsequently replaced by $^{37}$Cl in the M+3, M+5 and M+7 ions, the doublets' right-side peaks increase in intensity as the left-side peaks decrease; this is clearly shown by the overlaid traces in Figure 5.25.

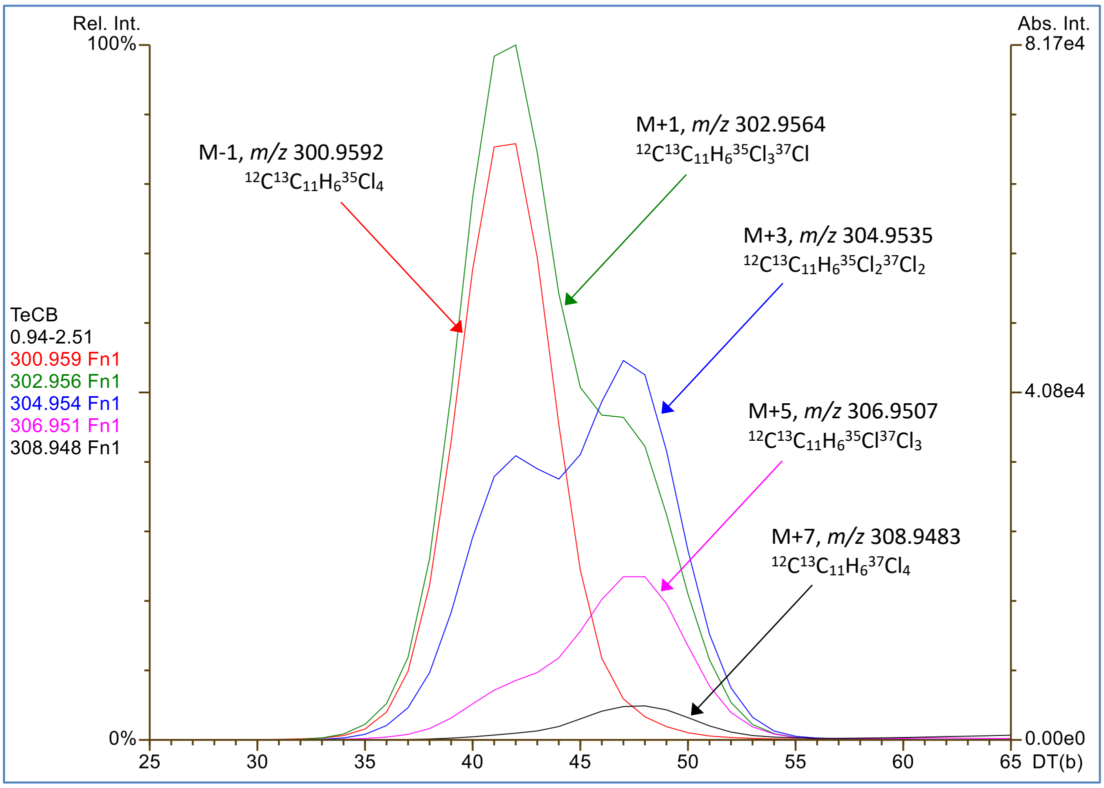

Figure 5.25 Overlaid traces (smoothed data) for the ATDs of the M-1 to M+7 secondary ion traces of $^{13}$C-labelled PCB-54 (2,2,',6,6'-TeCB) showing the variation in distribution with increasing $^{37}$Cl substitution.

## 5.4.6 Possible mechanisms for the observed artefacts in ion arrival time distributions

The separation of $^{13}C$-labelled glycine isotopomers has been previously reported using field asymmetric ion mobility spectroscopy (FAIMS), but the underlying mechanism for the variation in ATD could not be determined (Shvartsburg, Clemmer and Smith, 2010). The following mechanisms are therefore proposed for the observed artefacts affecting the secondary ions' arrival time distributions.

### 5.4.6.1 Changes to an ion's centre-of-mass

An initial supposition was that the peak broadening and doublet formation could result from centre-of-mass (CoM) differences according to the location of the single $^{13}C$ atom in the various isotopomers of the M+1, etc. isotopologues. E.g. for a symmetrical PCB such as 2,2',6,6'-TeCB (PCB-54), a $^{13}C$ atom in a para position would offset the CoM more than in one of the central C-C positions. Such an effect has been reported for variations in the diffusivity of water isotopes in gases, and a correlation established between the molecules' CoM and different D and $^{18}O$ substitutions (Merlivat, 1978).

Although this may be associated with minor peak broadening – such as that seen between a congener's primary ions – the magnitude of many of the secondary ion shifts is far greater than those due to the 2 Da addition from a $^{37}Cl$ substitution; it therefore seems unlikely that a 1 Da addition to either of the phenyl rings from a $^{13}C$ substitution could be responsible for this effect. Furthermore, no such effect is seen in any of the primary ions that would equally be affected by $^{37}Cl$ isotopomers, e.g. for the M+2 isotopologue of PCB-8 there are 2 possible Cl isotopomers as illustrated in Figure 5.26.

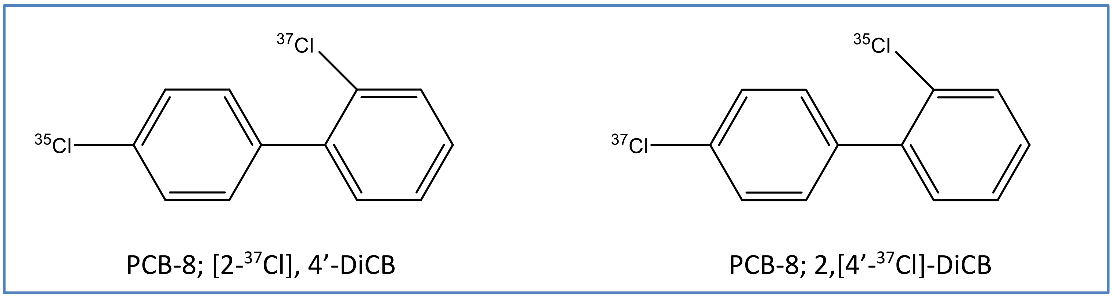

PCB-8; [2-$^{37}$Cl], 4'-DiCB

PCB-8; 2,[4'-$^{37}$Cl]-DiCB

Figure 5.26 Structures of the 2 possible isotopomers of the $C_{12}H_8Cl^{37}Cl$ isotopologue of PCB-8.

#### 5.4.6.2 Effects of nuclear spin

A key difference between a $^{13}C$ and $^{12}C$ atom is that the former, due to its imbalance of protons and neutrons, has non-zero spin. This attribute is normally associated with nuclear magnetic resonance (NMR) spectroscopy, however it has been reported that the rates of chemical reactions relating to radical pairs can be influenced by this spin even in ambient magnetic fields (Turro, 1983). It is not currently known whether any such effect could apply to this work and this idea is therefore a placeholder for potential future research. In a related thought experiment, could the radio-frequency (RF) conditions found within the travelling wave device interact with these $^{13}C$ containing species resulting in certain/partial alignment such that an ion's motion is no longer equally rotationally averaged over all axes, thus affecting its mobility?

#### 5.4.6.3 Thermal effects due to heating within the ion mobility cell

The intense electric fields encountered by ions within a TW device can lead to considerable ion heating, e.g. > 200 K above the gas temperature, and have been shown to induce fragmentation that is distinguishable from that occurring prior to entry into the TW device (Morsa, Gabelica and De Pauw, 2014).

Given this effect, detailed computational modelling of various PCBs and certain isotopologues and isotopomers was performed using the Orca program [as previously described in section 4.2.5, but here with the additional frequency parameter selected to create the infrared (IR) spectra]. In all cases, the resultant conformers, and hence their rotationally averaged CCS values, were identical – since the mean bond lengths and angles are unaffected by the presence of heavier isotope atoms – however, the vibrational characteristics of bonds involving isotopes do change and this is reflected in their modelled IR spectra.

### 5.4.7 Modelled PCB isotopologue and isotopomer IR spectra

Figure 5.27 shows the modelled IR spectrum for native PCB-188, i.e. where all carbons are $^{12}C$, Figure 5.28 shows that from its M+1 isotopologue due to the substitution of a single $^{13}C$ (in the ortho 2 position) and Figure 5.29 represents its fully labelled ($^{13}C_{12}$) isotopologue.

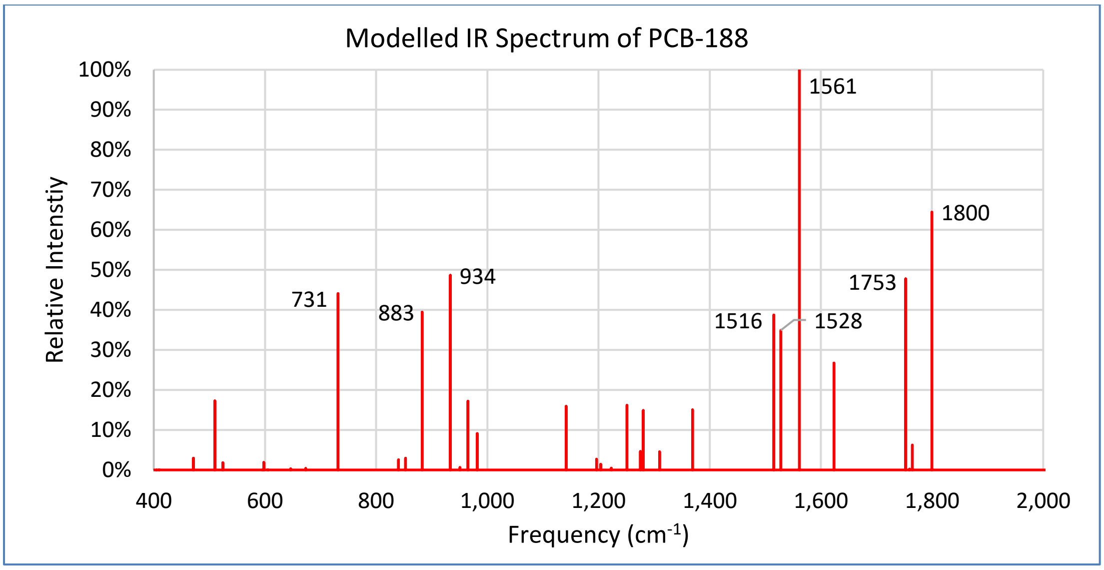

Figure 5.27 Modelled IR spectrum of PCB-188 (2,2’,3,4’,5,6,6’-HpCB, $C_{12}H_3Cl_7$).

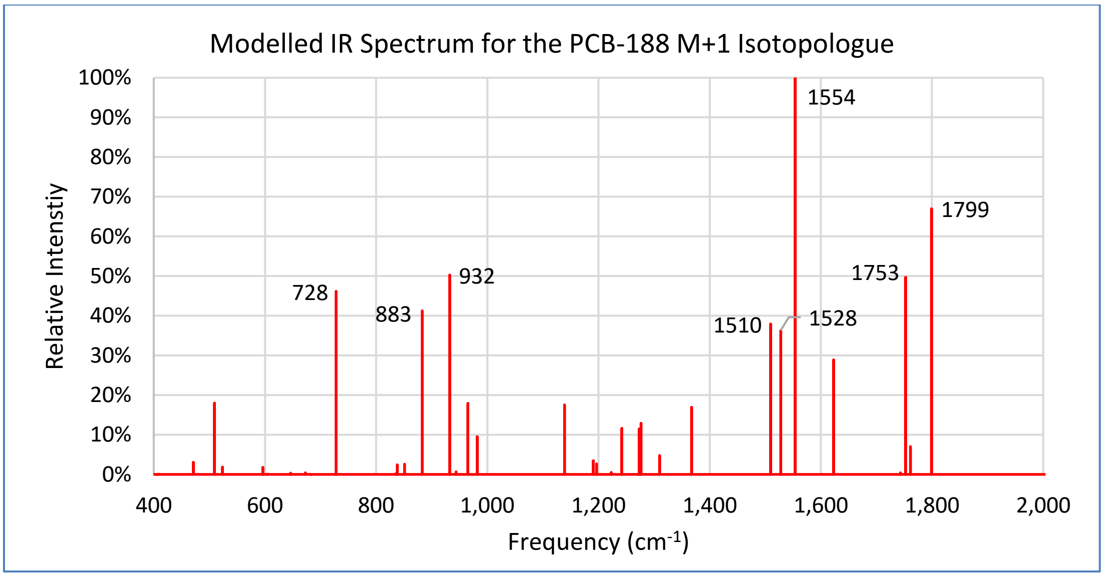

Figure 5.28 Modelled IR spectrum of the M+1 isotopologue of PCB-188 (2,2’,3,4’,5,6,6’-HpCB, $C_{11}{}^{13}CH_3Cl_7$) due to a single $^{13}C$ substitution.
This is one of 12 possible $^{13}C$ isotopomers (of the M+1 isotopologue), here in the ortho 2 position.

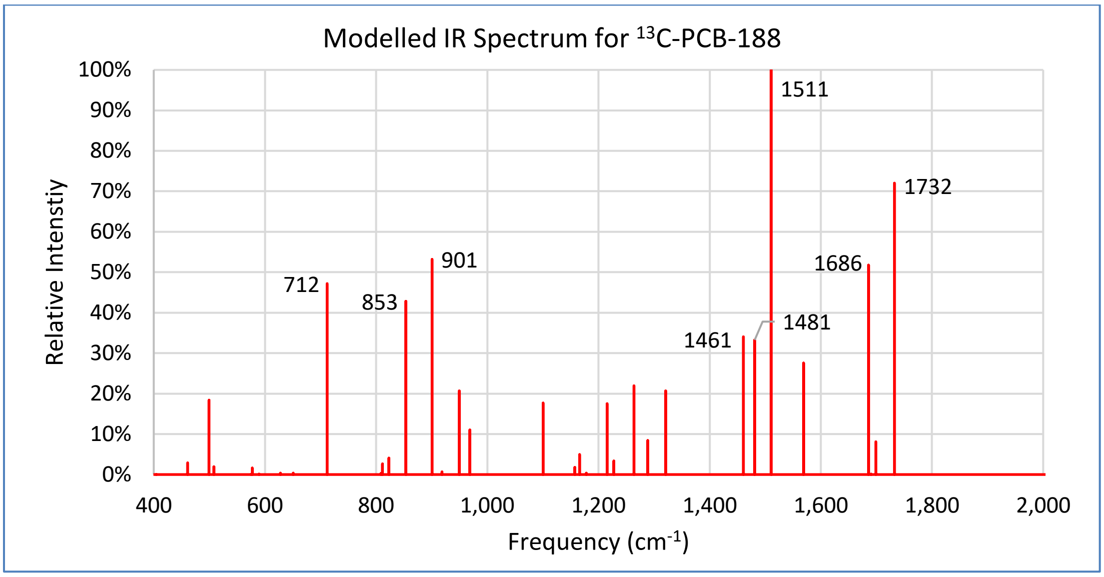

Figure 5.29 Modelled IR spectrum of fully labelled $^{13}C_{12}$-PCB-188 (2,2’,3,4’,5,6,6’-HpCB, $^{13}C_{12}H_3Cl_7$).

For all spectra, the x-axis is shown from 400 to 2,000 cm$^{-1}$ to emphasise the significant peaks (all peak intensities outside this range are < 3%). Bonds involving a $^{13}$C have a lower vibrational frequency compared to those with $^{12}$C and this is reflected in the peaks’ frequencies of the corresponding IR spectra from the $^{13}C_1$ and $^{13}C_{12}$ data relative to the $^{12}C_{12}$ modelled data. The above spectra, together with those from other isotopologues and isotopomers, were submitted to PCA with the results shown in Figure 5.30.

The 4 clusters due to PCB-188 (2,2’,3,4’,5,6,6’-HpCB) and PCB 189 (2,3,3’,4,4’,5,5’-HpCB) in their native and $^{13}C_{12}$-labelled forms are clearly shown in addition to the single spectrum points from the modelled $^{13}C_6$ isotopologues. Each cluster contains the base structure and all isotopomers of its $^{13}C_1$ isotopologue, and similarly all isotopomers of its $^{12}C_1$ isotopologue for the native and $^{13}C_{12}$-labelled PCB-188 and 189 respectively. Also present in each cluster are the $^{37}Cl_4$ and $^{37}Cl_7$ base isotopologues with a selection of isotopomers of their $^{13}C_1$ or $^{12}C_1$ isotopologues.

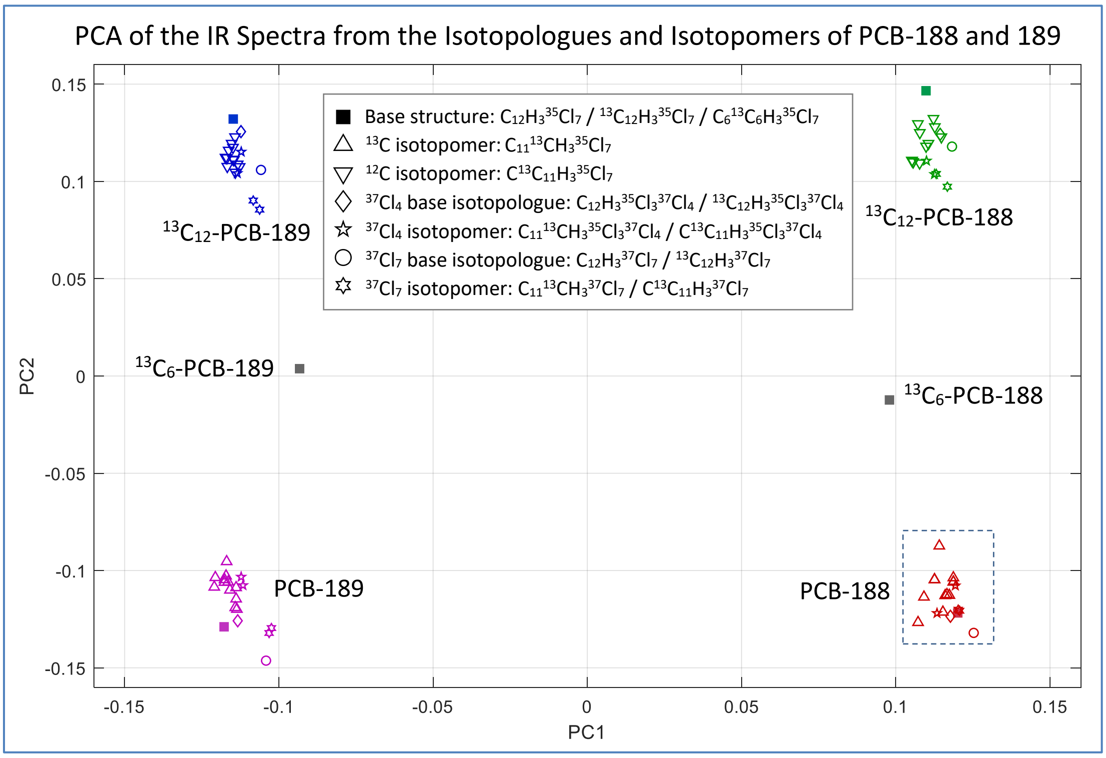

Figure 5.30 Principal component analysis (PCA) of modelled IR spectral data from the isotopologues and isotopomers of PCB-188 (2,2’,3,4’,5,6,6’-HpCB) and PCB 189 (2,3,3’,4,4’,5,5’-HpCB).
The clusters are clearly shown for the native and $^{13}C_{12}$-labelled PCBs. Also shown are the single points for the modelled $^{13}C_6$-labelled PCBs that lie approximately midway, on the PC2 axis, between the $^{12}C_{12}$ and $^{13}C_{12}$ clusters. Detail from PCB-188 (dashed rectangle) is shown in Figure 5.31.

The horizontal separation (PC1) is principally due to the isomeric structural differences between the two PCBs whereas the vertical separation (PC2) is principally due to the number of $^{13}C$ atoms, since any shifts due to $^{35}Cl$ substitution with $^{37}Cl$ are comparatively minor. I.e. the shift (in PC2 relative to the base structure) of the $^{37}Cl_7$ isotopologue (of either PCB-188 or 189) is ~10% of that due to the $^{13}C_{12}$ isotopologue even though the former contributes a greater (14 vs. 12) number of additional neutrons. Detail from the PCA of PCB-188 is shown in Figure 5.31.

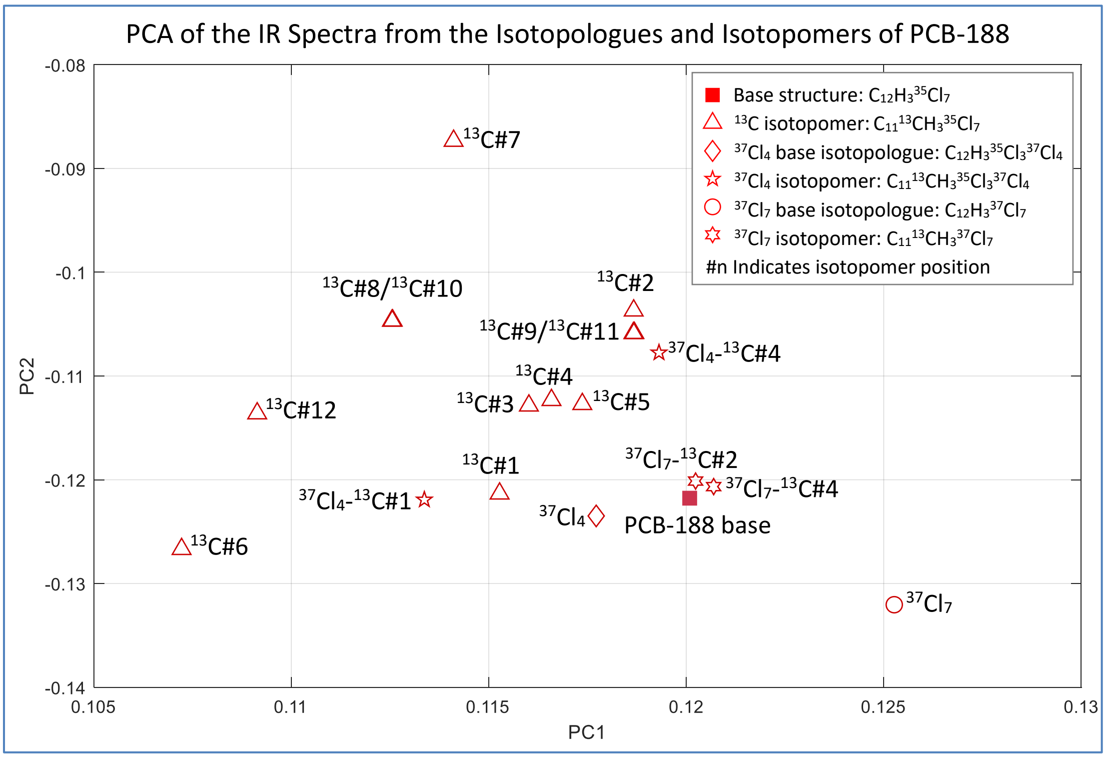

Figure 5.31 Principal component analysis (PCA) of modelled IR spectral data from the isotopologues and isotopomers of PCB-188 (2,2',3,4',5,6,6'-HpCB). (Detail from Figure 5.30.)

These changes to the frequency and amplitude relating to certain bonds could therefore be responsible for a particular isotopologue or one of its isotopomers absorbing either more, or less, energy (from the RF waveform) than another during its transit through the mobility cell. Whether any such effect – if substantiated – would be enough to cause any of the observed effects is unknown.

If this mechanism is viable, it would nevertheless fail to explain why any peak broadening, doublet formation or the proposed isomerisation is only observed for secondary ions: is a combination of the above required? E.g. could the spin effect result in a certain alignment or containment affecting only the secondary ions such that any RF field heating is more effectively focussed to supply sufficient energy for isomerisation to occur?

It has also been reported that, for experimental data from sodiated polyethylene glycol, the measured CCS increased both with temperatures above and also below 300 K (Wyttenbach *et al.*, 1997); if this effect also applies to PCBs it could, in conjunction with the above, explain why both positive and negative ATD shifts are observed for the certain PCBs' secondary ions.

### 5.4.8 Ion mobility of PCB fragment ions

The accurate mass fragment ion data discussed in the previous chapter (4.3.6) showed that for certain PCBs, e.g. PCB-169, the measured *m/z* of ions in the loss of Cl cluster at odd *m/z* agreed with expected M-Cl values, but even *m/z* data appeared to result from a mix of 2 ions: the expected $^{13}$C isotope of M-Cl and another due to Cl/H exchange.

The differences between these odd and even *m/z* fragment ions are also evident in the IMS-MS data. As shown in Figure 5.32, the ATD peaks of odd *m/z* are reasonably well aligned with each other (and with the loss of HCl peak) but are clearly offset from the alignment of the even *m/z* ions.

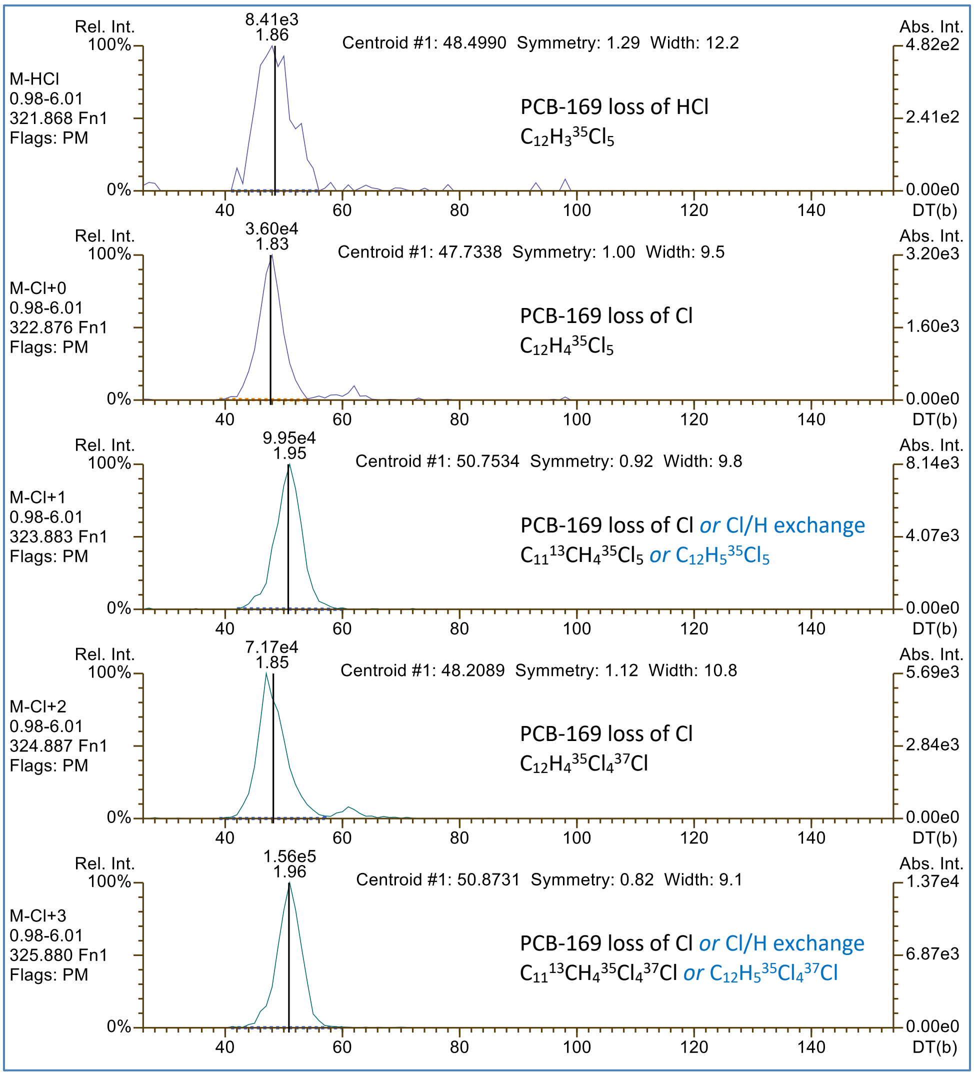

Figure 5.32 Ion mobility ATDs from the loss of Cl cluster of PCB-169 (3,3’,4,4’,5,5’-HxCB) showing data for M-HCl and M-Cl+0 to M-Cl+3. The M-Cl traces show increased ATDs for the even *m/z* fragment ions relative to those of odd *m/z*.

Although the even *m/z* ATDs show some tailing towards the lower time, the overall shift is significant and to higher ATDs relative to the odd *m/z* ions. This suggests that their structures differ and, together with the previous accurate mass data, would reinforce the idea that these are due to a Cl/H exchange process.

Given the symmetrical 4-meta, 2-para Cl structure of PCB-169 (3,3’,4,4’,5,5’-HxCB), there are only 2 viable outcomes of a direct Cl/H exchange: meta Cl/H would result in PCB-126 (3,3’,4,4’,5-PeCB) and para Cl/H would give PCB-127 (3,3’,4,5,5’-PeCB). Figure 5.33 shows a comparison of ATDs from *m/z* 323.88 from the PCB-169 loss of Cl fragment (upper trace), and from the molecular ions of PCB-126 (centre trace) and PCB-127 (lower trace).

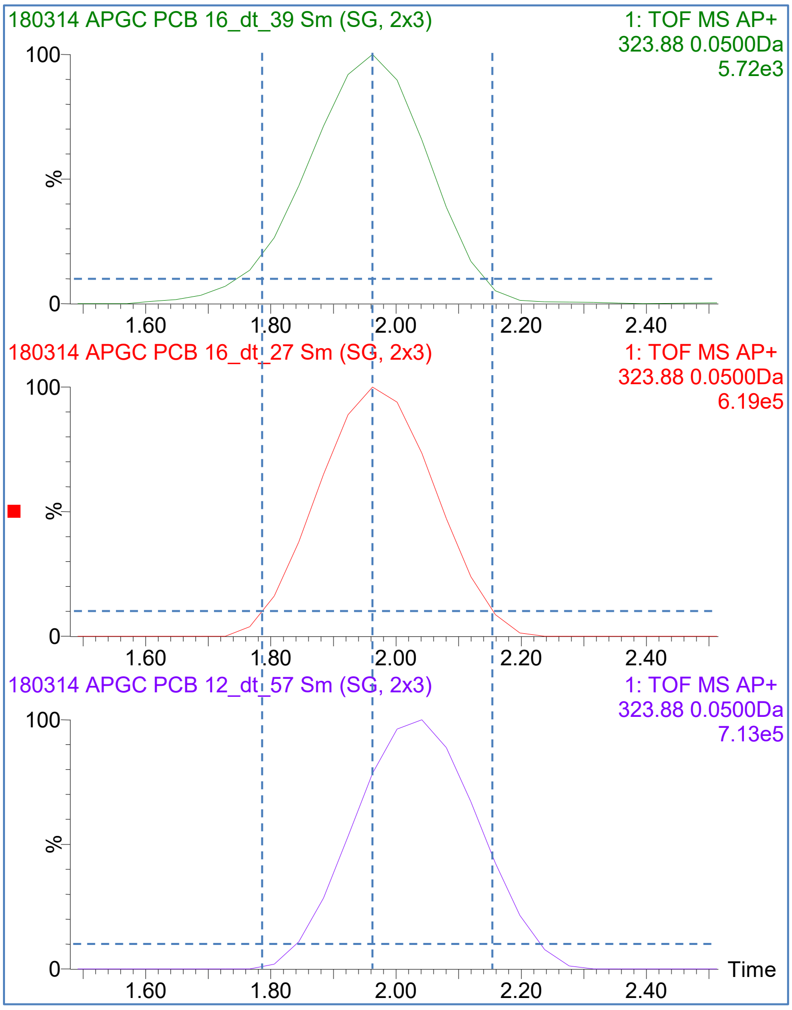

Figure 5.33 Ion mobility ATD data for *m/z* 323.88 from the loss of Cl cluster of PCB-169 (3,3’,4,4’,5,5’-HxCB, upper trace) and from the molecular ions of PCB-126 (3,3’,4,4’,5-PeCB, centre trace) and PCB-127 (3,3’,4,5,5’-PeCB, lower trace).

Although the presence of a peak tail in the fragment ion data – due to the partial contribution from the $^{13}C$ isotope of the Cl loss – confounds any exact match, it nevertheless shows reasonable alignment with the corresponding peak from PCB-126 rather than with PCB-127. This further supports the idea that Cl/H exchange has occurred for these even *m/z* ions, and more specifically at the meta position, and hence it is the 3,3’,4,4’,5-PeCB structure that has been formed.

Similar variations in the odd/even M-Cl *m/z* are observed for other congeners, but as with the fragmentation data discussed in Chapter 4 (e.g. see Figure 4.32), these effects are not observed for the molecular ion or for the loss of 2Cl data, as shown for PCB-114 (2,3,4,4’,5 PeCB) in Figure 5.34.

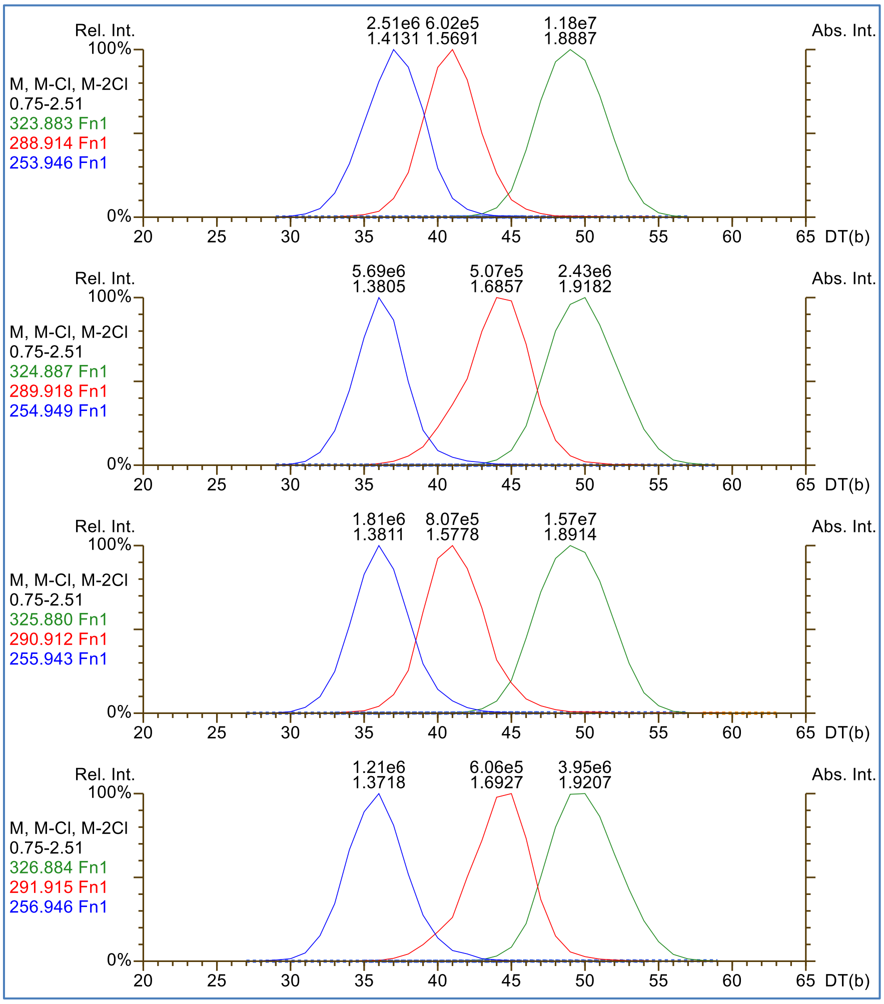

Figure 5.34 Ion mobility ATD for PCB-114 (2,3,4,4’,5-PeCB) showing M+0 to M+3 from the molecular ion cluster (green), the loss of Cl (red) and the loss of 2Cl (blue).
The ATDs show significant variations between the odd and even *m/z* for the loss of Cl but not for the molecular ion or for the loss of 2Cl.

The above variation in the ATD of fragment ion data can also be used as the basis to selectively filter spectra. The upper trace of Figure 5.35 shows the conventionally acquired MS spectrum for loss of Cl region of PCB-138 (2,2',3,4,4',5'-HxCB), the same *m/z* range is then extracted from the IMS-MS data over the ATD ranges corresponding to the odd and even *m/z* maxima to create the spectra shown in the centre and lower traces respectively. The conventional spectrum shows a mixture of M-Cl fragment ions and those from the Cl/H exchange process; these are effectively separated in the filtered IMS-MS data shown in the centre (M-Cl) and lower (Cl/H exchange) spectra.

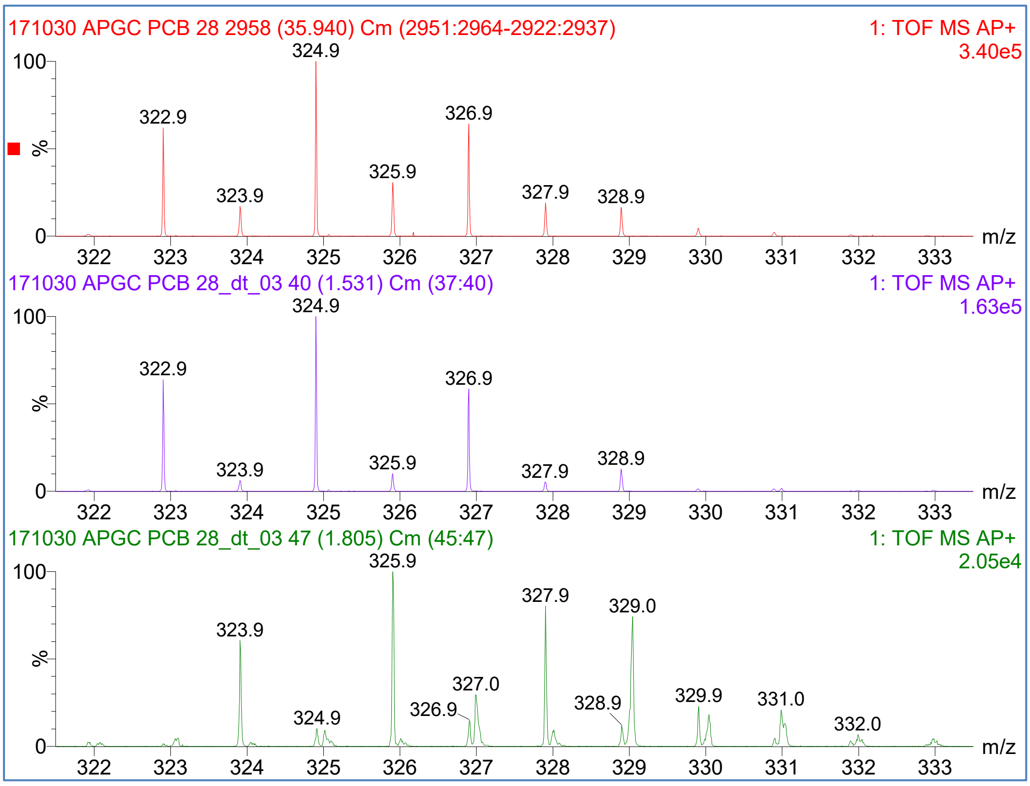

Figure 5.35 MS and IMS-MS data from the loss of Cl region for PCB-138 (2,2',3,4,4',5'-HxCB) at a CE of 20 eV.
The upper trace shows the conventional (averaged and background subtracted) MS spectrum, the centre trace was selectively extracted from the IMS-MS ATD region corresponding to the odd *m/z* maxima and the lower trace from the even *m/z* maxima; these result in spectra corresponding to the M-Cl and Cl/H exchange respectively.

## 5.5 Conclusions

The data in this chapter have shown that ion mobility separation coupled with mass spectrometry (IMS-MS) provides useful additional structural information for all 209 PCBs: the collisional cross sections (CCS) derived from the acquired IMS-MS data have shown good agreement with that published for the few (26) PCBs for which data is available and expands upon that by presenting CCS data for all 209 PCBs. These new data were also shown to match well with values obtained from molecular modelling calculations. The various processing and data visualisation tools developed as an aid to this work should also be of benefit to future researchers.

Various patterns have also emerged from the IMS-MS data that match key structural parameters, e.g. relating to the number of ortho substitutions, and importantly to those PCBs currently assessed as being toxic. It was also observed that PCB-37, a congener that has been previously suggested for inclusion in the toxic congener list, also fitted with this pattern.

Several unusual artefacts were also observed during this study. For certain PCBs, the arrival time distributions (ATD) of the M+1, M+3, etc. ions, i.e. those due to the naturally occurring $^{13}$C isotope, were not consistent with the ATDs of the primary (M+0, M+2, etc.) ions. This problem arises since it is assumed that a compound's structure, and hence its collision cross section (CCS), is invariant with isotopic substitution(s), and therefore any changes in its measured ATDs should only be due to differences in the (reduced) masses of those isotopologues' ions. Both positive and negative ATD offsets were observed and were often significant, i.e. far greater than could be explained by any mass differences. However, changes in ATDs within either the primary or secondary ion sub-groups were consistent with their *m/z*, and there were no unexpected shifts due to the various $^{37}$Cl isotopologues – the effect appears to be confined to isotopologues containing a single $^{13}$C. Furthermore, the behaviour of fully $^{13}C_{12}$-labelled standards appeared to be as expected (though only a few such standards were available to investigate this).

In addition to these offsets, several PCBs exhibited the formation of doublets in their ATD data – again, only affecting the $^{13}$C isotopologues. If such doublet peaks were split, it was found that the higher of the two resulting ATDs could be matched to that of another PCB and these suggested that isomerisation was occurring. In all cases observed, this was attributed to ortho substituted Cl atoms undergoing rearrangement to meta positions – subject to such positions being available and the process being energetically favourable.

Various mechanisms were considered for the above effects: changes to an ion's centre-of-mass, the nuclear spin of $^{13}$C and ion heating within the mobility cell. The first was considered unlikely given that the effects observed were far more significant where a $^{13}$C was involved compared to those with a $^{37}$Cl, i.e. counter to that expected due to changes in centre-of-mass. The effects of nuclear spin, i.e. as characterised by the angular momentum of $^{13}$C but not by $^{12}$C, are not known in the context of this work, but it remains a possible focal point for future research since many observations only pertain to ions containing a single $^{13}$C.

It was also suggested that spin could play a role in ion heating via some alignment or containment within the travelling wave RF field. Given that significant ion heating has been shown to occur in a mobility gas cell, this could affect an ion's mobility since, although a particular PCB structure is unaffected by isotopic substitution(s), the vibrational characteristics of the involved bonds can change and would thus be differently affected by energy imparted by the RF field.

To investigate this, computational modelling of various PCBs and their isotopologues and corresponding isotopomers was performed. For a given PCB, the resultant infrared (IR) modelled spectra showed various lowered frequencies, as expected, due to the influence of heavier isotopes on certain bonds. The modelled IR spectral data from PCB-188 and 189 – two congeners that exhibited opposite shifts of their $^{13}$C ion mobility ATDs – were also submitted to principal component analysis (PCA). This showed good clustering of the isotopologues and isotopomers from each PCB in both their natural and $^{13}C_{12}$-labelled forms but did not show any other distinguishing features that would explain the observed variations in their IMS-MS data.

IMS-MS fragment ion data were also examined to further investigate the proposed Cl/H exchange process observed in the loss of Cl cluster data for certain PCBs (as reported in Chapter 4). The analysis of the data from PCB-169 showed different ATDs for the odd and even integer *m/z* ions in the M-Cl region, with the even *m/z* ions' ATDs each having a significant component that is reasonably aligned with the ATD of the corresponding *m/z* of PCB-126. This would support the theory that a Cl/H exchange has occurred, in this case of a meta Cl, thus 3,3’,4,4’,5,5’ -> 3,3’,4,4’,5 (PCB-169 -> PCB-126).

Although much useful and novel data have been obtained from this study, several questions remain unanswered. In particular, the observed offsets and doublets in the ATDs of ions that include a single $^{13}C$, and the proposed isomerisations require further study: what is/are the mechanism/s involved and do these effects reflect different chemical and/or biological activity outside the gas phase arena?

The low resolution of the ion mobility data is clearly a limiting factor in some of this work where more definitive data is needed, e.g. only cases of obvious doublet formation could be studied, yet many other examples were seen of significant peak broadening – these are likely also doublets, or possibly multiplets, but this could not be ascertained. A recent development in travelling wave ion mobility spectrometry (TWIMS) is that of a cyclic TWIMS: a fundamental parameter governing the instrument’s resolution is the length of the mobility cell; by allowing the ions to make multiple passes through a looped cell this limitation can be significantly overcome (Giles *et al.*, 2019).

Although beyond the original scope of this thesis, further experimental work, using enhanced instrumentation such as the above, standards with different $^{13}C$ labelling (e.g. $^{13}C_1$, $^{13}C_6$, etc.), other mobility gases and variations in operational parameters (e.g. the amplitude and frequency of the travelling wave), could provide valuable insight into some of these previously unknown areas.

# Chapter 6

# Conclusions, Outlook and Future Research

## 6.1 Conclusions

The initial aims and objectives of this thesis stemmed from the need to address various concerns in the published methods for the ultratrace analysis of persistent organic pollutants (POPs) such as polychlorinated dioxins (PCDDs), furans (PCDFs) and biphenyls (PCBs). The introductory chapter discussed several historical and contemporary sources of these compounds and some of the known health effects. Of note was that current human exposure is primarily through food, and this has led to legislation within the EU and other territories that define the maximum permitted concentrations of PCDDs, PCDFs and PCBs in both food and in animal feed.

The correct determination of these compounds' concentrations is therefore a key requirement in food and feed testing, and e.g. epidemiological studies, and other environmental monitoring and remediation programs. Although that may seem to be an obvious, perhaps trite, statement, especially considering the complex sample preparation, use of carbon-13 labelled standards and the level of instrumentation required for such analyses, there are nevertheless aspects of the methods – measurement artefacts – that can result in incorrectly reported concentrations.

The methods in question were founded on two key pillars:

1. The use of isotope dilution, i.e. (briefly) where the responses of native ($^{12}C_{12}$) standards are referenced against $^{13}C_{12}$-labelled standards to determine relative response factors (RRFs) for calibration purposes; subsequently, the unknown sample concentrations can be calculated from their responses and those of the corresponding $^{13}C_{12}$-labelled standards together with their calibration RRFs. (See section 1.12 for comprehensive details on the isotope dilution technique.)
2. The use of gas-chromatography (GC) coupled with high-resolution mass spectrometry (HRMS) operating at a resolution of ≥ 10,000 (m/Δm, 10% valley definition) using selected ion monitoring (SIM) for data acquisition.

Other technologies, such as GC-MS/MS (tandem mass spectrometry using, e.g. triple-quadrupole or hybrid quadrupole/time-of-flight technologies) and bioanalytical (e.g. immunoassay) based techniques were also discussed as both are now used for limited testing of these compounds, but GC-HRMS based analysis remains the *de facto* standard as it complies with all current regulatory requirements.

The reasons for the use of both HRMS and SIM were also described in Chapter 1, but a consequence of using the latter (to achieve the required sensitivity) is that compound identification now relies on just 2 parameters: GC retention time (RT) and the isotope ratio determined from the peak areas measured from the 2 ion traces at that RT. If a detected compound elutes within its predicted RT window and the measured isotope ratio is within a specified tolerance of the theoretical value, then the compound is confirmed as that expected.

However, as discussed in Chapter 2, measurement variances due to the statistical nature of a mass spectrometer's ion production and detection methods can result in the failure to meet this ratio requirement, even for valid compounds. This led to an extensive review of the ion detection process, associated calculations and to the use of Monte Carlo techniques to model isotope ratio measurements for different peak intensities and measurement dwell times to determine the expected failure rates; simulations using this model compared well with actual data.

An interesting example based on some pentachlorinated biphenyl (PeCB) data was also shown. The isotope ratio test is based on the responses from the two most intense ions of the molecular ion cluster, but for PeCBs the M+0 and M+4 intensities are approximately equal, and therefore the ratio can be determined from either M+0/M+2 or M+2/M+4. Data were shown where the ion ratios had been determined from both pairs and produced the paradoxical result of PCB-114 (amongst others) being in-ratio in one case and out-of-ratio in the other. Although here it simply exposed the weakness of the ratio test, it must be realised that this would not ordinarily be possible since, in routine analyses, only one pair of ions would be monitored and thus any analyst would be unaware of such conflicting data. The modelling also showed that the failure rate is asymmetrical, i.e. more peaks fail with ratios > +15% than with those with ratios < -15%.

The use of toxic equivalency factor (TEFs) and their resulting toxic equivalent concentrations (TEQs) is also relevant here. These factors are used to scale the measured concentrations of each toxic congener and the results summed to produce a single concentration value. This allows direct comparisons between samples and, for regulatory work, a straightforward pass/fail determination. If one of the toxic compounds – such as PCB-114 in the above example – is then incorrectly assessed by the ratio test, a significant bias to the result can occur.

The idea of modifying the relative dwell times of the monitored ion pairs to minimise the ion statistical variances according to their theoretical isotope ratios was also explored and showed some unexpected results. E.g. monochlorinated biphenyl (MoCB) has a theoretical isotope abundance ratio of 3.06, therefore it was assumed that by proportioning the dwell times in a 25:75 ratio, rather than the default 50:50, the number of ions detected at each *m/z* would be equal and thus the performance would be optimal with each *m/z* showing the same statistical variance. The former was true (implicitly), the ion counts do then match, but not the latter. The model showed that the optimum occurred with a 37:63 ratio due to the greater overall number of primary ions detected. A related optimisation strategy based on expected signal levels also showed the benefit of reallocating some of the available channel dwell time from that used for the *m/z* channels of nominally high-level standards to those of the target compounds.

The observation was then made that the rationale behind the 15% isotope ratio tolerance, as used by the PCDD/F and PCB methods, has never been explained nor any supporting data or other references provided, and it was probably established empirically from early experimental work. Similarly, the published GC-HRMS method for organochlorine pesticides uses tolerances of 25% and 35% without justification. Irrespective of whether the 15% tolerance or any other value is chosen, it remains an arbitrary value that can only serve as a compromise: as discussed, it can be both too restrictive for the variances that accompany low-level signals and too broad to identify possible problems at higher levels. Therefore, a key proposal arising from this work is that the ratio tolerance should be a dynamic rather than static parameter, and a chart and associated calculations demonstrating its implementation were shown.

Although such an approach would formerly have presented technical challenges, it could now be readily incorporated into the data processing software and provide the users with a more fit-for-purpose identification schema. Its benefits were also shown in an example where a series of high-level peaks all fell within the original 15% tolerance, but failed the dynamic ratio test where a 2% value was suggested: since the absolute mean ratio error was ~9%, but the RSD was less than 1%, this immediately indicated a calibration or other instrument related problem. Such an approach can be equally useful for MS/MS data and has the side benefit of providing an alternative measure of a peak's signal-to-noise ratio.

Despite the weaknesses of the existing isotope ratio criterion, replacing or supplanting it with the proposed dynamic test is more likely to face ethical and political rather than technical barriers. For example, if a sample's reported TEQ is above some regulated level using the existing method, but below using the proposed version, or *vice-versa*, how is any legal action, product withdrawal or other consequence amended? In any event, a peer-reviewed inter-laboratory study is required in the first instance and, as discussed, some regions, such as the EU, may be more accepting of such changes as has previously been demonstrated by its adoption of GC-MS/MS instrumentation as a valid alternative to GC-HRMS for certain regulatory analyses of food and animal feed.

The concern over isotope ratios also revealed several discrepancies between the methods' quoted values and those given by the mass spectrometer's software and other online sources. This led to a validation exercise, discussed in Chapter 3, that included the development of "PureIso", an *ab initio* isotope cluster calculation program where the sources of all isotopic masses and abundances could be referenced. The program also addresses an important shortcoming of commercial isotope calculators by allowing the isotopic purities of $^{2}$H, $^{13}$C and $^{37}$Cl – as would be used by labelled standards in this work – to be defined. By limiting calculations to those of small molecules, i.e. as applicable to this study, the program did not need any filtering or other pruning type routines, as generally used to constrain the number of combinations to meet typical memory limitations, thereby further assuring its results.

A comparison between the calculated isotope ratios from PureIso and those from 3 out of 4 other programs showed excellent agreement (the 4th being a clear outlier from the consensus values). Comparisons between the calculated values and those published in the EPA methods showed errors <1.5% for all native PCB and PCDD/Fs but up to 3% for certain $^{13}$C-labelled PCDFs. Given the binary, detect vs. non-detect, result from applying the isotope ratio test – whether under the existing approach, or that proposed – the methods' values should be revised.

Given the increasing use of AP ionisation over traditional EI, the chapter discussed the potential effect on measured isotope ratios due to a mixture of both charge exchange and protonation occurring in the ion source. Although most ratio errors were small (or only affected the minor ions) they were, in the tests conducted, up to 4% which could contribute to uncertainty in peak confirmation, especially if coupled with other, e.g. statistical, errors.

Calculations to determine the degree of protonation were shown but it should be noted that this would require additional *m/z* or transitions for certain experiment types. As had been discussed in the previous chapter, any occurrences of incorrect ratio assessments can easily go unnoticed due to automated processing and reporting via databases, etc., with the unintended consequence of misreported concentrations or other inter-sample trends.

The discussion of measurement artefacts continued in Chapter 4 with an examination of the effects of fragmentation in PCB analysis. Unlike PCDD/F analysis, PCBs exhibit significant overlap of their analytical (*m/z* descriptor) functions that can result in interferences from fragment ions of more highly chlorinated congeners. Although the possibility of this occurring is referenced in the prevalent PCB method (EPA-1668C), there is no specific detail as to the nature of the problem and it incorrectly asserts that only a subset of 4 congeners are affected.

In cases where the interference is due to the loss of Cl, the ions formed would have the same isotope ratios (given the precision of the instrumentation used) and would thus be additive; for those due to the loss of 2Cl, the ratios would differ. Depending on the level of interference, the latter could cause an otherwise in-ratio peak to become out-of-ratio. Samples containing a small subset of known PCBs were analysed to demonstrate the formation of artefact peaks, i.e. false positives, due to the loss of Cl using both EI and AP ionisation. These were shown to be indistinguishable from the true congeners, with one example showing the formation of a peak identified as the toxic PCB-81. An analysis of the GC retention times of all 209 PCBs showed that 25 of these presented a potential problem due to the loss of Cl with 7 affecting one of the toxic compounds. For the loss of 2Cl, 4 PCBs were similarly identified with 3 affecting a toxic compound.

The loss of Cl was charted for all 209 PCBs using both EI and AP ionisation. These showed broadly similar patterns to each other with the highest level of fragmentation on those PCBs with Cl in at least the 2 and 2′ positions, i.e. ortho substituted on each ring. Less fragmentation was observed for non-toxic mono-ortho PCBs and the least for the toxic mono- or non-ortho substituted PCBs. This correlates with the steric hindrance imposed by the presence of Cl atoms in those positions and the consequent constrained rotation around the central C-C bond, and the more planar conformations that characterise the known toxic PCBs.

Analysis of the data from GC-MS/MS experiments using AP ionisation showed some surprising results. Although the isotope distribution of the molecular ion and loss of 2Cl clusters were as expected, this was not the case for several PCBs where the minor, M+1, M+3, etc. ions in the loss of Cl cluster – that should have been simply due to the natural $^{13}$C isotopes of M-Cl ions – suggested a mix of these with other odd electron species. The accurate mass data indicated that these were radical cations where the loss of Cl had occurred but with an H having been substituted. Although this possible Cl/H exchange mechanism, if correct, could not be explained, its occurrence was nevertheless supported by the ion mobility data shown in Chapter 5. The example discussed showed the formation of 3,3′,4,4′,5-PeCB from 3,3′,4,4′,5,5′-HxCB, i.e. with exchange occurring in one of the meta positions.

Further PCB studies using AP ionisation with GC-MS/MS at different collision energies led to the fragmentation profiles for a subset of 80 PCBs – this being limited by the available standards and potential coelution overlaps of the fragment ions. These profiles were submitted to principal component analysis (PCA) where certain groupings, such as for the non- and mono-ortho toxic PCBs, could be observed. A hypothesis being considered was that this analysis might identify certain PCBs as possible candidates for inclusion into the WHO list of known, and hence regulated, toxic compounds. Although PCB-11 and 37, both having been previously reported as having toxic properties, were shown to be close to the non-ortho substituted toxic PCB cluster, the cluster itself was not sufficiently separated from other, non-toxic, PCBs for it to be an unequivocal indicator of toxicity. This work would benefit from additional analyses using standards’ mixes where all PCBs and any fragment ions are distinctly resolved in retention time so that all 209 congeners can be analysed. A weakness of these data was that an insufficient number of collision energy (CE) points were used – due to instrument availability limitations – as some congeners showed rapid changes in fragmentation responses at, e.g. 10 and 20 eV CE, suggesting that data should also be acquired at 15 and 25 eV CE.

Such PCB mixes would also enable relative fragmentation responses to be determined for any molecular ion and their fragment losses for all cases where a coelution could exist; such a fragmentation calibration would address the method's deficiency in this regard by allowing interfering candidates to be automatically identified.

Chapter 5 showed that ion mobility separation in conjunction with mass spectrometry (IMS-MS) could provide an additional dimension to the data by showing the structural grouping for all 209 PCBs in terms of their degree of ortho substitution. Because of the very large number of peaks present in the IMS-MS data two different processing strategies were developed; this included the development of a novel program, DriftScope Analyser (DSA) to process and display the data exported from the instrument's software.

For each PCB, its collision cross section (CCS) was calculated from the arrival time distribution (ATD) data and molecular modelling software was used to determine its optimum structure conformation. The resulting modelled data was then submitted to 2 further programs to estimate CCS using both projection approximation and trajectory methods. The CCS results from the modelled data showed good agreement with those from the acquired mobility data, and for a subset of 26 PCBs for which published data were available.

Using the DSA program also revealed some unexpected offsets of the ATDs of the secondary (minor) – naturally occurring $^{13}C$ ions – relative to the primary (major) ions for some PCBs. It would be expected that the ATDs would simply increase in accordance with mass since an ion's structure – and hence its CCS – is nominally identical for all isotopologues of the same compound.

Modifications were then made to the MS processing software such that the ion mobility ATDs could be recalculated in greater detail from the extracted accurate mass data. This enabled more precise comparisons between the ATDs of isotopologues despite the very low ion mobility resolution available. These data were very surprising in that they showed the formation of doublets in the secondary ion ATD data. The centroids from these doublets matched the offsets observed in the DSA data but when these were split into 2 peaks, the lower ATD peak now aligned with the ATD of the primary ions; however, the upper in each of the examples studied matched the ATD of another compound – this suggested that (partial) isomerisation was occurring.

Because of the low ion mobility resolution, this study could only be performed for a small number of PCBs where the doublets were clearly present, but in each case the alignment indicated that a rearrangement of ortho-substituted Cl to meta was occurring. One example shown was the isomerisation of 2,2',3,4,6,6'-HxCB (PCB-145) to 2,3,3',4,5,5'-HxCB (PCB-159), i.e. the 2', 6 and 6' ortho Cl have rearranged to the 3', 5 and 5' meta positions respectively. This is also energetically favourable whereas certain other rearrangements, e.g. from 2,2',4,4',6,6'-HxCB (PCB-155) to 3,3',4,4',5,5'-HxCB (PCB-169), are not and therefore do not occur. A puzzle that remains with the above is that it is only observed for the secondary ($^{13}$C) ions.

Changes to an ion's centre-of-mass, the effects of nuclear spin and thermal effects due to heating in the ion mobility cell were considered as possible causes and this led to a computer-modelling based study of the certain PCB's infrared (IR) spectra. This showed different bond frequencies and magnitudes corresponding to the isotopologue and isotopomer variations. PCA analysis of these data showed clear clustering of the data from PCB-188 and 189 in both native and $^{13}C_{12}$-labelled forms together with their respective $^{13}C_1$ and $^{12}C_1$ isotopologues and corresponding isotopomers. However, these data did not explain why the presence of a single $^{13}$C could give rise to the effects observed and therefore some combination of the above, or an as yet unknown mechanism is responsible.

## 6.2 Outlook

Refinement of the analytical methods derived from this research should, following appropriate validation, lead to an increase in data quality by addressing the current weaknesses associated with isotope ratio measurements and fragmentation effects. This not only benefits data obtained from a single laboratory but, by providing a more scientifically sound method, it will also improve data integrity obtained from multiple sources. This is particularly important for large-scale studies which, by necessity, process samples using a network of laboratories and where unwanted variances could mask important patterns thereby reducing a study's effectiveness and potentially leading to incorrect assumptions or decisions. Although this research has primarily focussed on PCB analysis, many of the ideas are directly transferrable to the analysis of other POPs including brominated flame retardants, mixed halogenated compounds, polychlorinated naphthalenes and pesticides.

Over the last 3 decades since these analytical methods came into widespread usage, the performance of magnetic sector instruments, on which they were based (and still widely used), has seen only minor gains while other technologies, e.g. triple-quad or hybrid Q-TOF instruments and with other ionisation methods, have made impressive gains in performance; these are already used as viable alternatives in some areas of analysis – a trend that can only continue. This study has highlighted areas that impact these innovative technologies and will therefore help to transition the methods to accommodate them, especially given the legislation and legacy issues involved.

## 6.3 Future research

Alongside several useful and novel findings, this research also raised new questions – in particular, the proposed radical ion formation in the fragmentation experiments, and the ion mobility ATD doublets and their proposed rearrangements that appear to uniquely affect only the minor, e.g. M+1, M+3, etc., $^{13}C$ ions.

The fragmentation study needs to be extended to use PCB mixes with far greater retention time separation of individual components such that no coelutions are detectable even at much lower levels than considered acceptable in the mixes used here. Data needs to be acquired at additional collision energies and with different collision gases and pressures.

An instrument with higher resolution ion mobility – such as the recently developed cyclic travelling wave device – would be the single most beneficial factor in the study of the ATD doublets and isomerisation. The doublets were the clearest manifestation of more widespread peak broadening, but it is not yet known whether more complex structures, such as multiplets, exist due to the limited resolution available. In addition, the analysis of new PCB standards with different degrees of $^{13}C$-labelling and the use of other mobility cell gases and pressures would be required to investigate these effects in more detail.

Of course, this work does not need to be restricted to PCBs, but given the above discoveries, they would form a solid foundation for the investigative procedures needed for many of the related POPs – the data are the key.

# References

Adams, K.J., Smith, N.F., Ramirez, C.E. and Fernandez-Lima, F., 2018. Discovery and targeted monitoring of polychlorinated biphenyl metabolites in blood plasma using LC-TIMS-TOF MS. *International Journal of Mass Spectrometry,* 427, 133-140. doi:10.1016/j.ijms.2017.11.009.

Alford-Stevens, A., Bellar, T., Eichelberger, J. and Budde, W., 1985. *Method 680: Determination of Pesticides and PCBs in Water and Soil/Sediment by Gas Chromatography/Mass Spectrometry.*
United States Environmental Protection Agency.

Anderson, D.R. and Fisher, R., 2002. Sources of dioxins in the United Kingdom: the steel industry and other sources. *Chemosphere,* 46(3), 371-381. doi:10.1016/S0045-6535(01)00178-3.

Andersson, P., Haglund, P. and Tysklind, M., 1997. The internal barriers of rotation for the 209 polychlorinated biphenyls. *Environmental Science and Pollution Research,* 4(2), 75-81. doi:10.1007/BF02986283.

Anezaki, K., Kannan, N. and Nakano, T., 2015. Polychlorinated biphenyl contamination of paints containing polycyclic- and Naphthol AS-type pigments. *Environmental Science and Pollution Research,* 22(19), 14478-14488. doi:10.1007/s11356-014-2985-6.

Anezaki, K. and Nakano, T., 2014. Concentration levels and congener profiles of polychlorinated biphenyls, pentachlorobenzene, and hexachlorobenzene in commercial pigments. *Environmental Science and Pollution Research,* 21(2), 998-1009. doi:10.1007/s11356-013-1977-2.

Anscombe, F.J., 1948. The Transformation of Poisson, Binomial and Negative-Binomial Data. *Biometrika,* 35(3/4), 246. doi:10.2307/2332343.

Antunes Fernandes, E.C., Heniks, H.S., van Kleef, R. G. D. M, Reniers, A., Andersson, P.L., van den Berg, M. and Westerink, R.H.S., 2010. Activation and potentiation of human GABA(A) receptors by non-dioxin-like PCBs depends on chlorination pattern. *Toxicological Sciences,* 118(1), 183-190. doi:10.1093/toxsci/kfq257.

Atkinson, A.C., 1979. The Computer Generation of Poisson Random Variables. *Journal of the Royal Statistical Society. Series C (Applied Statistics),* 28(1), 29-35. doi:10.2307/2346807.

Baccarelli, A., Mocarelli, P., Patterson, J., Donald G, Bonzini, M., Pesatori, A.C., Caporaso, N. and Landi, M.T., 2002. Immunologic effects of dioxin: new results from Seveso and comparison with other studies. *Environmental Health Perspectives,* 110(12), 1169-1173.

Ballschmiter, K. and Zell, M., 1980. Analysis of polychlorinated biphenyls (PCB) by glass capillary gas chromatography. *Fresenius Zeitschrift für Analytische Chemie,* 302(1), 20-31. doi:10.1007/BF00469758.

Baston, D.S. and Denison, M.S., 2011. Considerations for potency equivalent calculations in the Ah receptor-based CALUX bioassay: Normalization of superinduction results for improved sample potency estimation. *Talanta,* 83(5), 1415-1421. doi:10.1016/j.talanta.2010.11.035.

Berglund, M. and Wieser, M.E., 2011. Isotopic compositions of the elements 2009 (IUPAC Technical Report). *Pure and Applied Chemistry,* 83(2), 397-410. doi:10.1351/PAC-REP-10-06-02.

Bernard, A. and Fierens, S., 2002. The Belgian PCB/Dioxin Incident: A Critical Review of Health Risks Evaluations. *International Journal of Toxicology,* 21(5), 333-340. doi:10.1080/10915810290096540.

Bettmann, H., 1901. "Chlor-Akne", eine besondere Form von professioneller Hauterkrankung ["Chloracne", a special form of occupational skin disease]. *Deutsche Medizinische Wochenschrift,* 27. doi:10.1055/s-0029-1186933.

Bhavsar, S.P., Reiner, E.J., Hayton, A., Fletcher, R. and MacPherson, K., 2008. Converting Toxic Equivalents (TEQ) of dioxins and dioxin-like compounds in fish from one Toxic Equivalency Factor (TEF) scheme to another. *Environment International,* 34(7), 915-921. doi:10.1016/j.envint.2008.02.001.

Birnbaum, L.S. and Cummings, A.M., 2002. Dioxins and endometriosis: a plausible hypothesis. *Environmental health perspectives,* 110(1), 15-21.

Box, G.E.P. and Muller, M.E., 1958. A Note on the Generation of Random Normal Deviates. *The Annals of Mathematical Statistics,* 29(2), 610-611. doi:10.1214/aoms/1177706645.

Bureš, M., Pekárek, V. and Ocelka, T., 2007. Thermochemical properties and relative stability of polychlorinated biphenyls. *Environmental Toxicology and Pharmacology,* 25(2), 148-155. doi:10.1016/j.etap.2007.10.010.

Carson, R., 1962. *Silent Spring.* Greenwich, Conn: Fawcett.

CEN, 2012. *BS EN 16215:2012: Animal feeding stuffs. Determination of dioxins and dioxin-like PCBs by GC/HRMS and of indicator PCBs by GC/HRMS.* British Standards Institute.

Charles, M.J. and Tondeur, Y., 1990. Choosing between high-resolution mass spectrometry and mass spectrometry/mass spectrometry environmental applications. *Environmental Science & Technology,* 24(12), 1856-1860. doi:10.1021/es00082a011.

Colombo, A., Benfenati, E., Bugatti, S.G., Celeste, G., Lodi, M., Rotella, G., Senese, V. and Fanelli, R., 2011. Concentrations of PCDD/PCDF in soil close to a secondary aluminum smelter. *Chemosphere,* 85(11), 1719-1724. doi:10.1016/j.chemosphere.2011.09.018.

Covaci, A., Voorspoels, S., Schepens, P., Jorens, P., Blust, R. and Neels, H., 2007. The Belgian PCB/dioxin crisis—8 years later. *Environmental Toxicology and Pharmacology,* 25(2), 164-170. doi:10.1016/j.etap.2007.10.003.

Croes, K., Colles, A., Koppen, G., De Galan, S., Vandermarken, T., Govarts, E., Bruckers, L., Nelen, V., Schoeters, G., Van Larebeke, N., Denison, M.S., Mampaey, M. and Baeyens, W., 2013. Determination of PCDD/Fs, PBDD/Fs and dioxin-like PCBs in human milk from mothers residing in the rural areas in Flanders, using the CALUX bioassay and GC-HRMS. *Talanta,* 113, 99-105. doi:10.1016/j.talanta.2013.03.086.

Djidja, M., Claude, E., Snel, M.F., Scriven, P., Francese, S., Carolan, V. and Clench, M.R., 2009. MALDI-Ion Mobility Separation-Mass Spectrometry Imaging of Glucose-Regulated Protein 78 kDa (Grp78) in Human Formalin-Fixed, Paraffin-Embedded Pancreatic Adenocarcinoma Tissue Sections. *Journal of Proteome Research,* 8(10), 4876-4884. doi:10.1021/pr900522m.

Dorofeeva, O., Novikov, V., Moiseeva, N. and Yungman, V., 2005. Density functional calculation of conformations and potentials of internal rotation in polychlorinated biphenyls. *Journal of Structural Chemistry,* 46(2), 237-242. doi:10.1007/s10947-006-0036-y.

Drinker, C.K., Warren, M.F. and Bennett, G.A., 1937. The Problem of Possible Systemic Effects from Certain Chlorinated Hydrocarbons. *Journal of Industrial Hygiene and Toxicology,* 19, 283-299.

Eckers, C., Monaghan, J.J. and Wolff, J., 2005. Fragmentation of Trimethoprim and other Compounds Containing Alkoxy-Phenyl Groups in Electrospray Ionisation Tandem Mass Spectrometry. *European Journal of Mass Spectrometry,* 11(1), 73-82. doi:10.1255/ejms.719.

Eppe, G., Van Cleuvenbergen, R., Smastuen Haug, L., Boulanger, B., Becher, G. and De Pauw, E., 2008. Empirical relationship between precision and ultra-trace concentrations of PCDD/Fs and dioxin-like PCBs in biological matrices. *Chemosphere,* 71(2), 379-387. doi:10.1016/j.chemosphere.2007.08.046.

Erickson, M., 1997. *Analytical Chemistry of PCBs.* 2 edn. CRC Press.

Erickson, M. and Kaley, R., 2011. Applications of polychlorinated biphenyls. *Environmental Science and Pollution Research,* 18(2), 135-151. doi:10.1007/s11356-010-0392-1.

European Commission, 2017. *Commission Regulation (EU) 2017/644: laying down methods of sampling and analysis for the control of levels of dioxins, dioxin-like PCBs and non-dioxin-like PCBs in certain foodstuffs and repealing Regulation (EU) No 589/2014.* Brussels, Belgium: European Commission.

European Commission, 2006. *Commission Regulation (EU) - Setting maximum levels for certain contaminants in foodstuffs.* Brussels, Belgium: European Commission.

European Council, 1985. *Directive 85/467/EEC of 1 October 1985 amending for the sixth time (PCBs/PCTs) Directive 76/769/EEC on the approximation of the laws, regulations and administrative provisions of the Member States relating to restrictions on the marketing and use of certain dangerous substances and preparations.* Luxembourg: European Council.

Falandysz, J., Rose, M. and Fernandes, A.R., 2012. Mixed poly-brominated/chlorinated biphenyls (PXBs): Widespread food and environmental contaminants. *Environment International,* 44, 118-127. doi:10.1016/j.envint.2012.03.006.

Ferrario, J.B., Byrne, C.J. and Cleverly, D.H., 2000. 2,3,7,8-Dibenzo-p-dioxins in Mined Clay Products from the United States:  Evidence for Possible Natural Origin. *Environmental Science & Technology,* 34(21), 4524-4532. doi:10.1021/es001052r.

Frumkin, H., 2003. Agent Orange and Cancer: An Overview for Clinicians. *CA: A Cancer Journal for Clinicians,* 53(4), 245-255. doi:10.3322/canjclin.53.4.245.

Gabelica, V. and Marklund, E., 2018. Fundamentals of ion mobility spectrometry. *Current Opinion in Chemical Biology,* 42, 51-59. doi:10.1016/j.cbpa.2017.10.022.

Gabelica, V., Shvartsburg, A.A., Afonso, C., Barran, P., Benesch, J.L.P., Bleiholder, C., Bowers, M.T., Bilbao, A., Bush, M.F., Campbell, J.L., Campuzano, I.D.G., Causon, T., Clowers, B.H., Creaser, C.S., De Pauw, E., Far, J., Fernandez-Lima, F., Fjeldsted, J.C., Giles, K., Groessl, M., Hogan, C.J., Hann, S., Kim, H.I., Kurulugama, R.T., May, J.C., McLean, J.A., Pagel, K., Richardson, K., Ridgeway, M.E., Rosu, F., Sobott, F., Thalassinos, K., Valentine, S.J. and Wyttenbach, T., 2019. Recommendations for reporting ion mobility Mass Spectrometry measurements. *Mass Spectrometry Reviews,* 38(3), 291-320. doi:10.1002/mas.21585.

Giles, K., Pringle, S.D., Worthington, K.R., Little, D., Wildgoose, J.L. and Bateman, R.H., 2004. Applications of a travelling wave-based radio-frequency-only stacked ring ion guide. *Rapid Communications in Mass Spectrometry,* 18(20), 2401-2414. doi:10.1002/rcm.1641.

Giles, K., Ujma, J., Wildgoose, J., Pringle, S., Richardson, K., Langridge, D. and Green, M., 2019. A Cyclic Ion Mobility-Mass Spectrometry System. *Analytical Chemistry,* 91(13), 8564-8573. doi:10.1021/acs.analchem.9b01838.

Greaves, J., Harvey, E. and MacIntyre, W.G., 1994. Correlation between electron capture negative chemical ionization mass spectrometric fragmentation and calculated internal energies for polychlorinated biphenyls. *Journal of the American Society for Mass Spectrometry,* 5(1), 44-52. doi:10.1016/1044-0305(94)85083-6.

Green, B., Gray, B., Guyan, S. and Krolik, S., 1986. An El Source Optimised for Low Level Pollutant Analysis by GC-HRSIR, *34th Annual Conference on Mass Spectrometry and Allied Topics*. ASMS.

Grein, F., 2002. Twist Angles and Rotational Energy Barriers of Biphenyl and Substituted Biphenyls. *The Journal of Physical Chemistry A,* 106(15), 3823-3827. doi:10.1021/jp0122124.

Hamers, T.H.M., Kamstra, J.H., Cenijn, P.H., Palkova, L., Simeckova, P., Vonacek, J., Andersson, P.L., Stenberg, M. and Machala, M., 2011. In vitro toxicity profiling of ultrapure non-dioxin-like polychlorinated biphenyl (NDL-PCB) congeners and their relative toxic contribution to PCB-mixtures in humans. *Toxicological Sciences,* 121(1), 88-100. doi:10.1093/toxsci/kfr043.

Hanwell, M.D., Curtis, D.E., Lonie, D.C., Vandermeersch, T., Zurek, E. and Hutchison, G.R., 2012. Avogadro: an advanced semantic chemical editor, visualization, and analysis platform. *Journal of Cheminformatics,* 4(1), 17. doi:10.1186/1758-2946-4-17.

Harrison, A.G., Onuska, F.I. and Tsang, C.W., 1981. Chemical ionization mass spectrometry of specific polychlorinated biphenyl isomers. *Analytical Chemistry,* 53(8), 1183-1186. doi:10.1021/ac00231a010.

Hass, J.R. and Friesen, M.D., 1979. Qualitative and Quantitative Methods for Dioxin Analysis. *Annals of the New York Academy of Sciences,* 320, 28-42. doi:10.1111/j.1749-6632.1979.tb56590.x.

Hu, D., Martinez, A. and Hornbuckle, K.C., 2008. Discovery of Non-Aroclor PCB (3,3’-Dichlorobiphenyl) in Chicago Air. *Environmental Science & Technology,* 42(21), 7873-7877. doi:10.1021/es801823r.

IARC, 2012. *IARC Monographs on the Evaluation of Carcinogenic Risks to Humans.* Lyon, France: International Agency for Research on Cancer.

Johansson, M.P. and Olsen, J., 2008. Torsional Barriers and Equilibrium Angle of Biphenyl: Reconciling Theory with Experiment. *Journal of Chemical Theory and Computation,* 4(9), 1460-1471. doi:10.1021/ct800182e.

Jones, G.R., Richardson, K. and Green, M., 2011. Analysis of halogenated aromatic compounds by electron impact ionisation and ion mobility separation on a GC-EI-Q-IMS-ToF, *59th Annual Conference on Mass spectrometry and Allied Topics*. ASMS.

Kahn, L.G., Han, X., Koshy, T.T., Shao, Y., Chu, D.B., Kannan, K. and Trasande, L., 2018. Adolescents exposed to the World Trade Center collapse have elevated serum dioxin and furan concentrations more than 12 years later. *Environment International,* 111, 268-278. doi:10.1016/j.envint.2017.11.026.

Klosterhaus, S., McKee, L.J., Yee, D., Kass, J.M. and Wong, A., 2014. Polychlorinated biphenyls in the exterior caulk of San Francisco Bay Area buildings, California, USA. *Environment International,* 66, 38-43. doi:10.1016/j.envint.2014.01.008.

Knutsen, H.K., Alexander, J., Barregård, L., Bignami, M., Brüschweiler, B., Ceccatelli, S., Cottrill, B., Dinovi, M., Edler, L., Grasl-Kraupp, B., Hogstrand, C., Nebbia, C.S., Oswald, I.P., Petersen, A., Rose, M., Roudot, A., Schwerdtle, T., Vleminckx, C., Vollmer, G., Wallace, H., Fürst, P., Håkansson, H., Halldorsson, T., Lundebye, A., Pohjanvirta, R., Rylander, L., Smith, A., van Loveren, H., Waalkens-Berendsen, I., Zeilmaker, M., Binaglia, M., Gómez Ruiz, J.Á, Horváth, Z., Christoph, E., Ciccolallo, L., Ramos Bordajandi, L., Steinkellner, H. and Hoogenboom, L., 2018. Risk for animal and human health related to the presence of dioxins and dioxin-like PCBs in feed and food. *EFSA Journal,* 16(11),. doi:10.2903/j.efsa.2018.5333.

Kotz, A., Hädrich, J., Wahl, K., Djuchin, K. and Malisch, R., 2014. Application of amended criteria for confirmatory methods for determination of PCDD/Fs and DL-PCBs in feed and food. *Organohalogen Compounds,* 76, 293-296.

Kuratsune, M., Yoshimura, T., Matsuzaka, J. and Yamaguchi, A., 1972. Epidemiologic study on Yusho, a Poisoning Caused by Ingestion of Rice Oil Contaminated with a Commercial Brand of Polychlorinated Biphenyls. *Environmental Health Perspectives,* 1, 119-128.

Kutz, F.W., Barnes, D.G., Bottimore, D.P., Greim, H. and Bretthauer, E.W., 1990. The international toxicity equivalency factor (I-TEF) method of risk assessment for complex mixtures of dioxins and related compounds. *Chemosphere,* 20(7), 751-757. doi:10.1016/0045-6535(90)90178-V.

Lanucara, F., Holman, S.W., Gray, C.J. and Eyers, C.E., 2014. The power of ion mobility-mass spectrometry for structural characterization and the study of conformational dynamics. *Nature Chemistry,* 6(4), 281-294. doi:10.1038/nchem.1889.

Lauby-Secretan, B., Loomis, D., Baan, R., El Ghissassi, F., Bouvard, V., Benbrahim-Tallaa, L., Guha, N., Straif, K. and Mattock, H., 2013. Carcinogenicity of polychlorinated biphenyls and polybrominated biphenyls. *The Lancet Oncology,* 14(4), 287-288. doi:10.1016/S1470-2045(13)70104-9.

Laušević, M., Splendore, M. and March, R.E., 1996. Modulated Resonant Excitation of Selected Polychlorobiphenyl Molecular Ions in an Ion Trap Mass Spectrometer. *Journal of Mass Spectrometry,* 31(11), 1244-1252. doi:10.1002/(SICI)1096-9888(199611)31:113.0.CO;2-U.

Lemieux, P.M., Lutes, C.C., Abbott, J.A. and Aldous, K.M., 2000. Emissions of Polychlorinated Dibenzo-p-dioxins and Polychlorinated Dibenzofurans from the Open Burning of Household Waste in Barrels. *Environmental Science & Technology,* 34(3), 377-384. doi:10.1021/es990465t.

Leng, L., Li, J., Li, Y., Li, G., Luo, X., Kim, J., Guo, X., Chen, X., Yang, Q. and Tang, N., 2016. Polychlorinated biphenyls and breast cancer: A congener-specific meta-analysis. *Environment International,* 88, 133-141. doi:10.1016/j.envint.2015.12.022.

Lin, K., Guo, N., Tsai, P., Yang, C. and Guo, Y.L., 2008. Neurocognitive changes among elderly exposed to PCBs/PCDFs in Taiwan. *Environmental Health Perspectives,* 116(2), 184-189. doi:10.1289/ehp.10134.

Loos, M., Gerber, C., Corona, F., Hollender, J. and Singer, H., 2015. Accelerated Isotope Fine Structure Calculation Using Pruned Transition Trees. *Analytical Chemistry,* 87(11), 5738-5744. doi:10.1021/acs.analchem.5b00941.

Malisch, R., Bernsmann, T., Ceci, R., Diletti, G., Eppe, G., Fernandes, A., Fiedler, H., Hart, J., Hoogenboom, R., Hove, H., Knetsch, G., Leondiadis, L., Lüth, A., Marchand, P., Maszewski, S., Rose, M., Schaechtele, A., Vanderperren, H., van Leeuwen, S., van Raamsdonk, L. and Vassiliadou, I., 2017. Interactive data base of PCDD/F and PCB congener patterns to aid identification of contamination sources in feed and food. *Organohalogen Compounds,* 79, 545-547.

Marklund, E., Degiacomi, M., Robinson, C., Baldwin, A. and Benesch, J.P., 2015. Collision Cross Sections for Structural Proteomics. *Structure,* 23(4), 791-799. doi:10.1016/j.str.2015.02.010.

Marsaglia, G., 1965. Ratios of Normal Variables and Ratios of Sums of Uniform Variables. *Journal of the American Statistical Association,* 60(309), 193-204. doi:10.1080/01621459.1965.10480783.

Mason, E.A. and MacDaniel, E.W., 1988. *Transport properties of ions in gases.* New York, USA: Wiley.

Massachusetts Department of Environmental Protection, 1991-last update, Assessment and Control of Dioxin in Massachusetts: https://www.mass.gov/files/documents/2017/11/08/Assessment%20%26%20Control%20of%20Dioxin%20in%20Massachusetts%20-%201991.pdf [Oct 3, 2019].

May, J.C. and McLean, J.A., 2015. Ion Mobility-Mass Spectrometry: Time-Dispersive Instrumentation. *Analytical Chemistry,* 87(3), 1422-1436. doi:10.1021/ac504720m.

McFarland, V.A. and Clarke, J.U., 1989. Environmental Occurrence, Abundance, and Potential Toxicity of Polychlorinated Biphenyl Congeners: Considerations for a Congener-Specific Analysis. *Environmental Health Perspectives,* 81, 225-239. doi:10.1289/ehp.8981225.

Megson, D., Robson, M., Jobst, K.J., Helm, P.A. and Reiner, E.J., 2016. Determination of Halogenated Flame Retardants Using Gas Chromatography with Atmospheric Pressure Chemical Ionization (APCI) and a High-Resolution Quadrupole Time-of-Flight Mass Spectrometer (HRqTOFMS). *Analytical Chemistry,* 88(23), 11406-11411. doi:10.1021/acs.analchem.6b01550.

Meija, J., Coplen, T.B., Berglund, M., Brand, W.A., De Bièvre, P., Gröning, M., Holden, N.E., Irrgeher, J., Loss, R.D., Walczyk, T. and Prohaska, T., 2016a. Atomic weights of the elements 2013 (IUPAC Technical Report). *Pure and Applied Chemistry,* 88(3), 265-291. doi:10.1515/pac-2015-0305.

Meija, J., Coplen, T.B., Berglund, M., Brand, W.A., De Bièvre, P., Gröning, M., Holden, N.E., Irrgeher, J., Loss, R.D., Walczyk, T. and Prohaska, T., 2016b. Isotopic compositions of the elements 2013 (IUPAC Technical Report). *Pure and Applied Chemistry,* 88(3), 293-306. doi:10.1515/pac-2015-0503.

Merlivat, L., 1978. Molecular diffusivities of H2[16O], HD[16O], and H2[18O] in gases. *The Journal of Chemical Physics,* 69(6), 2864. doi:10.1063/1.436884.

Metropolis, N. and Ulam, S., 1949. The Monte Carlo Method. *Journal of the American Statistical Association,* 44(247), 335-341.

Mills III, S.A., Thal, D.I. and Barney, J., 2007. A summary of the 209 PCB congener nomenclature. *Chemosphere,* 68(9), 1603-1612. doi:10.1016/j.chemosphere.2007.03.052.

Mocarelli, P., Marocchi, A., Brambilla, P., Gerthoux, P., Young, D.S. and Mantel, N., 1986. Clinical laboratory manifestations of exposure to dioxin in children. A six-year study of the effects of an environmental disaster near Seveso, Italy. *JAMA,* 256(19), 2687. doi:10.1001/jama.1986.03380190057025.

Mocarelli, P., Gerthoux, P., Ferrari, E., Patterson, D., Kieszak, S., Brambilla, P., Vincoli, N., Signorini, S., Tramacere, P., Carreri, V., Sampson, E., Turner, W. and Needham, L., 2000. Paternal concentrations of dioxin and sex ratio of offspring. *The Lancet,* 355(9218), 1858-1863. doi:10.1016/S0140-6736(00)02290-X.

Morsa, D., Gabelica, V. and De Pauw, E., 2014. Fragmentation and Isomerization Due to Field Heating in Traveling Wave Ion Mobility Spectrometry. *Journal of The American Society for Mass Spectrometry,* 25(8), 1384-1393. doi:10.1007/s13361-014-0909-9.

Muccio, Z. and Jackson, G.P., 2009. Isotope ratio mass spectrometry. *Analyst,* 134(2), 213-222. doi:10.1039/b808232d.

Murk, A.J., Legler, J., Denison, M.S., Giesy, J.P., van de Guchte, C. and Brouwer, A., 1996. Chemical-Activated Luciferase Gene Expression (CALUX): A Novel in Vitro Bioassay for Ah Receptor Active Compounds in Sediments and Pore Water. *Fundamental and Applied Toxicology,* 33(1), 149-160.

Murray, K.K., Boyd, R.K., Eberlin, M.N., Langley, G.J., Li, L. and Naito, Y., 2013. Definitions of terms relating to mass spectrometry (IUPAC Recommendations 2013). *Pure and Applied Chemistry,* 85(7), 1515-1609. doi:10.1351/PAC-REC-06-04-06.

Neese, F., 2012. The ORCA program system. *Wiley Interdisciplinary Reviews: Computational Molecular Science,* 2(1), 73-78. doi:10.1002/wcms.81.

Organtini, K.L., Haimovici, L., Jobst, K.J., Reiner, E.J., Ladak, A., Stevens, D., Cochran, J.W. and Dorman, F.L., 2015. Comparison of Atmospheric Pressure Ionization Gas Chromatography-Triple Quadrupole Mass Spectrometry to Traditional High-Resolution Mass Spectrometry for the Identification and Quantification of Halogenated Dioxins and Furans. *Analytical Chemistry,* 87(15), 7902-7908. doi:10.1021/acs.analchem.5b01705.

Pessah, I.N., Cherednichenko, G. and Lein, P.J., 2010. Minding the calcium store: Ryanodine receptor activation as a convergent mechanism of PCB toxicity. *Pharmacology and Therapeutics,* 125(2), 260-285. doi:10.1016/j.pharmthera.2009.10.009.

Popelier, P.L.A., Maxwell, P.I., Thacker, J.C.R. and Alkorta, I., 2018. A relative energy gradient (REG) study of the planar and perpendicular torsional energy barriers in biphenyl. *Theoretical Chemistry Accounts,* 138(1). doi:10.1007/s00214-018-2383-0.

Pradeep, P., Carlson, L.M., Judson, R., Lehmann, G.M. and Patlewicz, G., 2019. Integrating data gap filling techniques: A case study predicting TEFs for neurotoxicity TEQs to facilitate the hazard assessment of polychlorinated biphenyls. *Regulatory Toxicology and Pharmacology,* 101, 12-23. doi:10.1016/j.yrtph.2018.10.013.

Pringle, S.D., Giles, K., Wildgoose, J.L., Williams, J.P., Slade, S.E., Thalassinos, K., Bateman, R.H., Bowers, M.T. and Scrivens, J.H., 2007. An investigation of the mobility separation of some peptide and protein ions using a new hybrid quadrupole/travelling wave IMS/oa-ToF instrument. *International Journal of Mass Spectrometry,* 261(1), 1-12. doi:10.1016/j.ijms.2006.07.021.

Rappe, A.K., Casewit, C.J., Colwell, K.S., Goddard, W.A. and Skiff, W.M., 1992. UFF, a full periodic table force field for molecular mechanics and molecular dynamics simulations. *Journal of the American Chemical Society,* 114(25), 10024-10035. doi:10.1021/ja00051a040.

Rayne, S., Ikonomou, M., Butt, C., Diamond, M. and Truong, J., 2005. Polychlorinated Dioxins and Furans from the World Trade Center Attacks in Exterior Window Films from Lower Manhattan in New York City. *Environmental Science & Technology,* 39(7), 1995-2003. doi:10.1021/es049211k.

Revercomb, H.E. and Mason, E.A., 1975. Theory of plasma chromatography/gaseous electrophoresis. Review. *Analytical Chemistry,* 47(7), 970-983. doi:10.1021/ac60357a043.

Rice, J.A., 2007. *Mathematical statistics and data analysis.* Belmont, California, USA: Thomson Brooks/Cole.

Rivera-Austrui, J., Borrajo, M.A., Martinez, K., Adrados, M.A., Abalos, M., Van Bavel, B., Rivera, J. and Abad, E., 2011. Assessment of polychlorinated dibenzo- p-dioxin and dibenzofuran emissions from a hazardous waste incineration plant using long-term sampling equipment. *Chemosphere,* 82(9), 1343-1349. doi:10.1016/j.chemosphere.2010.11.054.

Roy, M.A., Sant, K.E., Venezia, O.L., Shipman, A.B., McCormick, S.D., Saktrakulkla, P., Hornbuckle, K.C. and Timme-Laragy, A.R., 2019. The emerging contaminant 3,3'-dichlorobiphenyl (PCB-11) impedes Ahr activation and Cyp1a activity to modify embryotoxicity of Ahr ligands in the zebrafish embryo model (Danio rerio). *Environmental Pollution,* 254(Pt A), 113027. doi:10.1016/j.envpol.2019.113027.

Safe, S., Bandiera, S., Sawyer, T., Robertson, L., Safe, L., Parkinson, A., Thomas, P., Ryan, D., Reik, L., Levin, W., Denomme, M. and Fujita, T., 1985. PCBs: Structure-Function Relationships and Mechanism of Action. *Environmental Health Perspectives,* 60, 47-56.

Salamanca, M., Chandía, C. and Hernández, A., 2016. Impact of forest fires on the concentrations of polychlorinated dibenzo-p-dioxin and dibenzofurans in coastal waters of central Chile. *Science of the Total Environment,* 573, 1397-1405. doi:10.1016/j.scitotenv.2016.07.113.

Savitzky, A. and Golay, M., 1964. Smoothing and Differentiation of Data by Simplified Least Squares Procedures. *Analytical Chemistry,* 36(8), 1627-1639. doi:10.1021/ac60214a047.

Schaechtele, A., Haedrich, J., Ceci, R., Diletti, G., Eppe, G., Fernades, A., Hart, J., Hove, H., Leondiadis, L., Marchand, P., Moche, W., Scholl, G., Scortichini, G., Tondeur, Y., Van Leeuwen, S., Vassiliadou, I. and Malisch, R., 2016. Estimation of LOQ for the Analysis of Persistent Organic Pollutants, in particular PCDD/Fs and PCBs. *Organohalogen Compounds,* 78, 829-831.

Schecter, A., Dai, L.C., Le, T., Quynh, H., Minh, D., Cau, H.D., Phiet, P., Nguyen, T., Constable, J.D., Baughman, R., Papke, O., Ryan, J., Furst, P. and Raisanen, S., 1995. Agent-Orange and the Vietnamese - The Persistence of Elevated Dioxin Levels in Human Tissues. *American Journal of Public Health; Am.J.Public Health,* 85(4), 516-522.

Schecter, A. and Tiernan, T., 1985. Occupational exposure to polychlorinated dioxins, polychlorinated furans, polychlorinated biphenyls, and biphenylenes after an electrical panel and transformer accident in an office building in Binghamton, NY. *Environmental Health Perspectives,* 60, 305-313.

Shvartsburg, A.A., Clemmer, D.E. and Smith, R.D., 2010. Isotopic Effect on Ion Mobility and Separation of Isotopomers by High-Field Ion Mobility Spectrometry. *Analytical Chemistry,* 82(19), 8047-8051. doi:10.1021/ac101992d.

Shvartsburg, A.A. and Smith, R.D., 2008. Fundamentals of Traveling Wave Ion Mobility Spectrometry. *Analytical Chemistry,* 80(24), 9689-9699. doi:10.1021/ac8016295.

Simon, T., Britt, J.K. and James, R.C., 2007. Development of a neurotoxic equivalence scheme of relative potency for assessing the risk of PCB mixtures. *Regulatory Toxicology and Pharmacology,* 48(2), 148-170. doi:10.1016/j.yrtph.2007.03.005.

Smith, D.P., Knapman, T.W., Campuzano, I., Malham, R.W., Berryman, J.T., Radford, S.E. and Ashcroft, A.E., 2009. Deciphering Drift Time Measurements from Travelling Wave Ion Mobility Spectrometry-Mass Spectrometry Studies. *European Journal of Mass Spectrometry,* 15(2), 113-130. doi:10.1255/ejms.947.

Solan, S., Wallenstein, S., Shapiro, M., Teitelbaum, S.L., Stevenson, L., Kochman, A., Kaplan, J., Dellenbaugh, C., Kahn, A., Biro, F., Crane, M., Crowley, L., Gabrilove, J., Gonsalves, L., Harrison, D., Herbert, R., Luft, B., Markowitz, S.B., Moline, J., Niu, X., Sacks, H., Shukla, G., Udasin, I., Lucchini, R.G., Boffetta, P. and Landrigan, P.J., 2013. Cancer Incidence in World Trade Center Rescue and Recovery Workers, 2001–2008. *Environmental Health Perspectives,* 121(6), 699-704. doi:10.1289/ehp.1205894.

Sorg, O., 2014. AhR signalling and dioxin toxicity. *Toxicology Letters,* 230(2), 225-233. doi:10.1016/j.toxlet.2013.10.039.

Sorg, O., Zennegg, M., Schmid, P., Fedosyuk, R., Valikhnovskyi, R., Gaide, O., Kniazevych, V. and Saurat, J., 2009. 2,3,7,8-tetrachlorodibenzo-p-dioxin (TCDD) poisoning in Victor Yushchenko: identification and measurement of TCDD metabolites. *The Lancet,* 374(9696), 1179-1185. doi:10.1016/S0140-6736(09)60912-0.

Stec, A.A., Dickens, K., Barnes, J.L.J. and Bedford, C., 2019. Environmental contamination following the Grenfell Tower fire. *Chemosphere,* 226, 576-586. doi:10.1016/j.chemosphere.2019.03.153.

Takasuga, T., Senthilkumar, K., Matsumura, T., Shiozaki, K. and Sakai, S., 2006. Isotope dilution analysis of polychlorinated biphenyls (PCBs) in transformer oil and global commercial PCB formulations by high resolution gas chromatography–high resolution mass spectrometry. *Chemosphere,* 62(3), 469-484. doi:10.1016/j.chemosphere.2005.04.034.

ten Dam, G., Pussente, I.C., Scholl, G., Eppe, G., Schaechtele, A. and van Leeuwen, S., 2016. The performance of atmospheric pressure gas chromatography–tandem mass spectrometry compared to gas chromatography–high resolution mass spectrometry for the analysis of polychlorinated dioxins and polychlorinated biphenyls in food and feed samples. *Journal of Chromatography A,* 1477, 76-90. doi:10.1016/j.chroma.2016.11.035.

Tlustos, C., Sheridan, M., O'Sullivan, D., Anderson, W. and Flynn, A., 2012. The dioxin contamination incident in Ireland, 2008: analytical results and congener patterns. *Food Additives & Contaminants: Part A,* 29(1), 128-138. doi:10.1080/19440049.2011.615030.

Tondeur, Y., Beckert, W., Billets, S. and Mitchum, R., 1989. Method 8290: an analytical protocol for the multimedia characterization of polychlorinated dibenzodioxins and dibenzofurans by high-resolution gas chromatography/high-resolution mass spectrometry. *Chemosphere,* 18(1), 119-131. doi:10.1016/0045-6535(89)90112-4.

Tondeur, Y. and Hart, J., 2009. Ultratrace extraction of persistent organic pollutants. *Trends in Analytical Chemistry,* 28(10), 1137-1147. doi:10.1016/j.trac.2009.07.009.

Tondeur, Y., Vining, B., Mace, K., Mills, W. and Hart, J., 2012. Environmental release of dioxins from reservoir sources during beach nourishment programs. *Chemosphere,* 88(3), 358-363. doi:10.1016/j.chemosphere.2012.03.057.

Turner, W., Welch, S., DiPietro, E., Cash, T., McClure, C., Needham, L. and Patterson, D., 2004. The Phantom Menace -- Determination of the True Method Detection Limit (MDL) for Background Levels of PCDDs, PCDFs, and cPCBs in Human Serum by High-Resolution Mass Spectrometry. *Organohalogen Compounds,* 66, 264-271.

Turro, N.J., 1983. Influence of Nuclear Spin on Chemical Reactions: Magnetic Isotope and Magnetic Field Effects (A Review). *Proceedings of the National Academy of Sciences of the United States of America,* 80(2), 609-621. doi:10.1073/pnas.80.2.609.

UNEP, 2019-last update, United Nations Treaty Collection: Stockholm Convention on Persistent Organic Pollutants: https://treaties.un.org/Pages/ViewDetails.aspx?src=IND&mtdsg_no=XXVII-15&chapter=27&clang=_en [Nov 9, 2019].

UNEP, 2018-last update, Chemicals proposed for listing under the Convention: http://chm.pops.int/TheConvention/ThePOPs/ChemicalsProposedforListing/tabid/2510/Default.aspx [Aug 7, 2019].

UNEP, 2017-last update, The new POPs under the Stockholm Convention: http://chm.pops.int/TheConvention/ThePOPs/TheNewPOPs/tabid/2511/Default.aspx [Mar 31, 2019].

UNEP, 2001. *Stockholm Convention on Persistent Organic Pollutants.* Geneva: United Nations Environment Programme.

USEPA, 2010. *Method 1668C: Chlorinated Biphenyl Congeners in Water, Soil, Sediment, Biosolids, and Tissue by HRGC/HRMS.* Washington, DC: United States Environmental Protection Agency.

USEPA, 2007a. *Method 1614: Brominated Diphenyl Ethers in Water, Soil, Sediment and Tissue by HRGC/HRMS.* Washington, DC: United States Environmental Protection Agency.

USEPA, 2007b. *Method 1699: Pesticides in Water, Soil, Sediment, Biosolids, and Tissue by HRGC/HRMS.* Washington, DC: United States Environmental Protection Agency.

USEPA, 1998. *Method 8290A: Polychlorinated Dibenzodioxins (PCDDs) and Polychlorinated Dibenzofurans (PCDFs) By High-Resolution Gas Chromatography/High-Resolution Mass Spectrometry (HRGC/HRMS).* Washington, DC: United States Environmental Protection Agency.

USEPA, 1994. *Method 1613B: Tetra- through Octa-Chlorinated Dioxins and Furans by Isotope Dilution HRGC/HRMS.* Washington, DC: United States Environmental Protection Agency.

USEPA, Apr 19, 1979-last update, EPA Press Release: EPA Bans PCB Manufacture; Phases Out Uses: https://archive.epa.gov/epa/aboutepa/epa-bans-pcb-manufacture-phases-out-uses.html [Mar 30, 2019].

Valkenborg, D., Mertens, I., Lemière, F., Witters, E. and Burzykowski, T., 2012. The isotopic distribution conundrum. *Mass Spectrometry Reviews,* 31(1), 96-109. doi:10.1002/mas.20339.

van Bavel, B., Geng, D., Cherta, L., Nácher-Mestre, J., Portolés, T., Ábalos, M., Sauló, J., Abad, E., Dunstan, J., Jones, R., Kotz, A., Winterhalter, H., Malisch, R., Traag, W., Hagberg, J., Ericson Jogsten, I., Beltran, J. and Hernández, F., 2015. Atmospheric-Pressure Chemical Ionization Tandem Mass Spectrometry (APGC/MS/MS) an Alternative to High-Resolution Mass Spectrometry (HRGC/HRMS) for the Determination of Dioxins. *Analytical Chemistry,* 87(17), 9047-9053. doi:10.1021/acs.analchem.5b02264.

Van den Berg, M., Birnbaum, L., Bosveld, A.T., Brunström, B., Cook, P., Feeley, M., Giesy, J.P., Hanberg, A., Hasegawa, R., Kennedy, S.W., Kubiak, T., Larsen, J.C., Leeuwen, F.X., Liem, A.K., Nolt, C., Peterson, R.E., Poellinger, L., Safe, S., Schrenk, D., Tillitt, D., Tysklind, M., Younes, M., Waern, F. and Zacharewski, T., 1998. Toxic equivalency factors (TEFs) for PCBs, PCDDs, PCDFs for humans and wildlife. *Environmental Health Perspectives,* 106(12), 775-792.

Van den Berg, M., Birnbaum, L., Denison, M., De Vito, M., Farland, W., Feeley, M., Fiedler, H., Hakansson, H., Hanberg, A., Haws, L., Rose, M., Safe, S., Schrenk, D., Tohyama, C., Tritscher, A., Tuomisto, J., Tysklind, M., Walker, N. and Peterson, R., 2006. The 2005 World Health Organization reevaluation of human and Mammalian toxic equivalency factors for dioxins and dioxin-like compounds. *Toxicological Sciences,* 93(2), 223.

Wang, S., Tsai, P., Yang, C. and Gueo, Y.L., 2008. Increased Risk of Diabetes and Polychlorinated Biphenyls and Dioxins: A 24-year follow-up study of the Yucheng cohort. *Diabetes Care,* 31(8), 1574-1579. doi:10.2337/dc07-2449.

Wayman, G., Yang, D., Bose, D., Lesiak, A., Ledoux, V., Bruun, D., Pessah, I. and Lein, P., 2012. PCB-95 Promotes Dendritic Growth via Ryanodine Receptor-Dependent Mechanisms. *Environmental Health Perspectives,* 120(7), 997-1002. doi:10.1289/ehp.1104832.

Weber, R., Herold, C., Hollert, H., Kamphues, J., Blepp, M. and Ballschmiter, K., 2018. Reviewing the relevance of dioxin and PCB sources for food from animal origin and the need for their inventory, control and management. *Environmental Sciences Europe,* 30(1), 1-42. doi:10.1186/s12302-018-0166-9.

Weber, R., Tysklind, M. and Gaus, C., 2008. Dioxin - Contemporary and Future Challenges of Historical Legacies. *Environmental Science and Pollution Research,* 15(2), 96.

Wenzl, T., Haedrich, J., Schaechtele, A., Robouch, P. and Stroka, J., 2016. *Guidance document on the estimation of LOD and LOQ for measurements in the field of contaminants in feed and food.* Luxembourg: European Union.

Wyttenbach, T., Helden, G.v., Batka, J.J., Carlat, D. and Bowers, M.T., 1997. Effect of the long-range potential on ion mobility measurements. *Journal of the American Society for Mass Spectrometry,* 8(3), 275-282. doi:10.1016/S1044-0305(96)00236-X.

Zheng, X., Dupuis, K.T., Aly, N.A., Zhou, Y., Smith, R.D., Smith, F.B., Tang, K. and Baker, E.S., 2018. Utilizing ion mobility spectrometry and mass spectrometry for the analysis of polycyclic aromatic hydrocarbons, polychlorinated biphenyls, polybrominated diphenyl ethers and their metabolites. *Analytica Chimica Acta,* 1037, 265-273. doi:10.1016/j.aca.2018.02.054.

# Appendix A

# Presentations, Software Development and Other Research Performed During the PhD

## A.1 Oral and poster presentations as primary author

Hart, J., 2016. Oral Presentation: Comparing the effect of varying collision energy on the fragmentation of toxic and non-toxic PCBs, *Workshop of the EURL and NRLs for Dioxins and PCBs in Feed and Food. Uppsala, Sweden*, 19 May 2016.

Hart, J., Jones, R. and Clench, M., 2016. Poster Presentation: The Analysis of PCBs using APGC-MS/MS at Varying Collision Energies, *BMRC/MERI Winter Poster Event. Sheffield Hallam University, Sheffield, UK*, 15 December 2016.

Hart, J., 2017. Oral Presentation: Development of a Practical Congener Profiling Utility for the Comparison of Dioxin, Furan and PCB Sample Data, *EURL and NRL Workshop for Dioxins and PCBs in Feed and Food. Prague, Czech Republic*, 30 May 2017.

Hart, J., Jones, R. and Clench, M., 2017. Poster Presentation: The Analysis of All 209 PCB Isomers using GC-APCI-MS/MS at Selected Collision Energies and Correlation with Toxicity, *65th ASMS Conference on Mass Spectrometry and Allied Topics. Indianapolis, IN, USA*, 5 June 2017.

Hart, J., Jones, R. and Clench, M., 2017. Oral Presentation: A Study of All 209 PCB Isomers using GC-APCI-MS/MS at Various Collision Energies: Correlations with EI Data and Toxicity, *37th International Symposium on Halogenated Persistent Organic Pollutants. Vancouver, BC, Canada*, 21 August 2017.

Hart, J., 2017. Oral Presentation: Development of a Congener Profiling Program and Results from the Database Evaluation Samples, *EURL Workshop of the Core Working Group "Dioxin Patterns". Freiburg, Germany*, 30 November 2017.

Hart, J., 2018. Oral Presentation: Background and Development of the Congener Profiling Program, *Workshop of the EURL and NRLs for Halogenated POPs in Feed and Food. Dublin, Ireland*, 8 May 2018.

Hart, J., Jones, R., Smith, D. and Clench, M., 2018. Oral Presentation: Ion Mobility Mass Spectrometry of All Mono to Deca-Chlorinated Biphenyl Isomers: Correlation with Known Structures and Toxicities, *66th ASMS Conference on Mass Spectrometry and Allied Topics. San Diego, CA, USA*, 6 June 2018.

Hart, J., 2018. Oral Presentation: Updated information on the "Congener Profiler" and results of the new test database, *EURL Workshop of the Core Working Group "Dioxin Patterns". Athens, Greece*, 20 June 2018.

Hart, J., 2019. Training course on the congener pattern database and software for data evaluation, *Workshop of EURL and NRLs for halogenated POPs in feed and food. Freiburg, Germany*, 26 November 2019.

## A.2 Co-authored work

Eppe, G., Diletti, G., Fernandes, A., Haedrich, J., Hart, J., Hove, H., Iamiceli, L., Kotz, A., Malisch, R., Marchand, P., Moche, W., Scholl, G., Scortichini, G., Bernsmann, T., Tondeur, Y. and Traag, W., 2014. Measurement uncertainty for persistent organic pollutants by isotope dilution mass spectrometry. *Organohalogen Compounds,* 76, pp. 1485-1488.

Vining, B., Tondeur, Y., Hart, J., Goodman, N., Blye, D., Michell, M. and Tordini, A., 2014. PCB Congener Analysis of High Concentration Samples for Toxic Equivalent (TEQ) Assessments. *Organohalogen Compounds,* 76, pp. 1537-1540.

Vining, B., Hart, J., Boivin, L., Saul, D., Appele, R. and Nichols, J., 2014. Analysis of POPs from 50 µL Dried Blood Spots. *Organohalogen Compounds,* 76, pp. 1541-1544.

Blye, D., Goodman, N., Hart, J., Michell, M., Tondeur, Y., Tordini, A. and Vining, B., 2014. PCB Congeners in Used Transformer Fluids; a Comparison of Aroclor TEQs from Three Studies. *Organohalogen Compounds,* 76, pp. 1549-1552.

Tondeur, Y., Vining, B., Serne, J. and Hart, J., 2015. Significance of measuring non-2,3,7,8-substituted PCDD/PCDF congeners and the identification of a new mechanism of formation for a high-temperature industrial process. *Chemosphere,* 126, pp. 47-52.

Eppe, G., Scholl, G., Schaechtele, A., Haedrich, J., Ceci, R., Diletti, G., Fernandes, A., Hart, J., Hove, H., Leondiadis, L., Vassiliadou, I., Marchand, P., Moche, W., Scortichini, G., Tondeur, Y., Van Leeuwen, S., Abballe, A., Iamicelli, A., Di Domenico, A., Bernsmann, T. and Malisch, R., 2016. Measurement Uncertainty Estimation for Laboratories Performing PCDD/F and PCB Analysis by Isotope Dilution Mass Spectrometry. *Organohalogen Compounds,* 78, pp. 781-784.

Schaechtele, A., Haedrich, J., Ceci, R., Diletti, G., Eppe, G., Fernades, A., Hart, J., Hove, H., Leondiadis, L., Marchand, P., Moche, W., Scholl, G., Scortichini, G., Tondeur, Y., Van Leeuwen, S., Vassiliadou, I. and Malisch, R., 2016. Estimation of LOQ for the Analysis of Persistent Organic Pollutants, in particular PCDD/Fs and PCBs. *Organohalogen Compounds,* 78, pp. 829-831.

Malisch, R., Bernsmann, T., Ceci, R., Diletti, G., Eppe, G., Fernandes, A., Fiedler, H., Hart, J., Hoogenboom, R., Hove, H., Knetsch, G., Leondiadis, L., Lüth, A., Marchand, P., Maszewski, S., Rose, M., Schaechtele, A., Vanderperren, H., Van Leeuwen, S., Van Raamsdonk, L. and Vassiliadou, I., 2017. Interactive data base of PCDD/F and PCB congener patterns to aid identification of contamination sources in feed and food. *Organohalogen Compounds,* 79, pp. 545-547.

## A.3 Development of the “Congener Profiler” software

Some parallel work concerned the development of a software program, “Congener Profiler”, intended for use within the EU National Reference Laboratories responsible for analysing PCDD/Fs and PCBs in food and feed products. The purpose of this program is to help identify possible sources of contamination when a sample’s (toxic equivalent) concentration exceeds the regulatory limit. The program uses an approach similar to conventional (spectral) library searching, with certain modifications, to compare a sample’s congener profile with those in a database containing patterns from known chemicals and historic food/feed contamination incidents (Malisch *et al.*, 2017).

Comparisons are made using an orthogonal vector method with the match being determined by the dot product of the vectors, i.e. the cosine of the angle between them. This can easily be envisaged for a system of just two components, e.g. a dioxin and a furan, expressed as vectors: if the two vectors match exactly (in direction, but irrespective of magnitude) the angle between them would be 0°, hence the cosine would be 1, i.e. indicative of an exact match; if the two vectors are orthogonal, the angle between them is 90°, hence Cos 90° = 0, i.e. no match.

As an example, the vectors shown in Figure A.1 in represent a sample (red) and 2 possible library matches (blue and green). Visually, the green vector appears to be a closer match, as indicated by the cosine of the angle between them being closer to 1.

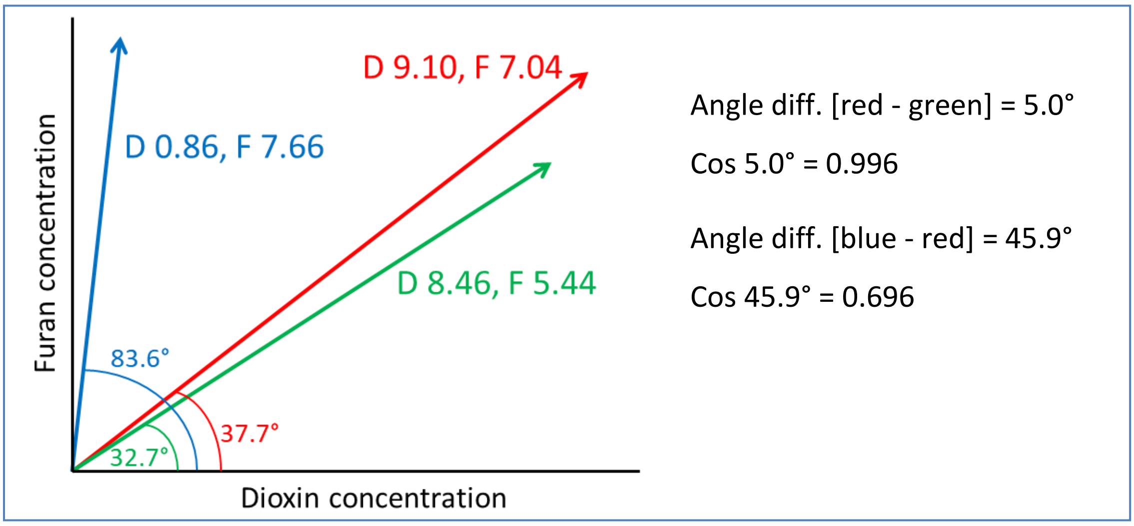

Figure A.1 Illustration of a comparison between an unknown sample and 2 library entries, each represented by 2-dimensional vectors for their PCDD and PCDF concentrations.

For real-world samples, the vectors have as many dimensions as the number of congeners analysed, e.g. 35 if all 17 PCDD/Fs, 12 WHO-PCBs and 6 Indicator PCBs are used. Generally, for n congeners, using their concentrations from the library database (L) and the unknown (U), the cosine of the angle, θ, between them can be calculated using:

$$Cos\ \theta = \sum_{i=1}^{n}(L_i \times U_i) \Bigg/ \left(\sqrt{\sum_{i=1}^{n} {L_i}^2} \times \sqrt{\sum_{i=1}^{n} {U_i}^2}\right) \qquad \text{(A.1)}$$

The output from the program consists of two graphical displays and a results table as shown in Figure A.2. The primary display (left panel) shows an x/y chart where the axes may be selected to various combinations of the congener groups. The unknown sample is represented by a point on the chart's origin, and the various matches as points spread across the chart depending on their match value, and a proportion in each axis according to the "distance", i.e. the relevance of that congener's group, in the calculation. The central panel display is a simple bar chart showing the target unknown entry in the top box, followed by a series of matched entries in descending order of their match value calculated as a percentage. The complete list of matches can be examined on the right-hand section from the Results tab. The graphics and results text can also be exported to files and/or to the clipboard for further examination, printing, etc.

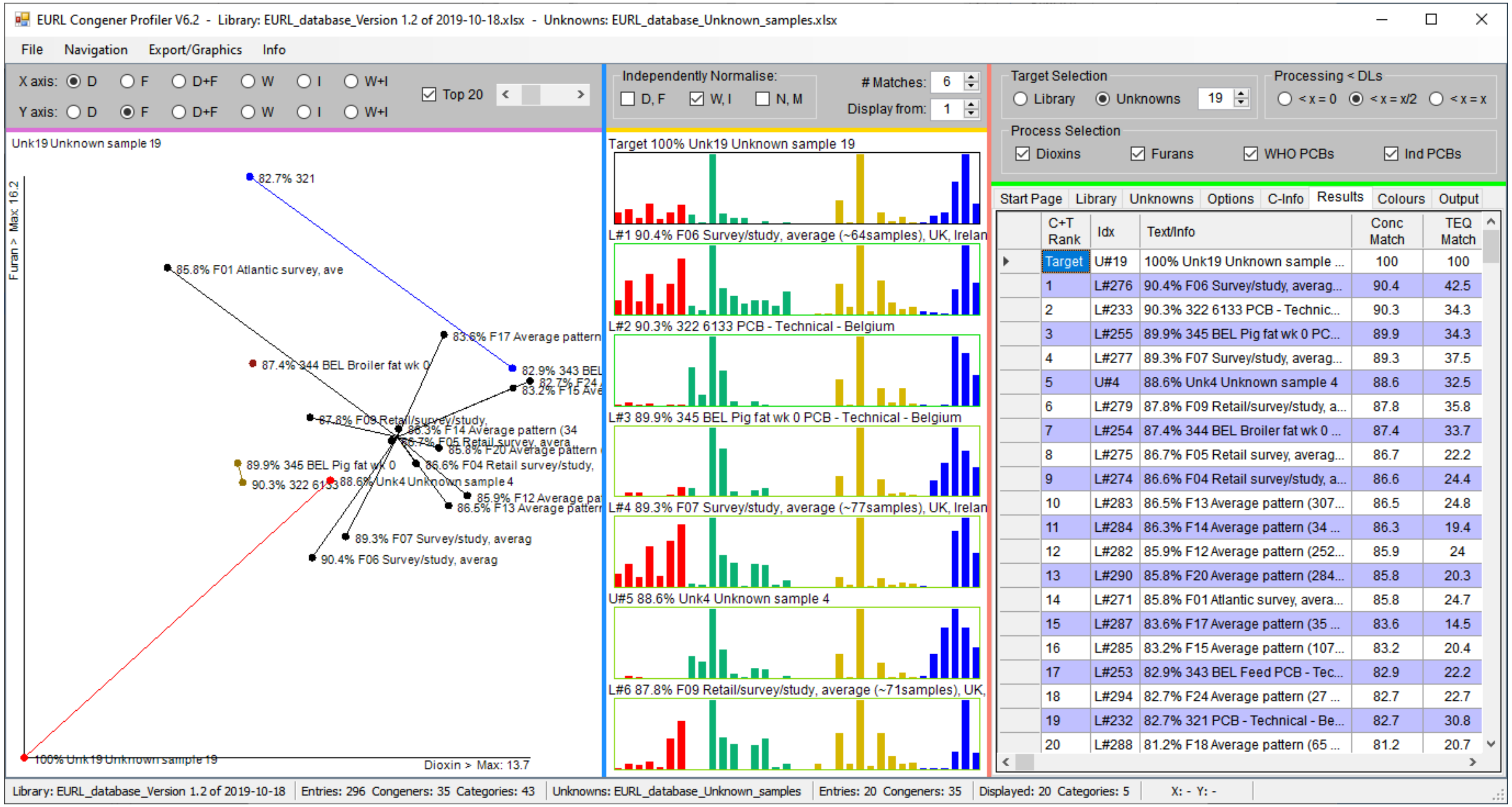

EURL Congener Profiler V6.2 - Library: EURL_database_Version 1.2 of 2019-10-18.xlsx - Unknowns: EURL_database_Unknown_samples.xlsx

X axis: ● D ○ F ○ D+F ○ W ○ I ○ W+I

Y axis: ○ D ● F ○ D+F ○ W ○ I ○ W+I

☑ Top 20

Independently Normalise: ☐ D, F ☑ W, I ☐ N, M

# Matches: 6

Display from: 1

Target Selection: ○ Library ● Unknowns 19

Processing < DLs: ○ < x = 0 ● < x = x/2 ○ < x = x

Process Selection: ☑ Dioxins ☑ Furans ☑ WHO PCBs ☑ Ind PCBs

| | C+T Rank | Idx | Text/Info | Conc Match | TEQ Match |
|---|---|---|---|---|---|
| ▶ | Target | U#19 | 100% Unk19 Unknown sample ... | 100 | 100 |
| | 1 | L#276 | 90.4% F06 Survey/study, averag... | 90.4 | 42.5 |
| | 2 | L#233 | 90.3% 322 6133 PCB - Technic... | 90.3 | 34.3 |
| | 3 | L#255 | 89.9% 345 BEL Pig fat wk 0 PC... | 89.9 | 34.3 |
| | 4 | L#277 | 89.3% F07 Survey/study, averag... | 89.3 | 37.5 |
| | 5 | U#4 | 88.6% Unk4 Unknown sample 4 | 88.6 | 32.5 |
| | 6 | L#279 | 87.8% F09 Retail/survey/study, a... | 87.8 | 35.8 |
| | 7 | L#254 | 87.4% 344 BEL Broiler fat wk 0 ... | 87.4 | 33.7 |
| | 8 | L#275 | 86.7% F05 Retail survey, averag... | 86.7 | 22.2 |
| | 9 | L#274 | 86.6% F04 Retail survey/study, a... | 86.6 | 24.4 |
| | 10 | L#283 | 86.5% F13 Average pattern (307... | 86.5 | 24.8 |
| | 11 | L#284 | 86.3% F14 Average pattern (34 ... | 86.3 | 19.4 |
| | 12 | L#282 | 85.9% F12 Average pattern (252... | 85.9 | 24 |
| | 13 | L#290 | 85.8% F20 Average pattern (284... | 85.8 | 20.3 |
| | 14 | L#271 | 85.8% F01 Atlantic survey, avera... | 85.8 | 24.7 |
| | 15 | L#287 | 83.6% F17 Average pattern (35 ... | 83.6 | 14.5 |
| | 16 | L#285 | 83.2% F15 Average pattern (107... | 83.2 | 20.4 |
| | 17 | L#253 | 82.9% 343 BEL Feed PCB - Tec... | 82.9 | 22.2 |
| | 18 | L#294 | 82.7% F24 Average pattern (27 ... | 82.7 | 22.7 |
| | 19 | L#232 | 82.7% 321 PCB - Technical - Be... | 82.7 | 30.8 |
| | 20 | L#288 | 81.2% F18 Average pattern (65 ... | 81.2 | 20.7 |

Library: EURL_database_Version 1.2 of 2019-10-18 | Entries: 296 Congeners: 35 Categories: 43 | Unknowns: EURL_database_Unknown_samples | Entries: 20 Congeners: 35 | Displayed: 20 Categories: 5 | X: - Y: -

Figure A.2 Screenshot of the Congener Profiler program developed for use by the EU Reference Laboratories for PCDD/Fs and PCBs in Food and Feed for comparisons between unknown and library database samples.

## A.4 Software developed for the PhD research

The following is a list of software programs created by the author specifically for the research within this thesis. These were all developed using Microsoft Visual Basic (VB), as part of the Visual Studio suite, versions 2015-2019 (Microsoft, Redmond, WA, USA), except for RaStats that used the Visual Basic for Applications (VBA) routines within Excel (Microsoft, Redmond, WA, USA).

DriftScope Analyser

> A program to process and visualise ion mobility data exported from the Waters *DriftScope* software. Detected chromatographic peaks due to selected *m/z* (from a built-in PCB database) are displayed as points on a chart of ion mobility arrival time distribution vs. GC retention time. The points are colour-coded by chlorination level and scaled by peak intensity. This program easily illustrates the various patterns related to structure and identifies potential interferences for peaks that overlap on either or both time axes.

OrcaControl

> A program to queue and submit input (structure coordinates and optimisation parameter) files, generated using the *Avogadro* molecular editing software, to the *Orca* molecular modelling program.

OrcaParse

> A program to extract centre-of-mass, dipole moments and single point energy values from *Orca* results files.

PDB processor

> A program to (1) automatically modify *Orca* input files to create $^{13}C$ isotopomer versions for subsequent computational modelling; (2) create PDB (Protein Database) format files from the *Orca* computed output files; (3) submit PDB files

to both the *Impact* and *CrossArea* ion mobility modelling programs to estimate rotationally averaged collisional cross-sectional areas.

PureIso

An *ab initio* program to calculate exact masses and isotopic abundances of the peaks within a molecular ion cluster. A unique feature relevant to this thesis, compared to online calculators or to those incorporated within various mass spectrometer vendors' software packages, is its ability to accommodate "fully-labelled" standards of varying isotopic purity. (This program is described in detail in Chapter 3 and specific code is shown in Appendix A.4.2)

RaStats

An Excel VBA macro to perform the ion statistics for both Gaussian and Poisson distributions, and the associated isotope ratio modelling used in Chapter 2. Details of the Poisson calculation code are shown in Appendix A.4.1.

*UltraTrace-Pro*

Custom add-ons developed for the proprietary (SGS) mass spectrometry software to enable the processing and display of ion mobility data.

### A.4.1 Software code for the Poisson modelling

The following VBA code documents the iterative calculations, developed for the ion statistics modelling in Chapter 2, using Atkinson’s Poisson rejection and multiplication methods (Atkinson, 1979).

```
Function myPoisson(ByVal lambda As Double) As Integer

Dim alpha, beta, k, r, s, u1, u2, x, c, lhs, rhs As Double
Dim n As Integer

If lambda > 30 Then ‘use the rejection method (for performance purposes)

        c = 0.767 – 3.36 / lambda ‘establish the required parameters
        beta = PI * (3.0 * lambda) ^ -0.5
        alpha = beta * lambda
        k = Log© – lambda – Log(beta) ‘note: Log in VB code is the natural log

        Do
                Do
                        u1 = Rnd() ‘create a random value > 0, <= 1
                        If u1 = 0.0 Then u1 = Rnd() ‘ensure non-zero
                        x = (alpha – Log((1.0 – u1) / u1)) / beta
                Loop Until x >= 0.5

                n = Int(x + 0.5)
                u2 = Rnd()
                If u2 = 0.0 Then u2 = Rnd()

                lhs = alpha – beta * x + Log(u2 / (1.0 + Exp(alpha – beta * x)) ^ 2.0)
                rhs = k + n * Log(lambda) – LogFactorial(n)

                If lhs <= rhs Then Exit Do
        Loop

Else ‘use the multiplication method

        r = Exp(-lambda)
        n = 0
        s = 1.0

        Do
                u1 = Rnd()
                s *= u1

                If s < r Then Exit Do
                n += 1
        Loop

End If

myPoisson = n

End Function
```

### A.4.2 Software code for the PureIso program

The following shows the VB code developed for the core calculation routines used within the PureIso program:

```
Private Function Isotope_Calc(ByVal trace As Integer) As Boolean

' This is top-level routine from which all others are called. It is initiated from
' either a calc request due to the user setting the various element values or from
' a graphics refresh. The trace parameter passed to this routine allows up to 8
' traces to be displayed as overlays.


    Dim eIdx, idx, totalCombs, eleCt As Integer
    Dim probability, mass As Double
    Dim formula As String
    Dim bDone As Boolean = False


    eleCt = 0
    For eIdx = 0 To ElementTable.GetUpperBound(0)
        If ElementTable(eIdx).element_count > 0 Then eleCt += 1
    Next
    eleCt -= 1

    Dim maxIndices(eleCt), curIndices(eleCt) As Integer
    Dim all_probs(eleCt)(), all_masses(eleCt)() As Double
    Dim all_formulae(eleCt)() As String


    eleCt = 0
    totalCombs = 1
    For eIdx = 0 To ElementTable.GetUpperBound(0)

        If ElementTable(eIdx).element_count = 0 Then Continue For

        CalcAtomDistribution(CType(eIdx, ElementsIdx), trace)

        ReDim Preserve all_probs(eleCt)(Probabilities(trace).GetUpperBound(0))
        ReDim Preserve all_masses(eleCt)(Masses(trace).GetUpperBound(0))
        ReDim Preserve all_formulae(eleCt)(Formulae(trace).GetUpperBound(0))

        For idx = 0 To Probabilities(trace).GetUpperBound(0)
            all_probs(eleCt)(idx) = Probabilities(trace)(idx)
            all_masses(eleCt)(idx) = Masses(trace)(idx)
            all_formulae(eleCt)(idx) = Formulae(trace)(idx)
        Next

        totalCombs *= Probabilities(trace).Length
        eleCt += 1
    Next

    If eleCt = 0 Then Return False

    'set the index arrays that hold the num of possibilities for each element
    eleCt -= 1
    For eIdx = 0 To eleCt
        maxIndices(eIdx) = all_probs(eIdx).GetUpperBound(0)
        curIndices(eIdx) = maxIndices(eIdx) 'start the current indices at max values
    Next

    LblInfo.Text = totalCombs.ToString("#,#")
```

```
'put all combinations into the arrays

totalCombs -= 1
ReDim Masses(trace)(totalCombs), Probabilities(trace)(totalCombs),
          Formulae(trace)(totalCombs)

Do
    mass = 0.0
    probability = 1.0
    formula = ""
    For eIdx = 0 To eleCt
        mass += all_masses(eIdx)(curIndices(eIdx))
        probability *= all_probs(eIdx)(curIndices(eIdx))
        formula &= all_formulae(eIdx)(curIndices(eIdx))
    Next

    Masses(trace)(totalCombs) = mass - (NumElectronCharges.Value * ElectronMass)

    Probabilities(trace)(totalCombs) = probability
    Formulae(trace)(totalCombs) = formula
    totalCombs -= 1

    Do

        If curIndices(eleCt) > 0 Then
            curIndices(eleCt) -= 1
            Exit Do
        Else
            'check if all entries are zero - we're done if they are
            bDone = True 'assume this for now
            For idx = 0 To eleCt
                If curIndices(idx) > 0 Then
                    bDone = False
                    Exit For
                End If
            Next idx
            If bDone Then Exit Do

            For idx = eleCt - 1 To 0 Step -1 'decrement entries to the 'left'
                curIndices(idx + 1) = maxIndices(idx + 1) 'reset this entry
                If curIndices(idx) > 0 Then
                    curIndices(idx) -= 1
                    Exit Do
                End If
            Next
        End If

    Loop

    If bDone Then Exit Do

Loop Until totalCombs < 0

If totalCombs <> -1 Then
    MessageBox.Show("An error has occurred in the calculations!", "PureIso",
                    MessageBoxButtons.OK, MessageBoxIcon.Exclamation)
    Return False
End If

If ChkFilter.Checked Then
    Dim threshold As Double

    Try
        threshold = CDbl(TxtFilter.Text)
    Catch ex As InvalidCastException
        threshold = 0.0
    End Try
```

```
        FilterArrays(threshold, trace)
    Else
        LblInfo2.Text = "-"
    End If
    SortArrays(trace)
    GroupMasses(trace)

    Return True

End Function


Private Sub CalcAtomDistribution(ByVal eIdx As ElementsIdx, ByVal trace As Integer)

' This routine calculates the distribution probabilities for each atom in the
' formulate according to the number of isotopes present in the table for that
' element. Currently elements with up to 3 isotopes are supported.


    Dim primary_atom_count, secondary_atom_count, tertiary_atom_count As Integer
    Dim idx, loopCt As Integer
    Dim factor As Double


    With ElementTable(eIdx)

        Select Case .isotope_count

            Case 1

                'with a mono-isotopic atom, there is just one possibility (e.g. 12^0)
                ReDim Probabilities(trace)(0), Masses(trace)(0), Formulae(trace)(0)

                Probabilities(trace)(0) = .abundances(0)
                Masses(trace)(0) = .element_count * .masses(0)
                Formulae(trace)(0) = .element_symbol_1

                If .element_count > 1 Then Formulae(trace)(0) &= CStr(.element_count)
                Formulae(trace)(0) &= " "

            Case 2

                'with 2 isotopes, there are num_atoms+1 possible combinations
                'so the array is num_atoms as we also have index=0
                ReDim Probabilities(trace)(.element_count),
                    Masses(trace)(.element_count), Formulae(trace)(.element_count)

                For idx = 0 To .element_count

                    primary_atom_count = .element_count - idx
                    secondary_atom_count = idx
                    factor = CalcFactor(.element_count,
                                 primary_atom_count,secondary_atom_count)

                    Probabilities(trace)(idx) = .abundances(0) ^ primary_atom_count *
                        .abundances(1) ^ secondary_atom_count * factor
                    Masses(trace)(idx) = primary_atom_count * .masses(0) +
                        secondary_atom_count * .masses(1)

                    If primary_atom_count > 0 Then
                        Formulae(trace)(idx) = .element_symbol_1
                        If primary_atom_count > 1 Then Formulae(trace)(idx) &=
                            primary_atom_count.ToString
                        Formulae(trace)(idx) &= " "
                    End If

                    If secondary_atom_count > 0 Then
```

```
            Formulae(trace)(idx) &= "[" &
                ElementTable(eIdx).element_symbol_2
            If secondary_atom_count > 1 Then Formulae(trace)(idx) &=
                secondary_atom_count.ToString
            Formulae(trace)(idx) &= "] "
        End If

    Next

Case 3

'with 3 isotopes, there are (num_atoms+2 * num_atoms+1)/2 possible combs.
    idx = ((.element_count + 2) * (.element_count + 1)) \ 2 - 1
    ReDim Probabilities(trace)(idx), Masses(trace)(idx),
             Formulae(trace)(idx)

    idx = 0
    loopCt = 0
    primary_atom_count = .element_count

    Do

        For secondary_atom_count = 0 To loopCt
            tertiary_atom_count = .element_count - primary_atom_count –
                secondary_atom_count

            factor = Factorial(.element_count) /
                Factorial(primary_atom_count) /
                    Factorial(secondary_atom_count) /
                        Factorial(tertiary_atom_count)

            Probabilities(trace)(idx) = .abundances(0) ^
                primary_atom_count * .abundances(1) ^
                    secondary_atom_count *
                        .abundances(2) ^ tertiary_atom_count * factor

            Masses(trace)(idx) = primary_atom_count * .masses(0) +
                secondary_atom_count * .masses(1) +
                    tertiary_atom_count * .masses(2)

            If primary_atom_count > 0 Then
                Formulae(trace)(idx) = .element_symbol_1
                If primary_atom_count > 1 Then
                    Formulae(trace)(idx) &= primary_atom_count.ToString
                Formulae(trace)(idx) &= " "
            End If

            If secondary_atom_count > 0 Then
                Formulae(trace)(idx) &= "[" &
                    ElementTable(eIdx).element_symbol_2
                If secondary_atom_count > 1 Then
                    Formulae(trace)(idx) &= secondary_atom_count.ToString
                Formulae(trace)(idx) &= "] "
            End If

            If tertiary_atom_count > 0 Then
                Formulae(trace)(idx) &= "[" &
                    ElementTable(eIdx).element_symbol_3
                If tertiary_atom_count > 1 Then Formulae(trace)(idx) &=
                    tertiary_atom_count.ToString
                Formulae(trace)(idx) &= "] "
            End If

            idx += 1
        Next

        loopCt += 1
```

```
                    primary_atom_count -= 1

                Loop Until primary_atom_count < 0

            Case Else
                'nothing else supported as yet
                ReDim Preserve Probabilities(trace)(0), Masses(trace)(0),
                    Formulae(trace)(0)

                Exit Sub

        End Select

    End With

End Sub
```

# Appendix B

# Supplemental Results

## B.1 Error modelling using the Poisson distribution

Figure B.1 shows the modelled variation in the number of peaks that fall within the 15% isotope ratio tolerance vs. the relative duty cycle of ion #1 for 5 different compounds. These data, summarised in Table B.1, were modelled using the Poisson distribution for comparison to Gaussian modelled data discussed in section 2.7 (p. 57).

The data (solid lines) were smoothed using a 5-point moving average; also shown are the expected (dotted lines) and actual maxima (dashed lines). The calculations were based on modelling using the Poisson distribution with 500 ions and $10^5$ iterations.

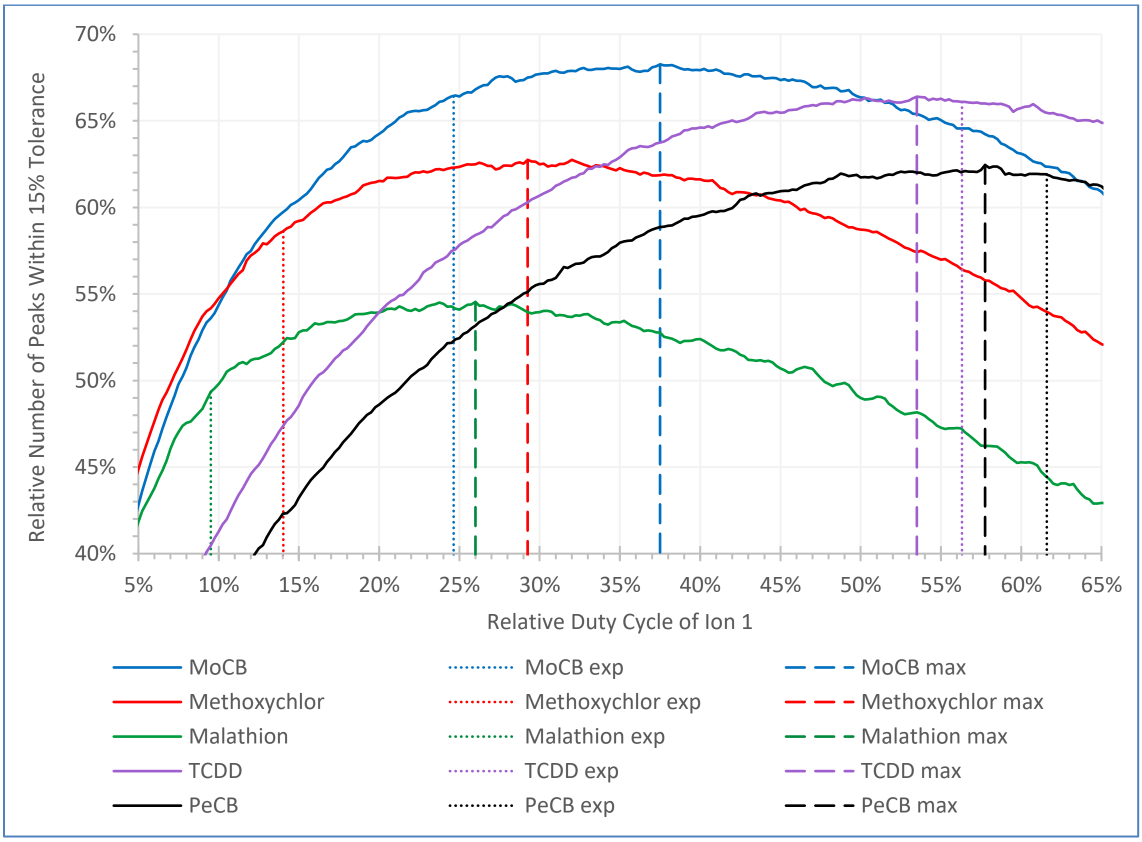

Figure B.1 Modelled data based on the Poisson distribution showing the relative number of peaks within 15% of the theoretical isotope ratio vs. relative duty cycle for MoCB, Methoxychlor, Malathion, TCDD and PeCB.

| | **MoCB** | **Methoxy-chlor** | **Malathion** | **TCDD** | **PeCB** |
|---|---|---|---|---|---|
| Theoretical isotope ratio | 3.06 | 6.13 | 9.51 | 0.78 | 0.62 |
| Expected optimum duty cycle (ion 1) | 24.6% | 14.0% | 9.5% | 56.3% | 61.6% |
| Modelled duty cycle for maximum pass rate (ion 1) | 37.5% | 29.3% | 26.0% | 53.5% | 57.8% |
| Pass rate at 50% duty cycle | 66.4% | 58.7% | 49.0% | 66.2% | 61.7% |
| Maximum pass rate | 68.3% | 62.7% | 54.5% | 66.4% | 62.5% |
| Increase | 2.9% | 6.8% | 11.3% | 0.3% | 1.2% |

Table B.1 Summary of the data from Figure B.1 showing the optimum duty cycle and increases in the "pass rate" for 5 different compounds.

## B.2 PFK data statistics used for detector gain calculations

The data shown in Table B.2 refers to that used for the discussion on detector gain calculations in Chapter 2.6.

| **Data Start Scan #** | **Data σ at Dwell Time = 100 ms** | **Data σ at Dwell Time = 50 ms** | **Data σ at Dwell Time = 10 ms** | **Ratio $\sigma_{50\ ms} / \sigma_{10\ ms}$** |
|---|---|---|---|---|
| 0 | 3.17E+04 | 4.02E+04 | 9.30E+04 | 2.31 |
| 50 | 2.67E+04 | 3.78E+04 | 8.11E+04 | 2.15 |
| 100 | 2.83E+04 | 3.56E+04 | 8.99E+04 | 2.53 |
| 150 | 3.32E+04 | 3.46E+04 | 8.42E+04 | 2.44 |
| 200 | 2.79E+04 | 3.02E+04 | 9.41E+04 | 3.11 |
| 250 | 3.15E+04 | 3.80E+04 | 9.83E+04 | 2.59 |
| 300 | 3.46E+04 | 3.48E+04 | 8.09E+04 | 2.32 |
| 350 | 2.90E+04 | 3.91E+04 | 9.12E+04 | 2.33 |
| 400 | 2.68E+04 | 4.43E+04 | 7.88E+04 | 1.78 |
| 450 | 2.78E+04 | 4.44E+04 | 7.91E+04 | 1.78 |
| 500 | 3.26E+04 | 4.31E+04 | 8.37E+04 | 1.94 |
| 550 | 2.69E+04 | 4.00E+04 | 8.82E+04 | 2.20 |
| 600 | 3.02E+04 | 4.17E+04 | 8.65E+04 | 2.07 |
| 650 | 2.50E+04 | 2.98E+04 | 9.25E+04 | 3.10 |
| 700 | 3.43E+04 | 3.60E+04 | 6.72E+04 | 1.87 |
| 750 | 2.76E+04 | 3.65E+04 | 1.02E+05 | 2.78 |
| 800 | 2.91E+04 | 4.66E+04 | 9.24E+04 | 1.98 |
| 850 | 2.64E+04 | 4.07E+04 | 8.66E+04 | 2.13 |
| 900 | 3.19E+04 | 4.22E+04 | 7.62E+04 | 1.80 |
| 950 | 2.93E+04 | 3.65E+04 | 9.21E+04 | 2.52 |
| Mean | 2.95E+04 | 3.86E+04 | 8.69E+04 | - |
| Mean σ as a % of the overall $\sigma_{n=1,000}$ | 23.0% | 18.2% | 2.6% | - |

Table B.2 PFK statistics showing the σ for each of the 20 x 50 scan data subsets from the overall (n = 1,000) datasets recorded using dwell times of 100, 50 and 10 ms.
Also shown are the ratio of the 50 and 10 ms subset σ, and the mean σ and its proportion relative to its corresponding overall dataset at each dwell time.

## B.3 Fragmentation charts for Mono to Tri and Octa to Deca CBs

The following charts show the relative fragmentation responses due to the loss of Cl, in both EI (Figure B.2 and Figure B.3) and APCI (Figure B.4 and Figure B.5) modes, for the $Cl_1$ to $Cl_3$ and $Cl_8$ to $Cl_{10}$ homologues that were not shown in Chapter 4 (please refer to that chapter for the experimental details). In each case, the data are normalised to the maximum of displayed values.

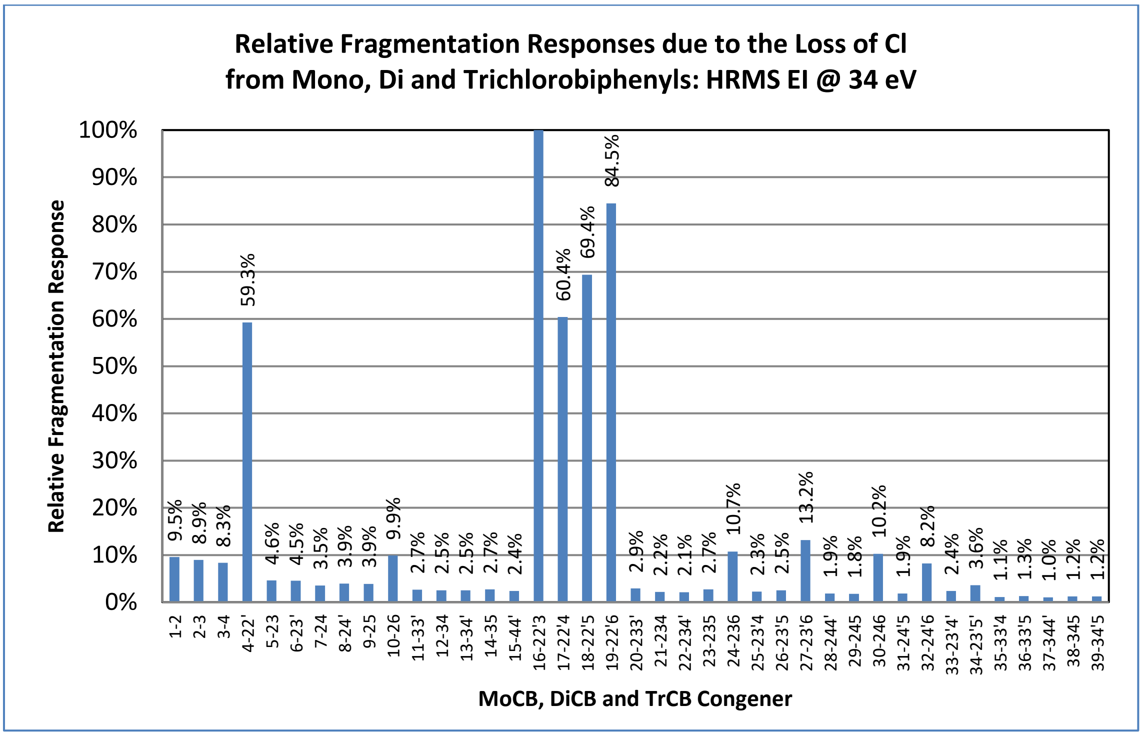

Figure B.2 Chart of the relative fragmentation responses due to the loss of Cl from MoCB, DiCB and TrCB congeners using GC-HRMS EI+ @ 34 eV.
The x-axis labels indicate the congener number and the chlorine substitution pattern.

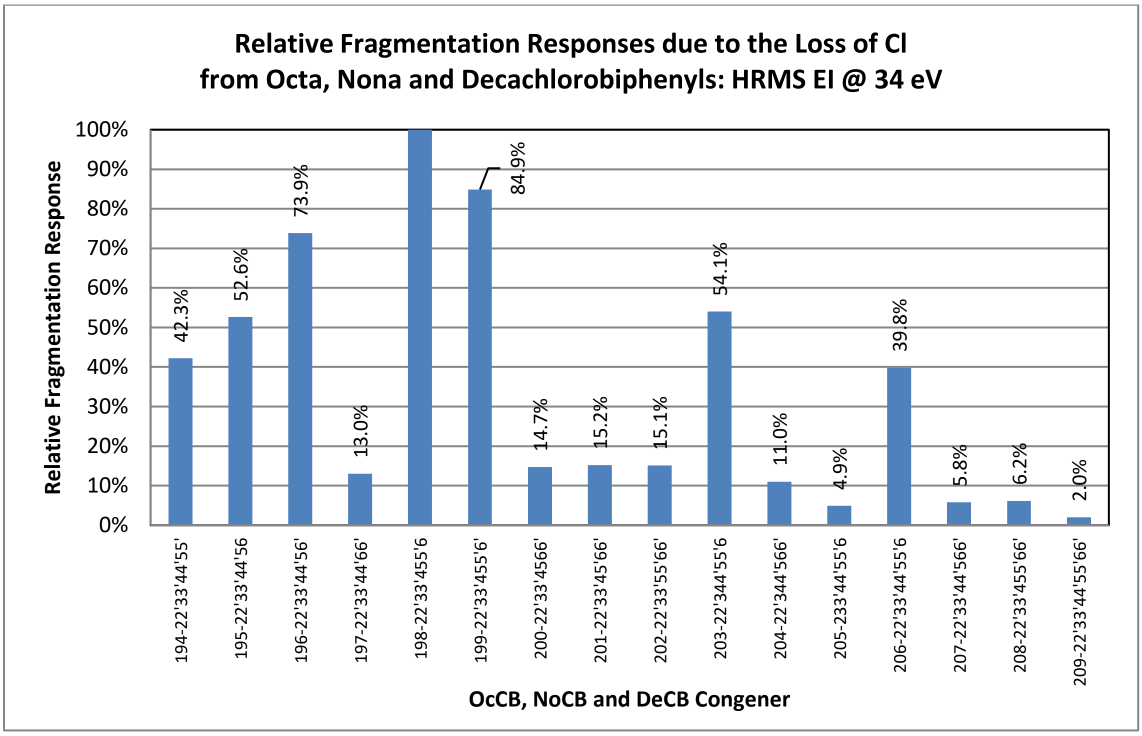

Figure B.3 Chart of the relative fragmentation responses due to the loss of Cl from OcCB, NoCB and DeCB congeners using GC-HRMS EI+ @ 34 eV.
The x-axis labels indicate the congener number and the chlorine substitution pattern.

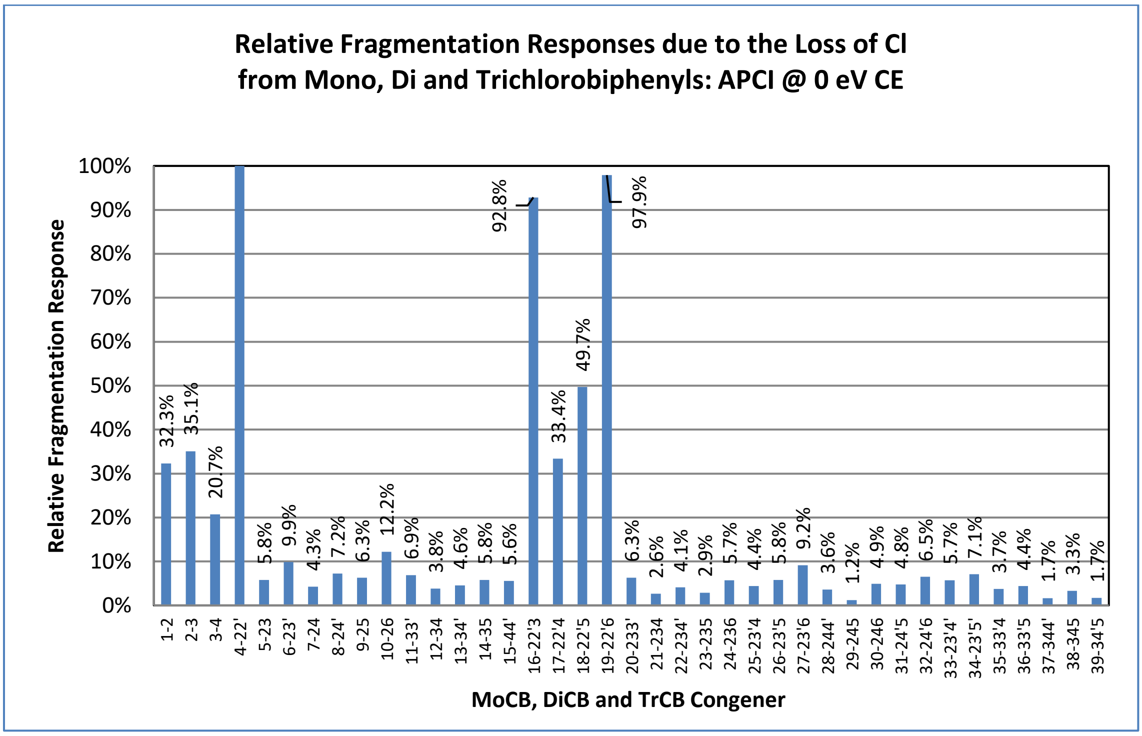

Figure B.4 Chart of the relative fragmentation responses due to the loss of Cl from MoCB, DiCB and TrCB congeners using GC-MS/MS APCI+ @ CE = 0 eV.
The x-axis labels indicate the congener number and the chlorine substitution pattern.

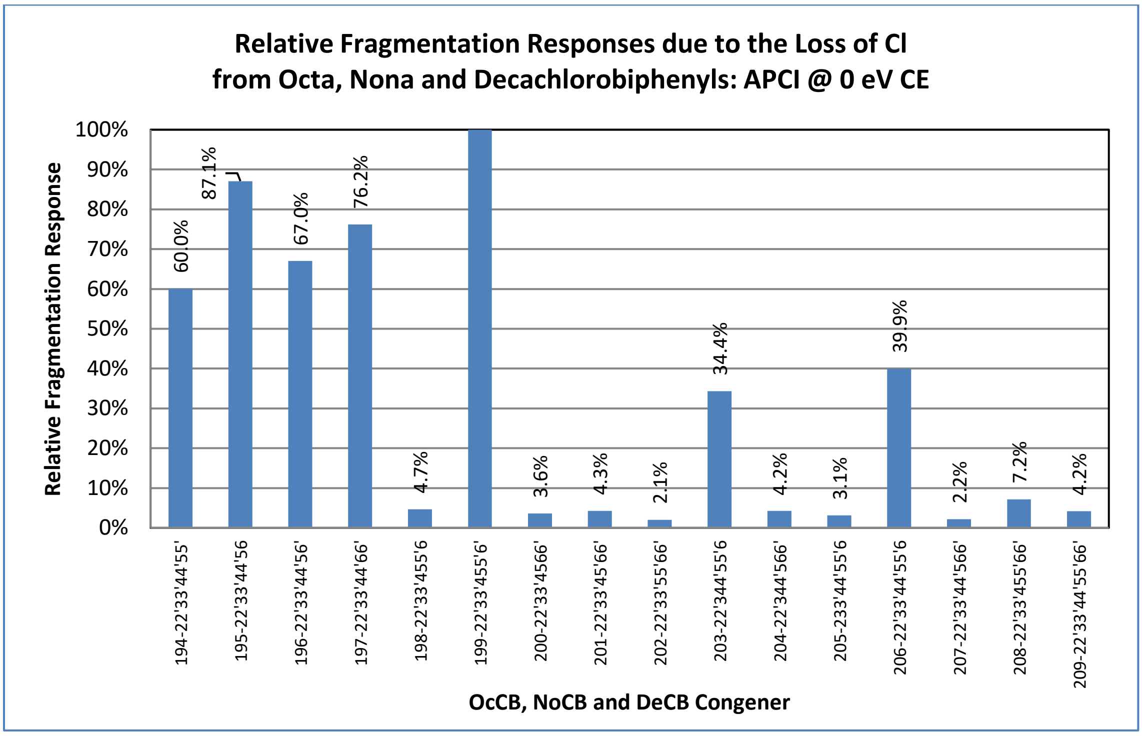

Figure B.5 Chart of the relative fragmentation responses due to the loss of Cl from OcCB, NoCB and DeCB congeners using GC-MS/MS APCI+ @ CE = 0 eV.
The x-axis labels indicate the congener number and the chlorine substitution pattern.

## B.4 PCB fragmentation profiles for PCA analysis

Figure B.6 to Figure B.10 show the PCB fragmentation profiles used for the PCA analysis in section 4.3.7. A red-coloured border indicates a WHO toxic PCB.

Figure B.6 Fragmentation profiles for PCBs: 4, 8, 11, 14, 19, 37, 40, 42, 43, 46, 47, 50, 52, 54 and 56.
The graphs show the relative responses of 6 selected mass losses vs. collision energy of 0 to 30 eV.

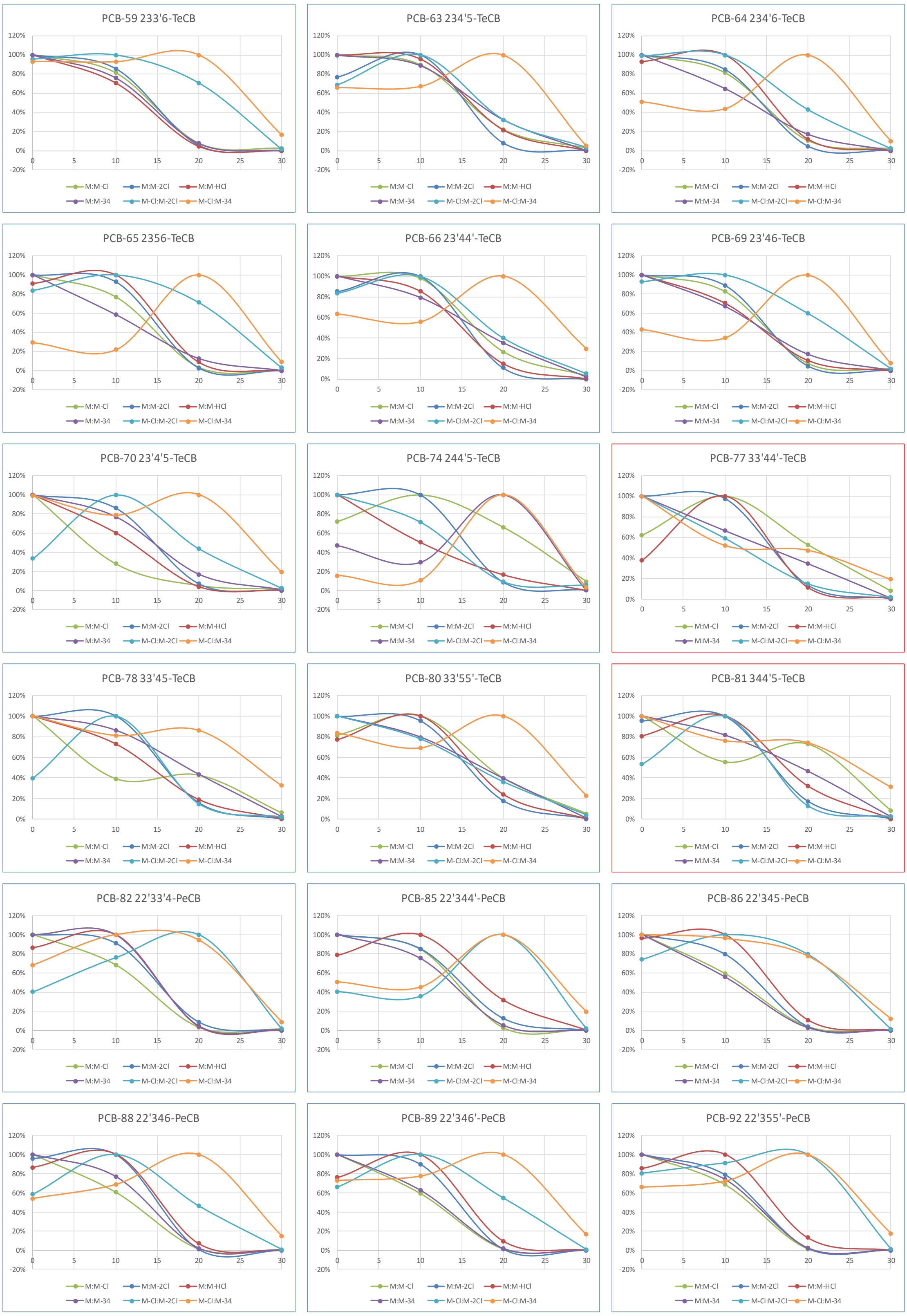

Figure B.7 Fragmentation profiles for PCBs: 59, 63, 64, 65, 66, 69, 70, 74, 77, 78, 80, 81, 82, 85, 86, 88, 89 and 92.
The graphs show the relative responses of 6 selected mass losses vs. collision energy of 0 to 30 eV.

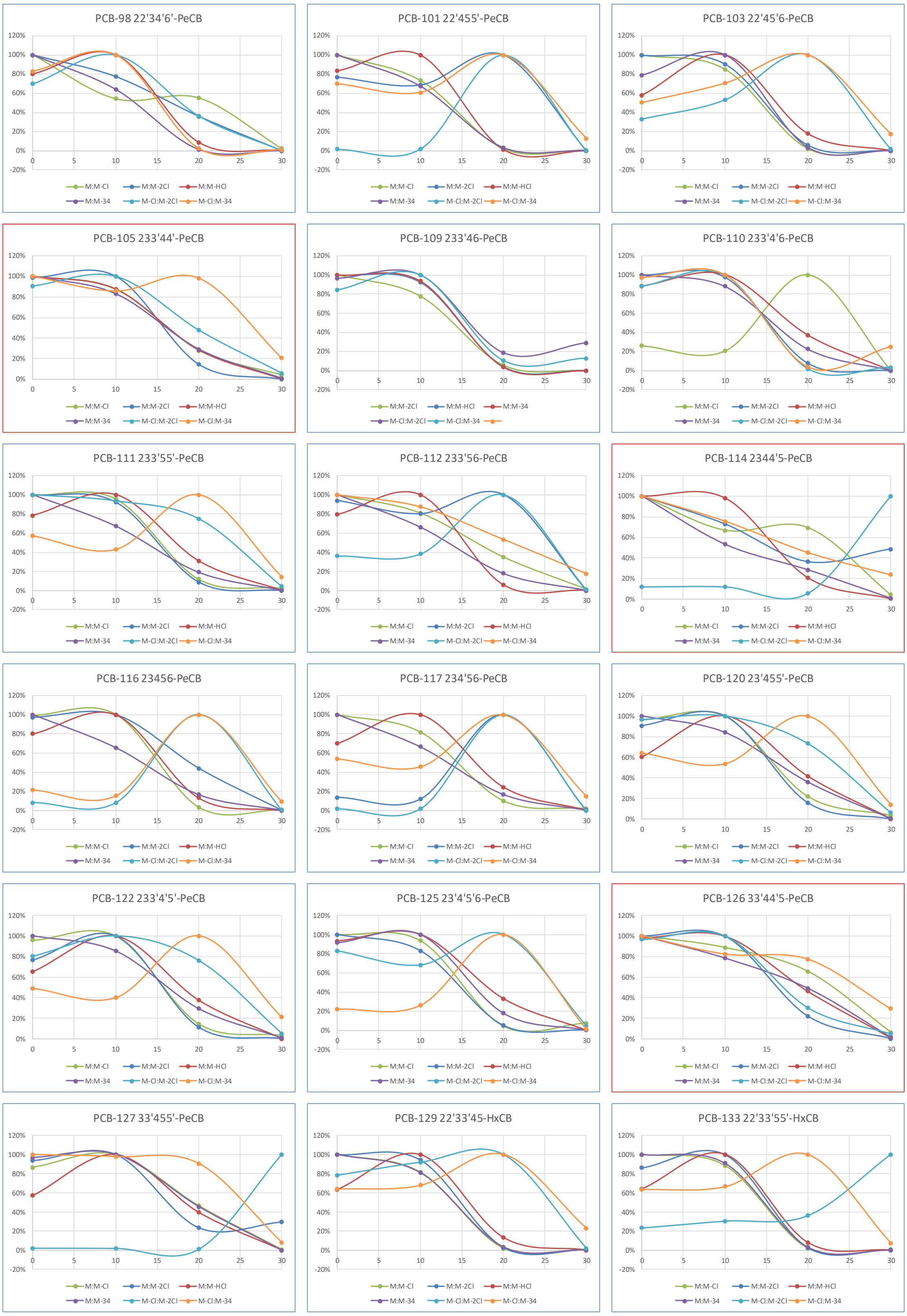

Figure B.8 Fragmentation profiles for PCBs: 98, 101, 103, 105, 109, 110, 111, 112, 114, 116, 117, 120, 122, 125, 126, 127, 129 and 133.
The graphs show the relative responses of 6 selected mass losses vs. collision energy of 0 to 30 eV.

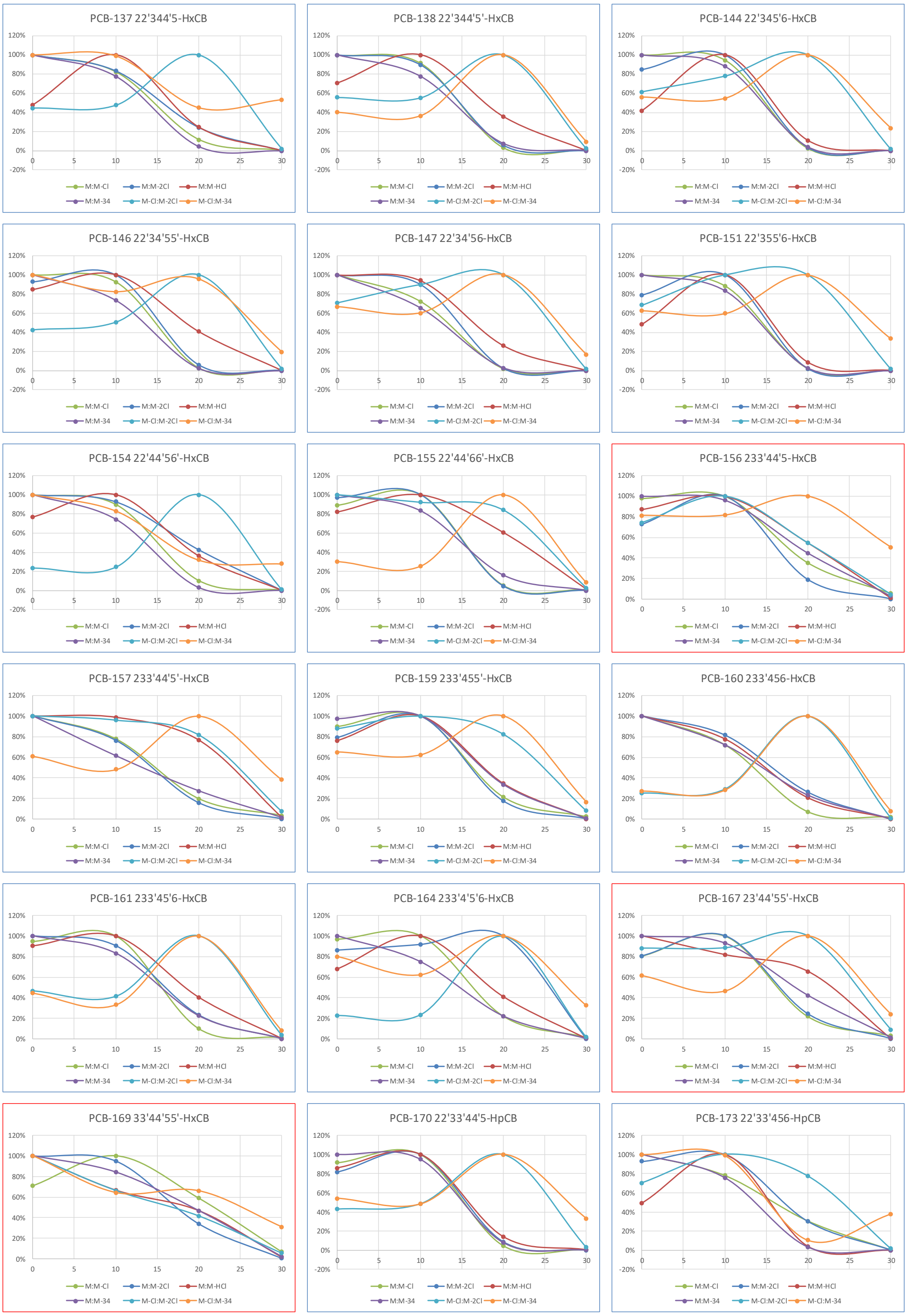

Figure B.9 Fragmentation profiles for PCBs: 137, 138, 144, 146, 147, 151, 154, 155, 156, 157, 159, 160, 161, 164, 167, 169, 170 and 173.
The graphs show the relative responses of 6 selected mass losses vs. collision energy of 0 to 30 eV.

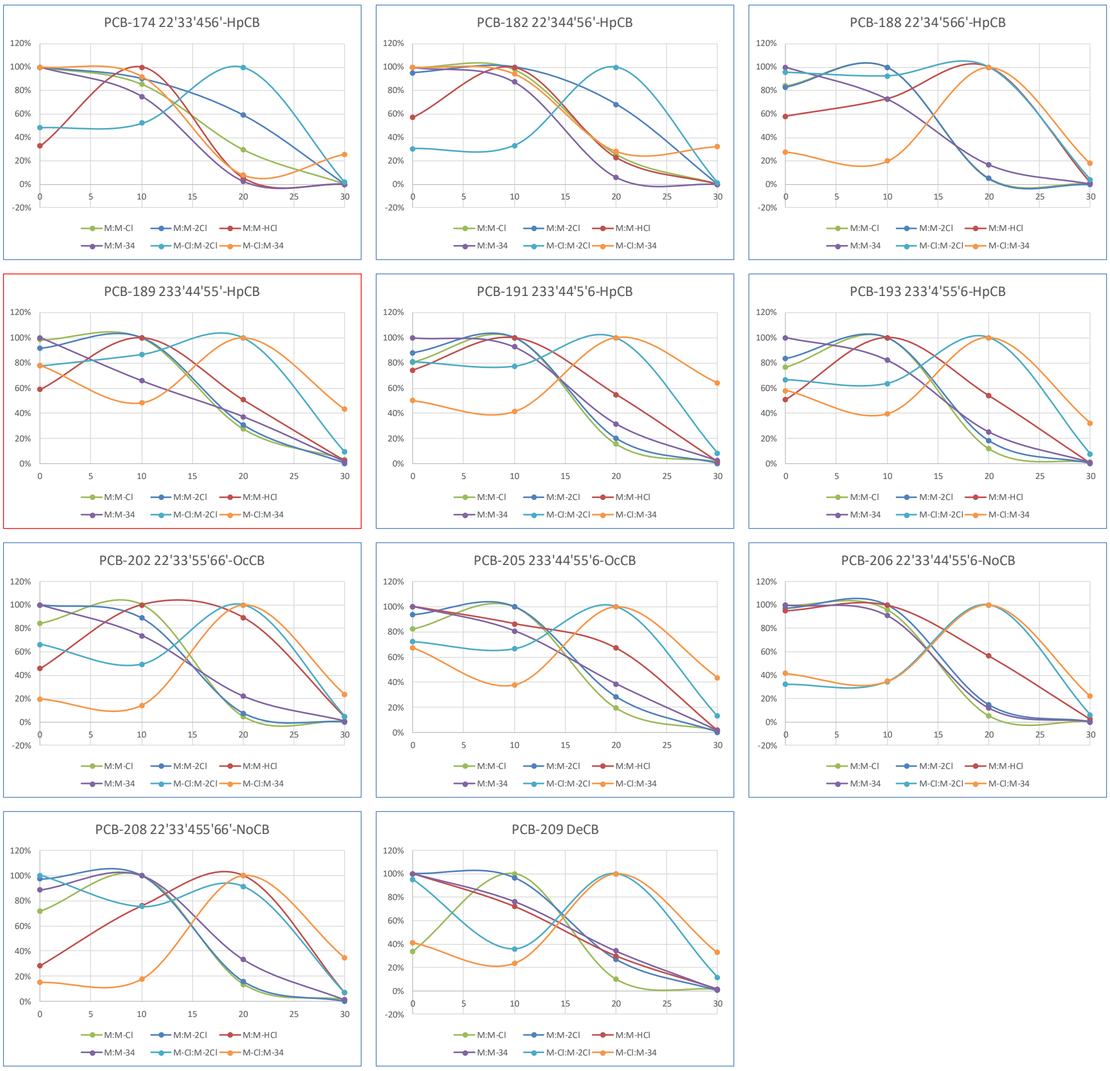

Figure B.10 Fragmentation profiles for PCBs: 174, 182, 188, 189, 191, 193, 202, 205, 206, 208 and 209.
The graphs show the relative responses of 6 selected mass losses vs. collision energy of 0 to 30 eV.

## B.5 Calculated CCS values for all 209 PCB congeners

Table B.3 shows the CCS values for all 209 PCB congeners calculated using the “Impact” projection approximation (PA) and trajectory (TJ) methods, the “CrossArea” PA method, and from the acquired (Synapt) data as discussed in section 5.4.2.

| **PCB BZ#** | ***Impact* PA (Å$^2$)** | ***Impact* TJ (Å$^2$)** | ***Cross-Area* PA (Å$^2$)** | **Expt. *(Synapt)* (Å$^2$)** | **PCB BZ#** | ***Impact* PA (Å$^2$)** | ***Impact* TJ (Å$^2$)** | ***Cross-Area* PA (Å$^2$)** | **Expt. *(Synapt)* (Å$^2$)** |
|---|---|---|---|---|---|---|---|---|---|
| 1 | 117.9 | 126.9 | 116.8 | 134.9 | 31 | 138.0 | 149.7 | 135.3 | 150.7 |
| 2 | 121.3 | 130.7 | 121.5 | 136.3 | 32 | 134.0 | 145.1 | 133.1 | 149.7 |
| 3 | 121.6 | 131.0 | 122.4 | 134.5 | 33 | 135.4 | 146.7 | 136.9 | 149.8 |
| 4 | 123.7 | 133.4 | 122.2 | 141.9 | 34 | 136.9 | 148.4 | 139.2 | 151.7 |
| 5 | 125.6 | 135.6 | 125.7 | 142.0 | 35 | 138.4 | 150.2 | 143.1 | 151.3 |
| 6 | 127.5 | 137.7 | 128.4 | 143.6 | 36 | 140.7 | 152.8 | 145.3 | 153.3 |
| 7 | 127.9 | 138.2 | 129.8 | 142.6 | 37 | 138.9 | 150.7 | 138.3 | 149.8 |
| 8 | 128.1 | 138.4 | 128.3 | 142.6 | 38 | 135.8 | 147.2 | 137.4 | 149.4 |
| 9 | 127.9 | 138.2 | 124.0 | 143.2 | 39 | 141.2 | 153.4 | 143.8 | 152.3 |
| 10 | 124.3 | 134.1 | 124.5 | 141.9 | 40 | 138.5 | 150.3 | 139.0 | 155.1 |
| 11 | 130.9 | 141.7 | 131.1 | 145.3 | 41 | 138.5 | 150.3 | 138.6 | 154.5 |
| 12 | 128.7 | 139.1 | 128.9 | 142.6 | 42 | 140.8 | 152.9 | 144.2 | 155.8 |
| 13 | 131.3 | 142.1 | 132.9 | 143.9 | 43 | 140.3 | 152.3 | 142.1 | 155.6 |
| 14 | 130.7 | 141.4 | 126.6 | 145.1 | 44 | 140.5 | 152.6 | 139.7 | 156.3 |
| 15 | 131.7 | 142.5 | 131.1 | 142.3 | 45 | 136.2 | 147.7 | 136.4 | 153.1 |
| 16 | 131.0 | 141.8 | 131.0 | 148.8 | 46 | 135.8 | 147.2 | 136.0 | 153.7 |
| 17 | 133.7 | 144.8 | 134.8 | 149.5 | 47 | 143.4 | 155.8 | 146.8 | 156.5 |
| 18 | 133.3 | 144.3 | 134.1 | 149.7 | 48 | 140.7 | 152.8 | 140.2 | 155.7 |
| 19 | 128.8 | 139.2 | 126.7 | 147.2 | 49 | 143.3 | 155.8 | 142.4 | 156.7 |
| 20 | 134.9 | 146.1 | 140.2 | 150.3 | 50 | 138.6 | 150.3 | 138.8 | 154.4 |
| 21 | 133.5 | 144.5 | 132.8 | 148.0 | 51 | 138.4 | 150.2 | 140.6 | 154.6 |
| 22 | 135.5 | 146.8 | 133.2 | 149.4 | 52 | 142.5 | 154.9 | 143.0 | 157.2 |
| 23 | 135.2 | 146.6 | 134.6 | 149.9 | 53 | 137.8 | 149.4 | 137.5 | 154.7 |
| 24 | 131.5 | 142.3 | 132.2 | 148.2 | 54 | 133.3 | 144.4 | 132.5 | 152.1 |
| 25 | 137.6 | 149.3 | 137.4 | 150.9 | 55 | 142.7 | 155.1 | 145.9 | 156.0 |
| 26 | 137.3 | 148.9 | 134.2 | 151.7 | 56 | 142.4 | 154.7 | 147.1 | 156.2 |
| 27 | 133.0 | 144.0 | 133.1 | 149.9 | 57 | 144.9 | 157.5 | 143.2 | 157.7 |
| 28 | 138.1 | 149.8 | 137.3 | 150.0 | 58 | 144.4 | 157.0 | 143.9 | 157.7 |
| 29 | 135.7 | 147.0 | 133.6 | 149.6 | 59 | 140.8 | 152.9 | 138.7 | 156.0 |
| 30 | 134.2 | 145.4 | 134.7 | 149.2 | 60 | 143.3 | 155.7 | 149.2 | 155.1 |

Table B.3 CCS values obtained from the “Impact” projection approximation (PA) and trajectory (TJ) methods, from the “CrossArea” PA method and from experimental data. *(Table continues overleaf)*

| **PCB BZ#** | ***Impact* PA (Å²)** | ***Impact* TJ (Å²)** | ***Cross-Area* PA (Å²)** | **Expt. *(Synapt)* (Å²)** | **PCB BZ#** | ***Impact* PA (Å²)** | ***Impact* TJ (Å²)** | ***Cross-Area* PA (Å²)** | **Expt. *(Synapt)* (Å²)** |
|---|---|---|---|---|---|---|---|---|---|
| 61 | 140.6 | 152.7 | 144.0 | 154.5 | 101 | 149.9 | 163.3 | 149.2 | 163.0 |
| 62 | 138.8 | 150.7 | 140.4 | 154.1 | 102 | 145.3 | 158.1 | 146.4 | 160.4 |
| 63 | 145.5 | 158.2 | 146.1 | 156.9 | 103 | 147.5 | 160.6 | 149.2 | 161.9 |
| 64 | 141.1 | 153.3 | 145.1 | 155.7 | 104 | 143.0 | 155.4 | 140.6 | 158.9 |
| 65 | 139.0 | 150.9 | 135.1 | 154.1 | **105** | **150.5** | **163.9** | **154.2** | **161.8** |
| 66 | 145.6 | 158.3 | 150.0 | 156.7 | 106 | 149.5 | 162.9 | 150.2 | 162.1 |
| 67 | 144.9 | 157.6 | 142.7 | 157.3 | 107 | 152.5 | 166.2 | 152.2 | 163.5 |
| 68 | 147.1 | 160.1 | 150.8 | 158.3 | 108 | 152.0 | 165.7 | 153.5 | 163.4 |
| 69 | 143.1 | 155.5 | 145.0 | 156.7 | 109 | 148.2 | 161.4 | 146.0 | 161.4 |
| 70 | 144.5 | 157.1 | 148.4 | 157.5 | 110 | 147.7 | 160.8 | 149.0 | 161.9 |
| 71 | 140.6 | 152.7 | 141.2 | 156.0 | 111 | 153.7 | 167.7 | 154.9 | 165.4 |
| 72 | 146.6 | 159.5 | 149.2 | 159.3 | 112 | 147.8 | 160.9 | 147.3 | 162.0 |
| 73 | 142.1 | 154.4 | 140.2 | 157.2 | 113 | 149.8 | 163.2 | 148.0 | 163.7 |
| 74 | 145.8 | 158.6 | 148.9 | 156.6 | **114** | **150.6** | **164.2** | **151.6** | **161.4** |
| 75 | 143.7 | 156.2 | 147.8 | 156.4 | 115 | 148.9 | 162.2 | 153.4 | 161.2 |
| 76 | 141.8 | 154.1 | 143.5 | 156.1 | 116 | 143.7 | 156.3 | 144.6 | 158.8 |
| **77** | **146.6** | **159.6** | **143.3** | **157.2** | 117 | 148.5 | 161.7 | 148.0 | 161.5 |
| 78 | 146.1 | 158.9 | 142.3 | 157.8 | **118** | **152.5** | **166.3** | **153.5** | **163.4** |
| 79 | 148.5 | 161.7 | 146.5 | 158.9 | 119 | 150.3 | 163.8 | 150.4 | 162.8 |
| 80 | 150.0 | 163.5 | 153.3 | 160.9 | 120 | 154.0 | 168.0 | 157.7 | 165.0 |
| **81** | **146.3** | **159.2** | **146.8** | **156.7** | 121 | 152.2 | 165.9 | 154.3 | 163.8 |
| 82 | 146.1 | 159.0 | 147.4 | 160.7 | 122 | 149.4 | 162.7 | 153.4 | 162.3 |
| 83 | 142.5 | 154.9 | 142.9 | 162.0 | **123** | **152.2** | **165.9** | **154.6** | **163.0** |
| 84 | 143.3 | 155.8 | 143.2 | 159.8 | 124 | 151.2 | 164.8 | 152.8 | 163.7 |
| 85 | 148.1 | 161.2 | 150.4 | 161.4 | 125 | 146.9 | 159.9 | 146.8 | 161.8 |
| 86 | 148.5 | 161.7 | 148.1 | 160.2 | **126** | **153.5** | **167.4** | **148.0** | **163.8** |
| 87 | 146.8 | 159.7 | 150.0 | 162.0 | 127 | 155.4 | 169.6 | 152.7 | 165.6 |
| 88 | 143.3 | 155.7 | 142.4 | 158.8 | 128 | 153.2 | 167.0 | 151.0 | 166.7 |
| 89 | 143.0 | 155.4 | 142.3 | 159.3 | 129 | 152.5 | 166.3 | 152.7 | 166.9 |
| 90 | 148.9 | 162.1 | 150.3 | 162.8 | 130 | 154.9 | 169.0 | 154.0 | 168.2 |
| 91 | 145.8 | 158.6 | 147.3 | 160.6 | 131 | 150.6 | 164.1 | 150.3 | 165.5 |
| 92 | 144.5 | 157.1 | 144.5 | 163.6 | 132 | 150.2 | 163.6 | 150.6 | 166.0 |
| 93 | 143.2 | 155.7 | 144.9 | 158.5 | 133 | 156.8 | 171.2 | 154.8 | 170.1 |
| 94 | 144.8 | 157.4 | 144.0 | 160.3 | 134 | 150.4 | 163.9 | 149.9 | 165.4 |
| 95 | 145.0 | 157.7 | 145.7 | 160.9 | 135 | 152.2 | 165.9 | 150.2 | 167.0 |
| 96 | 140.3 | 152.4 | 138.5 | 157.8 | 136 | 147.4 | 160.5 | 147.2 | 164.3 |
| 97 | 148.0 | 161.1 | 148.1 | 162.0 | 137 | 155.1 | 169.3 | 158.8 | 167.6 |
| 98 | 145.8 | 158.6 | 148.8 | 160.5 | 138 | 155.4 | 169.6 | 157.1 | 168.0 |
| 99 | 150.7 | 164.2 | 152.7 | 162.7 | 139 | 153.0 | 166.9 | 155.5 | 166.5 |
| 100 | 148.6 | 161.8 | 149.5 | 161.5 | 140 | 153.2 | 167.1 | 151.4 | 166.6 |

Table B.3 (continued) CCS values obtained from the "Impact" projection approximation (PA) and trajectory (TJ) methods, from the "CrossArea" PA method and from experimental data. The WHO toxic congeners are indicated by bold type.
*(Table continues overleaf)*

| PCB BZ# | *Impact* PA (Å$^2$) | *Impact* TJ (Å$^2$) | *Cross-Area* PA (Å$^2$) | Expt. *(Synapt)* (Å$^2$) | PCB BZ# | *Impact* PA (Å$^2$) | *Impact* TJ (Å$^2$) | *Cross-Area* PA (Å$^2$) | Expt. *(Synapt)* (Å$^2$) |
|---|---|---|---|---|---|---|---|---|---|
| 141 | 154.6 | 168.7 | 153.5 | 168.2 | 176 | 154.6 | 168.7 | 153.8 | 170.5 |
| 142 | 148.2 | 161.4 | 147.8 | 163.3 | 177 | 157.4 | 171.9 | 155.8 | 172.2 |
| 143 | 149.2 | 162.6 | 151.5 | 165.1 | 178 | 159.2 | 174.0 | 159.3 | 173.4 |
| 144 | 152.4 | 166.2 | 152.2 | 167.2 | 179 | 154.5 | 168.6 | 153.7 | 169.9 |
| 145 | 147.6 | 160.7 | 146.0 | 163.2 | 180 | 162.0 | 177.2 | 159.3 | 174.3 |
| 146 | 157.2 | 171.7 | 158.5 | 169.5 | 181 | 157.6 | 172.1 | 156.0 | 171.5 |
| 147 | 152.9 | 166.8 | 154.0 | 166.5 | 182 | 159.4 | 174.3 | 157.2 | 172.8 |
| 148 | 154.9 | 169.1 | 152.1 | 167.9 | 183 | 160.0 | 174.9 | 157.9 | 173.1 |
| 149 | 152.5 | 166.3 | 154.2 | 166.9 | 184 | 156.7 | 171.1 | 157.6 | 171.0 |
| 150 | 150.1 | 163.6 | 154.5 | 165.3 | 185 | 156.9 | 171.4 | 156.1 | 172.5 |
| 151 | 152.1 | 165.8 | 152.7 | 167.2 | 186 | 151.7 | 165.3 | 150.5 | 168.1 |
| 152 | 147.4 | 160.5 | 145.8 | 162.9 | 187 | 159.6 | 174.4 | 158.7 | 173.4 |
| 153 | 157.4 | 171.9 | 160.7 | 169.2 | 188 | 157.0 | 171.5 | 159.3 | 170.8 |
| 154 | 155.4 | 169.6 | 157.8 | 167.9 | **189** | **163.8** | **179.3** | **163.4** | **175.0** |
| 155 | 152.4 | 166.2 | 150.7 | 166.0 | 190 | 160.2 | 175.1 | 159.0 | 172.9 |
| **156** | **157.1** | **171.6** | **161.2** | **168.5** | 191 | 164.0 | 179.4 | 163.5 | 174.0 |
| **157** | **156.9** | **171.4** | **156.9** | **168.3** | 192 | 161.9 | 177.0 | 160.7 | 174.1 |
| 158 | 155.8 | 170.1 | 159.6 | 167.8 | 193 | 161.9 | 177.1 | 159.1 | 174.3 |
| 159 | 159.3 | 174.1 | 159.8 | 169.9 | 194 | 166.2 | 182.0 | 167.4 | 179.3 |
| 160 | 152.6 | 166.4 | 153.2 | 166.5 | 195 | 162.3 | 177.5 | 164.4 | 176.8 |
| 161 | 157.0 | 171.5 | 156.3 | 168.9 | 196 | 163.9 | 179.3 | 166.5 | 178.0 |
| 162 | 159.1 | 173.9 | 160.1 | 169.9 | 197 | 162.1 | 177.3 | 164.1 | 176.3 |
| 163 | 155.5 | 169.7 | 156.2 | 168.2 | 198 | 163.8 | 179.3 | 163.1 | 178.4 |
| 164 | 154.5 | 168.6 | 155.4 | 168.1 | 199 | 163.8 | 179.2 | 164.8 | 178.5 |
| 165 | 157.0 | 171.5 | 153.8 | 170.4 | 200 | 158.6 | 173.3 | 158.4 | 175.3 |
| 166 | 153.5 | 167.4 | 155.7 | 166.3 | 201 | 161.4 | 176.5 | 163.2 | 176.3 |
| **167** | **156.8** | **171.3** | **154.9** | **169.9** | 202 | 161.4 | 176.5 | 160.1 | 176.2 |
| 168 | 155.5 | 169.8 | 155.0 | 168.8 | 203 | 164.2 | 179.7 | 165.6 | 178.2 |
| **169** | **161.3** | **176.4** | **164.3** | **170.7** | 204 | 161.2 | 176.3 | 163.6 | 175.7 |
| 170 | 159.8 | 174.6 | 161.2 | 173.1 | 205 | 163.9 | 179.4 | 165.7 | 178.9 |
| 171 | 157.9 | 172.5 | 159.5 | 171.8 | 206 | 168.6 | 184.8 | 171.0 | 183.1 |
| 172 | 161.7 | 176.8 | 160.1 | 174.5 | 207 | 166.2 | 182.1 | 168.4 | 181.2 |
| 173 | 155.1 | 169.3 | 153.5 | 170.3 | 208 | 165.7 | 181.5 | 165.2 | 181.5 |
| 174 | 156.6 | 171.0 | 157.2 | 172.0 | 209 | 170.3 | 186.7 | 168.2 | 186.3 |
| 175 | 159.4 | 174.2 | 157.9 | 173.2 | | | | | |

Table B.3 (continued) CCS values obtained from the “Impact” projection approximation (PA) and trajectory (TJ) methods, from the “CrossArea” PA method and from experimental data. The WHO toxic congeners are indicated by bold type.

# Appendix C

# Supplemental Information

## C.1 Magnet scan equations

In a magnet scan experiment, the magnet is (traditionally[*]) scanned exponentially from high mass down to low mass. The scan law is expressed as:

$$m_x = m_0 e^{-k(t_x - t_0)} \tag{C.1}$$

Where $m_x$ and $m_0$ are the unknown (or end) and start masses, $t_x$ and $t_0$ are the measured times (within the scan) of the unknown (or end) and start masses, and $k$ is the rate constant.

The rate constant can be readily extracted from the above to give:

$$k = \frac{ln(m_0/m_x)}{t_x - t_0} \tag{C.2}$$

As an example, for a scan covering one decade of mass (*m/z* 500–50) with a scan time of 1 second, we would obtain: $k = \ln(500 / 50) / (1 - 0) \approx 2.3$.

An important benefit of this scan law is that it results in peaks of constant width – both in time-per-peak and in ppm terms – and hence is well suited to digitisation since, given the fixed frequency of the analogue-to-digital convertor (ADC), this will lead to a constant number of data points across the peak. This allows for straightforward optimisation of any subsequent digital filtering (smoothing) and other operations needed for (mass) peak detection.

---

[*] Although other functions, such as linear scans or up (in mass) scans are possible, the exponential down scan was traditionally the most straightforward to implement with analogue electronics (e.g. via capacitor discharge in a resistor-capacitor based circuit).

## C.2 Masses and abundances used by the PureIso program

| Element | Mass # | Exact Mass | Abundance[1] | Abundance[2] |
|---|---|---|---|---|
| H | 1 | 1.007825032 | 0.999885 | |
| | 2 | 2.014101778 | 0.000115 | |
| C | 12 | 12.0 | 0.9894 | 0.9893 |
| | 13 | 13.0033548378 | 0.0106 | 0.0107 |
| N | 14 | 14.003074 | 0.99632 | |
| | 15 | 15.000108 | 0.00368 | |
| O | 16 | 15.99491463 | 0.99757 | |
| | 17 | 16.9991312 | 0.00038 | |
| | 18 | 17.9991603 | 0.00205 | |
| F | 19 | 18.99840322 | 1.0 | |
| Si | 28 | 27.9769271 | 0.922297 | |
| | 29 | 28.9764949 | 0.046832 | |
| | 30 | 29.9737707 | 0.030872 | |
| P | 31 | 30.973762 | 1.0 | |
| S | 32 | 31.9720707 | 0.9493 | |
| | 33 | 32.97145843 | 0.0076 | |
| | 34 | 33.96786665 | 0.0429 | |
| Cl | 35 | 34.968852721 | 0.758 | 0.7576 |
| | 37 | 36.96590262 | 0.242 | 0.2424 |
| Br | 79 | 78.9183361 | 0.5069 | |
| | 81 | 80.916289 | 0.4931 | |

Table C.1 Elemental masses and abundances used by the PureIso program.

The masses in Table C.1 were obtained from IUPAC's "*Atomic weights of the elements 2013*" (Meija *et al.*, 2016a).

[1] Abundances were taken from "*Isotopic compositions of the elements 2013*" (Meija *et al.*, 2016b).

[2] Alternative abundances for C and Cl were taken from the previous "*Isotopic compositions of the elements 2009*" (Berglund and Wieser, 2011) and used for certain comparisons as described in the main text.

The current version of the program is limited to a maximum of 3 isotopes per element and therefore the minor sulphur isotope $^{36}$S with its abundance of ~0.00015 was omitted.

## C.3 Tables of the PCB congener mixes

Table C.2 lists the PCB congeners found in the C-CS-01 to C-CS-09 mixes as supplied by AccuStandard (New Haven, CT, USA). The 12 WHO toxic congeners are indicated by bold type.

| **PCB Mix C-CS-01** | | | | | |
|---|---|---|---|---|---|
| **BZ#** | **Structure** | **BZ#** | **Structure** | **BZ#** | **Structure** |
| 1 | 2-MoCB | 44 | 22’35’-TeCB | 147 | 22’34’56-HxCB |
| 2 | 3-MoCB | 52 | 22’55’-TeCB | 153 | 22’44’55’-HxCB |
| 3 | 4-MoCB | 56 | 233’4’-TeCB | 173 | 22’33’456-HpCB |
| 4 | 22’-DiCB | 66 | 23’44’-TeCB | 174 | 22’33’456’-HpCB |
| 6 | 23’-DiCB | 67 | 23’45-TeCB | 177 | 22’33’45’6’-HpCB |
| 8 | 24’-DiCB | 71 | 23’4’6-TeCB | 179 | 22’33’566’-HpCB |
| 9 | 25-DiCB | 74 | 244’5-TeCB | 180 | 22’344’55’-HpCB |
| 16 | 22’3-TrCB | 82 | 22’33’4-PeCB | 187 | 22’34’55’6-HpCB |
| 18 | 22’5-TrCB | 87 | 22’345’-PeCB | 194 | 22’33’44’55’-OcCB |
| 19 | 22’6-TrCB | 99 | 22’44’5-PeCB | 195 | 22’33’44’56-OcCB |
| 22 | 234’-TrCB | 110 | 233’4’6-PeCB | 199 | 22’33’455’6’-OcCB |
| 25 | 23’4-TrCB | 138 | 22’344’5’-HxCB | 203 | 22’344’55’6-OcCB |
| 28 | 244’-TrCB | 146 | 22’34’55’-HxCB | 206 | 22’33’44’55’6-NoCB |
| **PCB Mix C-CS-02** | | | | | |
| **BZ#** | **Structure** | **BZ#** | **Structure** | **BZ#** | **Structure** |
| 5 | 23-DiCB | 48 | 22’45-TeCB | 141 | 22’3455’-HxCB |
| 7 | 24-DiCB | 60 | 2344’-TeCB | 149 | 22’34’5’6-HxCB |
| 10 | 26-DiCB | 70 | 23’4’5-TeCB | 164 | 233’4’5’6-HxCB |
| 17 | 22’4-TrCB | 83 | 22’33’5-PeCB | 170 | 22’33’44’5-HpCB |
| 24 | 236-TrCB | 84 | 22’33’6-PeCB | 171 | 22’33’44’6-HpCB |
| 26 | 23’5-TrCB | 95 | 22’35’6-PeCB | 172 | 22’33’455’-HpCB |
| 31 | 24’5-TrCB | 103 | 22’45’6-PeCB | 178 | 22’33’55’6-HpCB |
| 32 | 24’6-TrCB | 107 | 233’4’5-PeCB | 183 | 22’344’5’6-HpCB |
| 37 | 344’-TrCB | 115 | 2344’6-PeCB | 193 | 233’4’55’6-HpCB |
| 41 | 22’34-TeCB | 131 | 22’33’46-HxCB | 196 | 22’33’44’56’-OcCB |
| 45 | 22’36-TeCB | 132 | 22’33’46’-HxCB | 197 | 22’33’44’66’-OcCB |
| 46 | 22’36’-TeCB | 135 | 22’33’56’-HxCB | 205 | 233’44’55’6-OcCB |
| **PCB Mix C-CS-03** | | | | | |
| **BZ#** | **Structure** | **BZ#** | **Structure** | **BZ#** | **Structure** |
| 15 | 44’-DiCB | 92 | 22’355’-PeCB | 144 | 22’345’6-HxCB |
| 20 | 233’-TrCB | 93 | 22’356-PeCB | 151 | 22’355’6-HxCB |
| 27 | 23’6-TrCB | 101 | 22’455’-PeCB | **157** | **233’44’5’-HxCB** |
| 29 | 245-TrCB | **105** | **233’44’-PeCB** | 158 | 233’44’6-HxCB |
| 34 | 23’5’-TrCB | **118** | **23’44’5-PeCB** | 190 | 233’44’56-HpCB |
| 40 | 22’33’-TeCB | 119 | 23’44’6-PeCB | 191 | 233’44’5’6-HpCB |
| 42 | 22’34’-TeCB | 128 | 22’33’44’-HxCB | 207 | 22’33’44’566’-NoCB |
| 47 | 22’44’-TeCB | 134 | 22’33’56-HxCB | 208 | 22’33’455’66’-NoCB |
| 69 | 23’46-TeCB | 136 | 22’33’66’-HxCB | 209 | 22’33’44’55’66’-DeCB |

Table C.2 PCB composition of the AccuStandard C-CS-01 to C-CS-09 mixes.
*(Table continues overleaf)*

**PCB Mix C-CS-04**

| BZ# | Structure | BZ# | Structure | BZ# | Structure |
|---|---|---|---|---|---|
| 13 | 34’-DiCB | **81** | **344’5-TeCB** | 163 | 233’4’56-HxCB |
| 14 | 35-DiCB | 90 | 22’34’5-PeCB | 165 | 233’55’6-HxCB |
| 35 | 33’4-TrCB | 100 | 22’44’6-PeCB | 175 | 22’33’45’6-HpCB |
| 51 | 22’46’-TeCB | 117 | 234’56-PeCB | 200 | 22’33’4566’-OcCB |
| 53 | 22’56’-TeCB | 122 | 233’4’5’-PeCB | 201 | 22’33’45’66’-OcCB |
| 54 | 22’66’-TeCB | 124 | 23’4’55’-PeCB | 202 | 22’33’55’66’-OcCB |
| 73 | 23’5’6-TeCB | 130 | 22’33’45’-HxCB | | |
| 75 | 244’6-TeCB | 154 | 22’44’56’-HxCB | | |

**PCB Mix C-CS-05**

| BZ# | Structure | BZ# | Structure | BZ# | Structure |
|---|---|---|---|---|---|
| 12 | 34-DiCB | 85 | 22’344’-PeCB | 137 | 22’344’5-HxCB |
| 33 | 23’4’-TrCB | 91 | 22’34’6-PeCB | **156** | **233’44’5-HxCB** |
| 49 | 22’45’-TeCB | 97 | 22’34’5’-PeCB | **167** | **23’44’55’-HxCB** |
| 59 | 233’6-TeCB | 104 | 22’466’-PeCB | 176 | 22’33’466’-HpCB |
| 63 | 234’5-TeCB | **114** | **2344’5-PeCB** | 185 | 22’3455’6-HpCB |
| 64 | 234’6-TeCB | **123** | **23’44’5’-PeCB** | **189** | **233’44’55’-HpCB** |
| **77** | **33’44’-TeCB** | 129 | 22’33’45-HxCB | | |

**PCB Mix C-CS-06**

| BZ# | Structure | BZ# | Structure | BZ# | Structure |
|---|---|---|---|---|---|
| 11 | 33’-DiCB | 65 | 2356-TeCB | 133 | 22’33’55’-HxCB |
| 21 | 234-TrCB | 86 | 22’345-PeCB | 139 | 22’344’6-HxCB |
| 38 | 345-TrCB | 102 | 22’456’-PeCB | 145 | 22’3466’-HxCB |
| 50 | 22’46-TeCB | 113 | 233’5’6-PeCB | 161 | 233’45’6-HxCB |
| 57 | 233’5-TeCB | **126** | **33’44’5-PeCB** | **169** | **33’44’55’-HxCB** |
| 61 | 2345-TeCB | 127 | 33’455’-PeCB | 181 | 22’344’56-HpCB |

**PCB Mix C-CS-07**

| BZ# | Structure | BZ# | Structure | BZ# | Structure |
|---|---|---|---|---|---|
| 36 | 33’5-TrCB | 96 | 22’366’-PeCB | 166 | 2344’56-HxCB |
| 72 | 23’55’-TeCB | 98 | 22’34’6’-PeCB | 182 | 22’344’56’-HpCB |
| 78 | 33’45-TeCB | 106 | 233’45-PeCB | 184 | 22’344’66’-HpCB |
| 79 | 33’45’-TeCB | 108 | 233’45’-PeCB | 204 | 22’344’566’-OcCB |
| 89 | 22’346’-PeCB | 152 | 22’3566’-HxCB | | |

**PCB Mix C-CS-08**

| BZ# | Structure | BZ# | Structure | BZ# | Structure |
|---|---|---|---|---|---|
| 30 | 246-TrCB | 76 | 23’4’5’-TeCB | 159 | 233’455’-HxCB |
| 43 | 22’35-TeCB | 109 | 233’46-PeCB | 186 | 22’34566’-HpCB |
| 55 | 233’4-TeCB | 112 | 233’56-PeCB | 192 | 233’455’6-HpCB |
| 58 | 233’5’-TeCB | 120 | 23’455’-PeCB | 198 | 22’33’455’6-OcCB |

**PCB Mix C-CS-09**

| BZ# | Structure | BZ# | Structure | BZ# | Structure |
|---|---|---|---|---|---|
| 23 | 235-TrCB | 111 | 233’55’-PeCB | 148 | 22’34’56’-HxCB |
| 39 | 34’5-TrCB | 116 | 23456-PeCB | 150 | 22’34’66’-HxCB |
| 62 | 2346-TeCB | 121 | 23’45’6-PeCB | 155 | 22’44’66’-HxCB |
| 68 | 23’45’-TeCB | 125 | 23’4’5’6-PeCB | 160 | 233’456-HxCB |
| 80 | 33’55’-TeCB | 140 | 22’344’6’-HxCB | 162 | 233’4’55’-HxCB |
| 88 | 22’346-PeCB | 142 | 22’3456-HxCB | 168 | 23’44’5’6-HxCB |
| 94 | 22’356’-PeCB | 143 | 22’3456’-HxCB | 188 | 22’34’566’-HpCB |

Table C.2 (continued) PCB composition of the AccuStandard C-CS-01 to C-CS-09 mixes.

Table C.3 lists the PCB congeners found in each of the RPCM-1668-A to -E mixes supplied by Ultra-Scientific* (North Kingstown, RI, USA). The 12 WHO toxic congeners are indicated by bold type.

| **PCB Mix RPCM 1668-A** | | | | | |
|---|---|---|---|---|---|
| **BZ#** | **Structure** | **BZ#** | **Structure** | **BZ#** | **Structure** |
| 2 | 3-MoCB | 79 | 33’45’-TeCB | 151 | 22’355’6-HxCB |
| 6 | 23’-DiCB | **81** | **344’5-TeCB** | 152 | 22’3566’-HxCB |
| 8 | 24’-DiCB | 82 | 22’33’4-PeCB | 153 | 22’44’55’-HxCB |
| 9 | 25-DiCB | 83 | 22’33’5-PeCB | **156** | **233’44’5-HxCB** |
| 10 | 26-DiCB | 85 | 22’344’-PeCB | 159 | 233’455’-HxCB |
| 11 | 33’-DiCB | 87 | 22’345’-PeCB | 161 | 233’45’6-HxCB |
| 14 | 35-DiCB | 88 | 22’346-PeCB | 166 | 2344’56-HxCB |
| 26 | 23’5-TrCB | 89 | 22’346’-PeCB | **167** | **23’44’55’-HxCB** |
| 27 | 23’6-TrCB | 92 | 22’355’-PeCB | 170 | 22’33’44’5-HpCB |
| 30 | 246-TrCB | 95 | 22’35’6-PeCB | 171 | 22’33’44’6-HpCB |
| 31 | 24’5-TrCB | 96 | 22’366’-PeCB | 172 | 22’33’455’-HpCB |
| 32 | 24’6-TrCB | 103 | 22’45’6-PeCB | 175 | 22’33’45’6-HpCB |
| 33 | 2’34-TrCB | **105** | **233’44’-PeCB** | 176 | 22’33’466’-HpCB |
| 34 | 2’35-TrCB | 106 | 233’45-PeCB | 177 | 22’33’4’56-HpCB |
| 35 | 33’4-TrCB | 113 | 233’5’6-PeCB | 178 | 22’33’55’6-HpCB |
| 36 | 33’5-TrCB | 119 | 23’44’6-PeCB | 179 | 22’33’566’-HpCB |
| 38 | 345-TrCB | 120 | 23’455’-PeCB | 183 | 22’344’5’6-HpCB |
| 41 | 22’34-TeCB | 122 | 2’33’45-PeCB | 190 | 233’44’56-HpCB |
| 45 | 22’36-TeCB | 124 | 2’3455’-PeCB | 191 | 233’44’5’6-HpCB |
| 49 | 22’45’-TeCB | 127 | 33’455’-PeCB | 194 | 22’33’44’55’-OcCB |
| 50 | 22’46-TeCB | 129 | 22’33’45-HxCB | 195 | 22’33’44’56-OcCB |
| 52 | 22’55’-TeCB | 130 | 22’33’45’-HxCB | 196 | 22’33’44’56’-OcCB |
| 57 | 233’5-TeCB | 133 | 22’33’55’-HxCB | 198 | 22’33’455’6-OcCB |
| 63 | 234’5-TeCB | 136 | 22’33’66’-HxCB | 200 | 22’33’4566’-OcCB |
| 66 | 23’44’-TeCB | 142 | 22’3456-HxCB | 201 | 22’33’45’66’-OcCB |
| 72 | 23’55’-TeCB | 143 | 22’3456’-HxCB | 204 | 22’344’566’-OcCB |
| 75 | 244’6-TeCB | 144 | 22’345’6-HxCB | 207 | 22’33’44’566’-NoCB |
| 78 | 33’45-TeCB | 148 | 22’34’56’-HxCB | | |
| **PCB Mix RPCM 1668-B** | | | | | |
| **BZ#** | **Structure** | **BZ#** | **Structure** | **BZ#** | **Structure** |
| 5 | 23-DiCB | 71 | 23’4’6-TeCB | 139 | 22’344’6-HxCB |
| 7 | 24-DiCB | 73 | 23’5’6-TeCB | 145 | 22’3466’-HxCB |
| 12 | 34-DiCB | 90 | 22’34’5-PeCB | 149 | 22’34’5’6-HxCB |
| 18 | 22’5-TrCB | 91 | 22’34’6-PeCB | 150 | 22’34’66’-HxCB |

Table C.3 List of PCBs in the 5 PCB Ultra-Scientific RPCM 1668-A to E mixes.
*(Table continues overleaf)*

---

* PCB-199, 200 and 201 were incorrectly named in the supplied documentation and have been revised here to match current nomenclature (Mills III, Thal and Barney, 2007).

**PCB Mix RPCM 1668-B (continued)**

| BZ# | Structure | BZ# | Structure | BZ# | Structure |
|---|---|---|---|---|---|
| 22 | 234’-TrCB | 94 | 22’356’-PeCB | **157** | **233’44’5’-HxCB** |
| 23 | 235-TrCB | 99 | 22’44’5-PeCB | 160 | 233’456-HxCB |
| 24 | 236-TrCB | 100 | 22’44’6-PeCB | 162 | 233’4’55’-HxCB |
| 28 | 244’-TrCB | 108 | 233’45’-PeCB | 165 | 233’55’6-HxCB |
| 39 | 34’5-TrCB | 109 | 233’46-PeCB | 168 | 23’44’5’6-HxCB |
| 48 | 22’45-TeCB | 111 | 233’55’-PeCB | 181 | 22’344’56-HpCB |
| 51 | 22’46’-TeCB | **114** | **2344’5-PeCB** | 184 | 22’344’66’-HpCB |
| 53 | 22’56’-TeCB | 117 | 234’56-PeCB | 185 | 22’3455’6-HpCB |
| 55 | 233’4-TeCB | **118** | **23’44’5-PeCB** | 186 | 22’34566’-HpCB |
| 58 | 233’5’-TeCB | 121 | 23’45’6-PeCB | 187 | 22’34’55’6-HpCB |
| 60 | 2344’-TeCB | 128 | 22’33’44’-HxCB | 192 | 233’455’6-HpCB |
| 61 | 2345-TeCB | 132 | 22’33’46’-HxCB | 197 | 22’33’44’66’-OcCB |
| 62 | 2346-TeCB | 135 | 22’33’56’-HxCB | 201 | 22’33’455’6’-OcCB |
| 68 | 23’45’-TeCB | 137 | 22’344’5-HxCB | 203 | 22’344’55’6-OcCB |

**PCB Mix RPCM 1668-C**

| BZ# | Structure | BZ# | Structure | BZ# | Structure |
|---|---|---|---|---|---|
| 13 | 34’-DiCB | 80 | 33’55’-TeCB | 146 | 22’34’55’-HxCB |
| 17 | 22’4-TrCB | 84 | 22’33’6-PeCB | 147 | 22’34’56-HxCB |
| 20 | 233’-TrCB | 86 | 22’345-PeCB | 154 | 22’44’56’-HxCB |
| 29 | 245-TrCB | 93 | 22’356-PeCB | 158 | 233’44’6-HxCB |
| 40 | 22’33’-TeCB | 101 | 22’455’-PeCB | 164 | 233’4’5’6-HxCB |
| 46 | 22’36’-TeCB | 107 | 233’4’5-PeCB | 173 | 22’33’456-HpCB |
| 59 | 233’6-TeCB | 112 | 233’56-PeCB | 174 | 22’33’456’-HpCB |
| 65 | 2356-TeCB | 116 | 23456-PeCB | 182 | 22’344’56’-HpCB |
| 67 | 23’45-TeCB | 140 | 22’344’6’-HxCB | 193 | 233’4’55’6-HpCB |
| 76 | 2’345-TeCB | 141 | 22’3455’-HxCB | | |

**PCB Mix RPCM 1668-D**

| BZ# | Structure | BZ# | Structure | BZ# | Structure |
|---|---|---|---|---|---|
| 21 | 234-TrCB | 69 | 23’46-TeCB | **123** | **23’44’5’-PeCB** |
| 25 | 23’4-TrCB | 70 | 23’4’5-TeCB | 131 | 22’33’46-HxCB |
| 42 | 22’34’-TeCB | 97 | 22’3’45-PeCB | 134 | 22’33’56-HxCB |
| 47 | 22’44’-TeCB | 102 | 22’456’-PeCB | 163 | 233’4’56-HxCB |
| 64 | 234’6-TeCB | 115 | 2344’6-PeCB | 180 | 22’344’55’-HpCB |

**PCB Mix RPCM 1668-E**

| BZ# | Structure | BZ# | Structure | BZ# | Structure |
|---|---|---|---|---|---|
| 1 | 2-MoCB | 56 | 233’4’-TeCB | **169** | **33’44’55’-HxCB** |
| 3 | 4-MoCB | 74 | 244’5-TeCB | 188 | 22’34’566’-HpCB |
| 4 | 22’-DiCB | **77** | **33’44’-TeCB** | **189** | **233’44’55’-HpCB** |
| 15 | 44’-DiCB | 98 | 22’3’46-PeCB | 202 | 22’33’55’66’-OcCB |
| 16 | 22’3-TrCB | 104 | 22’466’-PeCB | 205 | 233’44’55’6-OcCB |
| 19 | 22’6-TrCB | 110 | 233’4’6-PeCB | 206 | 22’33’44’55’6-NoCB |
| 37 | 344’-TrCB | 125 | 23’4’5’6-PeCB | 208 | 22’33’455’66’-NoCB |
| 43 | 22’35-TeCB | **126** | **33’44’5-PeCB** | 209 | 22’33’44’55’66’-DeCB |
| 44 | 22’35’-TeCB | 138 | 22’344’5’-HxCB | | |
| 54 | 22’66’-TeCB | 155 | 22’44’66’-HxCB | | |

Table C.3 (continued) List of PCBs in the 5 PCB Ultra-Scientific RPCM 1668-A to -E mixes.

Table C.4 lists the native ($^{12}C_{12}$) and labelled ($^{13}C_{12}$) PCB congeners present in the CS3 mix supplied by Wellington Laboratories, Inc. (Guelph, ON, Canada). The 12 WHO toxic congeners are indicated by bold type. Several PCBs are only present as labelled standards – these are used as clean-up and injection standards rather than for the quantification of native congeners.

| **Native Standards** | | **Labelled Standards** | |
|---|---|---|---|
| **BZ#** | **Name** | **BZ#** | **Name** |
| 1 | 2-MoCB | 1 | $^{13}C_{12}$-2-MoCB |
| 3 | 4-MoCB | 3 | $^{13}C_{12}$-4-MoCB |
| 4 | 22’-DiCB | 4 | $^{13}C_{12}$-22’-DiCB |
| - | | 9 | $^{13}C_{12}$-25-DiCB |
| 15 | 44’-DiCB | 15 | $^{13}C_{12}$-44’-DiCB |
| 19 | 22’6-TrCB | 19 | $^{13}C_{12}$-22’6-TrCB |
| - | | 28 | $^{13}C_{12}$-244’-TrCB |
| 37 | 344’-TrCB | 37 | $^{13}C_{12}$-344’-TrCB |
| - | | 52 | $^{13}C_{12}$-22’55’-TeCB |
| 54 | 22’66’-TeCB | 54 | $^{13}C_{12}$-22’66’-TeCB |
| **77** | **33’44’-TeCB** | **77** | **$^{13}C_{12}$-33’44’-TeCB** |
| **81** | **344’5-TeCB** | **81** | **$^{13}C_{12}$-344’5-TeCB** |
| - | | 101 | $^{13}C_{12}$-22’455’-PeCB |
| 104 | 22’466’-PeCB | 104 | $^{13}C_{12}$-22’466’-PeCB |
| **105** | **233’44’-PeCB** | **105** | **$^{13}C_{12}$-233’44’-PeCB** |
| - | | 111 | $^{13}C_{12}$-233’55’-PeCB |
| **114** | **2344’5-PeCB** | **114** | **$^{13}C_{12}$-2344’5-PeCB** |
| **118** | **23’44’5-PeCB** | **118** | **$^{13}C_{12}$-23’44’5-PeCB** |
| **123** | **23’44’5’-PeCB** | **123** | **$^{13}C_{12}$-23’44’5’-PeCB** |
| **126** | **33’44’5-PeCB** | **126** | **$^{13}C_{12}$-33’44’5-PeCB** |
| - | | 138 | $^{13}C_{12}$-22’344’5’-HxCB |
| 155 | 22’44’66’-HxCB | 155 | $^{13}C_{12}$-22’44’66’-HxCB |
| **156** | **233’44’5-HxCB** | **156** | **$^{13}C_{12}$-233’44’5-HxCB** |
| **157** | **233’44’5’-HxCB** | **157** | **$^{13}C_{12}$-233’44’5’-HxCB** |
| **167** | **23’44’55’-HxCB** | **167** | **$^{13}C_{12}$-23’44’55’-HxCB** |
| **169** | **33’44’55’-HxCB** | **169** | **$^{13}C_{12}$-33’44’55’-HxCB** |
| - | | 178 | $^{13}C_{12}$-22’33’55’6-HpCB |
| 188 | 22’34’566’-HpCB | 188 | $^{13}C_{12}$-22’34’566’-HpCB |
| **189** | **233’44’55’-HpCB** | **189** | **$^{13}C_{12}$-233’44’55’-HpCB** |
| - | | 194 | $^{13}C_{12}$-22’33’44’55’-OcCB |
| 202 | 22’33’55’66’-OcCB | 202 | $^{13}C_{12}$-22’33’55’66’-OcCB |
| 205 | 233’44’55’6-OcCB | 205 | $^{13}C_{12}$-233’44’55’6-OcCB |
| 206 | 22’33’44’55’6-NoCB | 206 | $^{13}C_{12}$-22’33’44’55’6-NoCB |
| 208 | 22’33’455’66’-NoCB | 208 | $^{13}C_{12}$-22’33’455’66’-NoCB |
| 209 | 22’33’44’55’66’-DeCB | 209 | $^{13}C_{12}$-22’33’44’55’66’-DeCB |

Table C.4 List of PCBs in the Wellington Laboratories’ 1668C CS3 mix.

Table C.5 lists the chemical standards used in the Waters' CCS calibration mix and their expected CCS values. (These values are based on the averages from multiple runs on an instrument calibrated using other compounds of known CCS acquired using electrospray ionisation.)

| **CCS Calibration Standard** | **CCS, Å$^2$** |
|---|---|
| 1,2-Dichlorobenzene | 117.4 |
| 2,3,7,8-Tetrachlorodibenzo-*p*-dioxin | 155.9 |
| Anthracene | 132.6 |
| Benzo(ghi)perylene | 153.7 |
| Endosulphan | 167.7 |
| Hexachlorobenzene | 136.1 |
| Octafluoronaphthalene | 130.6 |
| Phenanthrene | 133.0 |

Table C.5 List of standards used for ion mobility CCS calibration and their expected CCS values.

## C.4 Commercial/external software used throughout the PhD study

The following is a list of commercial or other externally sourced software used throughout this thesis:

*Avogadro*

An open-source molecular builder and visualization tool. Version 1.2.0 https://avogadro.cc/docs (Hanwell *et al.*, 2012)

*ChemCraft*

Graphical software for visualisation of quantum chemistry computations. Version 1.8 https://www.chemcraftprog.com

*ChemDraw*

Chemical structure drawing software. Version 16.0.1.4 http://www.perkinelmer.co.uk/category/chemdraw

*CrossArea*

A program (Univ. of Leeds) to provide collisional cross section area estimates based on the projection approximation method. Version dated 14-Sep-2018 https://github.com/tumbling-cross-section (Smith *et al.*, 2009)

*DriftScope*

Ion mobility data processing and visualisation software.
Version 2.9 http://www.waters.com

*Impact*

A program (Univ. of Oxford) to provide collisional cross section area estimates based on projection approximation and the trajectory method. Version 0.9.1 http://impact.chem.ox.ac.uk (Marklund *et al.*, 2015)

*MassLynx*

Mass spectrometry data acquisition and processing software.
Versions 4.1 and 4.2 http://www.waters.com

*MATLAB*

Numerical computing and analysis software. Version R2018b
https://uk.mathworks.com/products/matlab.html

*Microsoft Office (Word, Excel and PowerPoint)*

Versions 2010-2016 and Office 365 https://www.microsoft.com

*Orca*

A general-purpose quantum chemistry program package using density functional theory and semi-empirical methods. Version 4.0.1.2 https://orcaforum.kofo.mpg.de (Neese, 2012)

*RefWorks*

A web-based reference and citation management utility.
https://refworks.proquest.com

# Appendix D

# Tables of the Key MS Instrument Parameters

---

## D.1 GC-HRMS (EI)

| | |
|---|---|
| MS model | Waters AutoSpec-Ultima |
| Polarity | Positive ion |
| Source mode | Electron ionisation |
| Electron energy | 34 eV |
| Trap current | 500 µA |
| Source temperature | 280 °C |
| Photomultiplier voltage | 340 V |
| Accelerating voltage | 8,000 V (nominal) |
| Resolution (10% valley definition) | 10,000 (nominal) |
| Data format | Selected ion monitoring (SIM) |
| | |
| GC model | Agilent 6890 |
| Auto-sampler model | CTC Analytics GC-PAL |
| GC column type | Supelco SPB-Octyl |
| GC column length | 30 m |
| GC column internal diameter | 0.25 mm |
| GC column film thickness | 0.25 µm |
| Sample solvent | Nonane |
| Injector temperature | 270 °C |
| Injection volume | 1 µl |
| Injection mode | Splitless |
| Carrier gas | Helium |
| Gas (He) control mode | Constant flow |
| Gas (He) flow rate | 1.2 ml/min |
| Purge time | 1.0 min |
| Initial oven temperature | 90 °C |
| Initial hold time | 2.0 mins |
| Oven ramp rate #1 | 15 °C/min |
| Final temperature #1 | 150 °C |
| Hold time #1 | 0.0 mins |
| Oven ramp rate #2 | 3.0 °C/min |
| Final temperature #2 | 280 °C |
| Hold time #2 | 3.0 mins |

Table D.1 Key data acquisition parameters used for the GC-HRMS analyses (AutoSpec-Ultima, EI+).

## D.2 GC-Q-IMS-TOF (APCI)

| | |
|---|---|
| MS model | Waters Synapt G2-S |
| Polarity | Positive ion |
| Source mode | Atmospheric pressure chemical ionisation |
| Corona voltage | 5 kV |
| Corona current | 2 µA |
| Source temperature | 150 °C |
| Mass range | *m/z* 150–520 |
| Scan time | 0.5 s |
| Inter-scan time | 0.015 s |
| Data format (non-IMS expt.) | Centroid |
| Data format (IMS expt.) | Continuum |
| Resolution (50% valley definition) | 18,000 (nominal) |
| Collision cell gas | Argon |
| Collision cell (Ar) pressure | $1.0 \times 10^{-3} – 2.4 \times 10^{-2}$ mbar |
| Collision energy | 0–40 eV |
| Cone, auxiliary & make-up gas | Nitrogen |
| Cone gas ($N_2$) flow | 210 L/hr |
| Auxiliary gas ($N_2$) flow | 200 L/hr |
| Make-up gas ($N_2$) flow | 350 mL/min |
| Ion mobility cell gas | Nitrogen |
| Ion mobility cell ($N_2$) pressure | 3.29 mbar |
| Ion mobility wave velocity | 300 m/s |
| Ion mobility wave delay | 1000 µs |
| | |
| GC model | Agilent 7890 |
| Auto-sampler model | Agilent 7693 |

Table D.2 Key data acquisition parameters used for the GC-Q-IMS-TOF analyses (Synapt G2-S, APCI+).
*(Table continues overleaf)*

| 1. SPB-Octyl GC column experiments | |
|---|---|
| Column type | Supelco SPB-Octyl |
| Column length | 30 m |
| Column internal diameter | 0.25 mm |
| Column film thickness | 0.25 µm |
| Solvent | Nonane |
| Injector temperature | 270 °C |
| Injection volume | 0.7 µl |
| Injection mode | Splitless |
| Carrier gas | Helium |
| Gas (He) control mode | Constant flow |
| Gas (He) flow rate | 1.7 ml/min |
| Purge time | 1.0 min |
| Initial oven temperature | 90 °C |
| Initial hold time | 2.0 mins |
| Oven ramp rate #1 | 15 °C/min |
| Final temperature #1 | 150 °C |
| Hold time #1 | 0.0 mins |
| Oven ramp rate #2 | 3.0 °C/min |
| Final temperature #2 | 280 °C |
| Hold time #2 | 3.0 mins |
| | |
| 2. SPB-1 GC column experiments | |
| Column type | Supelco SPB-1 |
| Column length | 30 m |
| Column internal diameter | 0.25 mm |
| Column film thickness | 0.25 µm |
| Solvent | Nonane |
| Injector temperature | 270 °C |
| Injection volume | 1.0 µl |
| Injection mode | Splitless |
| Carrier gas | Helium |
| Gas (He) control mode | Constant flow |
| Gas (He) flow rate | 1.4 ml/min |
| Purge time | 2.0 min |
| Initial oven temperature | 90 °C |
| Initial hold time | 2.0 mins |
| Oven ramp rate #1 | 15 °C/min |
| Final temperature #1 | 150 °C |
| Hold time #1 | 0.0 mins |
| Oven ramp rate #2 | 3.0 °C/min |
| Final temperature #2 | 280 °C |
| Hold time #2 | 7.0 mins |

Table D.2 (continued) Key data acquisition parameters used for the GC-Q-IMS-TOF analyses (Synapt G2-S, APCI+).

## D.3 GC-MS/MS (EI)

| | |
|---|---|
| MS model | Micromass Quattro (Triple-Quad) |
| Polarity | Positive ion |
| Source mode | Electron ionisation |
| Source temperature | 200 °C |
| Electron energy | 34 eV |
| Trap current | 50 µA |
| Detector voltage | 500 V |
| Resolution | Unit mass |
| Collision cell gas | Argon |
| Collision cell pressure | $10^{-3}$ mbar |
| Data format | Multiple reaction monitoring (MRM) |
| | |
| GC model | Agilent 6890 |
| GC column type | J&W DB-5ms |
| GC column length | 30 m |
| GC column internal diameter | 0.25 mm |
| GC column film thickness | 0.25 µm |
| Sample solvent | Hexane |
| Injector temperature | 280 °C |
| Injection volume | 1 µl |
| Injection mode | Split 10:1 |
| Carrier gas | Helium |
| Gas (He) control mode | Constant flow |
| Gas (He) flow rate | 1.0 ml/min |
| Initial oven temperature | 80 °C |
| Initial hold time | 2.0 mins |
| Oven ramp rate #1 | 20 °C/min |
| Final temperature #1 | 200 °C |
| Hold time #1 | 5.0 mins |
| Oven ramp rate #2 | 10.0 °C/min |
| Final temperature #2 | 280 °C |
| Hold time #2 | 10.0 mins |

Table D.3 Key data acquisition parameters used for the GC-MS/MS analyses (Quattro, EI+).

## D.4 GC-TOF (EI)

| | |
|---|---|
| MS model | Waters GCT-Premier |
| Polarity | Positive ion |
| Source mode | Electron ionisation |
| Source temperature | 250 °C |
| Electron energy | 34 eV |
| Trap current | 250 µA |
| MCP voltage | 2,300 V |
| Resolution (FWHM) | 7,500 (nominal) |
| Mass range | *m/z* 50–650 |
| Scan duration | 0.2 s |
| Inter-scan duration | 0.1 s |
| | |
| GC model | Agilent 6890 |
| Auto-sampler model | CTC Analytics GC-PAL |
| GC column type | Supelco SPB-Octyl |
| GC column length | 30 m |
| GC column internal diameter | 0.25 mm |
| CGC column film thickness | 0.25 µm |
| Sample solvent | Nonane |
| Injector temperature | 270 °C |
| Injection volume | 1 µl |
| Injection mode | Splitless |
| Carrier gas | Helium |
| Gas (He) control mode | Constant flow |
| Gas (He) flow rate | 1.2 ml/min |
| Purge time | 1.0 min |
| Initial oven temperature | 100 °C |
| Initial hold time | 2.0 mins |
| Oven ramp rate #1 | 15 °C/min |
| Final temperature #1 | 150 °C |
| Hold time #1 | 0.0 mins |
| Oven ramp rate #2 | 3.0 °C/min |
| Final temperature #2 | 280 °C |
| Hold time #2 | 2.0 mins |

Table D.4 Key data acquisition parameters used for the GC-TOF analyses (GCT-Premier, EI+).